Backside absorbing layer microscopy : a new tool for the investigation of 2D materials

Kévin Jaouen

université PARIS-SACLAY

NNT : 2019SACLS296

Thèse de doctorat

Backside Absorbing Layer Microscopy: a new tool for the investigation of 2D materials

Thèse de doctorat de l'Université Paris-Saclay
préparée à l'Université Paris-Sud

Ecole doctorale n°575 Electrical, Optical, Bio: Physics and Engineering (EOBE)
Spécialité de doctorat : Physique

Thèse présentée et soutenue à Saint-Aubin, le 16/10/2019, par

KÉVIN JAOUEN

Composition du Jury :

Anna Proust Professeure, Sorbonne Université (IPCM)	Présidente
Emmanuel Maisonhaute Professeur, Sorbonne Université (LISE)	Rapporteur
Erik Dujardin Directeur de Recherche, CNRS (CEMES)	Rapporteur
Abdelkarim Ouerghi Directeur de Recherche, CNRS (C2N)	Examinateur
Vincent Derycke Chercheur, CEA (NIMBE, LICSEN)	Directeur de thèse
Renaud Cornut Chercheur, CEA (NIMBE, LICSEN)	Co-encadrant de thèse

In the PDF version of this manuscript, the section and figure numbers can be clicked to be redirected to the position of the section or figure.

The references in the text are linked to the reference section, which then provide a direct link to the online version at the editor website.

Some of the results were extracted from movies. These movies are accessible through the following links:

Movie-1: *Optical monitoring of NBD dimer photodeposition on graphene oxide*
https://youtu.be/0xnhTLa5z8k

Movie-2: *Electrografting of TBPFe on gold electrode by cyclic voltammetry*
https://youtu.be/n8jtcBx5UXk

Movie-3: *Electrodeposition of copper on gold by chronoamperometry at -140 mV*
https://youtu.be/dnyClC8RHUA

Movie-4: *Electrodeposition of copper on gold by chronoamperometry at -160 mV*
https://youtu.be/G7un94zrw0Y

Movie-5: *Electrodeposition of copper on GO by chronoamperometry at 0 V*
https://youtu.be/SfoJLhkmGEA

Movie-6: *Electrodeposition of copper on GO by cyclic voltammetry*
https://youtu.be/OXbbFoGmlUA

Movie-7: *Electrodeposition of copper on ErGO by cyclic voltammetry*
https://youtu.be/73O8l_AO1Ug

The publications related to this work are:

[1] K. Jaouen, R. Cornut, D. Ausserré, S. Campidelli, and V. Derycke, *Ideal optical contrast for 2D material observation using bi-layer antireflection absorbing substrates*, **Nanoscale**, 11 (13), 6129-6135, **2019**. http://dx.doi.org/10.1039/C8NR09983A

[2] K. Jaouen, F. Lebon, B. Jousselme, S. Campidelli, R. Cornut, and V. Derycke, *Optical monitoring of diazonium electrografting on gold and graphene oxide using Backside Absorbing Layer Microscopy*, **submitted**.

[3] S. Campidelli, R. Abou Khachfe, K. Jaouen, J. Monteiller, C. Amra, V. Derycke, and D. Ausserré, *Backside absorbing layer microscopy: Watching graphene chemistry*, **Science Advances**, 3 (5), e1601724, **2017**. http://dx.doi.org/10.1126/sciadv.1601724

[4] K. Jaouen, O. Henrotte, S. Campidelli, B. Jousselme, V. Derycke, and R. Cornut, *Localized electrochemistry for the investigation and the modification of 2D materials*, **Applied Materials today**, 8, 116-124, **2017**. http://dx.doi.org/10.1016/j.apmt.2017.05.001

[5] O. Henrotte, T. Bottein, H. Casademont, K. Jaouen, T. Bourgeteau, S. Campidelli, V. Derycke, B. Jousselme, and R. Cornut, *Electronic Transport of MoS_2 Monolayered Flakes Investigated by Scanning Electrochemical Microscopy*, **Chemphyschem**, 18 (19), 2777-2781, **2017**. http://dx.doi.org/10.1002/cphc.201700343

Notations

2D	2 Dimensions
ACN	Acetonitrile
AFM	Atomic Force Microscopy
AR	Anti Reflective
ARA	Anti Reflective Absorbing
ARPES	Angle-Resolved PhotoEmission Spectroscopy
BALM	Backside Absorbing Layer Microscopy
CE	Counter Electrode
CEA	Commissariat à l'Énergie Atomique et aux énergies alternatives
CNT	Carbon NanoTube
CV	Cyclic Voltammetry
CVD	Chemical Vapor Deposition
DMSO	DiMethyl SulfOxide
EDL	Electrical Double Layer
EIS	Electrochemical Impedance Spectroscopy
EQCM	Electrochemical Quartz Crystal Microbalance
ErGO	Electrochemically reduced Graphene Oxide
FQM	Fluorescence Quenching Microscopy
FRET	Fluorescence Resonance Energy Transfer
FTIR	Fourrier-Transform InfraRed spectroscopy
FWHM	Full Width-Half Maximum
GO	Graphene Oxide
***h*-BN**	hexagonal Boron Nitride
HER	Hydrogen Evolution Reaction
HOPG	Highly Oriented Pyrolytic Graphite
HRTEM	High-Resolution Transmission Electron Microscopy
IPA	IsoPropyl Alcohol
IRM	Interference Reflection optical Microscopy
ITO	Indium Tin Oxide
KPFM	Kelvin Prove Force Microscopy
LAO	Local Anodic Oxidation
LICSEN	Laboratoire Innovation, Chimie des Surfaces Et Nanosciences
MIM	Microwave Impedance Microscopy

MoS_2	Molybdenum disulfide
MS	Mass Spectroscopy
NA	Numerical Aperture
NBDT	4-Nitrobenzenediazonium tetrafluoroborate
NIMBE	Nanosciences et Innovation pour les Matériaux, la Biomédecine et l'Énergie
OCP	Open Circuit Potential
ORR	Oxygen Reduction Reaction
Ox	Oxidant
PDMS	Poly(dimethylsiloxane)
PIMI	Polarization parameter Indirect Microscopic Imaging
PMMA	Poly(methyl methacrylate)
QRCE	Quasi Counter Reference Electrode
qSTORM	quenching Stochastic Optical Reconstruction Microscopy
RE	Reference Electrode
Red	Reductant
rGO	reduced Graphene Oxide
SAM	Self-Assembled Monolayer
SECCM	Scanning ElectroChemical Cell Microscopy
SECM	Scanning ElectroChemical Microscopy
SEM	Scanning Electron Microscopy
SERS	Surface-Enhanced Raman Spectroscopy
SHG	Second Harmonic Generation
SNOM	Scanning Near-field Optical Microscopy
SPEM	Scanning PhotoElectron Microscopy
SPM	Scanning Probe Microscopy
STED	Stimulated Emission Depletion Microscopy
STM	Scanning Tunneling Microscopy
STS	Scanning Tunneling Spectroscopy
TBAP	Tetrabutylammonium hexafluorophosphate
TBPFe	Tris-bipyridine Iron (III)
TEM	Transmisson Electron Microscopy
TEPL	Tip-Enhanced PhotoLuminescence
TERS	Tip-Enhanced Raman Spectroscopy
THG	Third Harmonic Generation
THz TDS	TeraHertz Time-Domain Spectroscopy
TIRF	Total Internal Reflection Fluorescence
TMD	Transition Metal Dichalcogenide
UPD	Under Potential Deposition
UV	Ultra-Violet
WE	Working Electrode
WS_2	Tungsten disulfide
XPS	X-ray Photoelectron Spectroscopy
XRD	X-Ray Diffraction

Contents

Introduction

Optical microscopy is a simple yet powerful characterization tool which notably allowed the first observation of graphene despite its ultimate single-atom thickness.

Soon after graphene, other 2D materials were discovered or synthesized with the same key role of optical microscopy techniques. 2D materials present a large spectrum of interesting properties (optical, electrical, chemical, mechanical, etc.) and are expected to contribute in many fields of applications. But their nanoscale size makes them especially difficult to characterize. 2D materials are heterogeneous (edges, defects, single-layer *vs.* multilayers, etc.) and they also present a large dispersion of their properties depending on the synthesis, transfer and aging conditions. For some applications, the material heterogeneity can be the reason of its outstanding properties. As an example, some defects and the layer edges in graphene or MoS_2 are responsible for some of their attractive catalytic properties. Being able to probe locally the properties of 2D materials is key to understand the structure-properties relations and is a prerequisite for the design of efficient devices based on materials with perfectly controlled structures.

At present, most of the techniques for *local* study of 2D materials are based on electron microscopy and scanning probe techniques, whereas the use of wide-field microscopy techniques is still mostly limited to the initial step of the studies (to locate the material flakes and estimate their thickness). Nevertheless, the discovery of graphene was only possible thanks to an optical microscope. Graphene was deposited on a special substrate having anti-reflective properties which made few layers graphene observable. Since then, enhanced optical microscopy techniques using this principle were improved, optimized and applied to 2D materials.

Recently, D. Ausserré from IMMM (CNRS and Maine University) introduced a new type of microscopy technique based on a special type of anti-reflective coatings, light absorbing materials, associated with the inverted microscope observation geometry (so that light comes from the glass side). This contrast-enhanced optical microscopy

technique is named Backside Absorbing Layer Microscopy (BALM). It is particularly adapted to the study of ultrathin materials both in air and in liquids and its geometry allows its combination with an electrochemical setup.

In this context, the objective of this thesis is to evaluate the potential of the BALM technique in order to study *in situ* the local properties (optical, chemical and electrochemical) of 2D materials, without using a scanning probe.

The manuscript is organized as follows:

In a first chapter, the different techniques used to investigate the local properties of 2D materials are reviewed. A particular attention is given to the measurement scale, to the *in situ* studies (*i.e.* techniques able to follow a phenomenon directly where and when it takes place) and to the techniques providing local information without scanning a probe.

Chapter 2 introduces the principles of anti-reflective coatings in optical microscopy and the way they produce contrast-enhanced images of 2D materials. The specificities of BALM are described and compared with those of conventional anti-reflection techniques. The status of the BALM technique at the beginning of this thesis is presented. Then several new experiments are presented and showed different ways to improve the anti-reflective conditions for the visualization of 2D materials. The investigation of molecular layer deposition dynamics notably shows the extreme sensitivity of BALM for such measurements. The contribution of multilayers anti-reflective coatings to increase the contrast during the observation of 2D materials, and the new functionalities they bring to the BALM set-up are then showcased.

Chapter 3 presents the combination of BALM with electrochemistry. It first shows the influence of basic electrochemistry experiments on the optical signal. In particular, it shows how the changes in the electrochemical double-layer (EDL) during a voltammetry experiment lead to a measurable optical signal. Then, three studies coupling BALM and electrochemistry are detailed: first, the electrochemical reduction of graphene oxide is performed and optically monitored *in situ*. Then, the dynamic of diazonium salts electrografting is investigated at the local scale on gold electrodes, graphene oxide (GO) and reduced graphene oxide (rGO). Finally, the electrodeposition of copper is studied on gold, GO and rGO. The influence of the reduction state of GO on interlayer intercalation processes is notably studied.

In a concluding chapter, the main achievements of this work are first summarized and used to analyse the main assets and limitations of the technique. Then, further developments of the BALM microscopy and its combination with complementary techniques are discussed.

Chapter I

State of the art for local study of 2D materials

This chapter reviews the different techniques to *locally* study and characterize 2D materials. Optical techniques and local-electrochemistry techniques are more specifically emphasized. The choice was made to avoid a generic introduction on the 2D materials themselves, which are the subject of many comprehensive review articles. [6–11] Concentrating on the instrumental aspects of their study is more directly related to the core of the work and helps highlighting the associated challenges.

I.1 Observation of 2D materials

The discovery of graphene, [12] relied on two techniques, optical microscopy and Atomic Force Microscopy (AFM). The latter was essential in order to determine the number of atomic layers stacked within the aggregates produced by mechanical exfoliation of graphite. It led to the first characterization of single-layer graphene sheets. To do so, it was also coupled to Scanning Electron Microscopy (SEM) for imaging the field-effect devices. Since then, these three techniques remained predominant as a first characterization step in most studies. AFM and SEM for 2D material observation will not be described hereafter as it is already extensively done in the literature. [13]

The crucial role that optical microscopy played in the field of 2D materials, from its very beginning, is of special importance in the context of this thesis. Indeed, the fact that graphene was not discovered sooner was well explained by Geim and Novoselov in their first review article about graphene in 2007 ("The rise of graphene" [6]):

> *"The problem is that graphene crystallites left on a substrate are extremely rare and hidden in a 'haystack' of thousands of thick (graphite) flakes. So, even if one were deliberately searching for graphene by using modern techniques for studying atomically thin materials, it would be impossible to find those several micrometre-size crystallites dispersed over, typically, a 1-cm^2 area. For example, scanning-probe microscopy has too low throughput to search for graphene, whereas scanning electron microscopy is unsuitable because of the absence of clear signatures for the number of atomic layers."*

The innovative approach of the 2010 Noble Prize laureates was linked to the use of an optical microscope in a configuration capable of making few-layer graphene visible. This simple full-field microscope drastically reduces the time-effort to find interesting areas having as little stacked graphene layers as possible. Then AFM could be used on these areas to identify unambiguously single-layer graphene at the edges of the thinnest stacks. An example of a graphene deposition observed with an optical microscope is shown in Fig. I.1.a. [12] It first shows the chaos obtained after the deposition of graphene by mechanical exfoliation of graphite (the so-called scotch-tape method). On this image, the thickness of several flakes was measured by AFM and compared to their visibility. Few-layer graphene flakes as thin as 2 nm were observable using this fast optical technique.

The ultrathin material is visible because it was deposited on a special substrate which reflects very little light. This substrate is an oxidized silicon wafer with a precisely controlled SiO_2 thickness of 300 nm. Thanks to destructive interferences, this dielectric layer acts as an anti-reflective coating which provides contrast-enhanced. A deeper analysis of this type of anti-reflective substrates is presented in chapter II (section II.1). Since the discovery of graphene, this type of substrates have been improved and are routinely used for all types of 2D materials. [14, 17–21] An example of a single-layer Graphene Oxide flake deposited on silicon covered with 70 nm of Si_3N_4/Si is presented in Fig. I.1.b. [14]

Beside this interference based optical microscopy technique, which is still one of the most used techniques to locate 2D materials on surfaces, many other techniques were developed for the observation of single-layer materials. Two main optical techniques are notably employed: ellipsometry imaging and fluorescence quenching microscopy (FQM). The first one uses the modification of the polarization of the light reflected or transmitted by a material deposited on a surface. It was used to image many 2D ma-

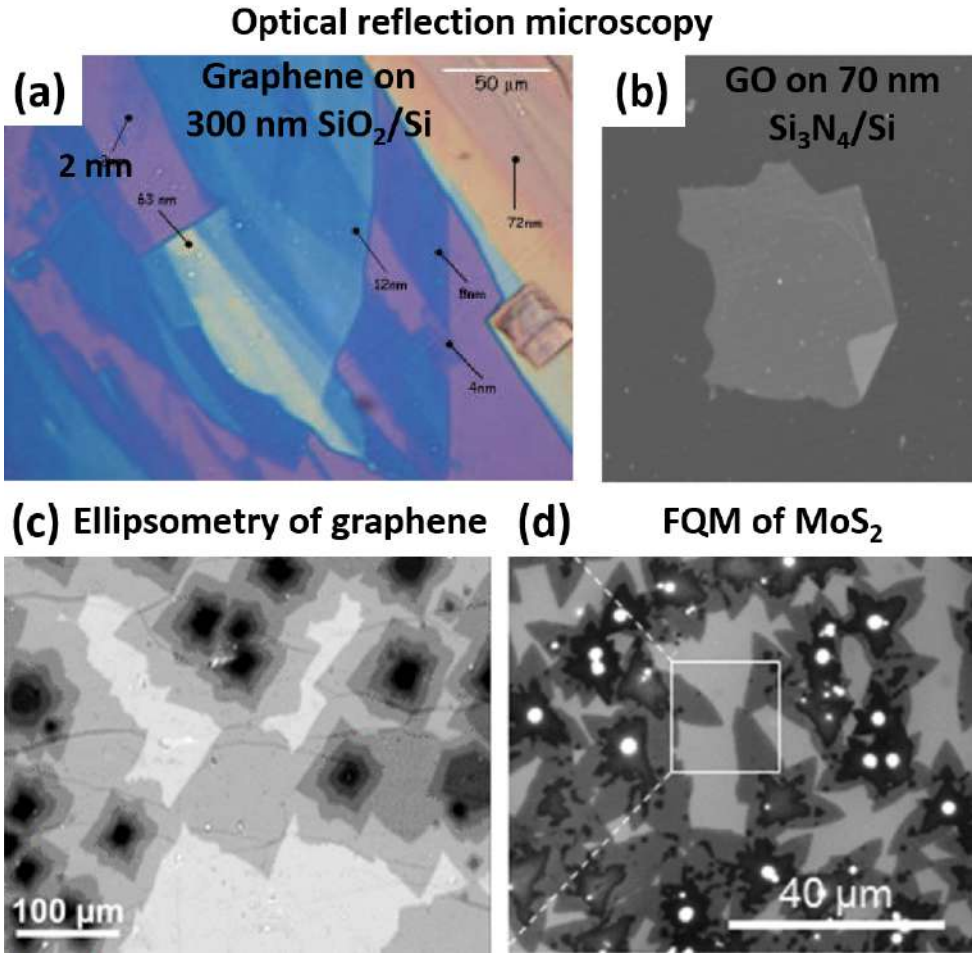

Figure I.1: Optical microscopy techniques to image 2D materials. (a) Original first observation of graphene in 2004 by optical reflection microscopy on a 300 nm SiO_2/Si substrate, reprinted with permission from [12], **(b)** optimized imaging of Graphene Oxide (GO) ($\sim$ 100 µm large) on 70 nm Si_3N_4/Si substrate, reprinted with permission from [14], **(c)** ellipsometry imaging of graphene, reprinted with permission from [15], **(d)** Fluorescence Quenching Microscopy (FQM) imaging of MoS_2, reprinted with permission from [16].

terials. [15, 22, 23] An example is shown in Fig. I.1.c in the case of graphene. [15] This technique uses the same substrate as for the first graphene observation (300 nm of SiO_2 on Si). The second technique (fluorescence quenching microscopy) is based on the fact that graphene and other 2D materials are efficient fluorescence quenchers of nearby dye molecules. The difference of fluorescence between the substrate and the deposited 2D materials produces contrasted images, [16, 24, 25] as presented in Fig. I.1.d. [16] It was demonstrated to be efficient on any substrate. [26, 27] With the recent progress in super-resolution fluorescence microscopy, graphene was imaged by a combination of Fluorescence Resonance Energy Transfer (FRET) and Stimulated Emission Depletion Microscopy (STED). [28] Lately, graphene oxide was also imaged

using quenched Stochastic Optical Reconstruction Microscopy (qSTORM) with a resolution of 16 nm. [29]

The development of high-throughput techniques was also driven by the necessity to characterize centimeter-scale graphene samples for future industrial applications. The goal is to develop inline measurement techniques for the structural characterization of 2D materials during their mass production. In this respect, optical techniques have remarkable assets in terms of versatility and speed.

I.2 Structural characterization

The first structural information usually needed after the synthesis is the number of stacked layers, the film continuity, the presence of cracks, etc. To get access to this, optical microscopy techniques were thoroughly applied. They were especially used to correlate the visibility of the flakes with the number of stacked layers as notably reviewed by Bing and co-workers in 2018. [30]. A machine-learning strategy was even applied to the optical identification of 2D materials. [31] All the techniques discussed above are able to observe single-layer materials as well as the continuity of the film. For centimeter-scale analysis, ellipsometry using only one adjustable parameter was performed on graphene and led to fast characterizations on various substrates. [32]

However, cracks and wrinkles are not always visible. To my knowledge, fluorescence quenching microscopy is the only optical technique which was used to quantify specifically the density of cracks in graphene. [33] But other types of enhanced microscopy configurations were also used to observe other types of defects. Dark-field microscopy is one of them, as it is very sensitive to small refractive index variations. It was in particular used to image graphene grain boundaries as shown in Fig. I.2.a. [34–36] Originally used in biology to study cell-substrate interactions, Interference Reflection Microscopy (IRM) was repurposed to image graphene on transparent substrates. [37] It allows the fast and label-free visualization of single-layers presenting defects, as presented in Fig. I.2.b. The substrate can be made of polymers; therefore the technique was used to probe *in situ* the graphene cracks propagation under mechanical strain, as shown in Fig. I.2.c-d. The mechanical properties of 2D materials are out of the scope of this work and were already described in the literature. [38–40] Yet, it is interesting to note that many studies have also used TEM, SEM or optical microscopy to observe *in situ* crack propagation, exfoliation, bending, etc. [37, 41–44]

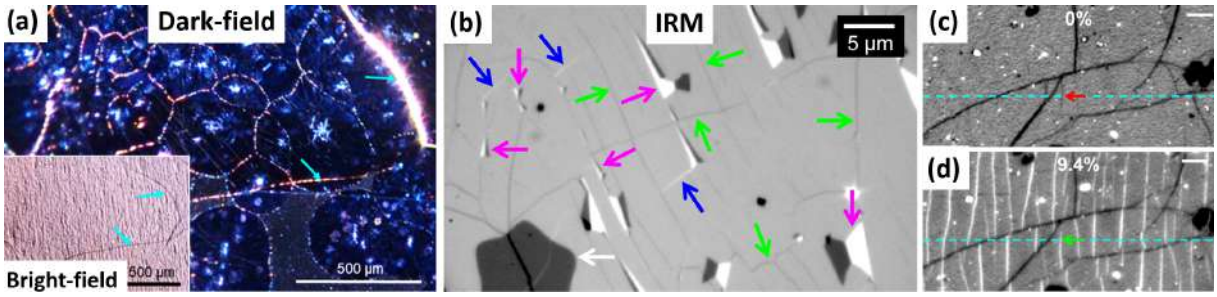

Figure I.2: Optical techniques to observe defects in 2D materials. (a) Dark-field microscopy, reprinted with permission from [36], **(b)** Interference Reflection Microscopy (IRM), **(c-d)** *in situ* IRM images of graphene under uniaxial strain. Scale bars: 5 µm. Reprinted with permission from [37].

Another way to reveal structural characteristics is to use indirect strategies. Different approaches were employed and combined to optical microscopy. Grain boundaries were selectively etched to create trenches which were then easily observable by microscopy. [45–50] It was also demonstrated that rhodamine B (a fluorescent dye) is selectively adsorbed at graphene edges. Then the reacted grain boundaries were imaged using fluorescence microscopy. [51] Wrinkles and grain boundaries can also be highlighted by the deposition of gold nanoparticles along them. [52] Another similar approach using water micro-droplets was investigated to increase the contrast of graphene flakes. [53] Crystal orientation and grain boundaries were evidenced using liquid crystals which orientation depends on the underlying 2D material. [54–58] The orientation of CVD-grown MoS_2 on graphene or WS_2 was also used to determine the crystal orientation of the 2D materials and locate their grain boundaries. [59]

The optical techniques used so far have a lateral resolution limited by diffraction (except fluorescence quenching microscopy but high-resolution studies using these techniques are scarce). To our knowledge, the only super-resolution microscopy, not based on dye molecules and applied to 2D materials is the Polarization parameter Indirect Microscopic Imaging (PIMI). [60] This technique uses the indirect optical wave parameters obtained with the modulation of polarization to produce contrasted images. It was used to visualize graphene defects with sub-100 nm lateral-resolution.

For higher resolution characterization, the use of Transmission Electron Microscope (TEM) or Scanning Tunneling Microscope (STM) is well-established. They both allow the structural characterization of 2D materials down to the atomic scale. TEM imaging of 2D materials is a wide research field in itself which has been increasingly important in the last decade with the rise of aberration-corrected and low-energy TEM. It has

been used to observe 2D materials lattices, [61–63] defects, [64–66] crystalline phases and their orientations, [67, 68] chemical doping, [69] etc. TEM and STM are the only techniques able to visualize 2D materials at the atomic scale, therefore their uses is of critical importance to understand their properties. Particularly, TEM is getting even more popular with the development of new generation sample holders able to apply *in situ* different stimuli: mechanical, thermal, electrical, optical, magnetic and even in liquid or gas environments. The nanoscale characterization and manipulation of 2D materials using TEM is notably reviewed in [70] and [71] with a particular focus on the most recent and most advanced *in situ* techniques.

Last but not least, the structural characterization of 2D materials by the previous methods is almost always coupled to AFM and/or Raman microscopy, which provide complementary information. As discussed previously, AFM is key to determine the number of stacked layers. But it is also commonly used to visualize defects like wrinkles and cracks. Soon after the first observation of single-layer graphene with AFM, Raman spectroscopy was shown to allow imaging graphene flakes using a scanning confocal setup. [72] It was demonstrated that Raman is sensitive to the number of layers and to their defects. Therefore, this technique has become one of the most extensively used for quality characterization of single-layer 2D materials.

Raman spectroscopy is typically mounted on a confocal microscope for high-resolution characterization and imaging of 2D materials but the development of wide-field Raman imaging allowed faster visualization. [73] With the rise of plasmonic research, Raman spectroscopy has been improved in two ways. First, 2D materials like graphene were used to produce Surface-Enhanced Raman Scattering (SERS), which improves the sensitivity of the technique. [74–77] Then, Tip-Enhanced Raman Spectroscopy (TERS) was found to be capable of imaging defects in graphene with an even better sensitivity and resolution than confocal Raman microscopy. [78, 79] It uses confined surface plasmon at the tip of a scanning probe to increase Raman signals. Therefore, the resolution is mainly defined by the immediate volume surrounding the tip and is typically around 10 nm [80] but it can reach sub-nm resolution under ideal conditions. [81] TERS is so sensitive that it can even probe single molecules. [82]

I.3 Optical and electronic properties characterization

Optical properties

The first optical characterization which is generally performed on materials is absorbance spectroscopy. This is especially difficult for few atoms thick materials and light transmittance of single-layer graphene was experimentally determined four years after the initial discovery. [83] Then few techniques were deployed to probe the local transmittance of other 2D materials. Confocal absorption spectral imaging was used to increase the resolution of the spectral analysis. [84] Lately, optical fibers were used to reduce the size of the light spot of a classic microscope with two different configurations. First, when the optical fiber is on the backside of the sample (it thus needs a transparent substrate), the technique is named hyperspectral imaging. [85] Second, when it is on top of the sample, it is named micro-reflectance and transmittance spectroscopy. [86] They both present absorbance spectra of TMDs with different thicknesses and the resolution is determined by the diameter of the optical fiber (but is still limited by diffraction).

Then the complex refractive index of materials is mainly extracted using optical reflectance microscopy and ellipsometry. To do so, the spectra are fitted using models incorporating the precise thickness of the layer (mainly extracted by AFM). Many studies extracting the complex refractive index using these two techniques are reported in the literature. [87–97] Few other techniques were used to image and extract optical constants. First, quantitative phase microscopy which is based on the use of quadriwave lateral shearing interferometry. [98] The special camera used in the set-up is capable of mapping both the intensity and wavefront profiles of a light beam passing through the material. Then, picometrology was also demonstrated. [99] It is based on interferometry (which measures the changes in reflection amplitude) but on a spinning disk in order to measure the phase shift at 2D materials edges.

One of the main techniques to probe the optical properties of 2D materials locally is photoluminescence. The characterization of 2D materials using photoluminescence has been reviewed by Jie and co-workers in 2018. [100]. In most cases, it is combined with Raman spectroscopy to measure the quality of the flakes. And like Raman, it is highly sensitive to defects therefore it can be used to visualize grain boundaries

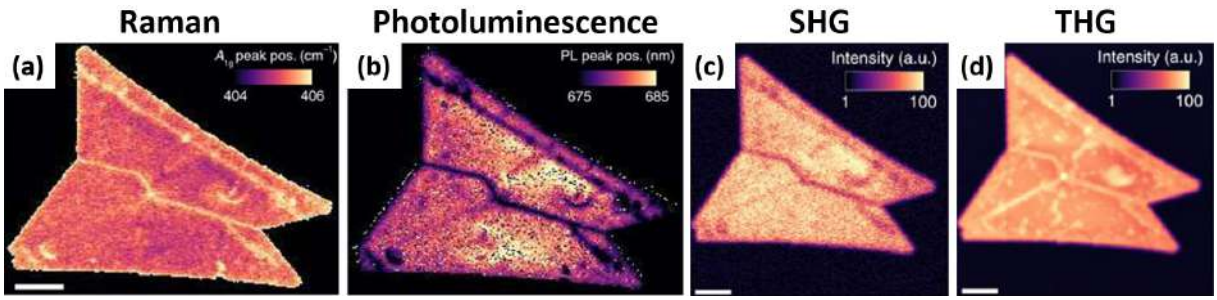

Figure I.3: Comparison of the observation of MoS_2 monolayers using different optical spectroscopy techniques. **(a)** Raman, **(b)** photoluminescence, **(c)** Second Harmonic Generation (SHG) microscopy, **(d)** Third Harmonic Generation (THG) microscopy. Scale bars: 10 µm. Reprinted with permission from [107].

and defects. [101–107] The resolution was mainly improved using Scanning Near-field Optical Microscopy (SNOM) with "Campanile" nano-optical probe. Resolution down to 60 nm was obtained. [108–111] As for Raman spectroscopy, the photoluminescence signal is also enhanced at a tip therefore Tip Enhanced PhotoLuminescence (TEPL) has been successfully used for 2D materials characterization. [112, 113]

Other optical effects were used to study the local properties of 2D materials. For example, polarized optical microscopy was applied to black phosphorus as it presents anisotropic properties, [114] or to 1T'- 2H $MoTe_2$. [115] Second Harmonic Generation (SHG) was showcased in TMDs. This nonlinear optical effect is based on the combination of two photons of the same energy, which produce one photon with twice the energy when they interact within a material. It is highly sensitive to edges and grain boundaries. [115–118] Third Harmonic Generation (THG) was also demonstrated in 2D materials and its sensitivity to grain boundaries is higher than for SHG. [107] A comparison of Raman, photoluminescence, SHG and THG in the case of MoS_2 is presented in Fig. I.3. [107]

Optical properties are directly related to electronic properties therefore both characterizations are ideally performed on the materials for a better comprehension.

Electronic properties

For the characterization of the band structure (specifically the valence band), Angle-Resolved PhotoEmission Spectroscopy (ARPES) is well-established. Its resolution is limited by the size of the beam but recent years have seen the development of micro- and nano-ARPES. Mapping the electronic properties of 2D materials is now possible. The use of ARPES on 2D materials was notably reviewed by Mo and co-workers in

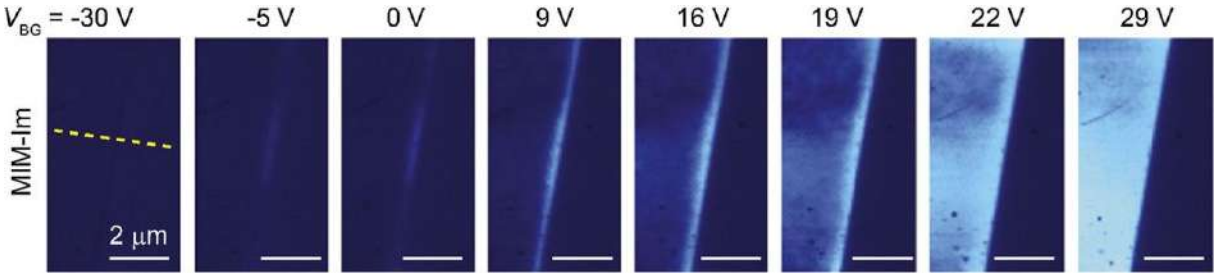

Figure I.4: Evidence of edge state conductance of MoS_2 by the MIM technique. In this technique, the microwave signal strikes on the surface and some is reflected by the sample, then the output signal is measured and related to the local resistance and capacitance of the sample. In this experiment, the local conductance was presented at different bias of a MoS_2 field-effect transistor. Reprinted with permission from [124].

2017 [119] and a focus on spatially resolved ARPES for 2D materials was reviewed by Cattelan and co-workers the following year. [120]

For the spatial mapping of band structures, Scanning Tunneling Spectroscopy (STS) is suited. Combined with STM for the topography, local tunneling I(V) characteristics provide information on the band gap and surface states. It was for example used to probe the band structure at the edge of MoS_2. [121] The influence of defects and boundaries on the electronic properties using the different STM techniques was reviewed by Hus and co-workers in 2017. [122]

Among the most widely used techniques for the analysis of 2D materials electronic properties, one finds several AFM-related techniques. In addition to the classical topography imaging mode, several other AFM-based modes were developed. The different methods used for local electrical characterization using scanning probe techniques were reviewed in details this year. [123] These AFM related techniques (current-sensing AFM, Electrostatic Force Microscopy, Kelvin Probe Force Microscopy, etc.) provide extensive information on surface potential distribution, local conductivity, etc. at the nanoscale.

From the above mentioned studies, one can note that *operando* (*i.e.* in an operating device configuration) analysis of electronic properties are limited. One example is the contribution of edge conductivity in MoS_2 field-effect transistors studied by Microwave Impedance Microscopy (MIM), as presented in Fig. I.4. [124] Other examples concern Kelvin Probe Force Microscopy (KPFM) studies on operating graphene, MoS_2 and van der Waals heterostructures devices. [125–128] One striking technique relies on photoluminescence to image local current flow. Graphene was deposited on a di-

amond substrate containing N-V centers. Depending on the local charge density in bias graphene, the photoluminescence of these N-V centers is more or less quenched therefore the photoluminescence microscopy indirectly maps the charge density in operating devices. [129]

For the future industrial production of high-quality graphene, being able to probe the electrical conductivity over large areas is important. To do so, the use of movable four point probes or dry laser lithography is common but it requires physical contacts which may damage graphene. For non-contact mapping, TeraHertz Time-Domain Spectroscopy (THz TDS) is being developed. It consists in the measurement of the absorption of terahertz radiation across the 2D material flakes (MIM is one of these techniques). A comparison of these three techniques is provided in Ref. [130].

Finally, Cornut and co-workers (at CEA-Licsen) previously used local electrochemical techniques to probe the conductivity of different 2D materials. The mapping of electrical conductivity was investigated with Scanning ElectroChemical Microscopy (SECM) coupled to numerical modeling. It was performed on Graphene Oxide (GO), [131] reduced Graphene Oxide (rGO) [132] and MoS_2. [5] Further explanations on local electrochemical methods are given in section I.5.

I.4 Chemical reactivity characterization

The most common combination of techniques for the local study of 2D materials chemical reactivity is Raman, photoluminescence and STM/AFM.

As described above, Raman and photoluminescence microscopy are able to image single-layers with high-resolution (for tip-enhanced versions) but at first they are spectroscopy techniques. They can investigate small changes in the quality or environment of 2D materials, therefore they have been thoroughly used coupled to STM/AFM topological information to probe the chemical reactivity of 2D materials. [133–144] A prototypical example of these studies is the functionalization of graphene by diazonium chemistry. The dynamic of the spontaneous chemical bonding process was extracted by Raman microscopy and it is presented in Fig. I.5. It is also important to note that the dynamic of graphene oxide photo-reduction was investigated using photoluminescence and absorption/emission microscopy. [145, 146]

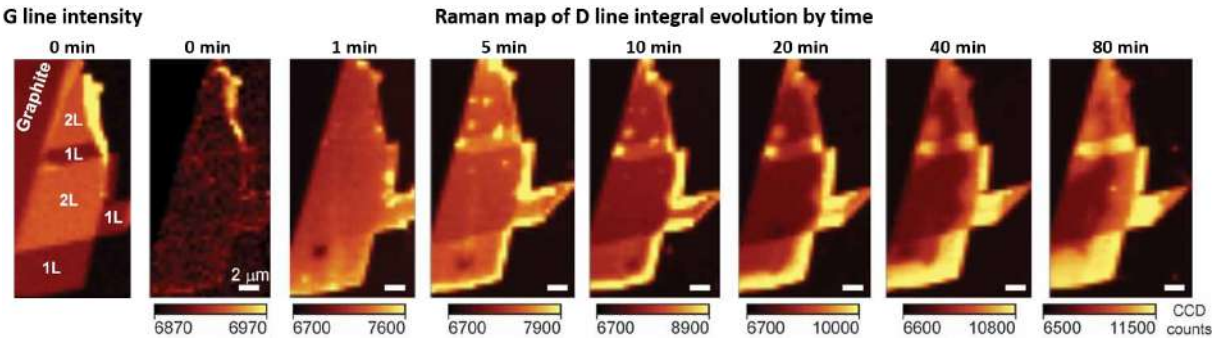

Figure I.5: Local dynamic of graphene functionalization followed by Raman mapping. Reprinted with permission from [142].

Raman was also coupled to Scanning PhotoElectron Microscopy (SPEM, or Spatially Resolved X-ray Photoelectron Spectroscopy) in order to map the quantity of diazonium molecules on graphene with a lateral resolution of 500 nm. [144] With the same goal, Mass Spectrometry (MS) techniques were employed using a local ionization beam. [147–149] XPS and MS also provide information on the type of molecules at 2D materials surfaces.

SNOM techniques previously discussed like TERS, TEPL and "Companile" probe are not limited to the visible range. Infrared was used and lead to nano-FTIR with enhanced chemical sensitivity. [150, 151]

At the atomic scale, STM was used to probe molecule adsorption and molecular organisation on 2D materials. [133, 152, 153] And HRTEM was used to investigate phase transition and intercalation processes. [154–156] It has to be noticed that the intercalation of alkali metals is TMDs was studied *in situ* by several groups. [157–159]

Of course AFM techniques are also widely used to probe local chemical reactivity. The topography can provide information on the layer thickness which depends on the functionalization. Most of the time, adding molecules on 2D materials modifies their electrical conductivity; therefore THz microscopy and conducting AFM were used to measure the dynamics of chemical reactions. [136, 160]

I.5 Electrochemical properties characterization

This part was the subject of a review by our team in 2017 and I was deeply involved in its redaction. [4] In the following, a summary of this review is first provided. Then a focus on the most recent studies that were published in and after 2017 is proposed.

The electrochemistry of 2D materials is of particular interest for energy conversion and storage applications. [161–164] Among others, graphite is used as anode electrode material in lithium-ion batteries. The issue with the study of 2D materials electrochemical properties is that the global efficiency of the system largely depends on inhomogeneity or imperfections (such as edges, defect sites or upon folding and stacking). Understanding how these features influence the performances is challenging from a characterization point of view. But defects can also be turned into an advantage since their precise control could improve the devices.

The most common way to correlate the electrochemical properties of 2D materials with local information is to perform standard electrochemistry on samples with precise knowledge of the defects under investigation. But this requires other techniques to characterize the samples first such as AFM, SEM, Raman, etc. and other unknown or unobservable parameters may have a significant influence on the results.

Another approach has been developed with the rise of scanning probe microscopy techniques. Several groups developed new SPM techniques to probe local electrochemistry. These techniques use different probes such as a scanning microelectrode (Scanning ElectroChemical Microscopy, SECM), a functional AFM cantilever, a scanning pipette (Scanning ElectroChemical Cell Microscopy, SECCM) or a confined microdroplet, as presented in Fig. I.6. Depending on the scanning conditions, local information can be obtained and plotted as electrochemical maps. The opposite is also possible as local modifications of 2D materials are possible using the same probes.

In [4], we first introduced the different local probe techniques that can be used to perform localized electrochemical investigations of 2D materials. The techniques can be separated in two classes: in the first one, a sized-controlled electrode is scanned over the surface (SECM or AFM-SECM); in the second one, the measurement is confined in a microdroplet (SECCM or Microdroplet Cell). Both, the working electrode and the substrate potentials are controllable using a bipotentiostat.

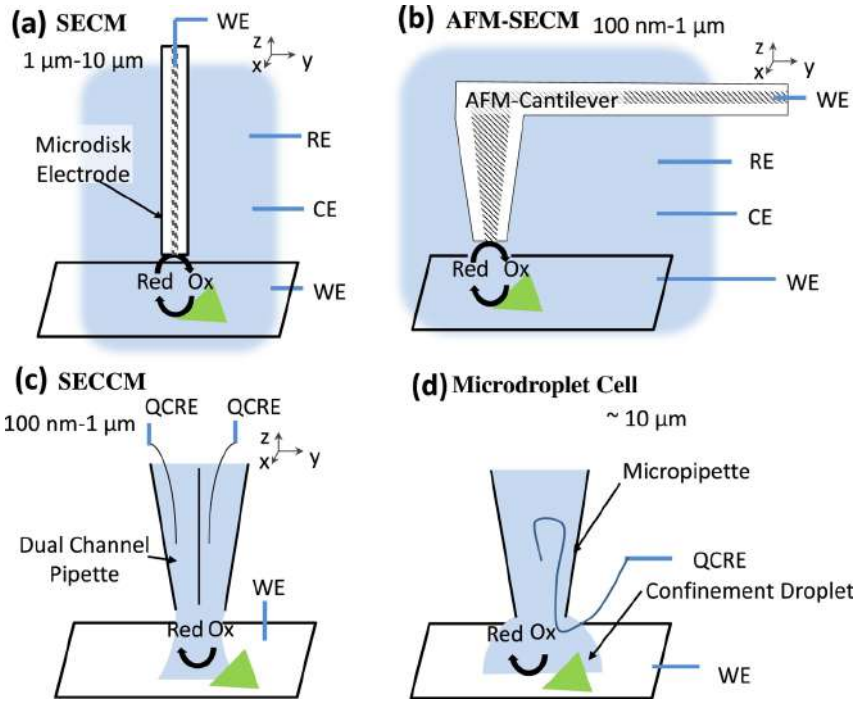

Figure I.6: Presentation of the different probe techniques to perform localized electrochemistry. (a) Scanning ElectroChemical Microscopy (SECM), **(b)** AFM-SECM, **(c)** Scanning ElectroChemical Cell Microscopy (SECCM), and **(d)** Microdroplet cell. WE: WorkingElectrode, CE: Counter Electrode, RE: Reference Electrode, and QCRE: Quasi Counter Reference Electrode. The green triangle represents a piece of 2D material under study. [4]

Then, we presented the studies in which localized electrochemistry experiments are used to evaluate some key properties of 2D materials. For example, electronic conductivity (as discussed in I.3), ionic and molecular transport can be investigated using these techniques as well as charge transfers at surfaces using redox mediators.

Finally, we focused on contributions related to material modifications (electrochemical functionalization, etching, etc.), which allow modulating the properties in a spatially controlled manner. This field is mainly driven by conducting AFM, notably for the fabrication of graphene nanoribbons by Local Anodic Oxidation (LAO) [165–167] or for the local reducion of graphene oxide. [168, 169] Only few studies present the local electrochemical functionalization of 2D materials. [169, 170]

At the end of 2016, the field was rapidly growing but most of the reported studies focused on graphene. The most typical characterization concerned the evaluation of the kinetic constants associated to simple charge transfers, which is a basic electrochemical process to characterize. The studies were mostly based on scanning probe microscopy with the associated drawbacks: it is difficult to locate areas of interest and

the small selected area under study may not be completely representative of the whole surface; it is very slow; the probe itself may impact the result; etc. Nevertheless, with the development of new 2D materials showing interesting properties for electrocatalysis, [171] localized electrochemistry should have a key role in order to better understand 2D materials electrochemical properties. A way to improve the characterization could be the combination of local electrochemistry with other microscopy techniques.

Since 2017

The study of the electrochemical properties of graphene continued but the investigation of other 2D materials increased more significantly, especially for TMDs which present interesting electrocatalytic properties. The field is now mainly driven by the group of Pr. P. Unwin at Warwick. This group notably improved drastically the SECCM technique and is intensively using it to study materials at the nanoscale. They reviewed their progress in a 2019 article. [172]

Simple charge transfer at the basal plane or at the edges of Highly Oriented Pyrolytic Graphite (which serves as a model for graphene) is still studied by SECCM, [173, 174] as well as electron transfers at MoS_2 by SECM. [175]

Studies of the electrocatalytic properties have rapidly progressed in particular with TMDs in the case of the Hydrogen Evolution Reaction (HER). MoS_2 is particularly investigated to sort out the relative catalytic properties of edges, defects, crystalline phases and basal plane. [176, 177] To do so, SECM and SECCM were used. It has to be pointed out that SECCM recently allowed the video-rate electrochemical mapping of HER at MoS_2. [177] Graphene and h-BN were also studied for HER using SECCM. [178, 179] However graphene materials are mostly investigated for the Oxygen Reduction Reaction (ORR), which is the limiting reaction in hydrogen fuel cells. Nitrogen or metal doped graphene were studied by SECM in order to show the influence of doping on the electrocatalytical properties. [180, 181]

Similar to the Microdroplet Cell technique, a masking method has arisen. The 2D materials and the substrate are covered with a polymer resist and then a hole in this coating is produced using lithography. Therefore, only the selected hole contributes to the electrochemical reactions. HER at MoS_2 was investigated using this technique. [182, 183] The same approach was performed on MoS_2 but for the intercalation of ions. [184] It was shown that lithium and sodium can intercalate through the basal plane

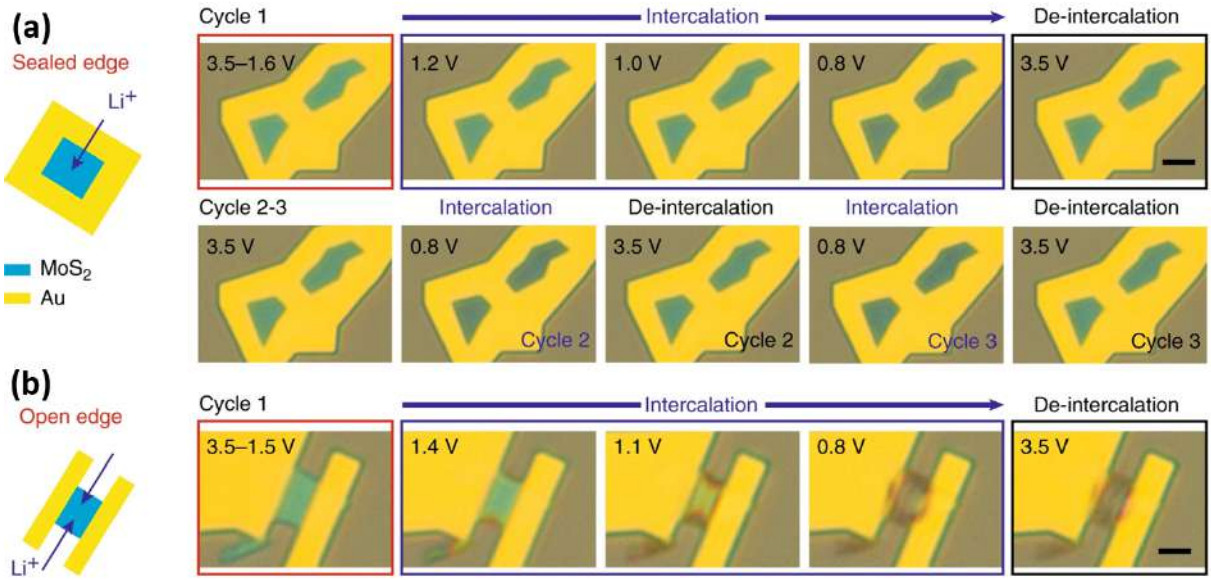

Figure I.7: *In situ* optical images of Li intercalation in MoS_2. **(a)** Through the top surface, **(b)** through open edges. Scale bars: 5 µm. Reprinted with permission from [184].

while potassium can only intercalate by the edges. The control over the intercalation of lithium is notably improved (reversibility and stability) when lithium intercalates through the top surface, as presented in Fig. I.7. The intercalation was followed by *in situ* Raman spectroscopy. Raman was also coupled to SECM in order to probe the redox activity of graphene. [185]

Interestingly, the intercalation in MoS_2 induces a modification of the optical properties, therefore, in 2018, it was followed *in situ* by optical reflection microscopy as shown in Fig. I.7. [184] The electro-ablation of TMDs was also investigated in 2018 by optical reflection microscopy and the dynamic of the process was showcased. [186] Recently, the Interference Reflection Microscopy (IRM) and the fluorescence microscopy techniques were used to study the oxidation and reduction of graphene. [187, 188] The local dynamics are reported at video-rate and a mechanism is suggested. Examples of IRM images of graphene during the oxidation and reduction process are presented in Fig. I.8.

Finally, the work on the local modification of 2D materials continued using Local Anodic Oxidation with the goal of improving the resolution. [189–191] Graphene nanoribbons are still studied as well as TMDs. [190,192] To our knowledge, no studies were reported for the local electrochemical functionalization of single-layer 2D materials since 2017.

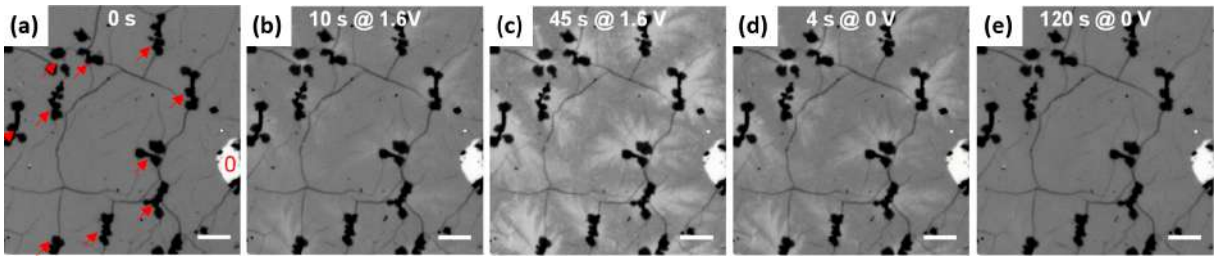

Figure I.8: *In situ* Interference Reflection Microscopy (IRM) images of electrochemical oxidation and reduction of monolayer graphene. (a-c) Oxidation at 1.6 V, **(d-e)** reduction at 0 V. Scale bars: 5 µm. Reprinted with permission from [187].

Within the two last years, the field has extented both through the study of new materials and through the improvement of the characterization techniques. The local electrochemical studies are no more limited to SECM related techniques. Other approaches have emerged and the combination of electrochemistry at 2D materials surfaces with complementary techniques like Raman spectroscopy is spreading. Optical microscopy starts being used to observe *in situ* the modification of 2D materials under electrochemical reactions, in particular in the case of intercalation.

I.6 Summary and outlook

High-sensitivity optical microscopy has been the missing key for the emergence of 2D materials as it allowed the fast visualization and localization of single-layer flakes. Since 2004 many techniques have been used to image and characterize 2D materials providing critical information for the development of the field.

Reflection optical microscopy and ellipsometry imaging are two important optical microscopy techniques not only capable of imaging but also used to extract the optical properties of 2D materials. The complex refractive index extracted using these methods critically depends on the thickness measurement of the 2D material which is not always reliable by AFM. [193] This error combined with the imperfections of the models induce large differences between studies in the reported results (as will be detailed in Chapter II for MoS_2). The third main optical technique is Fluorescence Quenching Microscopy, which is interesting and very powerful because its lateral resolution is not limited by diffraction (when used in a super-resolution configuration). Furthermore, it was proven to be usable on any substrates. The drawback is that it requires dye molecules at the surface, which is hardly compatible with chemistry-oriented studies.

For high resolution imaging, TEM and STM are the only two techniques achieving atomic resolution. Especially, TEM has been increasingly used within the last decade with huge technological improvements. It can combine atomic resolution with elemental/chemical information. With the development of environmental TEM and sample holders applying external stimuli, *in situ* studies start to come out. For now, *in situ* TEM is still limited to simple reactions and imaging in liquid is still in its infancy.

AFM is ideal for structural characterization and is almost always performed in 2D material studies. Its use is not limited to topography but variants of the AFM technique have been applied to 2D materials to probe notably the local electrical properties, the reactivity (combined with TERS) and the electrochemical properties. These techniques are also becoming faster with technological improvements, therefore *in situ* and video-rate investigation of 2D materials are expected to appear soon. The main issue for the study of 2D materials is that the thickness measurement accuracy highly depends on the measurement and quality of the flake. [193] The extracted properties are also probed at a very local scale and one must be careful that the probed area is fully representative of the system since homogeneity at a large scale is sometimes difficult to guaranty (and reproduce) with nanomaterial deposition techniques.

Optical spectroscopy techniques like Raman, Photoluminescence and FTIR are extensively used as they are capable of imaging 2D materials ant their defects. They are highly sensitive to chemical changes in the environment of the flakes which makes them suitable for chemical sensing. The resolution is enhanced by near-field microscopy at a tip (TERS or TEPL) or using a "Campanile" probe (nano-PL).

For local electrochemical characterization, SECM and related techniques are prominent. Lately, SECCM was improved and the electrochemical mapping speed reached video-rate with a pixel size of 1 μm^2. The use of lithography to give access only to the surface of interest is increasing as it uses well-known processes and the electrochemistry is performed using standard equipment. The drawback is that at some point, the surface is entirely covered with a polymer and some residues can be left on the developed surface. Such residues are known to impact significantly the electrical properties of 2D materials and a similar impact is thus expected for the electrochemical properties.

Most of the time several of these techniques are combined in order to provide complementary information at different scales. As they all have their own pros and cons, it is

important to cross-check the data for highly accurate characterization. The ideal would be to combine the techniques in the same experiment like topological AFM with TERS for chemical sensing at the local scale. Examples of such strategy were developed lately: a combination of electrochemistry with AFM-TERS was demonstrated for the first time in 2019 by the group of P. Van Duyne (Northwestern University) in order to map the redox activity on an electrode surface *in situ* and at the sub-µm scale. [194] There is no doubt that such combination will be applied to 2D materials very soon.

Except for some specific TEM studies or some studies of mechanical properties, the local characterization of 2D materials is either *in situ* but not local or local but not *in situ* (*i.e.* based on before/after type of comparisons). Only very few studies combine *in situ* operation with local information. This is especially the case for electrochemical properties for which *in situ* studies are mainly performed on electrode materials. [195, 196] Furthermore, the catalytic or energy storage capacities are highly dependent on defects which are still important features in 2D materials. [197] So there is a need for additional local techniques to probe the impact of defects, edges, etc. that can be combined with *in situ* analysis.

Almost all the techniques described above are based on scanning probe microscopy. Wide-field techniques are mostly limited to the static observation of 2D materials. It is in this context that this thesis presents an optical microscopy technique to investigate *in situ* chemical and electrochemical reactions at single-layer 2D material surfaces.

Chapter II

Backside Absorbing Layer Microscopy

In the first chapter, the different ways to observe and analyze the local properties of 2D materials were presented. From this we can see that there is a lack of wide-field, *in situ* / real-time techniques and especially to study their local electrochemical properties. In this chapter, we introduce a recently developed enhanced optical microscopy technique and determine its performances for the observation of 2D materials as well as for monitoring chemical reactions.

II.1 BALM principle

Optical microscopy was invented in the 17th century and had a tremendous impact on society, as it allowed scientists to observe a world they could only imagine before. Conventional optical microscopy, the oldest and simplest type of microscopy, is present in every research labs. The last century saw the emergence of many new types of enhanced optical microscopy techniques with the aim of improving, among others, the two main criteria of performance: lateral resolution and contrast.

Lateral resolution represents the minimum distance (d) between two distinguishable points. The resolution of conventional optical microscopes is limited by diffraction and was fully described by Ernst Abbe in 1873. [198] He notably introduced the following equation quantifying diffraction-limited microscopy:

$$d = \frac{\lambda}{2NA} \tag{II.1}$$

with λ, the light wavelength and NA, the Numerical Aperture (depending on the objective quality and provided by the manufacturer). The BALM technique being based on a conventional microscope, its lateral resolution is also limited by diffraction. The specific lateral resolution of our set-up will be briefly described later for clarity.

Indeed, the main goal of BALM is to improve the second criterion: contrast. It characterizes the intensity or color distribution within an image. It is important to understand that an image with a poor contrast can only be slightly improved by post-treatments and that this manipulation can distort the results. In this thesis, we consider the contrast resulting from instrumental considerations and not the one resulting from post-treatments.

Contrast can be defined in several ways. In this work it was decided to use the definition proposed by Michelson, [199] which is particularly suited for an object deposited on a support. This Michelson-contrast is calculated using the following equation:

$$C = \frac{I_{object} - I_{support}}{I_{object} + I_{support}} \tag{II.2}$$

By looking at this equation, there are two ways of maximizing the contrast. First, $I_{support} = 0$ (observing bright object on a dark background), and second, $I_{object} = 0$ (dark object of a bright background), so that $|C| = 1$. From an experimental point of view, it is easier to control the intensity of the support. This solution is experimented by everyone observing the sky: the stars are only visible when the sky is dark ($I_{support} = 0$) and not during daytime. This type of contrast-enhanced images is also produced by the darkfield microscopy technique.

BALM is a new type of contrast-enhanced optical microscopy technique, which comes from the use of specific substrates with $I_{support}$ close to zero.

II.1.1 Anti-reflective coating principle

When light crosses an interface between two transparent media with different optical properties, one part is transmitted and the other part is reflected. The ratio is quantified by Fresnel equations [200, 201] and in the special case of normal incidence, the reflected light is calculated by the following equation:

$$R = \left| \frac{n_i - n_e}{n_i + n_e} \right|^2 \tag{II.3}$$

with n_i and n_e, the refractive index respectively of the incident and emergent media. For example, the light crossing perpendicularly a window is reflected at 4% by the air/glass interface and around 7.7% considering the two interfaces. This is due to the difference between the refractive index of air (n = 1) and glass (n = 1.5). An optical microscope has two most common configurations, in transmission and in reflection. In the later case, the light comes from the objective, is reflected by the object/support, and the image is captured by the same objective.

In this configuration, there is a well-known solution in order to obtain $I_{support} = 0$: Anti-Reflective (AR) coatings. These coatings have many industrial applications, [202–204] with the most known being on glasses. As for windows, the air/glass interface reflects light and this coating allows people to see the eyes of the persons wearing glasses without seeing in addition their own reflection.

These coatings are based on the control of the light reflected by the interfaces. To do so, a new layer with precisely-selected optical properties and thickness is added on glass, as shown in Fig. II.1. This coating adds one interface and thus, the incident light is first partially reflected by the {incident medium/coating layer} interface and partially transmitted. The light transmitted in the coating layer is then partially reflected by the {coating layer/emergent medium} interface. The layer properties (refractive index and thickness) are chosen so that, the light reflected by the two interfaces interfere destructively, resulting in no reflected light ($I_{support} = 0$).

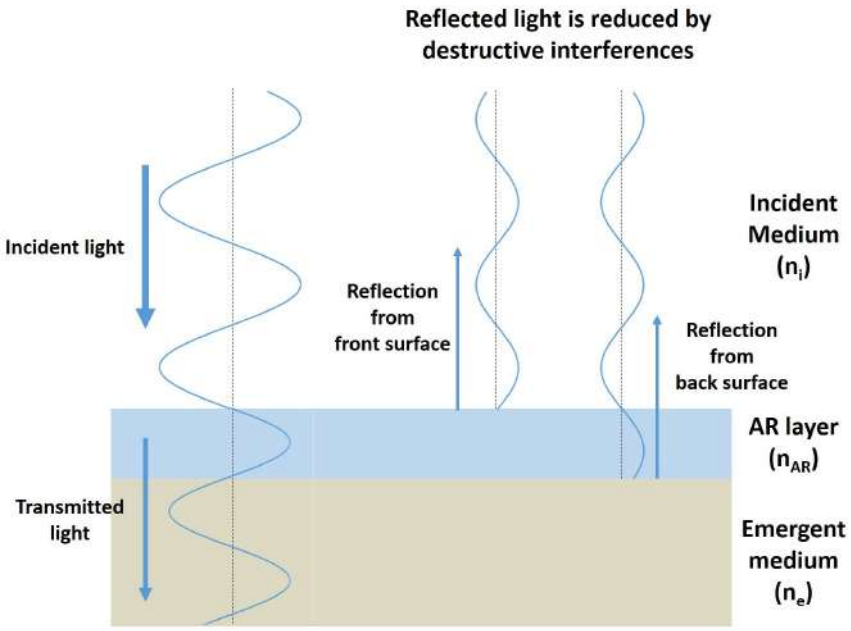

Figure II.1: Schematic explanation of Anti-Reflective coatings.

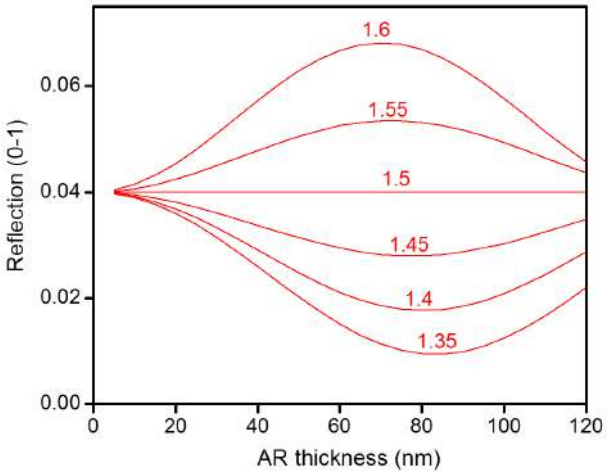

Figure II.2: Effect of a transparent coating on the reflection of the air/glass interface (simulation results for λ = 450 nm, n_{air} = 1, n_{glass} = 1.5, and light perpendicular to the interface).

II.1.2 Transparent anti-reflective layers

Most of the time, the anti-reflective layer is made of a transparent material as it was discussed in the bibliography part I. The transparent AR coatings have been studied for decades and the two equations, derived from Fresnel equations, governing the choice of the perfect AR layer are well-known:

$$n_{AR}{}^2 = n_i n_e \tag{II.4}$$

Ensuring that the same amount of light is reflected by the two interfaces of the AR layer. And:

$$e_{AR} = \frac{\lambda}{4 n_{AR}} \tag{II.5}$$

Defining the AR coating thickness, e_{AR}, as a function of n_{AR} and λ. It ensures that the phase difference between the reflected light from the front and back surfaces generates destructive interferences.

The respective impact of n_{AR} and e_{AR} within these two equations can be illustrated using simple simulations (Comsol-based model using the Fresnel equations). The model includes a single AR layer between two semi-infinite media (air and glass). Then the refractive index of the transparent AR layer was parametrized and the reflection was plotted against AR thickness, as shown in Fig. II.2. The refractive indexes chosen were typical of polymer materials used for conventional AR coatings. It can be observed that for $n_{AR} < n_{glass}$, eq: II.4 is approached and therefore it decreases the reflected light.

All the curves reach a minimum reflection at $\lambda/4n_{AR}$, that is why the single AR coatings are called quarter-wave layers.

Theoretically the perfect coating can give zero reflection but equation II.4 shows that the optimum refractive index for the AR coating layer is $\sqrt{n_i n_e}$ so n_{AR} = 1.22 for the air/glass interface. Unfortunately, materials with n < 1.3 are not usual therefore the anti-reflective conditions can only be approached using a single transparent AR layer.

However, single transparent layer AR coatings allow a good approximation of the anti-reflective conditions and are cheap to produce. AR layers were also improved by realizing multilayer AR coatings. [204]

II.1.3 Absorbing anti-reflective layer

Absorbing materials like metals are not commonly used for AR purpose because of their well-known high reflectivity, which is conversely put at profit to produce mirrors. Nevertheless, few systems using absorbing coatings are described in the literature. They are useful when light transmission is not important for the AR coating. They can even produce thinner and cheaper AR layers. [204–211]

From an analytical point of view, only few treatments were developped. [205] It was previously demonstrated that in a classical single-layer configuration, the AR layer must be thicker than $\lambda/4$, [201, 212, 213] therefore the light cannot pass through these highly absorbing layers and consequently there is no output signal.

That was until Dominique Ausserré from IMMM (Université du Maine) and co-workers demonstrated in 2014 the use of a single Anti-Reflective Absorbing (ARA) layer at the air/glass interface. [214] When a material absorbs light, its refractive index is a complex refractive index, $n_{ARA} - jk_{ARA}$, k being the extinction coefficient of the material. In the publication, [214] they derived Fresnel equations by taking into account the complex refractive index of the ARA layer and by making the approximation of a strongly absorbing material (high k). A full demonstration is provided in the supplementary information section of [3] and the following equations were obtained for ideal AR conditions:

$$n_{ARA}{}^2 - k_{ARA}{}^2 = n_i n_e \tag{II.6}$$

$$e_{ARA} \simeq \frac{\lambda}{4\pi} \frac{(n_i - n_e)}{n_{ARA} k_{ARA}} \tag{II.7}$$

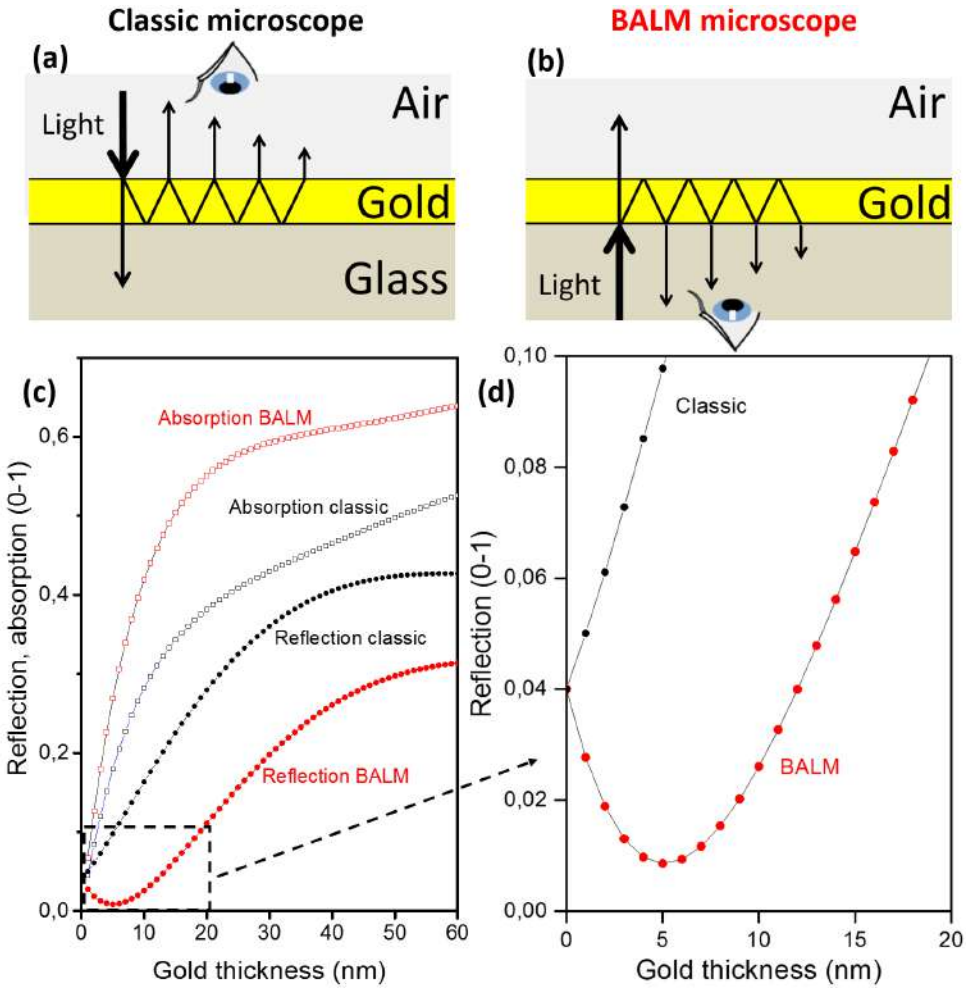

Figure II.3: Gold ARA layer at the air/glass interface. Schematics with **(a)** light coming from the air, **(b)** light coming from the glass. Comsol calculations of **(c)** reflection and absorption in the two configurations, **(d)** zoom on the reflection of a very thin gold layer.

The most important information extracted from these equations is that, in order to obtain a real thickness value (e_{ARA}) in eq: II.7, n_i has to be higher than n_e. This means that light has to come from the higher refractive index medium.

As for transparent AR coatings, simple simulations can be used to evaluate the amount of reflected light in such configuration. The reflection and the absorption of the air/glass interface are compared when a gold layer is used as ARA layer. The difference between light coming from the air (classical configuration) and from the glass (inverted microscope) are compared. Schematics and results are presented in Fig. II.3.

The light absorption and reflection of the classic configuration (light coming from the air in a classical set-up), are plotted in black. The addition of the gold layer increases the reflected light as its thickness grow and it behaves as a mirror. In regard to eq: II.7, the

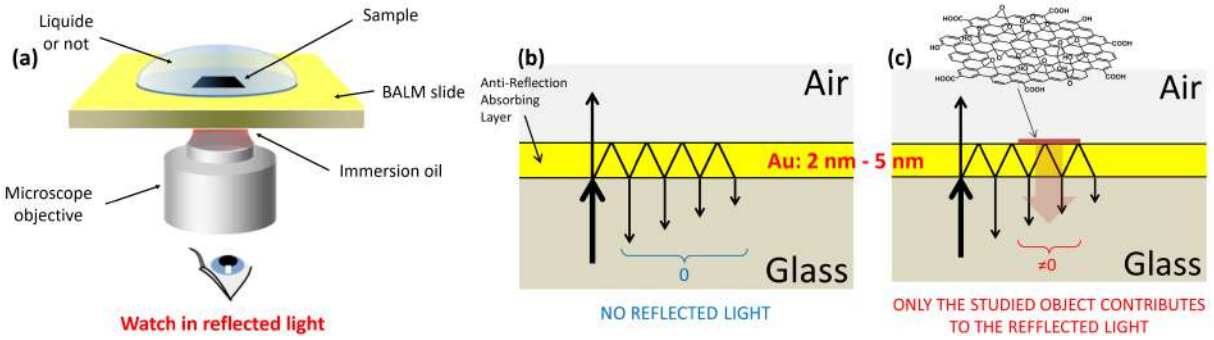

Figure II.4: BALM configuration. (a) Schematic, **(b-c)** anti-reflective properties of the BALM configuration and effect of the addition of a material at the imaging surface.

AR properties emerge only with the inverted configuration (light coming from the glass), as it is plotted in red. For really thin gold layer, the reflected light initially decreases and reaches a minimum around 5 nm. Meanwhile, the absorption is around 20% so contrarily to the previous publications the AR properties are not lost by the presence of a highly absorbing material.

D. Ausserré and co-workers named this new combination (absorbing AR layer + observation from the glass side): the Backside Absorbing Layer Microscopy (BALM).

II.1.4 BALM configuration

A schematic of the BALM set-up is presented in Fig. II.4. Since light has to come from the higher refractive index material, BALM uses a simple inverted microscope on top of which is placed a glass coverslip covered with an ultrathin gold ARA coating. The layer thickness depends on the emergent medium and is typically around 5 nm in air or 2 nm in water. The microscope is placed in reflection configuration therefore, light is sent through the objective, reflected by the object/support, and the image is created by the same objective. Finally, in order to obtain the best possible images, the microscope is equipped with a high numerical aperture oil immersion objective (NA = 1.4). The immersion oil is here to create a continuous refractive index medium between the objective and the glass. This prevents unwanted reflections and also increases the resolution of the objective by increasing its numerical aperture.

All of this combined, creates a "near-ARA" coating with $I_{support}$ close to 0 and when a 2D material, or any other material leading to a modification of refractive index, is deposited on top, the microscope produces contrast-enhanced images as represented by the two schematics of Fig. II.4.b,c.

The contrast enhancement of the BALM configuration will be studied in details but is first simply exemplified in Fig. II.5. MoS_2 flakes were deposited on a gold BALM support and the sample was imaged with a classic microscope (light coming from the air side) (a) and with the BALM microscope (light coming from the glass side) (b). The result is that the monolayer domains are barely distinguishable from the surrounding gold surface with our classic microscope whereas the BALM microscope clearly reveals additional details of the sample. Note that better images of MoS_2 than the one reported in (a) can be obtained with conventional microscopes when the substrate is, for example, Si/SiO_2 but ultrathin gold on glass is a chalenging substrate for microscopy in reflection. In any case, reported MoS_2 images in conventional microscopy configurations do not reach the level of contrast provided by BALM, as shown in Fig. II.5.b. The impact of the ARA layer will be further shown in Fig. II.13 and Fig. II.14.

Looking at Fig. II.5.b, it is also important to note that the MoS_2 appears darker than the background. When explaining the BALM principle, it was assumed that the ARA thickness would correspond to the minimum of the curve in Fig. II.3.c so that any additional material could only increase the amount of reflected light. In practice, additional material can also bring the system closer to the minimum of reflection case so that depending on the ARA thickness and type of observed object, materials can appear brighter or darker than the background. This will be detailed later (notably in Fig. II.15).

In terms of lateral resolution, BALM is equipped with a high Numerical Aperture objective (NA = 1.4), therefore, when used at wavelength of λ = 450 nm, the set-up could theoretically achieve a lateral resolution of d = 160 nm. In practice, the actual lateral

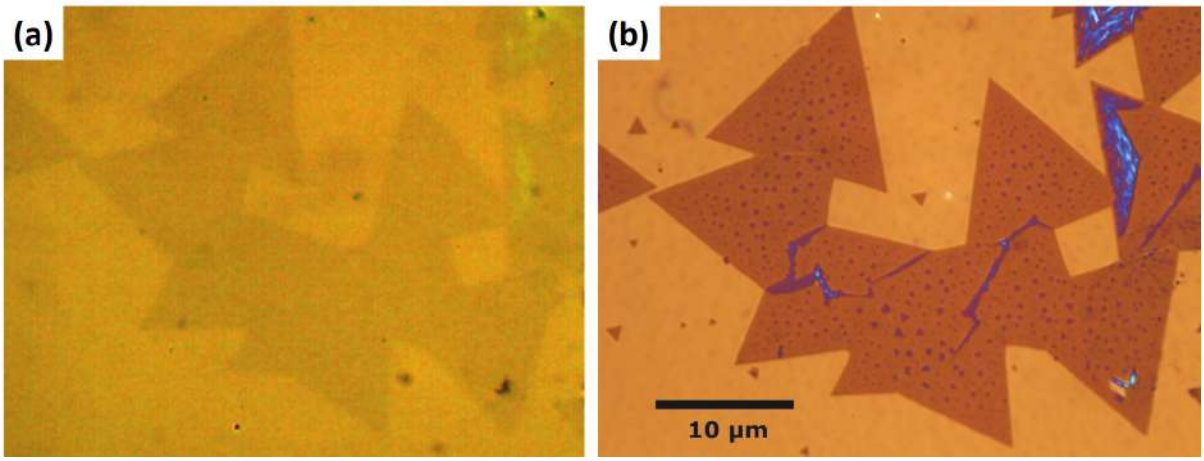

Figure II.5: Representation of contrast enhancement by the BALM microscope. Images of MoS_2 flakes deposited on a gold BALM substrate(0.5 nm Cr + 3 nm Au), **(a)** imaged with a classic optical microscope, **(b)** imaged with BALM.

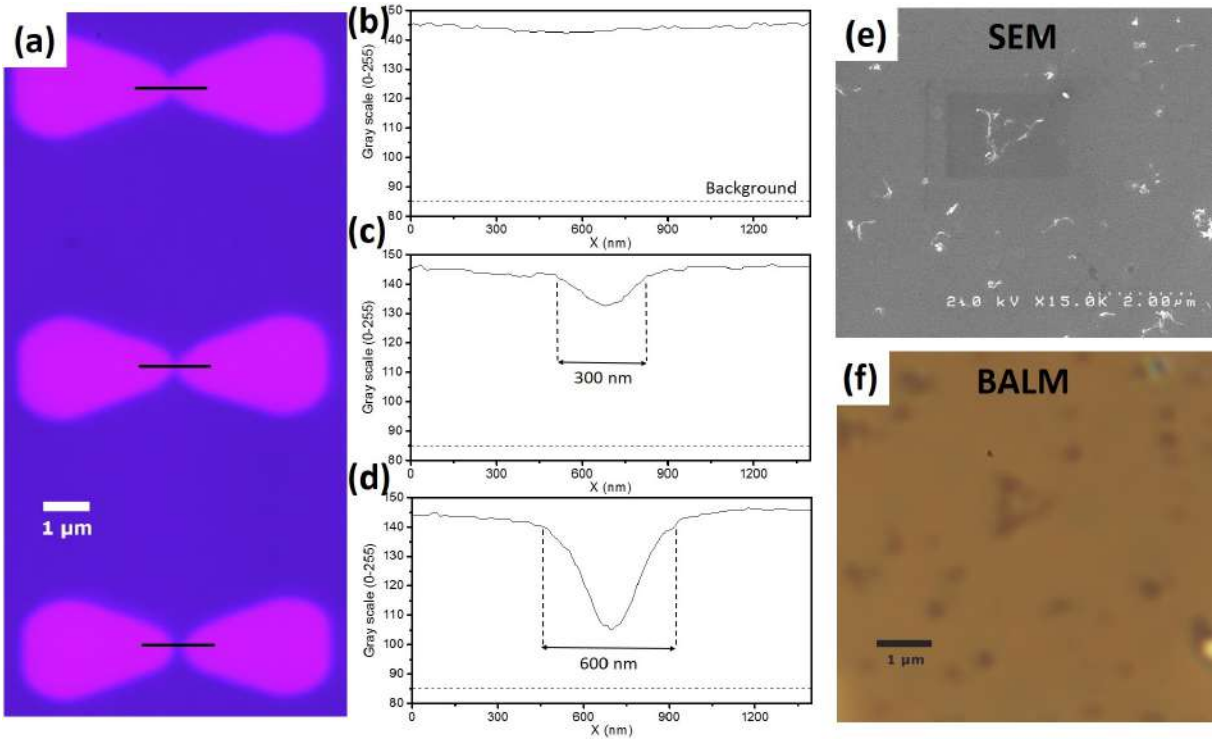

Figure II.6: Experimental resolution limit of the BALM set-up. (a) BALM image of chromium triangles on gold with increasing separation, **(b,c,d)** associated gray scale profiles. Carbon nanotubes imaged with **(e)** SEM and **(f)** BALM.

resolution is closer to 300 nm as illustrated in Fig. II.6. This figure displays BALM images of micro-fabricated pairs of chromium triangles (thickness 2 nm) deposited above a gold thin film. Triangles separated by different distances are produced by e-beam lithography. Chromium patterns separated by $\sim$ 300 nm are distinguishable in the line profile (c), even though the color dip becomes shallow.

It is important to note that lateral resolution does not correspond to the minimal size of individual objects that can be observed. Individual particles smaller than 160 nm can readily be observed but pairs of such objects cannot be distinguished from individual objects. This is exemplified in Fig. II.6.e-f, Carbon NanoTubes (CNT) around 50 nm in diameter are deposited on a BALM substrate and then imaged by SEM and BALM. The BALM technique clearly detects particles smaller than the diffraction limit. Other experiments able to distinguished nano-objects using the BALM microscope were also performed: in our group for Fe_3O_4 nanoparticles [3] and in 2018 at Itodys (Paris-Diderot University) with silver nanoparticles [215, 216] and at CRPP (CNRS Bordeaux) with single-wall CNTs (see figure S5 in the Supporting Information of Ref. [217]).

II.2 Status of BALM developments at the beginning of this work

In 2014, D. Ausserré co-founded a startup named Watchlive to develop the technique and the BALM microscope is now protected by 6 patents. [218–223] After the first publication, [214] a collaboration started between D. Ausserré and the Licsen using a prototype set-up. The goal of this collaboration was to demonstrate the capabilities of BALM to observe graphene-derivatives and their chemical reactivity. The work led to a publication in 2017. [3] I started my PhD project while this article was in preparation. I notably performed experiments to address some of the reviewers' questions. Hereafter, I review the results of this initial work which serves as an introduction for the presentation of my contributions.

II.2.1 Observation of Graphene Oxide

Graphene Oxide (GO) was of particular interest for the collaboration and is the most studied 2D material in this thesis. GO is one of the most difficult 2D material to observe by optical microscopy. This one atom-thick graphene derivative is indeed highly transparent. [24] GO flakes were deposited on a 5 nm gold ARA layer by the so-called "bubble deposition technique". [224] This method developed at CEA consists in transferring nano-object concentrated in a water film stabilized by surfactants such as the wall of a bubble (or a flat water film). It notably allows depositing graphene oxide flakes with a limited amount of folds and wrinkles. Contrast enhancement provided by the BALM configuration allowed high-contrast visualization of the flakes as presented in Fig. II.7. On the left image, taken in air, it is straightforward to distinguish the flakes from the surface. As GO tends to fold and creates multilayers, the image allows counting the number of layers stacked on top of each others. This is exemplified by the gray scale profile across the flake as multilayers are incrementally darker. Furthermore, the image shows even small defects like wrinkles. Interestingly, due to the inverted microscope configuration, the emergent medium can be replaced by any liquid. Air (left image) was then replaced by water (right image) while keeping the same level of information.

In order to compare the different ways to observe Graphene Oxide, the same flake was imaged by BALM, AFM and SEM, as illustrated by Fig. II.8. First, AFM confirms that the observed flake is one layer thick (1.3 nm) which gives a first idea of the nanometric

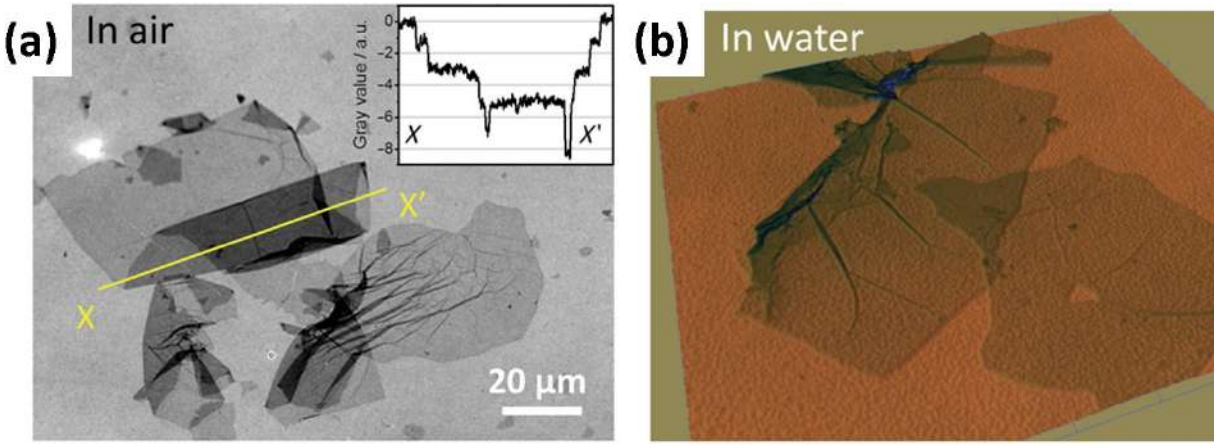

Figure II.7: BALM images of graphene oxide. (a) In air with associated gray scale profile, **(b)** in water, green channel only. [3]

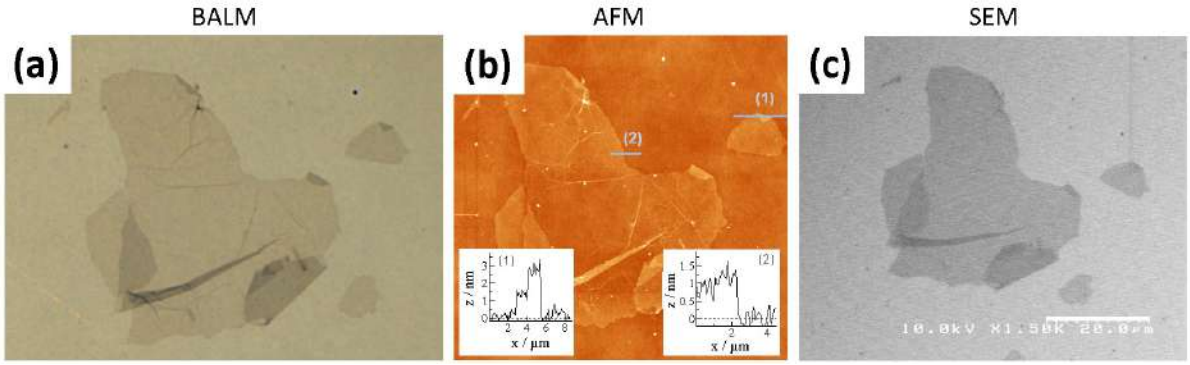

Figure II.8: Imaging techniques comparaison on the same GO flake. (a) BALM in air, **(b)** AFM with thickness profiles, **(c)** SEM. [3]

z-resolution of BALM. Then, BALM and AFM show the same level of details but BALM is an optical microscope so it is faster, simpler and cheaper than AFM or SEM. Moreover the inverted configuration allows the addition of a solvent without disturbing the observation and thus paves the way to surface reaction monitoring.

II.2.2 Discrimination between GO and rGO

Graphene Oxide was initially a way to produce graphene at large scale. [225] The last and crucial step to achieve graphene is the reduction of GO. The obtained material is called reduced Graphene Oxide (rGO). It still contains oxygen groups and the lattice is far from perfect. It should thus be clearly distinguished from graphene. One way to reduce GO is through a simple thermal treatment, preferentially in vaccum. [226, 227] In the following experiment, Graphene Oxide was deposited on a gold BALM support, then the sample was placed at 350°C in vacuum (10^{-6} bar) for 1 hour and a BALM image was taken (Fig. II.9.a). Then, new GO flakes were deposited on the same area

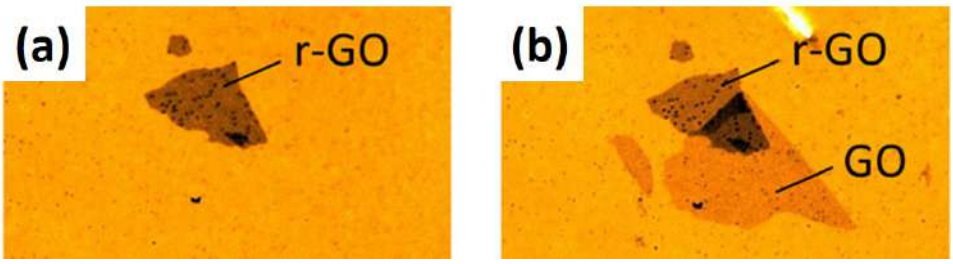

Figure II.9: GO / rGO discrimination. (a) BALM image in air of rGO, **(b)** same rGO flake with the addition of a fresh GO flake. Red channel only. [3]

and BALM images containing both rGO and GO were recorded (Fig. II.9.b).

It is striking to see the color difference between the two materials even though they only differ by the amount of oxygen groups. The removal of these species and the partial recovery of the graphene lattice result in a strong increase of the light absorption which would reach 2.3% for perfect graphene. [226] As a result, reduced Graphene Oxide appears darker than GO. One should note that rGO is slightly thinner than GO. If thickness was the only probed parameter, GO would appear darker. In this case, the change in optical properties is the most relevant effect.

This experiment shows that BALM is highly sensitive to changes in refractive index produced by small chemical differences.

II.2.3 Adsorption of nanoparticles on rGO

As discussed earlier, adding a solvent on top of the BALM microscope is simple. Meaning that the technique is able to observe reactions at the interface. To do so, the next experiment reported in [3] presents the functionalization of rGO with oleic acid-coated Fe_3O_4 nanoparticles. Fig. II.10 shows images in air of the rGO flake before and after deposition. The particles were dispersed in toluene, then a drop was dried onto the rGO BALM surface and finally a drop of toluene was added to remove the particles.

First of all, the nanoparticles are 5 nm in diameter and still they are distinguishable on the images, but it is not possible to say if it is a single nanoparticle or several particles aggregated. Then, the images show a preferential adsorption of the particles along the wrinkles of rGO.

BALM is able to observe nanoparticles and probe local interaction between two nanomaterials.

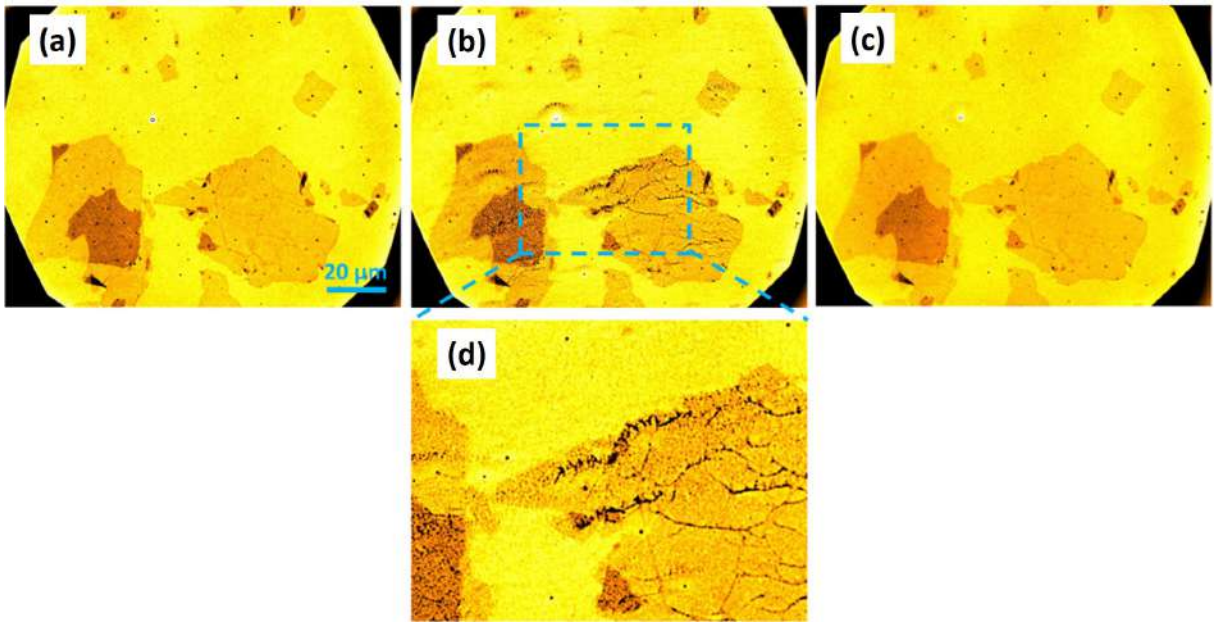

Figure II.10: Adsorption of Fe_3O_4 nanoparticles on rGO. (a) BALM image in air before deposition, **(b)** in air after deposition, **(c)** after rinsing with toluene, **(d)** zoom of (b). [3]

II.2.4 Adsorption of pyrene on GO

BALM is a wide-field optical microscope able to take movies. So images like those previously shown are the first step toward the study of dynamic systems. The next step is to take images at regular intervals as it allows the monitoring of reaction dynamics. For this purpose, the adsorption of a pyrene derivative on GO was studied. A drop of water containing the pyrene was added on GO and images were taken every 6 seconds. For each image, the gray scale value was averaged on 4 different areas: gold, mono-, bi-, and tri-layers GO. The intensity was then plotted against time for the 4 areas and fitted with a simple exponential decay function. Details on the experiments are presented in [3]. The experiment shows that the adsorption is faster when increasing the number of GO layers, as it was quantified by the optical characteristic time constants.

As a conclusion, BALM is able to follow organic molecules adsorption at 2D materials and to extract the local dynamics.

II.2.5 First conclusions on the status of BALM at the beginning of this work

This publication highlighted several advantages of the BALM configuration, in particular the possibility to obtain local information coupled to the observation 2D materials. The set of experiments were selected to illustrate the diversity of the obtainable information. However, most experiments were preliminary and the experimental setup was limited to experiments in air or water. They only used a single type of BALM substrates and only slow acquisition (one image every 6 seconds) was possible. In the following, we show how BALM was improved in different ways during this thesis and how it impacted the type of experiments that can be addressed as well as their precision.

II.3 Optimizing the BALM conditions

In 2016, the BALM substrates were provided by the startup and they were made of a 5 nm gold near-ARA layer. With the aim of understanding and controlling the anti-reflective properties, we decided to produce the ARA coating ourselves as it provides more flexibility to adjust the substrates to each specific study. Note that to complete this thesis project, more than 600 substrates were produced, using different configurations of material stacks. Most experiments presented in the following would not have been possible with standard BALM substrates as the ones available in 2016.

In this section, the different parameters influencing the ARA properties are discussed. Indeed, regarding equation II.7:

$$e_{ARA} \simeq \frac{\lambda}{4\pi} \frac{(n_i - n_e)}{n_{ARA} k_{ARA}}$$

several parameters could be modified in order to adjust the BALM substrates.

First, the optical properties (n_{ARA}, k_{ARA}) could be modified by changing the ARA layer with any high extinction coefficient material. It was decided to focus on gold ARA coating for several reasons: *(i)* the optical properties of very thin gold films are better documented than those of any other metal, *(ii)* gold is stable against oxidation (considering that the thickness range of interest for BALM is below 10 nm, even an extremely thin oxide layer can have a significant impact), *(iii)* an important part of this work relates to electrochemistry for which gold is also a substrate of choice. The deposition of gold directly on glass is challenging with a classical thermal evaporator as noble metals do

not form an intermediate oxide layer promoting the adhesion on glass. [228,229] To address this issue, the use of a chromium or titanium thin layer between glass and gold is a common practice. In order to decrease the impact of this adhesion layer on the ARA properties, it was decided to reduce the chromium thickness to the minimum possible. After a few step by step improvements, the thickness was decreased to 0.5 nm for regular experiment and to a simple "flash type deposition" which yield a chromium thickness of approximately 0.1-0.2 nm when necessary (notably for the experiments reported in section II.4).

II.3.1 Gold thickness

The ARA layer used for most experiments consists of 0.5 nm chromium and *X* nm gold. This last parameter is the one influencing the most the AR properties. It was decided to study the impact of the gold thickness on the contrast of graphene oxide. To do so, BALM substrates with gold thickness ranging from 1 nm to 7 nm were prepared. Then the AR properties were characterized by placing the slides on the BALM microscope and making sure that the settings remain the same (light power, diaphragm aperture, etc.). For each different thickness, BALM images were taken in air and in water. Then the reflected intensity was obtained by dividing the gray scale with the exposure time of the camera and it was plotted against ARA thickness, as presented in Fig. II.11.a. The two curves present a minimum reflection for really thin ARA layer as previously explained in Fig. II.3.c using the numerical simulations. The experimental results show that the optimum gold thickness for AR substrates is around 3 nm in air and around 1 nm in water. It reflects respectively 2.7 and 3 times less light than glass alone. The reflection is lower for water than air as its refractive index is higher.

Then graphene oxide was deposited on the BALM slides and the contrast of the monolayers was plotted in Fig. II.11.b. GO images with really low contrast (< 1%) were not plotted due to difficult extractions leading to significant errors. In air, GO monolayers are only visible with at least 2 nm of gold and the contrast is maximum for 3 nm of gold before it decreases. Images in water are even more interesting: first, GO is visible even on glass alone but with a really limited contrast (< 2%) as shown in Fig. II.11.c. Then, the contrast is maximum for 1 nm gold but interestingly with a positive value contrarily to the observations so far (Fig. II.11.d). This means that GO reflects more light than the ARA coating. Finally, the contrast is inverted (negative value) and decreases when increasing the ARA layer thickness.

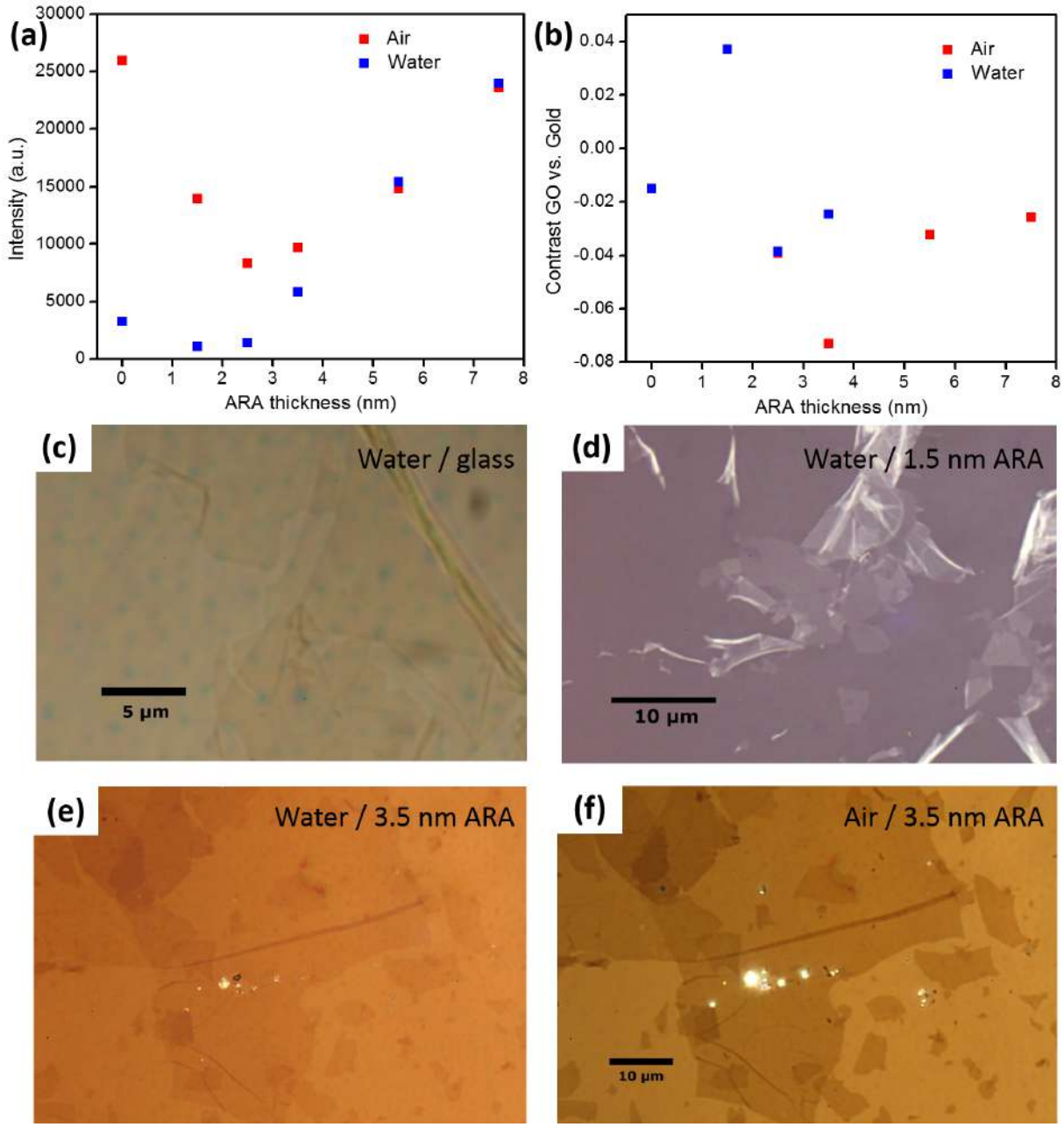

Figure II.11: Impact of gold thickness, (a) on reflected light, **(b)** on monolayer GO contrast, **(c-f)** examples of GO images in different configurations.

During this thesis, the type of ARA layer mainly used is a 0.5 nm chromium + 3 nm gold because it provides a good compromise between imaging in air and in water, as presented in Fig. II.11.e,f. The contrast in air being excellent, it notably enables an easy selection of interesting areas before a solvent is added without moving the BALM slide. Furthermore, 3 nm of gold is the limit to obtain a conductive coating.

II.3.2 Refractive index

The refractive indexes of the incident (n_i) and emergent (n_e) media are also used to adjust the anti-reflective conditions. Considering the BALM configuration, the easiest medium to change is the emergent one as any liquid can be added on top of the slide. The following experiment presents the dependence of the GO contrast as a function of the solvent refractive index. To do so, GO was deposited on a 0.5 nm Cr + 1 nm Au coating because we wanted to show that even though the AR coating is almost optimum in water, it can be further improved. Mixtures of water and glycerol were added in order to obtain refractive indexes ranging from 1.33 to 1.47. The contrast of GO monolayers was extracted from the images and plotted in Fig. II.12.

The starting system was already the one showing the best contrast in water but increasing the emergent refractive index almost doubles the contrast of the GO monolayers as perfect AR properties are approached.

The incident medium could also be used to modify the AR properties. For example, replacing glass (n = 1.5) with sapphire (n = 1.77 [230]) could increase the optimum thickness for imaging in water (obtained with equation II.7) by a factor of 2.6. The possibility to use thicker gold layers is very interesting in order to increase the conductivity of the ARA coating for electrochemistry.

But several drawbacks have to be considered. First, the new material has to be thin because of the short focal distance of the objective (the glass coverslip used here is 130 µm thick). Then the rugosity of the substrate has to be very low and the transparency very high. Such sapphire substrates are scarce and expensive. They were not used in the following but could be considered as an interesting option for specific experiments

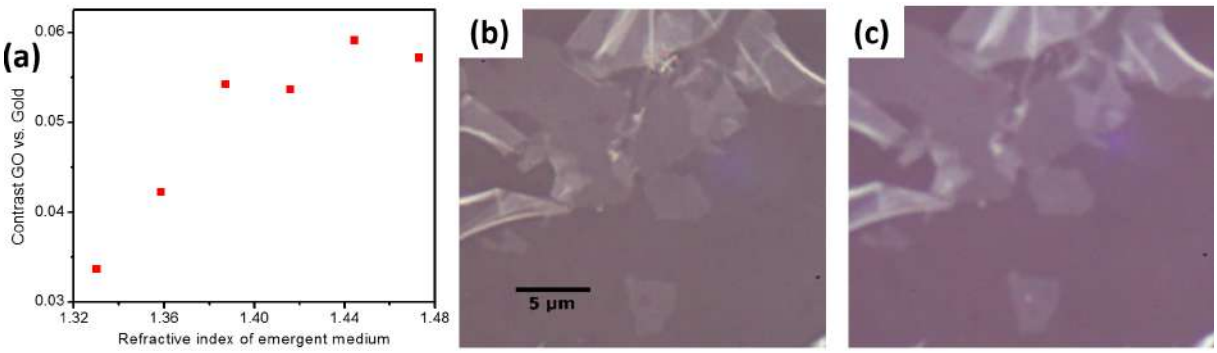

Figure II.12: Impact of the emergent medium refractive index, (a) on the contrast of monolayer GO deposited on 0.5 nm Cr + 1 nm Au, **(b)** BALM image in water (n = 1.33), **(c)** same flake but using a mixture of 80% glycerol and 20% water (n = 1.44).

requiring thicker gold in the future.

II.3.3 Wavelength

Looking at equation II.7, the AR properties also depend on wavelength. This parameter is well-known to adjust the contrast of 2D materials when observed with classic anti-reflective coatings. To study this parameter, we decided to use MoS_2 as its monolayer form is a direct band-gap semimeconductor. Its complex refractive index is much more dependent on wavelength than the one of graphene or graphene oxide, therefore the contrast should be significantly modulated by the wavelength.

First, we present BALM images of monolayer MoS_2 synthesized at Licsen by Chemical Vapor Deposition (CVD), as shown in Fig. II.13.a-b. Images are taken in air and water and they both present monolayer sheets with high contrast. The same flakes were also imaged by AFM and compared to BALM in air and water, as presented in Fig. II.13.c-e. BALM and AFM show the same level of details of the flakes and it confirms that the flakes are monolayers and that the small triangles in the middle of the flakes correspond to the beginning of a second layer. BALM can thus be used as an efficient characterization technique for the post-synthesis imaging of MoS_2 over very large areas. Two examples are presented in Fig. II.13.f-g. The left image shows a MoS_2 flake obtained in CVD conditions where there was oxygen left during the growth. The flakes were partially oxidized at high temperature (after the triangular domains were formed), probably preferentially at defect sites and along grain boundaries resulting in fragmented flakes. Such issue was not observable with our conventional microscope (except for the most defective synthesis and only once the problem was known). It was confirmed by AFM on selected triangles but BALM allows scanning cm^2 areas within seconds, which is helpful considering the limited homogeneity of our CVD process. The right image (Fig. II.13.g) shows a typical CVD MoS_2 flake with different types of defects originated both from the synthesis (nucleation of second layer) and from the transfer (folded edge) as well as the nucleation point at the center of the triangle. This type of image could particularly be used to study the fractal growth of the second layer. To our knowledge, this is among the most contrasted optical images of MoS_2 reported to date.

As MoS_2 is highly light absorbing, it is quite easy to observe with a classic microscope. We show here the additional benefits of the gold anti-reflective layer for MoS_2 imaging. Flakes were deposited on a glass slide and imaged using the same inverted

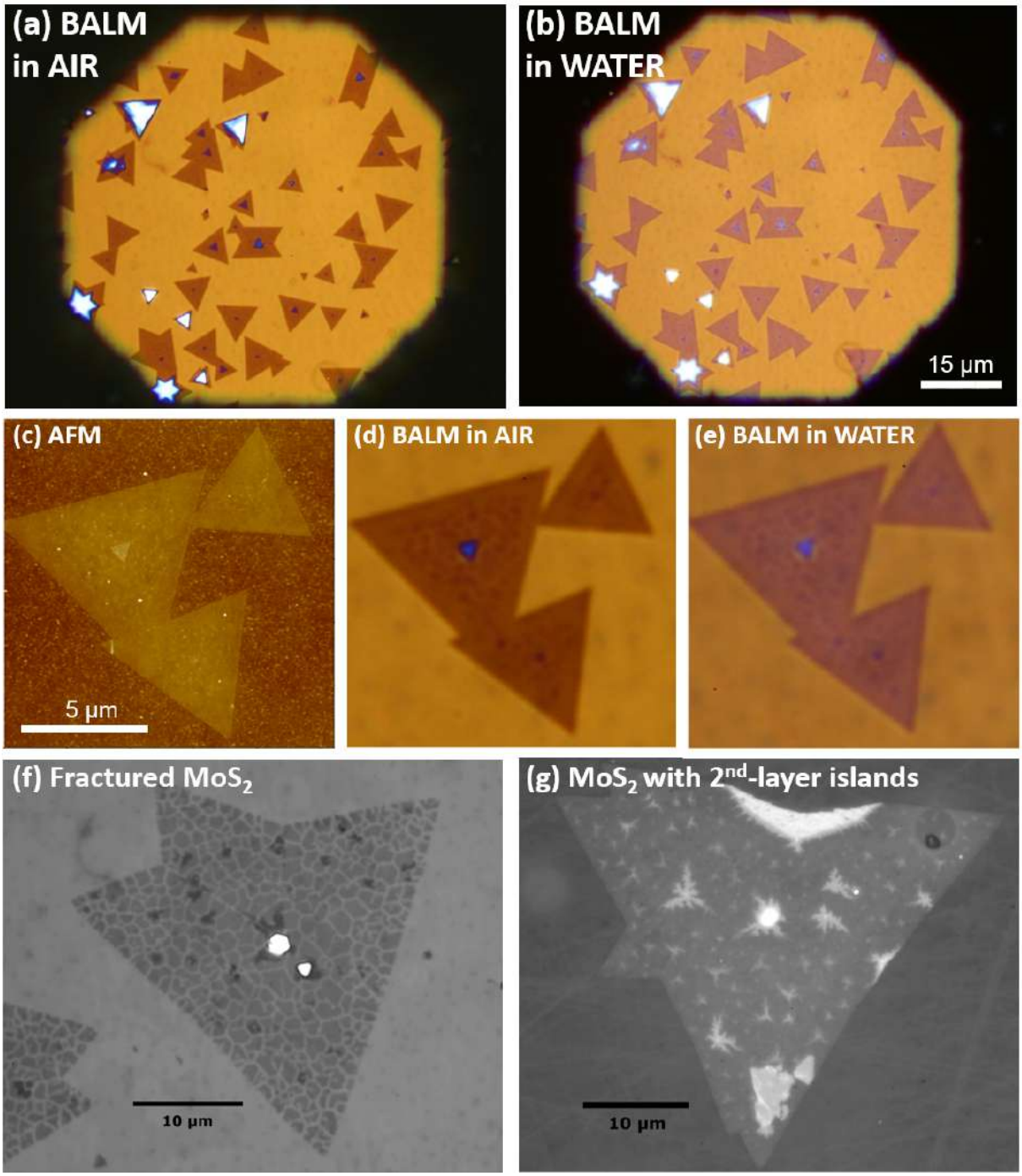

Figure II.13: Imaging MoS_2 with BALM. (a) BALM image in air, **(b)** in water, **(c-e)** comparison of the same flakes by AFM and BALM, (c) AFM topography, BALM images (d) in air and (e) in water, **(f-g)** examples of BALM images in air of CVD grown MoS_2 (black and white images).

microscope and high quality immersion objective (x63 and NA = 1.4) but without the anti-reflective layer. In Fig. II.14, one can see that the MoS_2 flakes are indeed visible in air and much less in water. Even though, the monolayers are observable, the defects and the second layer are not distinguishable, at the exception of the nucleation points

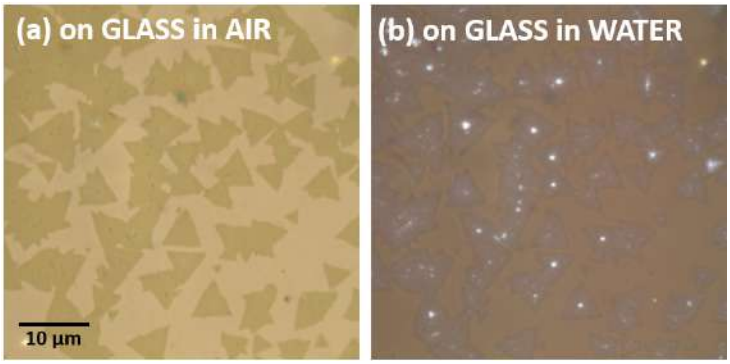

Figure II.14: Images of MoS_2 taken with the same microscope as BALM images but without the gold ARA coating, (a) in air, **(b)** in water

which are observable in water. Comparing Fig. II.13.g and Fig. II.14.a confirms the enhancement of contrast and shows how BALM allows revealing details not observable without the anti-reflective layer.

We now turn to the observation of MoS_2 flakes deposited on a 0.5 Cr + 3 nm Au BALM substrate using light filters. Fig. II.15 shows the same area imaged in air and in water: (a) without any filter, (b) using a bandpass filter at λ = 450 nm filter and selecting only the blue channel of the camera, (c) using a bandpass filter at λ = 550 nm filter and selecting only the green channel of the camera, (d) using a bandpass filter at λ = 650 nm filter and selecting only the red channel of the camera (filters are 10 nm FWHM). It is first striking to see that MoS_2 can appear either much brighter or much darker than gold depending on the selected wavelength. It thus immediately illustrates the drastic impact of λ on the BALM conditions and points toward the opportunity of selecting a particular wavelength to further improve contrast. To this end, the contrast of the monolayers and bilayers were extracted from these images and plotted in Fig. II.16.a-b. One can see that in air, the MoS_2 is more contrasted using the 550 nm filter, whereas in water, the wavelength does not have a tremendous impact (the contrast is inverted when using blue or green light but the absolute values are comparable). Therefore, for the best imaging quality of MoS_2 sheets, it is preferential to use a green filter. It is however important to notice, that BALM relies on very little reflected light. Adding a filter significantly decreases this already weak signal. Additional contrast may thus come at the expense of signal quality (in particular when recording movies for which it cannot be compensated by a longer acquisition time).

We then compare these results with the simple optical model based on the Fresnel equations using the Comsol software. The model uses six parameters: the gold thick-

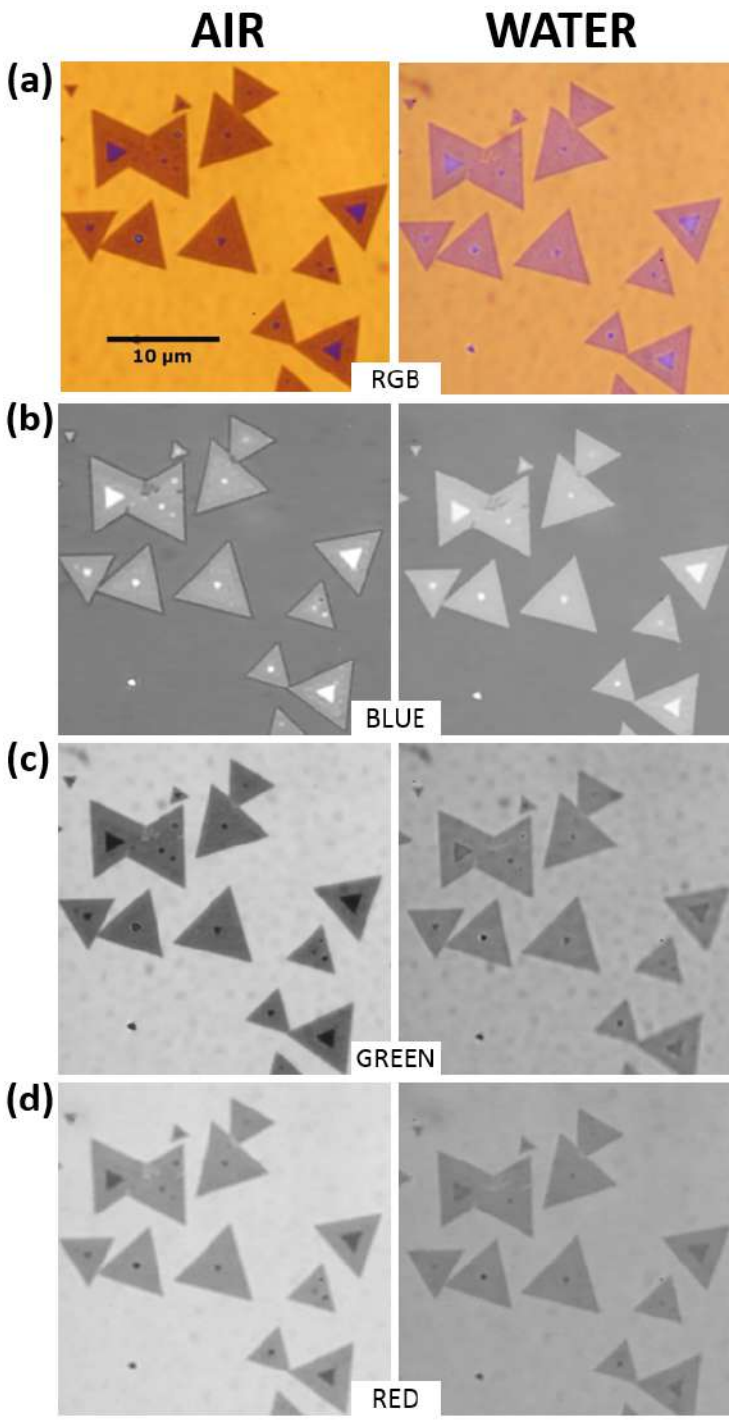

Figure II.15: Wavelength dependence of MoS_2 BALM contrast. Images in air and water **(a)** without filters, **(b)** 450 nm filter and only the blue channel of the camera, **(c)** 550 nm filter and only the green channel, **(d)** 650 nm filter and only the red channel.

ness, its complex refractive index (n_{gold}, k_{gold}), and the MoS_2 complex refractive index (n_{MoS_2}, k_{MoS_2}). This model is clearly not quantitative because of the many approximations used: simulations are performed at a single angle (normal incidence only, instead of considering the numerical aperture of the objective), at a single wavelength, layers are considered flat (while the rugosity of gold is not negligible at the 5 nm scale), etc.

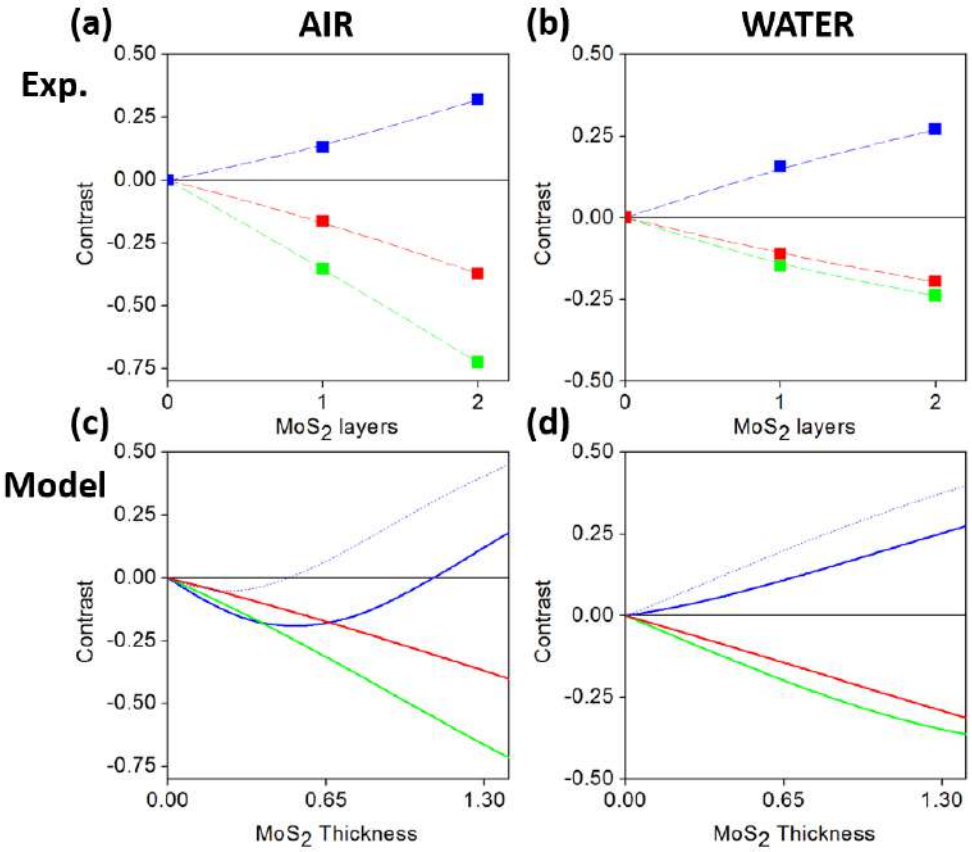

Figure II.16: Experimental and theoritical contrast of monolayer MoS_2. (a-b) Experimental contrast extracted from the images of Fig. II.15, (a) in air and (b) in water, blue curves correspond to images taken at 450 nm, green curves at 550 nm and red curves at 650 nm. **(c-d)** Calculated contrast (a) in air and (b) in water. The dotted blue curves correspond to the modification of k only at 450 nm to $k_{MoS_2} = 2.25$ whereas the plain blue curves correspond to $k_{MoS_2} = 1.5$.

The model is thus just used to help clarifying the wavelength dependance of the images. We set the gold thickness of the simulation at 5.5 nm which is higher than the 0.5 + 3 nm because the model does not take into account the chromium adhesion layer which is even more light absorbing than gold. For the gold refractive index, we used the data implemented in the Comsol software for 3.96 nm gold layer which were provided by Lemarchand and co-workers using their own method developed in [231].

In terms of MoS_2 complex refractive index, the determination of the monolayer properties is challenging and was the subject of several studies. In 2017, the team of Guillaume Baffou at Institut Fresnel (Marseille), measured and compared the different n and k values from the available publications at that time. [98] These values, extracted from [92, 94, 97, 232] are presented in Fig. II.17. One can see that the refractive index differs a lot from the publications.

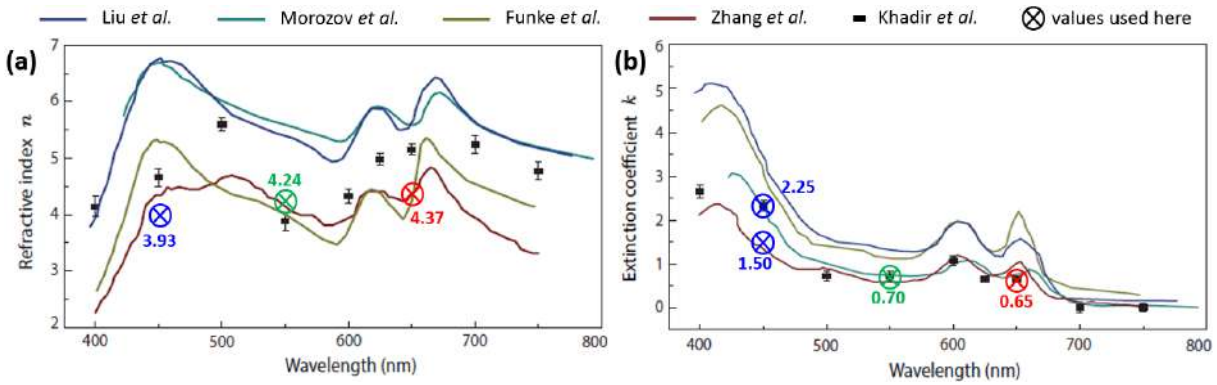

Figure II.17: Comparison of the complex refractive index of MoS_2. (a) refractive index, **(b)** extinction coefficient. [92, 94, 97, 232] Reprinted with permission from [98]

For our simulations, we first tried to use the refractive index and extinction coefficient values from Liu *et al.* [97] but it proved impossible to account for the observed images. Then, we used the values of Zhang *et al.* [232]. We averaged the brown curve in Fig. II.17 in three different ranges, around λ = 450, 550 and 650 nm and considered the values represented by crossed-circles in this figure. The simulated contrast for mono- and bi-layer MoS_2 are plotted in Fig. II.16.c-d considering a MoS_2 thickness of 0.65 nm/layer. These simulations provide a reasonable approximation of the experimental contrasts in all cases at the notable exception of one image. Indeed, the model indicates that in air and at λ = 450 nm, the MoS_2 monolayers should be darker than gold but the experimental image clearly shows that they are brighter. To tentatively explain this single discrepancy, we first note that the extinction coefficient of MoS_2 obtained by the different groups highly differ for wavelength below 500 nm. We thus investigated the influence of k_{MoS_2}(λ 450 nm) on the simulated contrast. To do so, we progressively modified this value from 1.5 (Zhang *et al.* value) to 2.25 (a value representative of average literature values and very close to the values reported by Khadir *et al.* [98] and Morozov *et al.* [94] as shown in Fig. II.17.b). This k = 2.25 value produces the simulated blue-dotted curve in Fig. II.16.c-d. With this change, the calculated contrast now follows the experimental trend (*i.e.* monolayers are brighter than gold in air at 450 nm). We also verified that this change in k_{MoS_2} at λ = 450 nm does not impact the result in water (blue dotted-curve in Fig. II.16.d).

All together, this study shows that wavelength can be used as an adjustable parameter to tune contrast in BALM experiments. The comparison with simple simulations also validates the fact that the generic principles of anti-reflection from equation II.7 account for the observed behavior in different conditions of material thickness (mono- and bi-

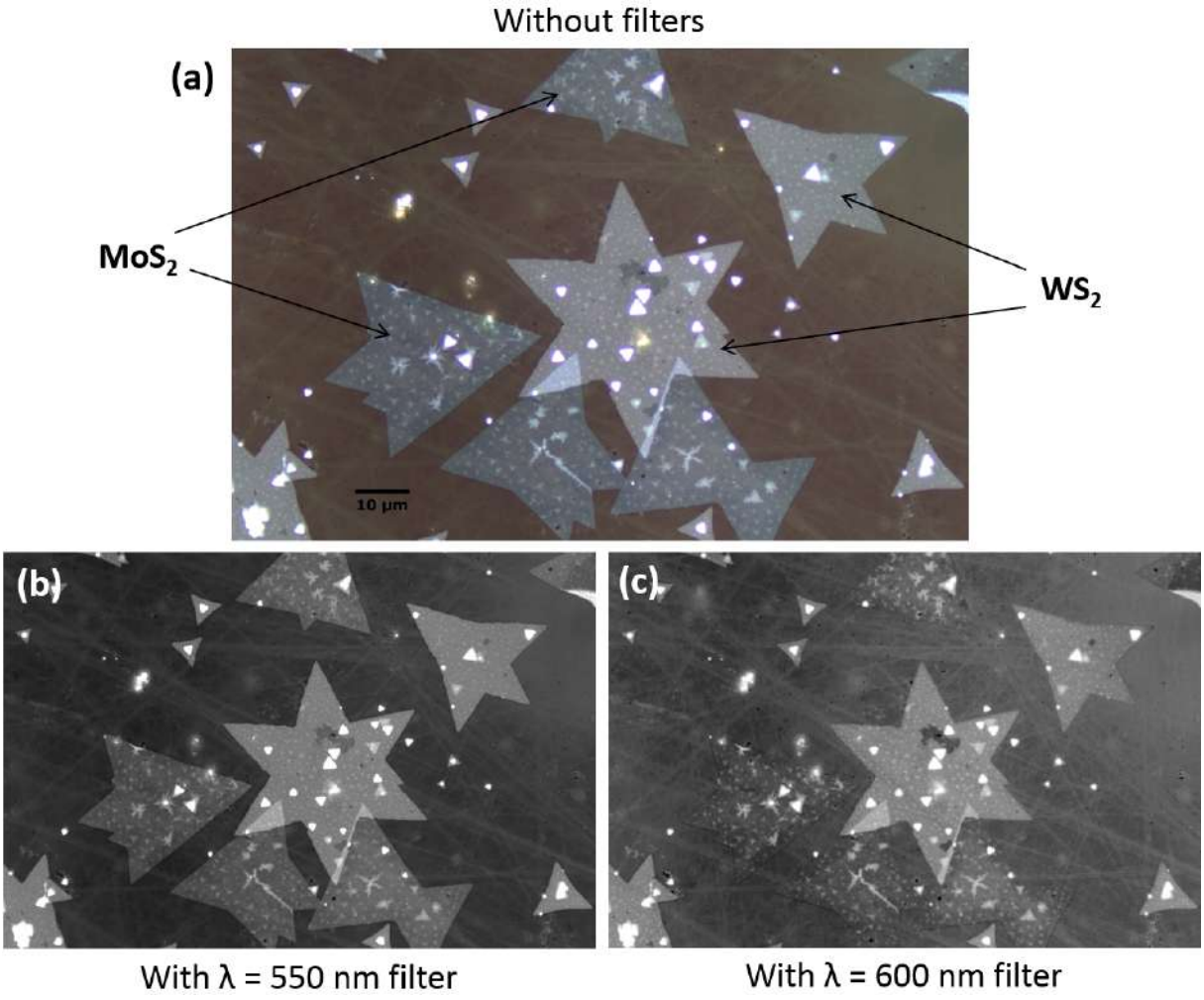

Figure II.18: Maximizing the contrast difference between MoS_2 and WS_2. **(a)** BALM image without filters, **(b)** with a λ = 550 nm band-pass filter, **(c)** with a λ = 600 nm band-pass filter.

layers), wavelength and air/solvent configurations, despite the approximations (notably observation angle and rugosity). Interestingly, our study globaly supports the measurement of n_{MoS_2} and k_{MoS_2} by Zhang *et al.* However, it clearly rules out the possibility for k_{MoS_2} to be below 2.25 at λ = 450 nm. By extending the model (to account for different angles, include the chromium adhesion layer and the surface rugosity), BALM could bring precise and quantitative information on the complex refractive index of 2D materials. In its present form, it already provides values with a precision comparable to the one of other techniques.

The previous experiment showed that the optimal imaging wavelength for MoS_2 is 550 nm. But wavelength can also be used as a way of maximizing the difference between two materials. To demonstrate this, MoS_2 and WS_2 were deposited on a 0.5 Cr + 1 nm Au slide and BALM images were taken as presented in Fig. II.18. First, one can

see that the two materials have different colors. So, even without filters, BALM can be used to easily differentiate MoS_2 from WS_2. This could be very helpful for the study of van der Waals heterostructures. Using filters, the contrast difference between the two materials is varied. At λ = 550 nm, the difference is comparable to the one obtained with white light, whereas at 600 nm, the contrast of the MoS_2 monolayers versus gold is almost zero while the WS_2 monolayers are still easily observable. The difference of visibility between the two materials is thus maximized. This last feature adds to the interest of using monochromatic light of adjustable wavelength.

Filtering the source drastically reduces the intensity reaching the camera and so, it increases the time to take an image. In the following, the full spectra was used whenever possible. Replacing the halogen lamp by a series of laser diodes could be an important upgrade to the microscope.

II.4 Improving BALM and adding new functionalities

Adjusting the observation conditions using the previous parameters (ARA thickness, ARA and solvent refractive index, wavelength) allows a good approximation of the anti-reflective conditions as equation II.7 is verified. But as described in section II.1.3, BALM ideal conditions are governed by two equations. A metallic ARA coating cannot be ideal as the second equation:

$$n_{ARA}{}^2 - k_{ARA}{}^2 = n_i n_e \tag{II.8}$$

quantifying the amount of reflected light can only be approached. Indeed, for metals, k is almost always higher than n, therefore $n_{ARA}{}^2$ - $k_{ARA}{}^2$ is negative whereas $n_i n_e$ is positive. Even though, using 3 nm of gold on glass as BALM substrate already results in a high contrast suitable for most experiments. Further improvement could be obtained if one could further reduce the amount of light reflected by the substrate.

Classic AR coatings have been improved for a long time using multilayer coatings. [203, 204] They are composed of two or more stacked materials, each having a precisely selected optical properties and thicknesses. With more interfaces and more adjustable parameters, one can better adjust the conditions for destructive interferences.

Hereafter, we decided to study the addition of a second layer on the gold BALM sub-

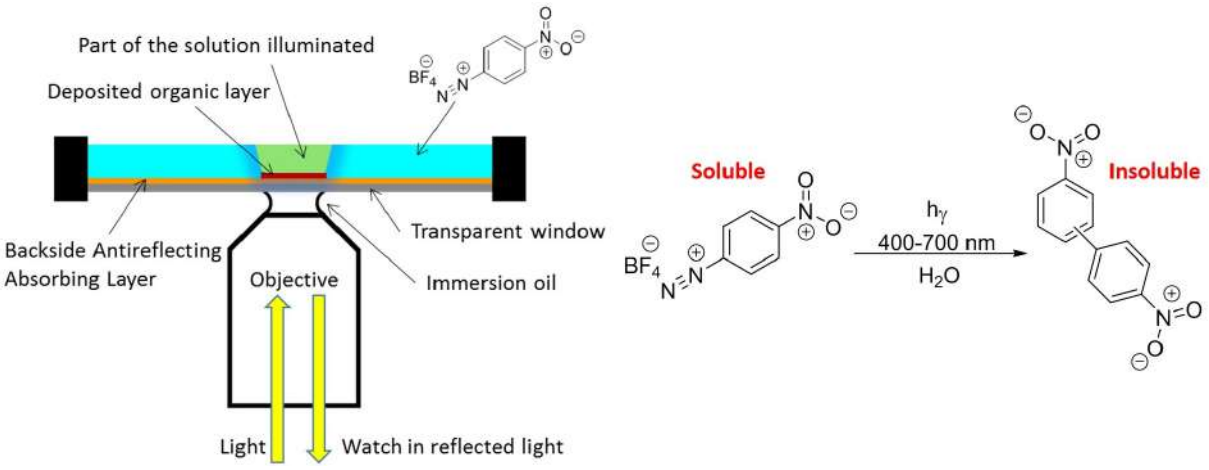

Figure II.19: BALM set-up for the study of organic layer deposition by photodimerization of NBDT.

strate, using an original approached. We show that it improves contrast for the observation of 2D materials. The work described in the following section was recently published. [1]

II.4.1 *In situ* controlled deposition of molecules

As a first step, we studied the deposition of an organic layer on top of the BALM substrate. To do so, we used the capability of BALM to follow *in situ* the addition of a material modifying the refractive index at the interface. In practice, we used a photochemical reaction to control the organic layer deposition. This light-induced deposition is performed using 4-nitrobenzenediazonium tetrafluoroborate (NBDT) solubilized in water. When exposed to light, this compound is known to dimerize [233] and produce a water-insoluble molecule which gets deposited only in the observed area, as presented in Fig. II.19. This configuration has several advantages: *(i)* the deposited layer is spatially controlled, meaning that an area of the substrate can be selected and the size of the deposited pattern can be modified using a diaphragm (the diaphragm has an hexagonal shape resulting in hexagonal patterns of deposited molecules); *(ii)* The deposition speed is controlled by the optical power which can be tuned; *(iii)* Movies are recorded during the light-induced molecule deposition so that the dynamic of reflectivity and contrast can be extracted (using an home-made *Mathematica* program).

Technically, the experiment is performed on the BALM microscope using a $\sim$ 0.1-0.2 nm Cr + 3 nm Au ARA coating. After the focus was set in air and the diaphragm was set to be smaller than the image ($\sim$ 50 µm), a solution of NBDT (10^{-3} mol L^{-1}) in water was added on top and recording of a movie was started. After a few minutes, the position of

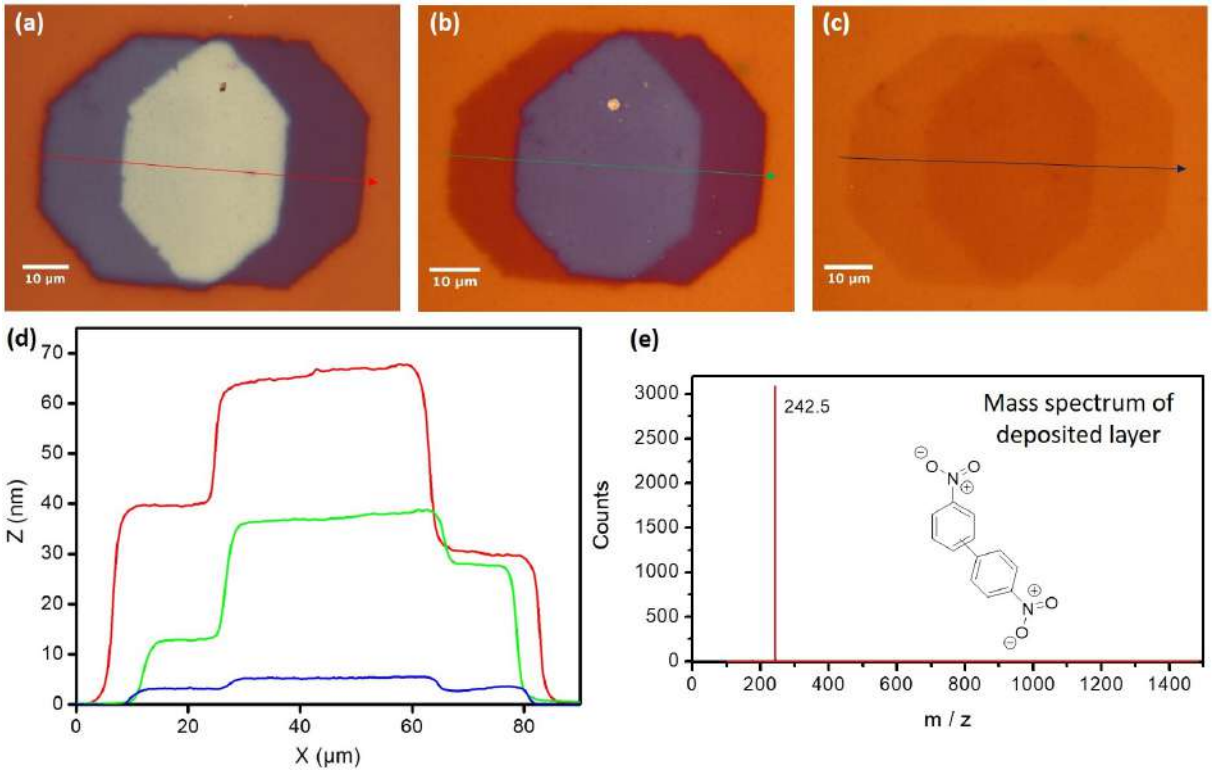

Figure II.20: Light-induced deposition of molecules at three optical powers. The deposition is performed with the hexagonal diaphragm partly closed and the BALM images are acquired with the diaphragm fully opened. At mid experiment, the exposed area is moved by $\sim$ 20 µm along the arrow direction, **(a)** maximum intensity (I_0), **(b)** 0.4 * I_0, **(c)** minimum intensity, **(d)** AFM profiles along the arrow direction, **(e)** mass spectrum of the deposited layer showing that it is mainly composed of dinitro-diphenyl resulting from the light-induced dimerization of NBDT.

the BALM substrate was moved by $\sim$ 20 µm without stopping the recording in order to ease the understanding of the figures and the measurement of the deposited thickness. After 20 minutes, the movie was stopped and the solution was replaced by water. Then an image was taken with the diaphragm fully opened. Finally, AFM was performed to determine the final thickness. At the end, the deposited layer was removed from the substrate using a drop of acetonitrile. This drop was then used to perform the mass spectrum of the final product which confirmed the dimerization of NBDT, as presented in Fig. II.20.e.

This experiment was repeated for three optical powers: first, at the maximum light power possible with our lamp, then we added a filter reducing the incoming light intensity to 40% of its initial value, and finally, at the minimum light intensity possible while still being able to record a movie. The final BALM images (diaphragm fully open) and AFM profiles are presented in Fig. II.20.

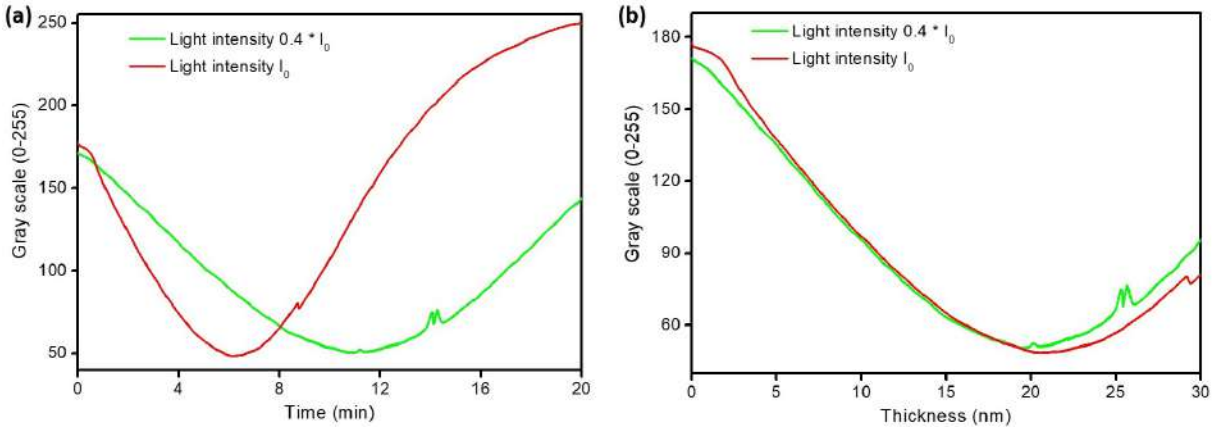

Figure II.21: Reflected light during the photo-deposition, (a) against time, **(b)** against layer thickness.

One has to notice that the deposited patterns appears either darker or brighter than the surrounding gold substrate depending on the deposited thickness. This result has some similarities with the one from the experiment on the gold thickness impact in section II.3.1 (Fig. II.11.a) in which the thickness was modified step by step in order to quantify the amount of reflected light. But contrarily to this previous experiment, the evolution is continuous and a movie is recorded during the full photo-deposition process so that the gray scale value can be extracted at video rate (25 images/sec). To do so, for the two light intensities, I_0 and 0.4 * I_0, the data from the green channel are averaged in an area of 100 * 100 pixels on each image of the movies and plotted as a function of time, as presented in Fig. II.21.a.

Even though the gold BALM substrate was chosen for its good AR properties, the gray scale starts by decreasing and reaches a minimum when adding this organic layer on top of it. This first observation already shows that simple metallic BALM substrates can be further improved (*i.e.* being made even less reflective) with the addition of a second layer of appropriate thickness.

Using the final AFM profiles and assuming that the deposition occurs at constant rate (which is a reasonable assumption considering the mechanism), the time scale is translated into a height scale. As expected both curves overlap as the deposition speed is proportional to the optical power. Especially, this transformation allows the determination of the second layer thickness at minimum reflection ($\sim$ 22 nm), and this with only one experiment.

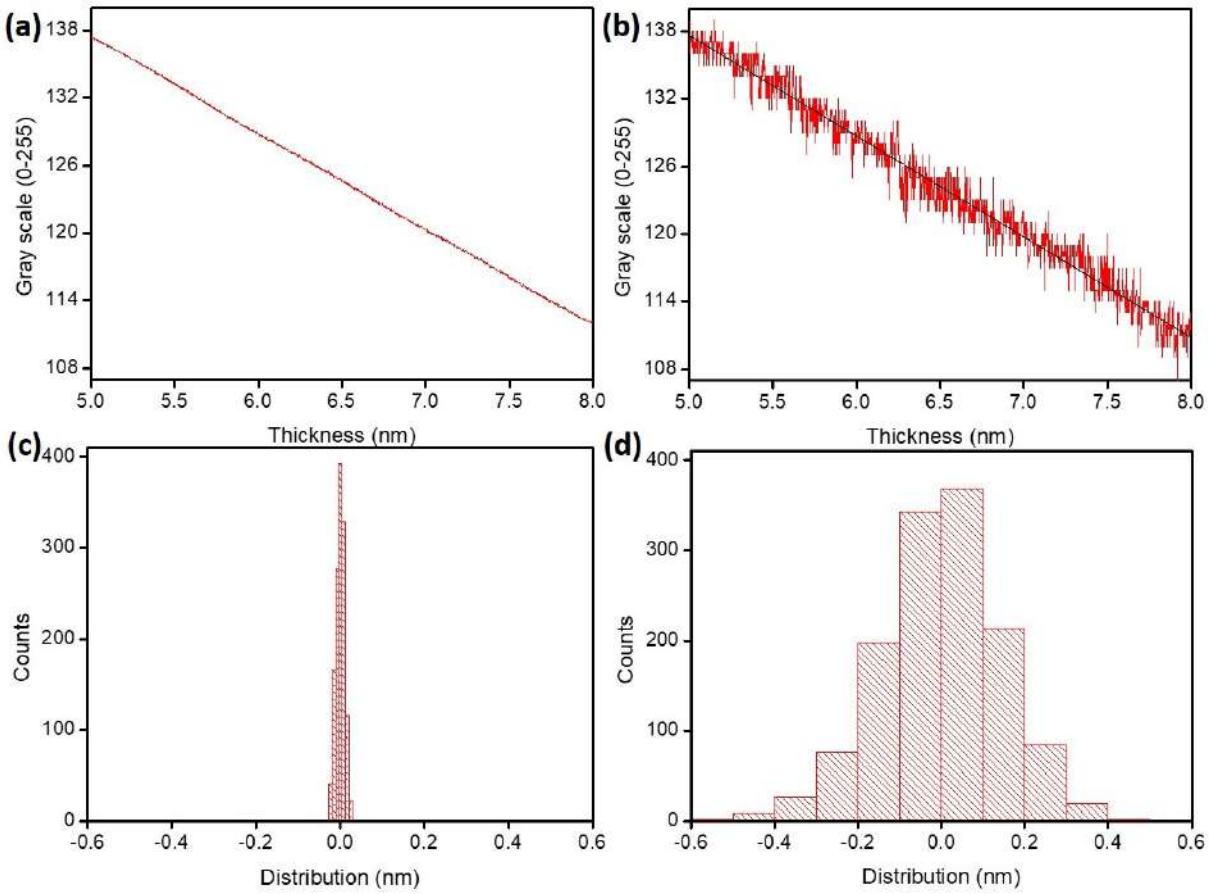

Figure II.22: Evaluation of the vertical resolution of the BALM technique. **(a)** Zoom on a part of the reflectivity curve of Fig. II.21.b corresponding to data averaged over 100 * 100 pixels, **(b)** same area but using data from a single pixel, **(c-d)** distribution around a linear fit. The standard deviation is 10 pm and 147 pm in **(c)** and **(d)** respectively.

II.4.2 Sub-nm vertical resolution

In the previous section, the light-induced deposition was used to determine the optimal thickness of a second layer then minimizes reflection. It is striking to note how smooth are the curves presented in Fig. II.21. From such experiment, the capability of BALM to detect extremely small changes at the substrate surface can be evaluated by estimating the vertical resolution, as presented in Fig. II.22. To do so, we used the reflectivity curve at maximum light power plotted as a function of the organic film thickness. A zoom on the curve (in the 5-8 nm of deposited thickness range) is used and linearly fitted. The distribution of the data around this linear fit is plotted in Fig. II.22.a,c. The obtained standard deviation is as low as 10 pm.

This very high vertical resolution is obtained with gray scale data averaged over 100 * 100 pixels corresponding to $\sim$ 7 * 7 μm^2. Such small area is perfectly suited for

homogeneous surfaces or for typical chemical- or bio-sensing experiments. But the same information can also be obtained at the single pixel level corresponding to $\sim$ 70 * 70 nm^2. The reflectivity was also extracted at this single pixel scale and plotted against thickness. It was similarly fitted linearly and the distribution was plotted in Fig. II.22.b,d. As expected, the standard deviation is higher than previously but it remains as low as 147 pm. This is lower than the molecule size and comparable to the surface roughness. It proves that BALM is able to monitor molecular-scale changes at video rate and at a single pixel level. This high vertical resolution is of particular importance for the used of BALM as a sensing technique and will be put at profit in chapter III.

II.4.3 Guidelines for a 2nd ARA layer selection

The thickness corresponding to minimum reflection ($\sim$ 22 nm), obtained here, is specific to the dimer molecule used since it is linked to its complex refractive index but the improvement of AR properties by the addition of a second layer is generic and, can be achieved with other materials. When taking into account the six adjustable parameters (thickness, refractive index and extinction coefficient of the metal and the second layer), it should be possible to design an AR coating adapted to any given experiment. This is exemplified by computing the reflectivity of the glass/gold/layer2/water interface using Comsol and Fresnel equations (with the already mentioned approximations). The impact of the second layer complex refractive index is presented in Fig. II.23.

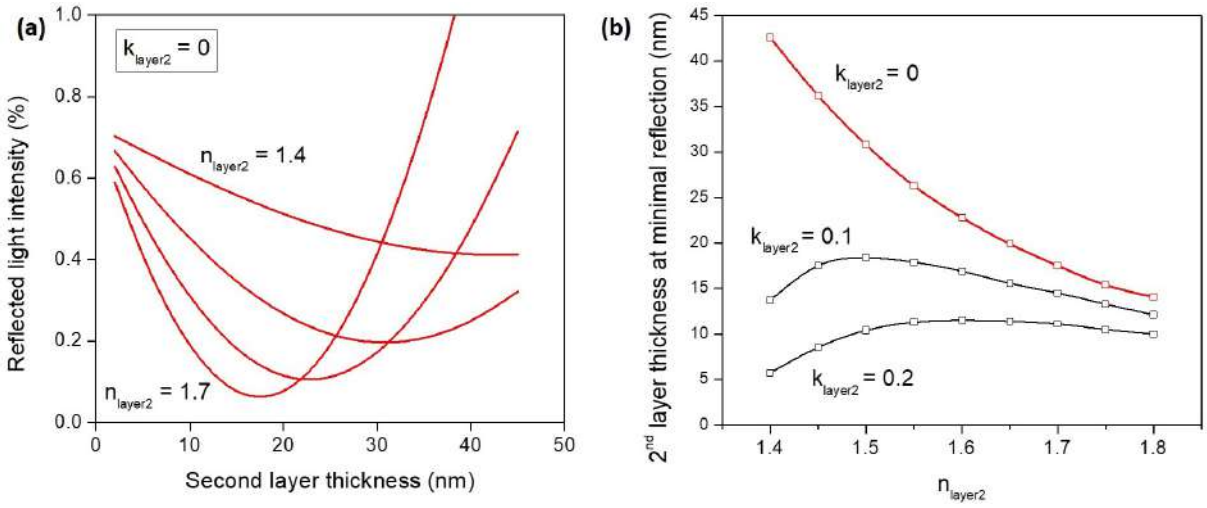

Figure II.23: Comsol simulation of the reflected light by a double layer coating composed of 3 nm of gold and a 2nd of material with complex refractive index (n_{layer2}; k_{layer2}) (at λ = 550 nm and normal incidence). **(a)** For k_{layer2} = 0, as a function of the second layer thickness and refractive index, **(b)** thickness of the second layer giving minimal reflection for different values of (n_{layer2}; k_{layer2}).

First, the gold thickness is set at 3 nm (with n and k taken from ref. [231]) and the evolution of the reflected light is shown as a function of the thickness and refractive index of a transparent second layer (its extinction coefficient is first set at zero), as presented in Fig. II.23.a. The estimations show the impact of the refractive index on the layer thickness at minimal reflection as well as the quality of the obtained AR coating. They particularly display the same parabolic curve as obtained experimentally in Fig. II.21. With this particular gold thickness, it shows for example that a higher n value for the second layer gives lower reflectivity at the optimal thickness.

Then, Fig. II.23.b, presents the impact of the extinction coefficient of the second layer on its thickness at minimal reflection. When working with a second layer of known optical properties, this graph can be used as an indicative abacus to help selecting the preferable thickness. Note that since gold is already strongly absorbing, applying second layers with higher k is not efficient.

Using the dimerization of NBDT molecules, the n and k values of the resulting film are unknown. But using the two graphs in Fig. II.23, one can see that in order to obtain the minimum reflection at a thickness of $\sim$ 22 nm, the organic coating must have k $<$ 0.1 and n around 1.55. This confirms (as discussed in section II.3.3) that with the support of a more accurate model, BALM could in principle be used to estimate the complex refractive index of any deposited material. It would notably require the precise knowledge of n an k values of the ultra thin gold coating and to include the contribution of angles and surface roughness.

II.4.4 GO contrast during the deposition

We showed above that a second layer can significantly improve the AR properties of the BALM coating but the demonstration of an associated contrast improvement is still to be done. In section II.3.1, the gold thickness was modified steply on different glass substrate and graphene oxide flakes were deposited on each substrate separately. The benefit of the organic photo-deposition is that the layer grows continuously while a movie is recorded, meaning that the contrast of GO can be extracted at the same time.

We used this deposition method on GO flakes to extract the contrast continuously. To do so, we performed the same experiment as in Fig. II.19 but GO flakes were first deposited on the gold substrate. Then an area containing non-folded flakes is chosen and the light deposition is performed on top while recording a movie. From this movie,

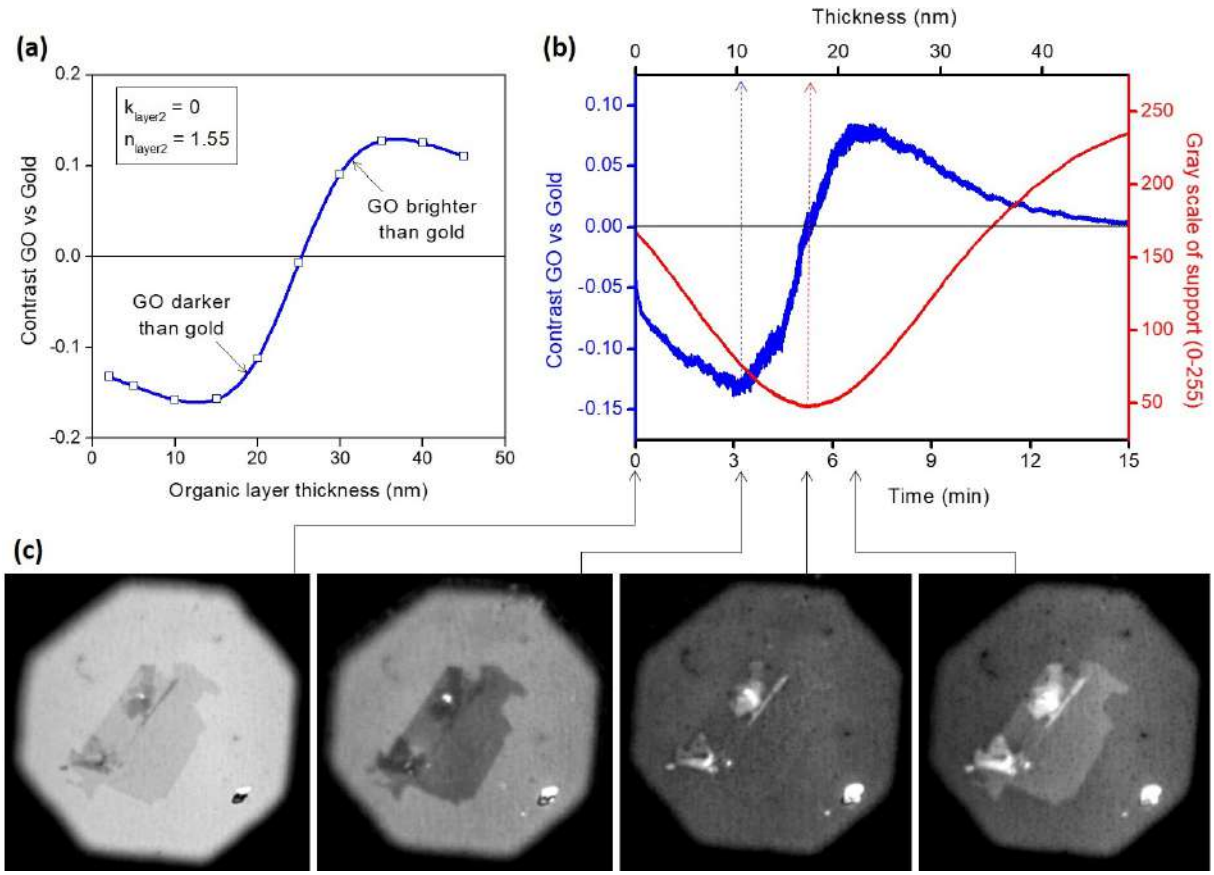

Figure II.24: Contrast of monolayer GO on gold during the light-induced deposition. (a) Contrast estimation using n_{layer2} = 1.55 and k_{layer2} = 0, **(b)** reflectivity of gold (red curve) and experimental GO contrast (blue curve) **(c)** BALM images extracted from the green channel at t = 0, t = 3 min 6 s, t = 5 min 12 s and t = 6 min 43 s. For clarity, the gray scale was restricted to 0-196, 0-100, 0-75 and 0-75 because the images are progressively darker. This correction does not impact the contrast values.

the gray scale value of the substrate and of GO monolayers are extracted. Then the contrast is plotted first as a function of time, and then as a function of the second layer thickness (using one final AFM thickness calibration). Fig. II.24.b presents the experimental evolution of the contrast compared to the reflectivity of the ARA substrate and Fig. II.24.c exemplifies the main features of the extracted movie.

During the first three minutes of molecule deposition the contrast of GO is enhanced and reaches a minimum at $\sim$ 10 nm, as the reflectivity of the substrate decreases. Then the contrast decreases and is lost (becomes zero) after $\sim$ 5 minutes even though the AR coating reflectivity reaches its minimum. Then the contrast is reversed (GO appears brighter than gold), reaches a maximum inverted value after $\sim$ 6.5 minutes and is finally lost. It is important to point out that the best contrast for GO does not occur when the reflectivity of the surrounding substrate is at its minimum. So in order

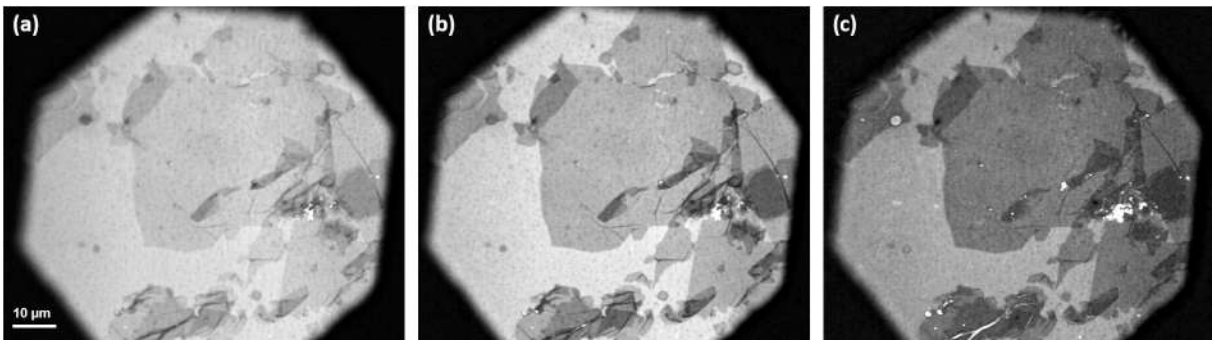

Figure II.25: BALM images of GO flakes on gold, extracted from the green channel of Movie-1. The images were corrected as follow: the gray scale was simply restricted to 0-128, 0-96 and 0-64 to compensate the progressive darkening of the images. This does not impact the extracted contrast. **(a)** At t = 0 s, C = -0.046, **(b)** at t = 50 s, C = -0.119, **(c)** at t = 156 s, C = -0.167.

to select the perfect combination of AR coating layers, the optical properties of the 2D material (or generaly speaking, of the material being studied) need to be taken into account.

This selection of coatings can be approached using the simple model. The contrast of GO is estimated for this experiment using 3 nm gold, a single GO layer (at λ = 550 nm and normal incidence with n_{GO} = 2, k_{GO} = 0.3 [14]). The contrast is plotted as a function of the second layer thickness (using n_{layer2} = 1.55 and k_{layer2} = 0, as previously estimated for the dimer) in Fig. II.24.a. This calculated contrast qualitatively corresponds to the experimental observation.

A focus on the contrast improvement emerging during the first step of the second layer deposition is presented in Fig. II.25. Three images (green channel) were extracted from Movie-1. The contrast is C = -0.046 at t = 0, C = -0.119 after 50 s and it reaches a maximal value of C = -0.167 after 156 s. This represents a contrast improvement by a factor of 3.6, which is a major step for the observation of GO, notably when considering that images in Fig. II.25 are taken in water where high contrast optical images of GO are particularly difficult to obtain.

II.4.5 Contrast enhancement with conventional 2nd layer materials

The molecule deposition method used above is very specific and was principally useful to show the impact of a second layer AR coating and estimate the vertical sensitivity. In addition, having the second layer above the studied material is not the best configu-

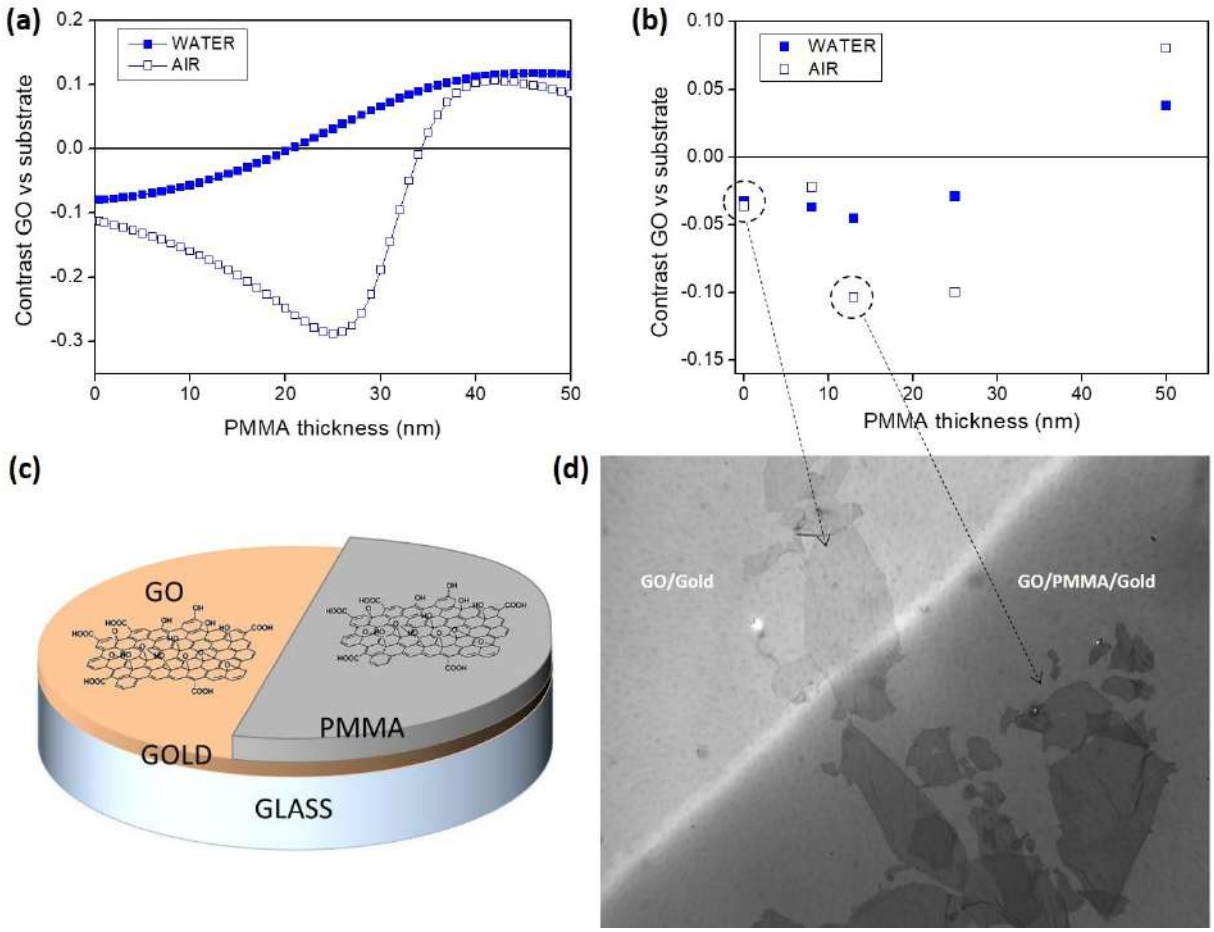

Figure II.26: Contrast of GO monolayers on PMMA/gold 2-layer AR substrates. **(a)** Estimation of GO contrast for PMMA above 4 nm gold in air and in water, **(b)** experimental GO contrast in air and water, **(c)** schematic of the experiment, **(d)** BALM image showing the best contrast for GO in air (the gray scale of the image was restricted to 0-150 for clarity. This does not affect contrast extraction).

ration. However, as seen in Fig. II.23, the thickness at minimal reflection in a two-layer configuration is below 50 nm. This thickness range is ideally suited for conventional deposition techniques like spin-coating or evaporation. Furthermore, materials with extinction coefficient $k < 0.1$ are really common and include many polymers and oxides.

In the next experiment, we show that the contrast of GO can be improved using conventional methods and materials for the preparation of the observation substrate. To do so, PMMA thin films with a thickness ranging from 8 to 50 nm were deposited by spin-coating above 3 nm of gold on glass. Then the polymer layer was partially etched by directive oxygen plasma through a mask in order to produce steps and measure the deposited thickness. Then GO flakes were deposited and BALM images were taken in air and water. The contrast was extracted and presented in Fig. II.26.

It clearly shows that a 13 nm PMMA layer can double the contrast of graphene oxide in

air. Interestingly, areas of the substrate where GO flakes are present both on the bare gold part and on the PMMA covered part can be selected. An example is displayed in Fig. II.26.d. The experimental results were also compared to the numerical estimation. Both the simulation and experimental graphs follow the same trend: with this particular gold thickness, the contrast in water can only degrade (and reverse), whereas the contrast in air is strongly improved when using a thin PMMA layer on top of gold. The improvement is significant in a range, 10 and 35 nm of PMMA, which is experimentally accessible by spin-coating.

This second layer provides new opportunities for the future applications of the technique as the ARA surface is not limited to metals anymore. We can imagine, for example, working with a PDMS 2^{nd}-layer for microfluidic applications. We are also currently developing BALM substrate covered with alumina which will allow to couple imaging and electrical measurements in a near future.

II.5 Conclusions on Chapter II

In this chapter, the BALM optical microscopy technique was presented and its performances were discussed. We first described the anti-reflective coating principle as a way of improving contrast. The classic use of transparent materials as AR coating was explained on the basis of the Fresnel equation. As BALM is an contrast-enhanced optical microscopy technique based on highly light Absorbing Anti-Reflective (ARA) coating, these equations were explained for those materials and compared to the one of transparent layers. Using absorbing materials like metals, the layer has to be really thin, in the 1-10 nanometer range, and light has to come from the higher refractive index material in order to obtain anti-reflective conditions. The ARA coating is typically made of gold deposited on a glass substrate. This BALM substrate is then imaged with an inverted microscope so that light comes from the objective, is reflected by the studied object and imaged with the same objective.

It was shown that this type of AR coating produces highly contrasted images of 2D materials, GO and MoS_2. BALM has a diffraction limited lateral resolution but it can detect smaller materials like CNTs or nanoparticles. The refractive index sensitivity of BALM was showcased by several experiments. Images of GO and rGO presented a large difference of contrast even though they only differ by their oxidation state. The dynamic of pyrene derivative adsorption on GO was also discussed.

The parameters influencing the contrast of 2D materials were experimentally investigated. The ARA layer composition and thickness were optimized and a BALM layer of 0.5 nm chromium + 3 nm gold was chosen for the rest of the thesis as it shows a good balance between air and water imaging. The refractive index of the top medium was also presented as a way of increasing contrast. Finally, the wavelength was used to adjust the contrast of monolayer MoS_2. Furthermore, it was shown that BALM coupled to numerical simulations allows the discrimination of the complex refractive indexes obtained by different techniques. The wavelength dependance was also used to differentiate MoS_2 from WS_2 by canceling the contrast of only one of the monolayer.

In a last part, we studied the dynamic of molecular layer deposition by controlled photodeposition. To do so, we used the photo-dimerization of NBDT whose product is insoluble in water and thus gets deposited on the lighted area. These experiences notably showed the extreme sensitivity (way below the nanometer, even at the single pixel level) of BALM for this type of measures. They also showed the significant improvement of a second transparent and organic layer on top of the gold ARA layer to upgrade the anti-reflective properties of the BALM slide. Finally, this second anti-reflective layer was extended to more common materials (like PMMA) and stacking order (2D material on top).

Chapter III

Combining BALM and electrochemistry

In the previous chapter, we have seen that the BALM configuration has several advantages: it is highly sensitive to refractive index modifications; it is adapted to the high-contrast observation of 2D materials; it allows monitoring molecule deposition at interfaces in real-time and with sub-nm vertical sensitivity.

In addition, BALM presents two interesting properties for its combination with electrochemistry: (1) The anti-reflective coating is made of a metal, therefore it can be used as electrode; (2) the inverted microscope configuration allows the observation of the interface in liquids and leaves space for additional equipment on top.

The interface observation is made through the anti-reflective layer which, in the following, is also the Working Electrode (WE) of a typical three-electrodes electrochemical set-up, as presented in Fig. III.1.a. Thanks to a dedicated home-made cell, an electrolytic solution can be added on top and a Counter Electrode (CE) and a Reference Electrode (RE) can be placed in the solution. In such configuration, it is possible to work with as much solvent as needed preventing the potential impact of solvent evaporation during kinetic studies. Furthermore, the cell can be closed and placed under argon or oxygen for electrochemical studies in a controlled atmosphere.

As seen in the previous chapter, most ARA layers used in this work are made of gold which is a well-studied material in electrochemistry. The typical ARA layer thickness suited for observation in liquids is around 3 nm. With such thickness, we have observed that the electrochemistry is heterogeneous over the slide because of the layer electrical

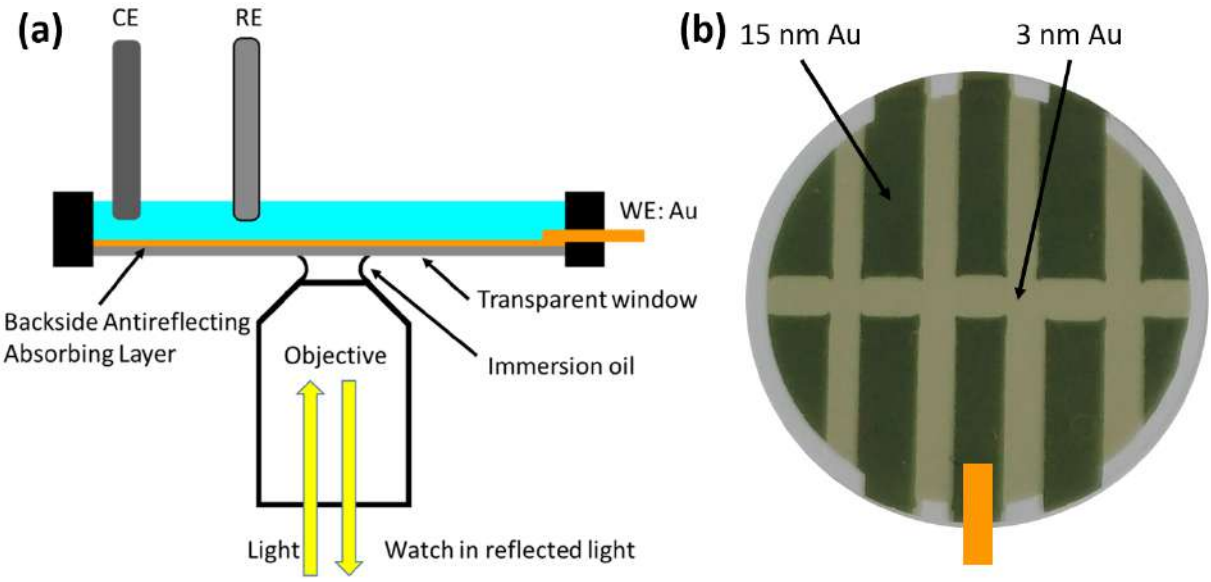

Figure III.1: BALM set-up combined with electrochemistry. (a) Schematic of the cell using the gold ARA layer as Working Electrode, **(b)** image of a BALM slide (24 mm in diameter) used for electrochemistry and composed of gold patterns of different thicknesses (3 nm in observation areas and 15 nm to suppress the impact of the thin layer resistivity).

resistivity. To solve this problem, we added thicker (15 nm) contact electrodes on top of the ARA layer, as presented in Fig. III.1.b. These large electrodes improve the contact to the external wire and prevent a voltage drop between the side and the center of the slide. This configuration was tested using a simple protocol (similar to the one that will be described in III.1.3.a) at several spots increasingly distant from a thick electrode. The obtained results were the same on the whole surface showing that the electrochemical response is homogeneous. Still as an additional precaution, we decided to perform all experiments close (< 300 µm) to a thick contact.

III.1 Electrochemistry of ultrathin gold

The electrochemistry of gold is widely studied in the literature [234–236] but the vast majority of the studies concerns thick gold films. In our case, the gold thickness is in the 2-5 nm range so that different behaviors from the typical thick film case can be expected. Furthermore, the BALM substrates include a 0.5 nm chromium adhesion layer, which can potentially have a non-negligible impact. The first step when performing a new electrochemical experiment is to determine the potential window accessible to the system which depends on solvent and substrate stability.

III.1.1 Electrochemical window of thin gold

While trying to find the electrochemical window of the BALM substrates using cyclic voltammetry, we observed results that are specific to ultrathin gold. An example is shown in Fig. III.2. We performed cyclic voltammetry in water and 0.1 M $LiClO_4$ as supporting electrolyte. We scanned 10 times from 700 to -700 mV (*vs.* Ag/AgCl) at 50 mV/s. The obtained current response clearly shows a reversible redox process at 400 mV. During the CV, we observed the modification of the surface with the emergence of black dots all over the observed area. A BALM image of the surface after the 10 cycles is shown in Fig. III.2.b. The surface was also characterized by AFM (Fig. III.2.c) and it appears that the surface has become highly heterogeneous and presents lots of craters which were not observable before the electrochemical experiment.

The redox couple at 400 mV seems to be responsible for the deterioration of the surface and the crater shapes observed by AFM suggests that the metallic layer surface is re-organized. This redox process may arise from the ultrathin gold or from the chromium adhesion layer. This experiment shows that the potential window of the gold BALM substrate is between 300 and -700 mV (*vs.* Ag/AgCl) in water. Most of the experiments reported in the following sections were performed within these limits at the exception of few cases (see section III.1.4) which were performed up to 500 mV. This possibility is explained by the previous experiment since, during the cyclic voltammetry, a BALM movie was recorded and Fig. III.3 reports the images at the end of the 6 first cycles. One can see that the degradation becomes critical after 3 cycles. So, when positive bias above 300 mV were necessary, the experiments were performed with only 2 cycles to exclude a potential impact of the ARA layer degradation on the results.

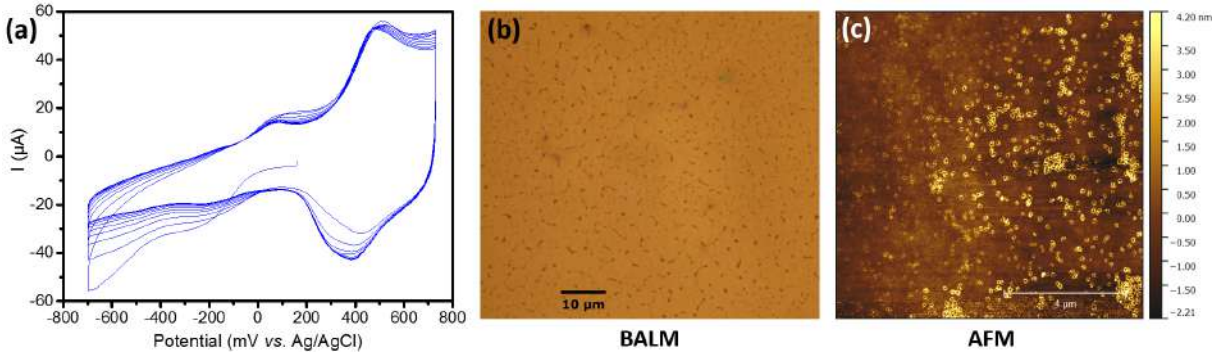

Figure III.2: Potential window of the gold BALM substrate. (a) 10 cycles of cyclic voltammetry at 50 mV/s in water with 0.1 M $LiClO_4$ and placed under argon, **(b)** BALM image at the end of the 10 cycles, **(c)** AFM image after the CV.

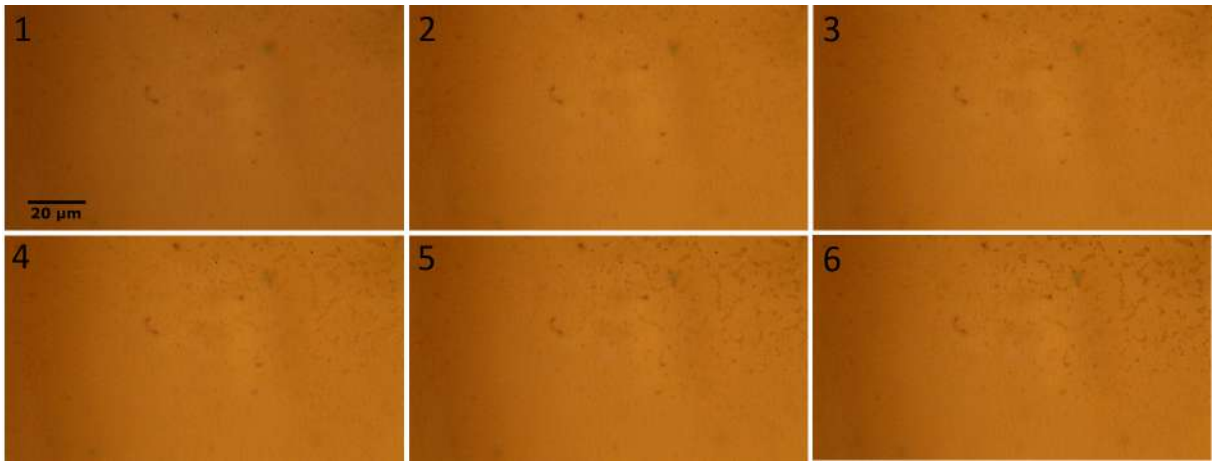

Figure III.3: BALM images at the end of each cycles of the previous CV (Fig. III.2).

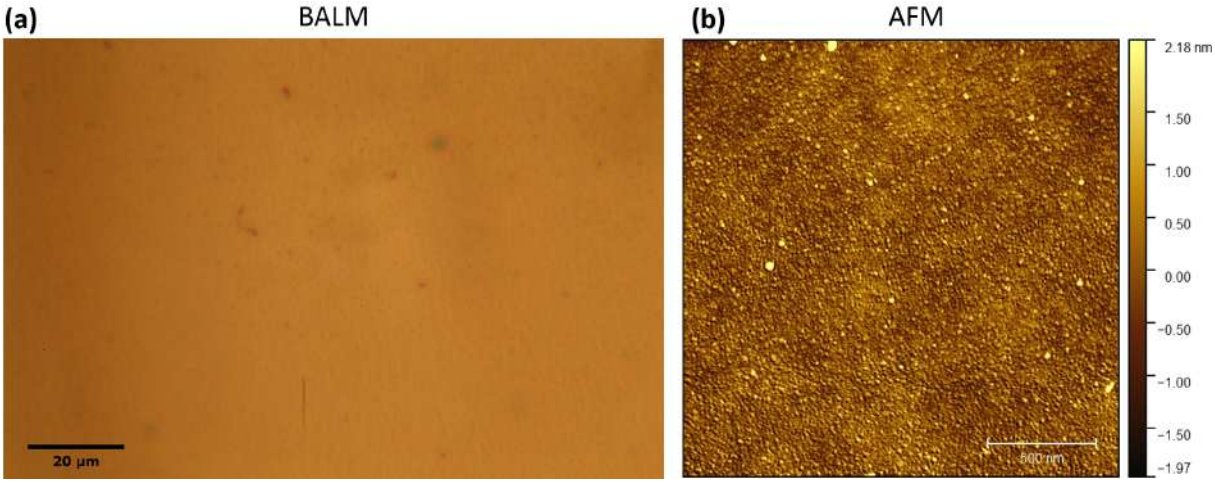

Figure III.4: Stability of the gold BALM substrate. A CV of 30 cycles was performed in water with 0.1 M $LiClO_4$ under argon. The CV was performed at 50 mV/s between 0 and -700 mV (*vs.* Ag/AgCl). **(a)** Final BALM image, **(b)** AFM image after the CV.

The stability of the gold layer, when scanning at lower potentials, was further evaluated using cyclic voltammetry as the potential was scanned 30 times between 0 and -700 mV (*vs.* Ag/AgCl). The final BALM and AFM images (shown in Fig. III.4) are exactly the same than at the beginning of the experiment. Therefore, the BALM slide seems stable in this potential window and for these conditions (water/$LiClO_4$).

In the following experiments, we will be cautious with the potential window, especially in the positive direction.

III.1.2 Impact of UV-ozone on gold

Considering the sensitivity of BALM (its capacity to discriminate the deposition of molecular monolayers), an important part of the preparation of the BALM substrates is

the cleaning of the gold layer surface. Gold is known to get polluted by carbonaceous contamination really fast (few minutes time scale) when exposed to air. [237] This is an issue for several studies in particular for Self-Assembled Monolayer (SAM) of thiolates [238] or Surface-Enhanced Raman Spectroscopy (SERS). [239] More importantly for us, it can change the quality of the active surface in electrochemistry therefore detection applications rely on clean gold surfaces. [240]

Among the different ways to clean gold substrates, we decided to use the UV-ozone technique as it is effective at removing contaminants from surfaces and as it is already used for the cleaning of the glass slides prior metal deposition by thermal evaporation (as described in the experimental section). The UV-ozone equipment we used only serves for bare substrates cleaning (no lithography resists or molecular layers allowed) in order to have the less contaminant possible inside the chamber.

Nevertheless, Gold is known to form an oxide layer, Au_2O_3, when exposed to UV-ozone. [241] Therefore, we first need to check its impact on the electrochemistry of the gold substrates. To do so, we first performed the following experiment: a 0.5 nm chromium + 3 nm gold BALM substrate was placed in a UV-ozone chamber for 30 min, then washed with isopropanol (IPA), dried with a N_2 flux and then directly placed in the BALM cell for analysis. Cyclic voltammetry was performed in water with 0.1 M $LiClO_4$ under argon, the potential was scanned 10 times at 50 mV/s between 730 and -700 mV (*vs.* Ag/AgCl) and the current response is presented in Fig. III.5.a.

The CV clearly shows, during the first cycle, an irreversible reduction peak at 300 mV which seems correlated with the reduction observed previously (part III.1.1) and is drastically decreased after the first cycle. Final AFM and BALM images are provided in Fig. III.5.b-d. The AFM image shows the same crater shapes as before and the BALM images show dots (which are probably the some craters) all over the surface. Consequently, the reduction peak and the surface deterioration seem to be correlated to the formation of a gold oxide layer.

From this experiment, we conclude that UV-ozone alone is not usable to clean the gold BALM substrates. But the gold oxide Au_2O_3 is known to be unstable in air [242] as it is dissociated. Additionally, increasing the temperature activates this reaction. Therefore, we then study the addition of a thermal treatment after the UV-ozone cleaning to produce clean gold substrates.

To that end, we first analyzed a not-cleaned BALM substrate by CV (0 to -700 mV),

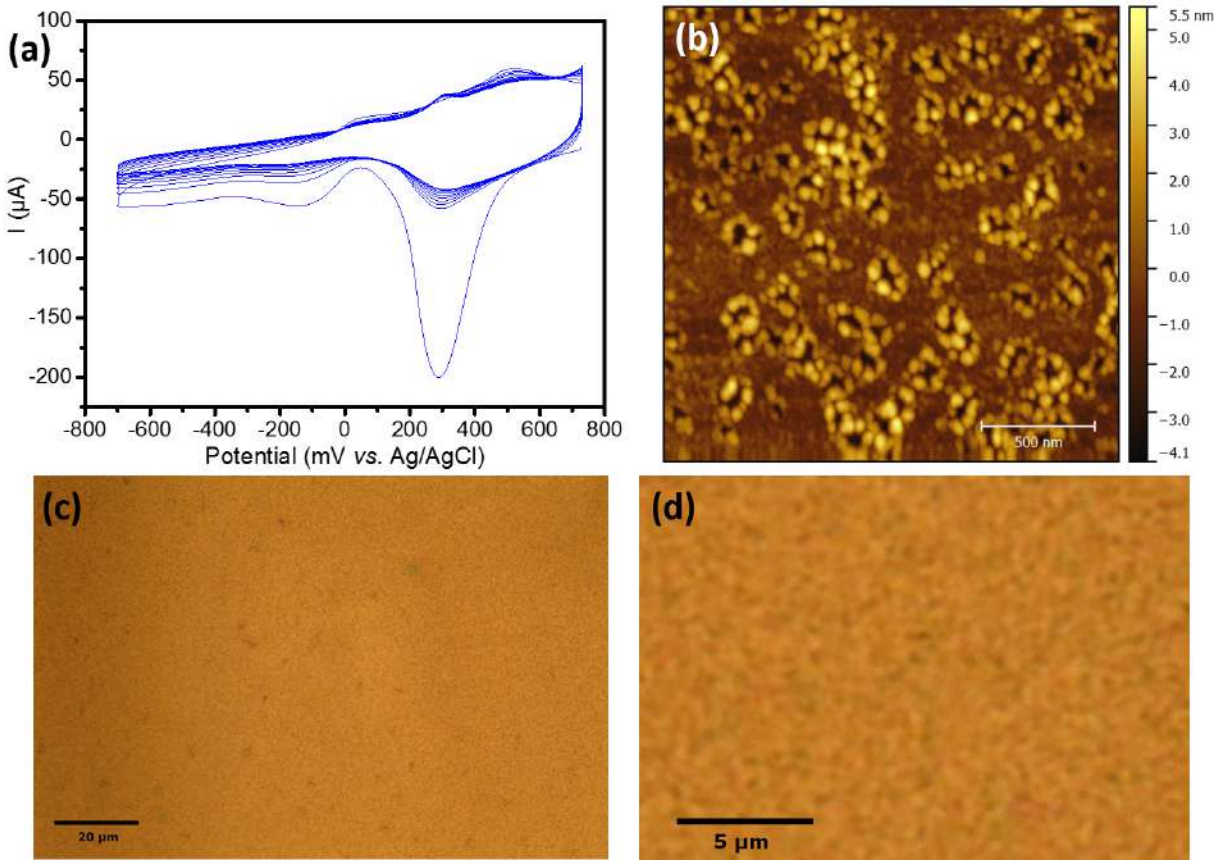

Figure III.5: Impact of UV-ozone on the gold BALM substrate. (a) CV after 30 min of exposure to UV-ozone, **(b)** AFM image after the CV, **(c)** final BALM image, **(d)** zoom of (c).

then the same substrate was rinsed with water and dried with N_2 flux. This substrate was then placed in the UV-ozone chamber for 15 min, washed with isopropanol, dried with a N_2 flux and analyzed by CV. Finally, the experiment was repeated a second time but with the addition of a thermal treatment after the UV-ozone. Final treatment is 15 min UV-ozone, washed with IPA, dried with N_2 flux, annealed at 70°C in air for 10 min and analyzed by CV. The electrochemical currents are presented in Fig. III.6.

After the first 15 min UV-ozone exposure, the OCP (open-circuit potential) is shifted toward high potentials and the reduction peak at 300 mV appears. Even though the BALM substrate was exposed a second time to UV-ozone, the thermal treatment reduced the OCP to its "before cleaning" value and the peak is no more observable. All of this proves that the addition of a thermal treatment reduces this irreversible peak and that it corresponds to the dissociation of the gold oxide layer formed by UV-ozone.

The cleanliness and quality of the gold layer after treatment was then verified using AFM and water contact angles. Fig. III.7 presents AFM images as well as contact an-

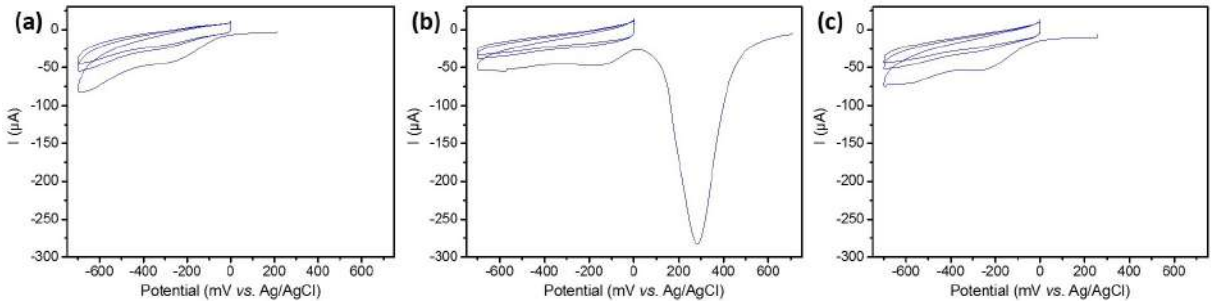

Figure III.6: Impact of UV-ozone and thermal treatment on the reduction peak of gold oxide. (a) CV of uncleaned gold, **(b)** CV after a 15 min exposure to UV-ozone on the same BALM substrate, **(c)** CV after an exposure to 15 min of UV-ozone followed by a thermal treatment (10 min at 70°C).

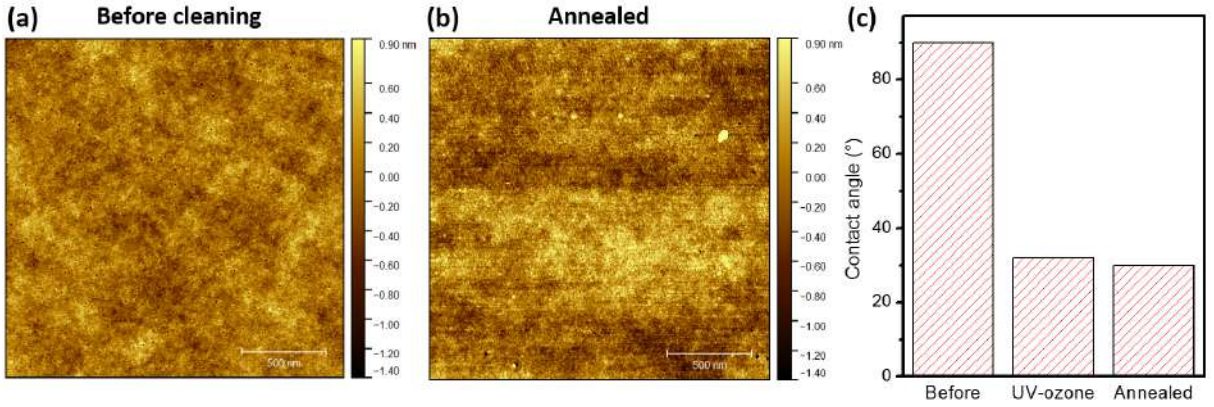

Figure III.7: Impact of the cleaning method on the surface properties of gold. (a-b) AFM images before and after, **(c)** contact angle.

gles of the same BALM substrate, before and after the cleaning method. First thing to be noticed is that the UV-ozone oxidation followed by the thermal dissociation does not produce the crater-shaped holes in the surface. The gold dissociation is homogeneous on the surface as also observed in [243]. Then the contact angle measurement shows that the UV-ozone clearly decreases the hydrophobicity of the surface. Finally, the thermal treatment does not modify this value which means that the surface is less contaminated than before. A perfectly cleaned gold surface has a theoretical value of 0° but 30° is typical of a clean surface measured in air. [241]

We also tried to use X-ray Photoelectron Spectroscopy (XPS) to quantify the carbon/gold ratio but we observed no difference before and after cleaning. It could be due to the fact that the samples have to be pumped over-night before analysis.

Later on, we use the following cleaning method: 15 min UV-ozone, washed with isopropanol, dried with a N_2 flux and finally annealed at 70°C for 10 min.

Now that the potential window of a clean gold substrate is determined, we are going to study the impact of simple electrochemical methods on the optical reflectivity of the gold surface.

III.1.3 Optical changes during basic electrochemical methods

In the next experiments, electrochemistry is performed on the whole slide while the microscope is observing locally the solution/gold interface. The electrochemical response is recorded and synchronized to the movie taken by the microscope. From each image composing the BALM movies, the gray scale of the red channel is averaged on an area of 100 * 100 pixels and compared to the electrochemical response.

a) Cyclic voltammetry

A very used electrochemical method to characterize a system is cyclic voltammetry (CV). We first studied one of the simplest possible system: the CV of 0.1 M KCl in water. The potential was cycled 3 times at 50 mV/s from 0 to -700 mV *vs.* Ag/AgCl, then the current (blue curve) and the gray scale obtained from the movie were plotted against the potential, as presented in Fig. III.8.a. A first thing to notice is that the reflectivity of the interface is modified when applying a potential, even though the CV mainly shows capacitive current. After the first cycle, which is slightly different for both electrochemical current and reflectivity, the optical response is reversible and almost linear. We explain this as resulting from the Pockels effect of water.

The Pockels effect is a linear electro-optic effect in which the refractive index of materials is modified by an electric field. This effect was observed and measured for water in different configurations by Tokunaga and co-workers. [244–250] It is linked to the evolution of the charge in the electrical double layer (EDL) at the electrode interface. They indeed showed that the refractive index of water within the EDL is different from the one of bulk water. They also proved that the electrode material has an important impact on the Pockels effect of water. The effect is for example higher on indium-tin oxide (ITO) than on platinum.

This effect is observable by different techniques but there is still a lot of work to be done (notably with the help of a theoretical support) in order to thoroughly explain why the EDL shows such a different refractive index when compared to the bulk part of the water solution. In future work, thanks to its high refractive index sensitivity, BALM could

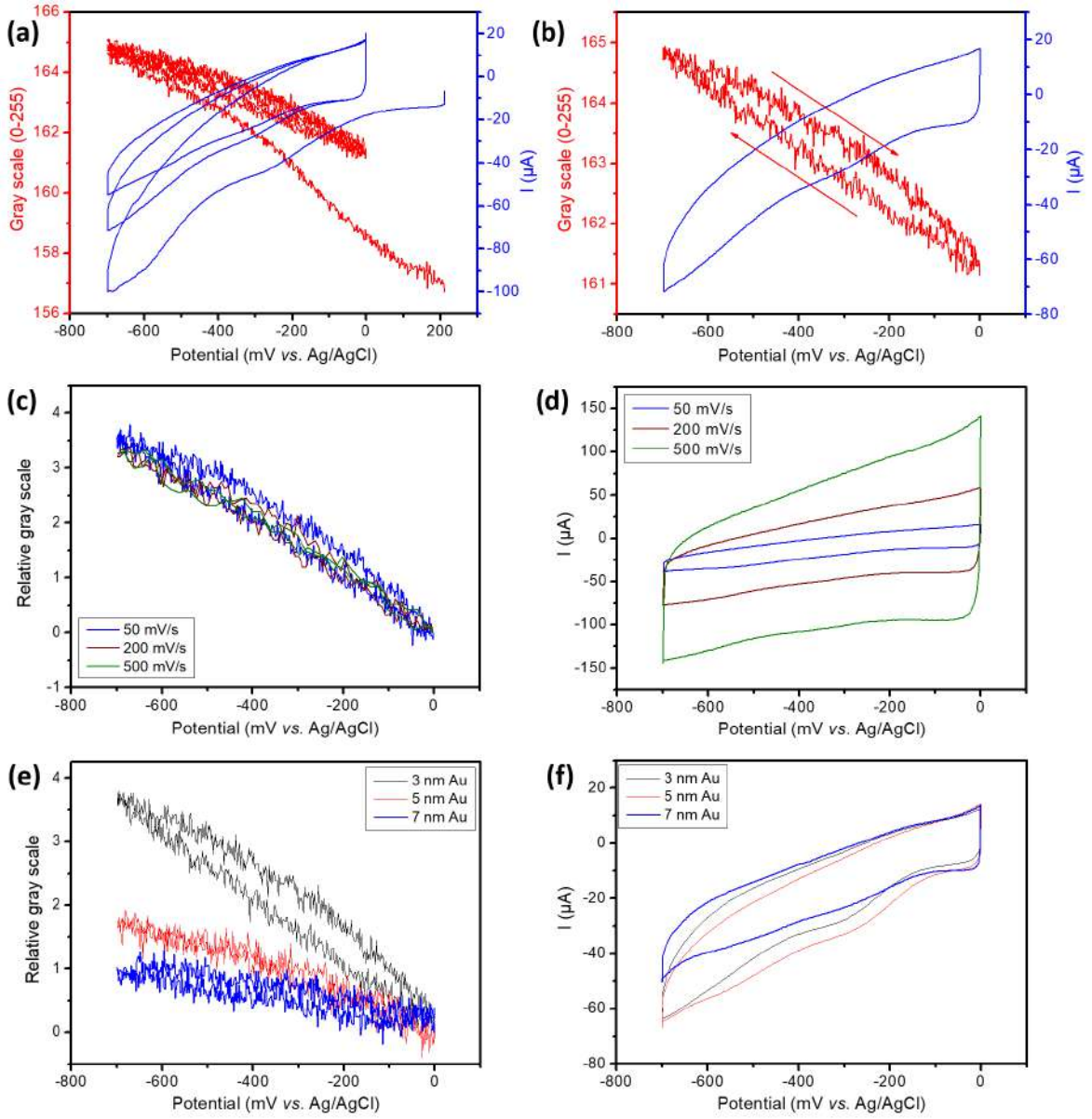

Figure III.8: Cyclic voltammetry of gold. (a) CV at 50 mV/s in 0.1 M KCl in water, red curve is the gray scale response and the blue curve is the current response, **(b)** same data but only the second cycle is plotted, **(c)** CV at different scan rates in KCl 0.1 M in water, **(d)** associated current responses, **(e)** CV for different gold thicknesses at 50 mV/s in KCl 0.1 M in water, **(f)** associated current responses.

provide new insights in the underlying phenomenon. In the context of this thesis, which is focused on the investigation of potential application of BALM, our goal regarding this effect was limited to the evaluation of its impact on typical electrochemical experiments. We indeed needed to evaluate its amplitude to be able to recognize its importance or negligible character in the next studies (in particular the electrografting of thin molecular films).

First of all, when only one cycle is plotted, the optical response shows a slight hystere-

sis as presented in Fig. III.8.b. This is maybe a sign of a different charge dynamics at the interface (accumulation *vs.* depletion). The impact of the scanning speed was studied. To do so, CVs were performed in 0.1 M KCl in water on the same gold BALM substrate. In order to compare the results, the gray scale at 0 mV *vs.* Ag/ACl is subtracted to the obtained optical response and plotted as presented in Fig. III.8.c,d. The scanning speed does not show any impact in the 50-500 mV/s range.

Then, CVs on BALM substrates with a gold thickness of 3, 5 and 7 nm were performed. The optical and electrochemical responses are presented in Fig. III.8.e,f. The thinner the gold, the higher is the optical response. For 7 nm of gold the reflectivity variation is close to the detection limit (noise level) in this configuration. This thickness effect may have two reasons: first, the refractive index sensitivity of BALM depends on the AR properties of the substrate and we showed in the previous chapter that for observation in water, 3 nm of gold is better than 5 and 7 nm. Additionally, the space charge layer in ultrathin gold layer could have a greater impact than the one observed by Tokunaga and co-workers. [246, 247] In their work, they concluded that the Pockels effect is produced at 90% by the EDL on the water side of the interface and at 10% by the space charge layer within the ITO substrate. In our experiment we use a gold layer so the space charge layer in the metal should have almost zero thickness. However, for the thinnest gold layer this behavior is not well-known.

Finally, Tokunaga and co-workers showed that the Pockels effect was also observable for organic solvents like methanol, ethanol and dimethyl sulfoxide (DMSO). [247] DMSO is used for electrochemical experiments but in order to be coupled to BALM, the refractive index of the solvent is important. DMSO has a refractive index of 1.48 [251] which is very close to the one of glass therefore it is not ideally compatible with BALM (at least using conventional glass slides). Looking at the most used organic solvents for electrochemistry, acetonitrile (ACN) seems to be particularly suited as it is stable and has one of the largest electrochemical window. Furthermore the refractive index of ACN is 1.34 [251] which is similar to water so that the same gold thickness for BALM substrates can be used for experiments in water or ACN. We then performed cyclic voltammetry in ACN as presented in Fig. III.9. To do so, we used 0.1 M tetrabutylammonium hexafluorophosphate (TBAP) as supporting electrolyte. The solution was purged under argon for 15 min and a CV was performed at 50 mV/s. The optical and current responses are presented in Fig. III.9.a. The gray scale shows the same linear and reversible response as for water but the slope is much lower (the change in

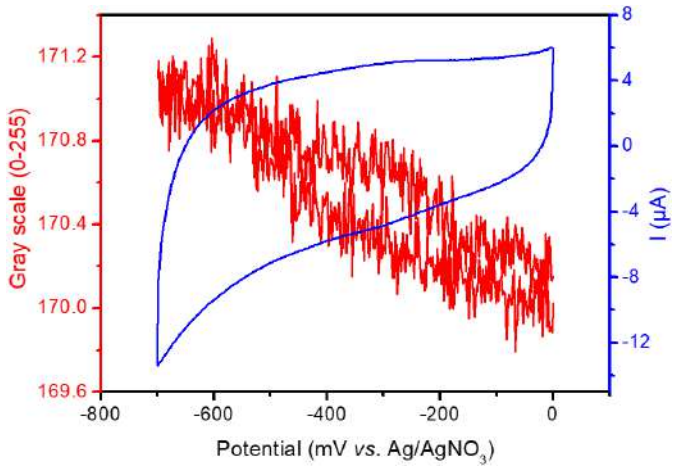

Figure III.9: Cyclic voltammetry of gold in acetonitrile, at 50 mV/s with 0.1 M TBAP in the potential range 0 to -800 mV.

color is close to unity on the 0-255 scale as compared with 3.5-4 in the water case). This means that the Pockels coefficient is lower for ACN than for water. It corresponds to what was suggested in the previous work, [247] which is that the Pockels effect is dependent on the hydrogen-bond strength of the solvent.

b) Chronoamperometry

We then investigate chronoamperometry which is a pulsed technique. First, we studied the dynamic of the Pockels effect which is related to the charge/discharge of the electrical double layer. To do so, we performed the following experiment in water while recording a BALM movie: 10 s at Open Circuit Potential (OCP), 10 s at 0 V *vs.* Ag/AgCl, 10 s at -600 mV and finally 50 s at OCP. This procedure was compared for two different supporting electrolyte concentrations: 0.1 M and 10^{-4} M KCl. The applied potential, the current and the optical response are presented in Fig. III.10.

First, when abruptly changing the potential from 0 to -600 mV, the optical response makes a jump. Then, when the applied potential is stopped, the response relaxes to the initial value. Both electrolyte concentrations show the same curves except for the response to the 600 mV potential jump which is slightly different. To quantify this, the two optical curves were fitted with a simple exponential function and the time constants were extracted. For the 0.1 M KCl concentration, the time constant is τ = 70 ms. Considering that images are taken only every 40 ms, this τ value must be considered with caution. At the scale of the measurement, the change in reflectivity at this concentration is almost instantaneous. Whereas for the 10^{-4} M KCl concentration, the rise time is slower: τ = 230 ms and is in a range accessible to the acquisition dynamic. This

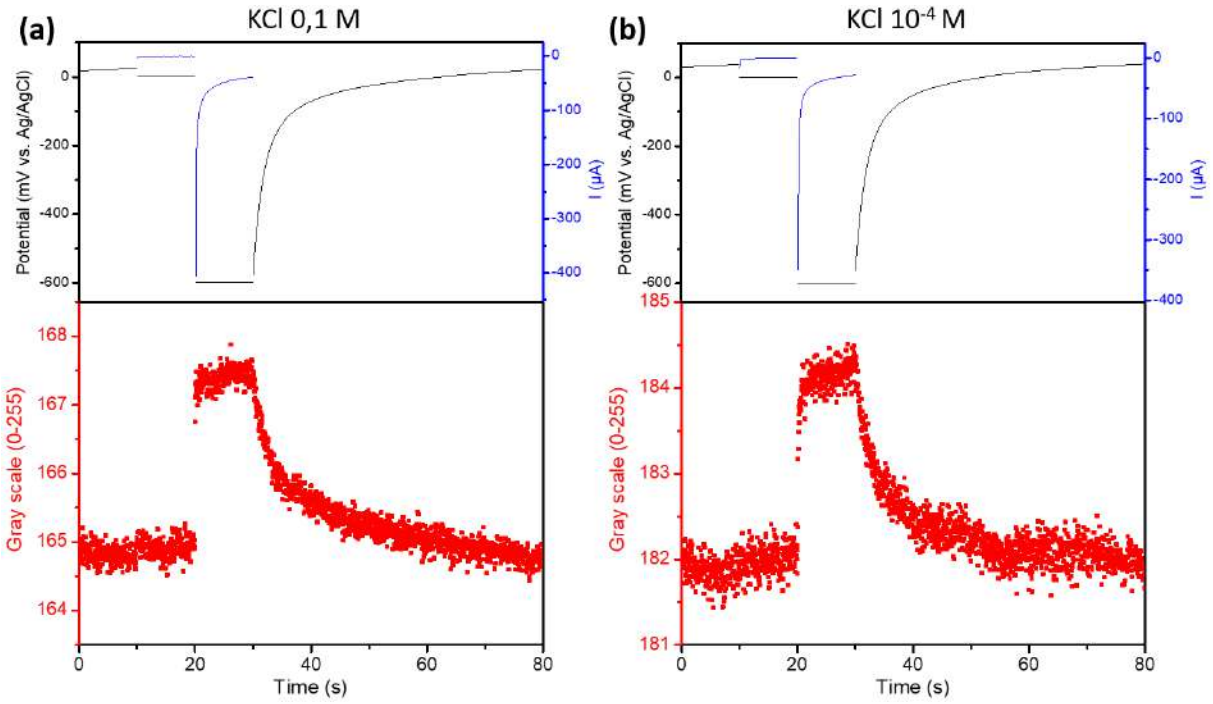

Figure III.10: Optical response to chronoamperometry in water. (a) 0.1 M KCl, **(b)** 10^{-4} M KCl.

is well-known that when the electrolyte concentration decreases, the solution is more and more resistive and the EDL is slower to establish.

These experiments confirm that the BALM technique is able to detect very subtle EDL changes. With improvement in the acquisition speed, it would give access to their dynamics for typical solvent and typical concentration conditions.

c) Electrochemical impedance spectroscopy

Electrochemical Impedance Spectroscopy (EIS) is a more advanced technique analyzing the response of a system over a range of frequency. In the following, our goal is to evaluate if BALM could be used as an optical electrochemical impedance spectroscopy technique and/or what improvement would be needed.

Usually, in EIS experiments, the applied signal is centered on the open circuit potential and its amplitude is lower than 10 mV in order to be in a system independent in time. However, the response to such a small signal is not detectable optically with our set-up. That is why in the following experiment we chose to increase the amplitude of the perturbative signal to 200 mV (peak to peak value). Then an EIS-like experiment was performed in water with 0.1 M $LiClO_4$ as supporting electrolyte (the cell being in argon), the frequency was set from 1 kHz to 10 mHz while applying a static potential of -300

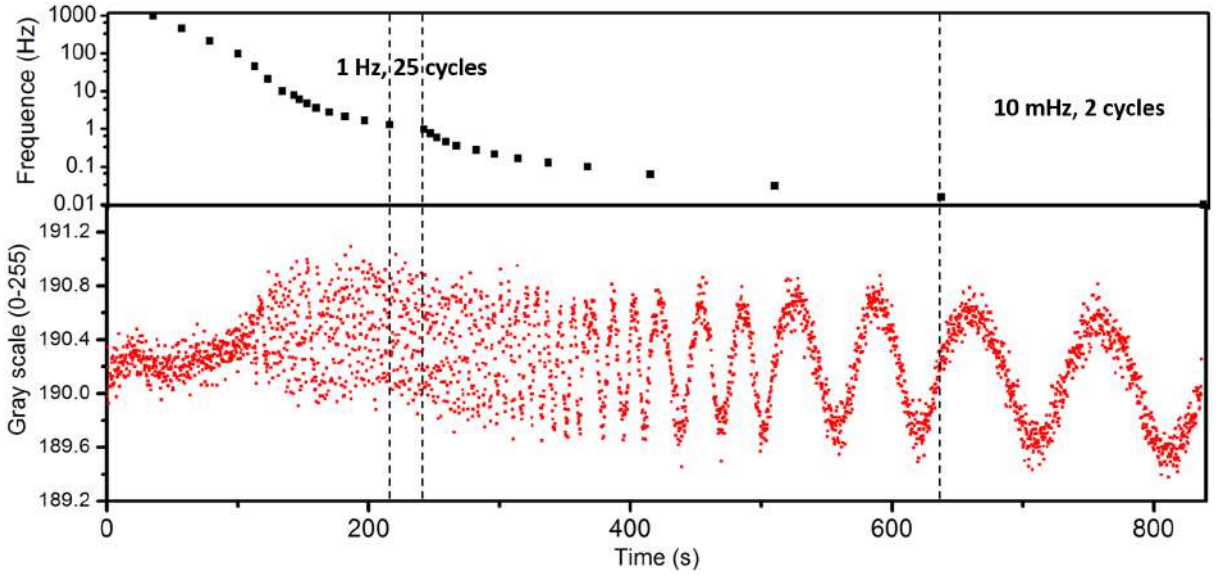

Figure III.11: Raw optical response to an Electrochemical Impedance Spectroscopy experiment, top graph is the time at the end of the applied frequency and bottom graph is the corresponding optical response. EIS is performed in water with 0.1 M $LiClO_4$ under argon and by applying a 200 mV amplitude sinusoidal signal centered at -300 mV *vs.* Ag/AgCl.

mV. The optical signal was plotted against time in Fig. III.11. We chose to perform the EIS at -300 mV because of the gold stability in the -100 to -500 mV range.

On the graph, one can see that for frequencies higher than 10 Hz, the BALM signal cannot be differentiated from the background noise. This is due to the measurement itself as the camera images at 25 Hz (one image every 40 ms) and with an exposure time of 25 ms. Above 10 Hz, one cycle is done within less than 25 ms, thus the optical signal is averaged over one or more full cycles giving zero optical changes.

For frequencies lower than 10 Hz, the amplitude of the sinusoidal signal increases and a sinusoidal signal is observed. We decided to stop the experiment at 10 mHz because slower frequencies would require filming for hours which is problematic from a data handling and analysis point of view (for example a 15 min movie corresponds to more than 1 Go of data and contains 22500 images from which it takes around 10 hours to extract local contrast with a conventional processor). Another technical issue is the mechanical stability of the microscope at long time scales (the focus slightly degrades over time at a pace that does not affect the other experiments presented in this manuscript).

We tried to extract the amplitude and the phase of the optical response by fitting optical signal at each frequency with a sinusoid using an home-made *Mathematica* program

but the results were not conclusive. For frequencies close to 10 Hz, the number of points per cycle is too small to obtain a correct fit. Indeed, considering the sampling theorem [252] which states that to reconstruct a sinusoidal signal, the sampling rate has to be at least twice the frequency of the analyzed signal. This means that with a standard camera, event if the exposure time was reduced, only signals with a frequency lower than 12.5 Hz could be analyzed precisely. Furthermore, the obtained phase is inconsistent which is probably due to the synchronization between the EIS and the camera. More work is thus needed to properly extract the optical response of an electrochemical impedance spectroscopy experiment.

This experiment shows the first technical limitations of the set-up: stability of the focus over long time, synchronization between the optical and electrochemical signals, imaging rate and sensibility of the camera. In order to push the boundaries, a high speed / high sensitity camera could bring significant improvements to the EIS experiments but also to the study of any fast reactions at an interface. One needs to note though that the amount of reflected light in a BALM experiment is always low by definition (ARA substrates are optimized to decrease reflectivity). Combining high rate, and high sensitivity without degrading lateral resolution (*i.e.* without reducing the number of pixel per image) is an instrumental challenge common to many optical techniques and recent progress in commercial scientific cameras are extremely rapid.

III.1.4 Impact of charge transfer on optical changes

Being able to observe faradaic reactions using an optical microscope could bring valuable information to the electrochemical community, as it would allow to locally study the charge transfer. For this purpose, redox mediators are important to characterize the charge transfer at interfaces.

We performed the cyclic voltammetry of a redox mediator on the gold BALM substrate as presented in Fig. III.12. On the same slide, we first performed a similar CV without the redox mediator (blue curves) and then with 10^{-2} M ferrocyanide (red curves).

The current response clearly shows the typical "duck-shape" corresponding to the ferricyanide / ferrocyanide redox couple. Whereas the optical response is nearly the same in both cases. This is understandable as the BALM technique is mainly sensitive to refractive index changes and we do not expect it to be different between ferricyanide and ferrocyanide as they only differ in redox state.

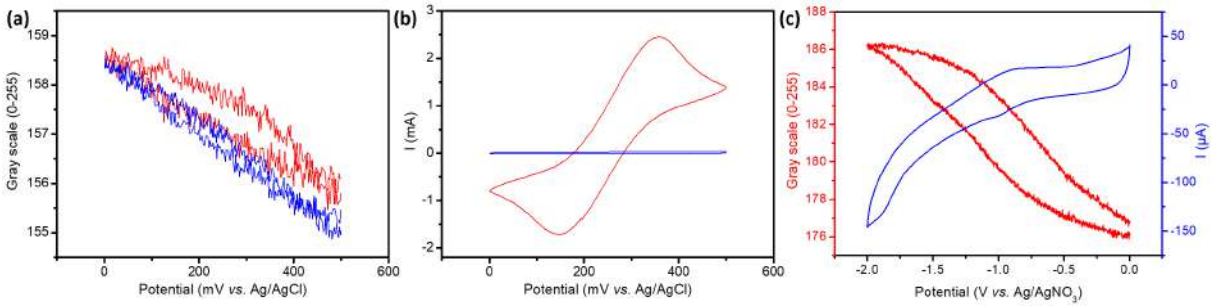

Figure III.12: CV of ferrocyanide on a gold BALM substrate. (a) Optical responses, **(b)** current responses. Blue curves without redox mediator and red curves using 10^{-2} M ferrocyanide. CVs are performed at 50 mV/s in 0.1 M KCl as supporting electrolyte in water and placed under argon, **(c)** CV of 0.1 M TBAP in ACN at 50 mV/s.

It does not mean that all faradaic reactions do not have an optical response. We performed cyclic voltammetry in acetonitrile (0.1 m TBAP, 50 mV/s) from 0 to -2 V *vs.* $Ag/AgNO_3$, as presented in Fig. III.12.c. It shows that the optical response is not linear and that the changes in the slope of the optical signal seem correlated with the one of the cyclic voltammogram as faradaic reactions occur.

In order to observe the charge transfer of a redox mediator with an optical microscope, one should use a different approach like fluorescence microscopy if one state is fluorescent and the other one is not. [253, 254] This type of microscopy could in principle be coupled to the BALM technique and bring complementary information.

III.2 Electrochemical reduction of graphene oxide

Now that we have an approximate overview of the BALM signal within different basic electrochemical investigations, we implement this to the study of 2D materials.

Graphene can be mainly produced by three different ways: mechanical exfoliation of graphite, chemical vapor deposition on metallic surface and decomposition of silicon carbide. Its preparation in solution by oxidation of graphite, exfoliation in single layer of graphene oxide and then reduction of graphene oxide to graphene would be very advantageous, in particular for applications requiring a large amount of graphene. It is however well-known that reduced graphene oxide (rGO) is quite different from graphene. The reduction of graphene oxide by chemical, thermal or electrochemical methods has been thoroughly studied for the last fifteen years [225, 255–258] with, as

a main objective, the quest for a final product having properties as close as possible to those of pristine graphene. Many techniques have been used to follow the reduction of graphene oxide: Raman spectroscopy, XPS, XRD, conductivity measurements. Only few publications report information at the single layer level and as discussed in the first chapter, only two techniques, Total Internal Reflection Fluorescence (TIRF) microscopy [188] and Interference Reflection optical Microscopy (IRM), [187] were used to locally study the dynamic of electrochemically driven reduction. They notably concluded that the electrochemical reduction was homogeneous. But both of them used graphene as starting material and then alternated between oxidation and reduction steps controlled by electrochemistry. Moreover they did not use potentials reductive enough (more negative than -0.8 V *vs.* Ag/AgCl) to completely reduce the functional groups of GO. [259]

We study here the electrochemical reduction dynamic of mono- and bi-layer graphene oxide. To do this, we prepared large monolayered GO flakes from graphite powder using an evolution of the conventional Hummers' method. [260] Then such flakes were deposited from a water/surfactant solution on gold BALM substrates using the so-called "bubble deposition" technique. [224] When used on Si/SiO_2 substrates, this technique produces very homogeneous GO films with almost non-folded flakes. It is more difficult to apply to gold substrates but can still produce small aggregates of GO flakes with large areas of monolayers and limited amount of wrinkles and folds. A BALM image (in air) of GO flakes on gold is presented in Fig. III.13.a. Then the slide was placed in water with 0.1 M Na_2SO_4 as supporting electrolyte and flushed with argon. A chronoamperometry method was applied (using typical parameters from the literature, [261]), -1.1 V (*vs.* Ag/AgCl) during 6.5 h, and BALM images were taken every minute. Note that taking regular snapshots in place of recording a full movie allows adjusting the focus once in a while. At the end of the experiment, the solution was removed and an image was taken in air (Fig. III.13.b).

The before / after comparison of BALM images shows that Electrochemically reduced Graphene Oxide (ErGO) is obviously darker than GO as previously discussed in II.2.2. It also confirms that the reduction is homogeneous at this micrometric observation scale. From the series of *in situ* images, the contrast of mono- and bi-layer GO was extracted for each images using a home-made *Mathematica* program. It was then plotted against time and fitted by a simple exponential decay function (Fig. III.13.c).

The two dynamics are quantitatively described by the extracted time constant (τ) which

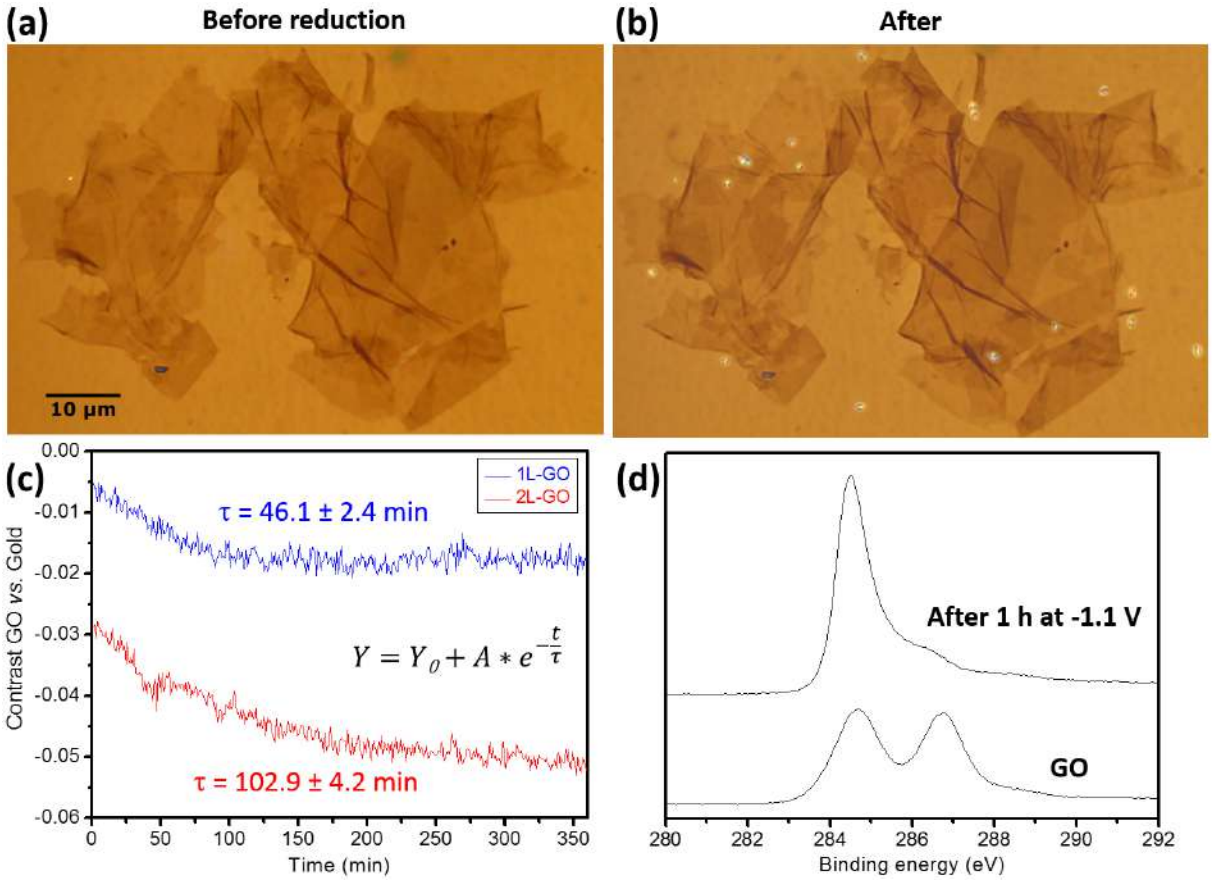

Figure III.13: Electrochemical reduction of graphene oxide. (a) BALM image in air before reduction, **(b)** BALM image in air after reduction for 6.5 h at -1.1 V *vs.* Ag/AgCl in 0.1 M Na_2SO_4 in water and under argon. **(c)** contrast of monolayer GO (1L-GO) and bilayer (2L-GO) during the electrochemical reduction (extracted from the green channel and fitted with a simple exponential decay function), **(d)** C_{1s} XPS spectrum of GO and electrochemically reduced GO (only 1 h at -1.1 V).

is twice higher for bilayers than monolayers (τ_{1L} = 46.1 +/- 2.4 min, τ_{2L} = 102.9 +/- 4.2 min). It shows that the electrochemical reduction of GO depends on the number of stacked layers, which is consistent with the fact that as long as the first layer is insulating, it prevents the efficient injection of electrons from the gold to the second layer. We also tried to extract the dynamic of three GO layers stacked but the areas of interest were too small and the contrast was difficult to extract with enough precision to be conclusive. To our knowledge, this is the first time the dynamic of GO electrochemical reduction is extracted *in situ* with monolayer precision.

To confirm that the darkening of the GO is indeed related to its reduction, we performed XPS analysis before and after 1 h at -1.1 V. XPS requires samples with much more GO flakes than the density used in a typical BALM experiment. We thus prepared a sample with an increased GO coverage by repeating the bubble deposition technique

10 times (on a 50 nm-tick gold substrate). The sample was cut in two pieces and one was submitted to the electrochemical treatment. Fig. III.13.d reports the C_{1s} core level spectra of the GO and ErGO thin films. The obtained C_{1s} spectra are typical of literature results for GO reduced by different methods (see for example Ref. [262]). In particular, the reduction process reduces the intensity of all contributions at high binding energies corresponding to the different C-O bonds (C=O-OH, C≡O, C-OH,...) and conversely increases the sp^2 C-C contribution. The reduction remains incomplete. This is probably due to the deposition method which produced mostly multilayers and to the limited time of the reduction used for the XPS analysis. In any case, no reduction methods can completely remove all oxygen and reform a fully sp^2 lattice.

III.3 Electrografting of diazonium salts

The following section is the topic of an article recently submitted for publication (July 2019).

Surface functionalization techniques are being used in many different domains such as sensors, anticorrosion, electronics, energy, textile, etc. Electrografting is one of these techniques, which consists of the growth of a covalently bonded organic layer on a conducting substrate through an electrically controlled charge transfer. [263] It has been studied since the 1980s and led to several applications at the industrial stage. The surface modification can be performed on many different types of substrates using many different types of organic layers. Such versatility, resulted in its integration in applications as diverse as interface engineering in organic electronic devices, [264–266] anticorrosion coatings, [267] (bio)sensing, [268] batteries, [269, 270] etc.

The most studied electrografting method relies on the reduction of diazonium salts. [271] Several aryldiazonium salts (such as 4-nitrobenzenediazonium tetrafluoroborate, called NBDT hereafter) are stable and easy to synthetize (some being commercially available), and their electrografting forms thin and robust organic films that have been largely studied by different techniques. The use of XPS and infrared spectroscopy [272–274] is typical to evaluate the chemical nature of the organic coating. To evaluate the homogeneity of the grafted film, atomic force microscopy (AFM) and scanning electron microscopy (SEM) are regularly used but they only provide post-grafting information.

The real-time process is mostly investigated using the Electrochemical Quartz Crys-

tal Microbalance (EQCM) technique. [272, 275–278] It provides a very sensitive and continuous evaluation of the film thickness but the information is averaged over the entire grafted surface. None of these techniques combine spatial resolution and real time monitoring. To achieve this necessary combination, different types of optical microscopy techniques have been combined with electrochemistry, for example surface plasmon resonance (SPR) [279–283] and ellipsometry imaging. [284, 285] These techniques are sensitive to local refractive index changes induced by electrochemical reactions at interfaces. In the case of local mapping of electrografting, ellipsometry [286] and light reflectivity microscopy [287] revealed that NBDT growth occurs at a higher grafting rate along gold step edges of micro-fabricated surfaces. These techniques are powerful to understand the physico-chemical processes at play during deposition by establishing how the heterogeneity of the surface and the solution supply impact the film formation.

Here, we show that BALM can address different classes of problems in the field of electrografting by taking advantage of its real-time imaging and high-contrast capabilities. We notably perform the *in situ* monitoring of the electrografting of two different diazonium salts on gold. Our results first demonstrate the equivalence between BALM and EQCM responses in terms of precision. More importantly, the next experiments investigate heterogeneous surfaces: gold step edges, graphene oxide (mono- and multi-layers), and electrochemically reduced graphene oxide (mono- and multi-layers). They very clearly establish the advantages of combining wide-field observation, very high sensitivity in the vertical direction and real-time operation to unambiguously measure local differences in grafting behavior.

III.3.1 Comparison between BALM and EQCM

One of the first challenges when grafting a new material on a surface is to determine the growth speed. AFM is very precise to compare before- and after-grafting situations and to deduce the deposited thickness. Real-time information on the process dynamics are yet preferable, in particular when the initial grafting speed is high and then saturates. In principle, establishing a precise relationship between the electrochemical current during the grafting and the actual thickness of deposited species is possible for homogeneous surface of precisely known geometry. It is however not straightforward as shown in several studies from different groups. [288–290] To get access to the dynamics on homogeneous surfaces, EQCM is presently the technique of choice.

To show how BALM opens new perspectives on electrografting dynamics measurement, the electro-reduction of a diazonium salt on gold was studied using the configuration displayed in Fig. III.14.a. In this experiment, an organic layer is grafted by cyclic voltammetry on the thin gold electrode. The grafted layer obtained from the reduction of 4-nitrobenzenediazonium (NBDT) changes the amount of reflected light depending on its optical properties and thickness. Thus, by monitoring the reflected light in the observed area, information on the grafting dynamic is obtained. In practice, a glass slide covered with 3 nm of gold is placed on a reverse microscope and then a solution of NBDT (1 mM) with tetra-butylammonium hexa-fluorophosphate (TBAP) (0.1 M) in acetonitrile is added on top. The cell is closed and placed under argon for electro-reduction of NBDT by cyclic voltammetry. Fig. III.14.b presents the BALM signal upon grafting (red curve) obtained by averaging the reflected light intensity in a 50 μm^2 area on each image of a full movie, and the electrochemical signal for the entire immersed surface (blue curve). Both signals were synchronized and recorded simultaneously. Independently, the same electrografting experiment is performed on a typical EQCM set-up. In Fig. III.14.c, both the frequency shift of the quartz balance upon grafting (black curve) and the voltammetry signal (blue curve) are displayed. Strikingly, the reflectivity curve extracted with BALM strictly reproduces the results obtained by Electrochemical Quartz Crystal Microbalance, by us and by several other groups before. [276, 278, 291, 292] This proves that BALM brings equivalent information to the one obtained using EQCM.

In this first experiment, the grafting of NBDT stops after only a few nanometers. In Fig. III.14.b, $\sim$84% of the grafting occurs during the first voltammetry cycle (from the open-circuit potential to -900 mV *vs.* $Ag/AgNO_3$). Then the deposition speed rapidly decreases (<9% during the second cycle) and eventually stops after four cycles. However, BALM can also be used to study thicker electrografted films, which growth is not self-limited by the insulating nature of the grafted material. As an example, Fig. III.15 reports a similar experiment but conducted with a different diazonium salt: tris-bipyridine iron (II) diazonium salt (called TBPFe in the following). Since TBPFe is redox-active the grafted film can provide electrons at its surface allowing the growth to continue upon cycling (see Ref. [293, 294] for details on the synthesis and electrochemical properties of TBPFe). Fig. III.15 shows that for five voltammetry cycles, the first cycle only accounts for 44% of the reflectivity change, while the fourth and fifth cycles still correspond to approximately 10% each.

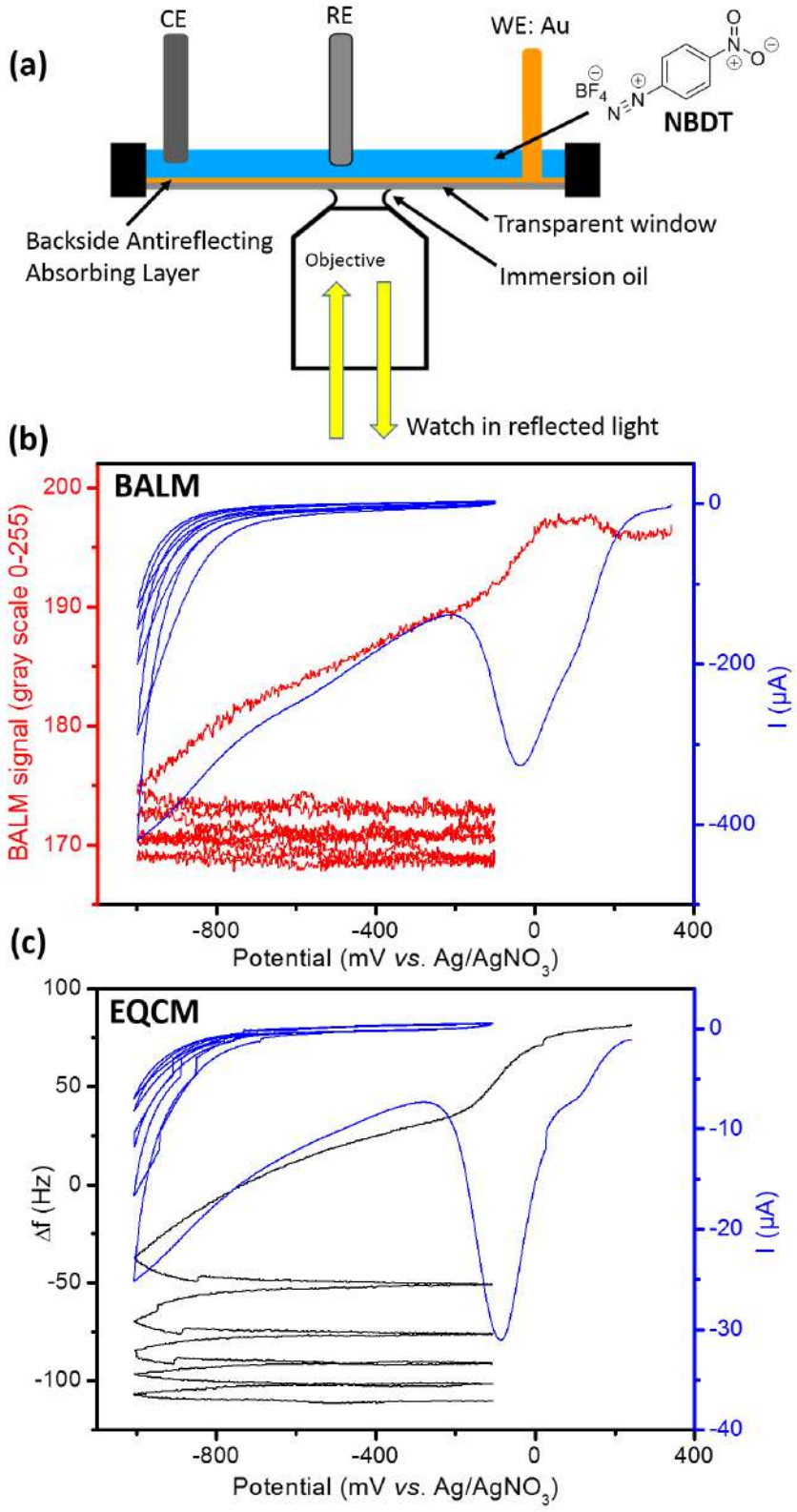

Figure III.14: Comparison between BALM and EQCM. (a) Schematic of the BALM set-up, **(b)** electrografting of NBDT by cyclic voltammetry (50 mV/s) on the BALM set-up. The red curve is the reflected light intensity measured on the red channel of the camera and averaged over 50 μm^2. The blue curve is the global cyclic voltammetry signal, **(c)** same electrografting experiment but on an EQCM set-up. The black curve is the change of frequency of the quartz crystal (corresponding to the mass change).

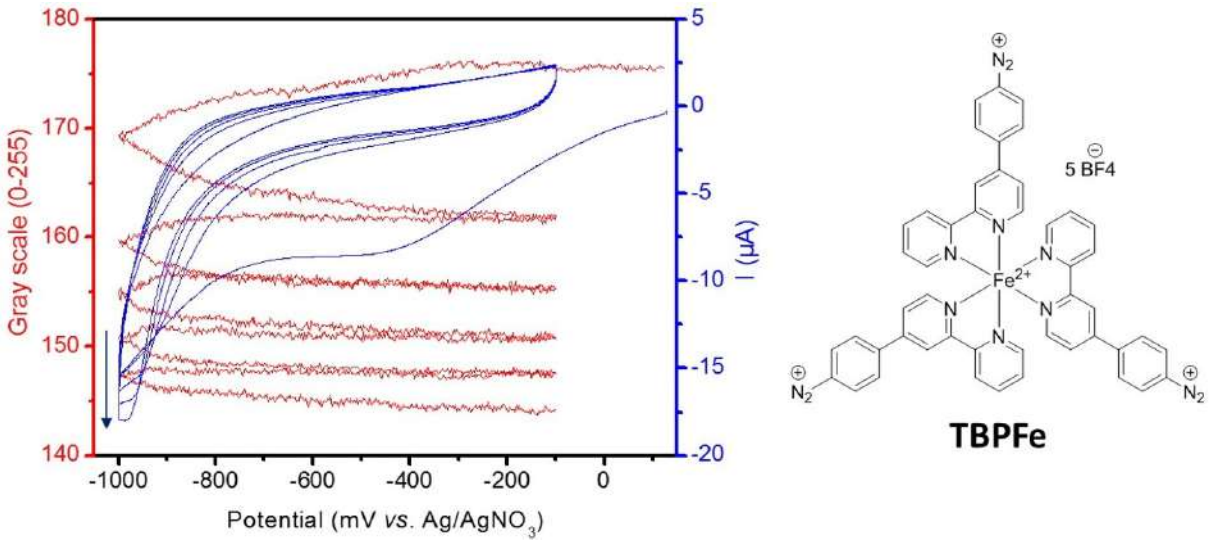

Figure III.15: Electrografting of TBPFe on gold, by cyclic voltammetry (50 mV/s) on a gold BALM substrate. The red curve is the reflected light intensity measured on the red channel of the camera and averaged over 50 μm^2. The blue curve is the global cyclic voltammetry signal.

III.3.2 Grafting at gold step edges

After having established the sensitivity of BALM to study electrografting dynamics, we now turn to the benefit of its imaging capabilities, which is the main asset of a microscopy-based technique. A very important aspect in the investigation of electrografting relates to the modification of heterogeneous surfaces. With BALM, the reflectivity and its dynamics can be studied locally, down to the single pixel scale and at video-rate. We first consider a simple example of heterogeneous surface: gold electrodes step edges. While simple, this example is representative of large classes of experiments that use micro-fabricated electrodes in particular in the field of electrochemical sensors, where differences in grafted speed at electrode edges can have an important impact. We connect a gold electrode on a glass substrate and use it as a working electrode for the electrografting of TBPFe by cyclic voltammetry. The BALM optical monitoring is shown in Movie-2. Fig. III.16.a and III.16.b display BALM images and AFM profiles of the edge of the gold electrode respectively before and after grafting in the conditions reported in Fig. III.16.c. Both the BALM image and the AFM profile acquired after grafting in such potential range (down to -1.5 V *vs.* $Ag/AgNO_3$) clearly evidence a very significant excess of grafted TBPFe at the edge of the electrode. The final grafted thickness is indeed $\sim$131 nm at the edge and $\sim$44 nm away from the edge.

The dynamic of this process, studied through the evolution of the reflectivity, is pre-

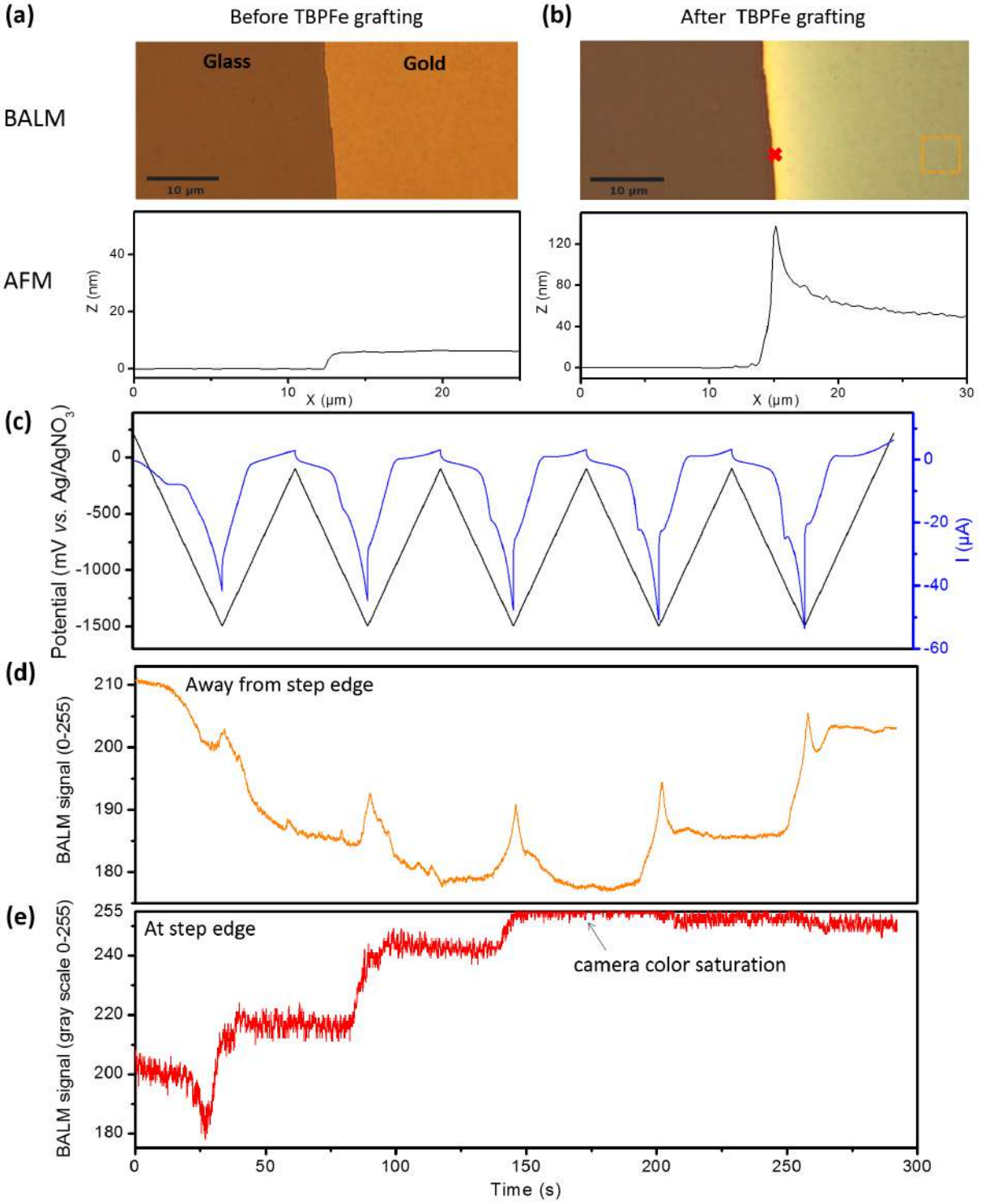

Figure III.16: Electrografting of TBPFe at step edges of gold on glass. BALM images in air with associated AFM profiles, **(a)** before grafting, **(b)** after grafting by cyclic voltammetry (50 mV/s, 5 cycles, -0.1 V to -1.5 V), **(c)** cyclic voltametry signals: applied potential (black curve) and measured current (blue curve), **(d-e)** BALM signal during the grafting of TBPFe recorded at two different areas of the gold electrode: **(d)** away from the step edge, **(e)** single pixel location at the step edge.

sented in Fig. III.16.d,e which reports the evolution of the BALM signal at two different locations of the gold electrode: away from the edge (orange curve, Fig. III.16.d) and at the step edge (red curve, Fig. III.16.e). Away from the edge, the reflectivity first decreases (*i.e.* the gold surface becomes progressively darker upon grafting), then reaches a minimum and finally increases. This shape of the reflectivity evolution is typical of BALM signals for thick coatings. With TBPFe grafted in the conditions of Fig. III.16.c, the minimum of the curve (*i.e.* the ideal anti-reflective configuration) is reached after $\sim$155 sec and corresponds to $\sim$24 nm of TBPFe. Conversely, at the electrode edge, the grafting is very fast so that the reflectivity decreases only during the first cycle and then rapidly increases up to a point where the saturation of the color scale is reached (after $\sim$145 sec of grafting). Such large edge effect has been predicted theoretically and higher grafting rate on gold edges was also observed experimentally in the case of NBDT (not TBPFe). [287]

Our present study establishes BALM as a very powerful tool for the direct study of such effects and of their dynamics. Note that Fig. III.16.e sets a limit to the use of our setup for TBPFe films that should not be thicker than $\sim$50 nm. This limit is however not intrinsic to the technique and only relates to the color dynamics of our conventional camera. In addition, the range of thickness where BALM is the most suited (0.5-50 nm) is the one of interest in most studies and the most difficult to access with other techniques (in particular the sub 10 nm range).

III.3.3 Electrografting on 2D materials

As a matter of fact, the BALM technique can go much further in terms of complexity of heterogeneous surfaces. Below, we combine the observation of atomically thin (2D) materials to the operando study of diazonium electrografting. Chemical modifications of 2D materials are key to extend their uses in several fields. [162, 295–297] In particular, diazonium chemistry is intensively studied as a way to improve their functionality in the fields of energy, electronics, filtration and sensors. [268, 298–302] Here, the ability of BALM to monitor in-situ the electrografting of diazonium salts is combined with the high z-axis resolution enabling the observation of graphene oxide (GO) and electrochemically reduced graphene oxide (ErGO) mono and multilayers.

To investigate the diazonium functionalization of GO, large single-layer GO flakes are deposited on a gold BALM substrate using the same method as in Part III.2 above. Since some of the flakes fold or overlap, different areas composed of one, two or three

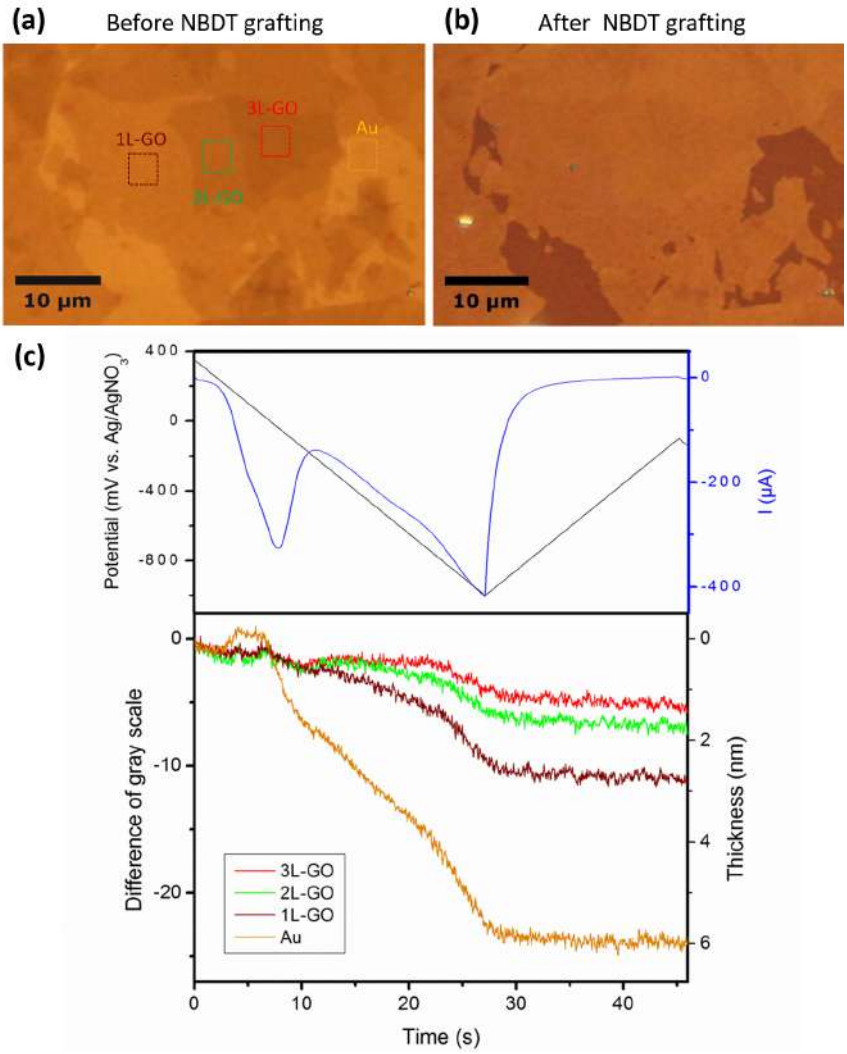

Figure III.17: Electrografting of NBDT on Graphene Oxide. (a) BALM image in air before grafting. The colored dash boxes represent the areas used for reflectivity extraction on the bare gold surface (orange), on monolayer GO (brown), on two stacked GO layers (green) and three stacked GO layers (red), **(b)** BALM image in air after grafting, rinsing in acetonitrile and drying in a nitrogen flux, **(c)** Upper panel: first cycle of the cyclic voltammetry, lower panel: change in reflectivity induced by the electrografting of NBDT and extracted in the area marked in (a).

GO layers are observable. A sample containing these three types of GO layer stacks is selected for observation during NBDT electrografting by cyclic voltammetry (5 cycles). Fig. III.17 displays BALM images in air before (Fig. III.17.a) and after grafting (Fig. III.17.b) as well as the electrochemical response of the system and the BALM reflectivity evolution during the first cycle (Fig. III.17.c), which contains the most interesting information about the grafting process. The full five cycles are reported in Fig. III.18. Importantly, BALM allows measuring local changes in reflectivity by extracting data in different areas of the images. In Fig. III.17.c, the four traces correspond

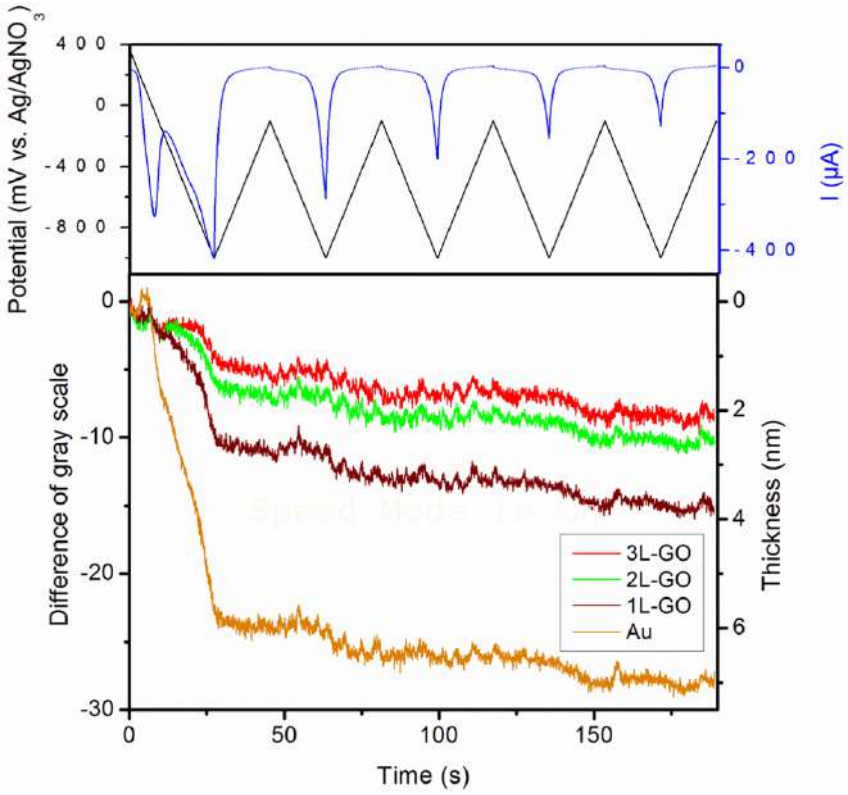

Figure III.18: Electrografting of NBDT on Graphene Oxide. Upper panel: 5 cycles of the cyclic voltammetry, lower panel: change of reflectivity induced by the electrografting of NBDT.

to data from the areas marked by dotted squares in Fig. III.17.a and associated to bare gold, single-layer, two-layers and three-layers GO. Using AFM measurements performed before and after grafting, BALM data are also calibrated in nm (see right Y-axis in Fig. III.17.c).

From both the BALM images and the dynamics of the reflectivity, one deduces that: *(i)* grafting is much faster on gold and the grafting speed sharply decreases with increasing number of GO layers; *(ii)* the potential at which grafting starts is lower on gold and shifts toward more reducing potential for thicker GO stacks. A Log-Log presentation of Fig. III.17.c (provided in Fig. III.19) shows that the change in reflectivity becomes measurable (above noise) at -20 mV *vs.* $Ag/AgNO_3$ on gold and -160 mV, -445 mV and -760 mV on single-, double- and triple-layer GO respectively, *(iii)* the edges of GO layers do not display an excess of grafting; *(iv)* at the end of the five cycles, gold areas are the darkest part of the sample and have been grafted by $\sim$7 nm of NBDT, while the three different thicknesses of GO have the same color corresponding to a homogeneous height of $\sim$5 nm above the gold surface.

Before discussing the results, it is interesting to compare this situation with the one

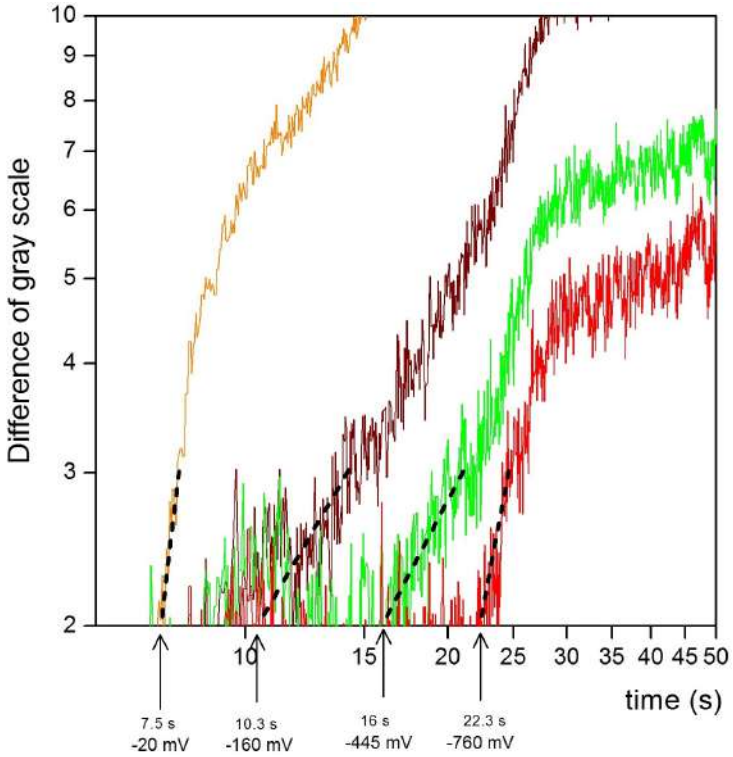

Figure III.19: Log-Log presentation of Fig. III.17.c (lower panel). By extrapolating the linear part of the curves down to the noise level (gray scale difference below 2), one can more easily visualize that grafting starts at a lower potential for gold than for GO and that the thicker the GO stacks are, the more negative the starting potential to graft is.

observed for reduced graphene oxide. For that purpose, GO flakes from the same GO source were first reduced electrochemically, directly on a BALM substrate, and then electrografted with NBDT. The reduction was performed by chronoamperometry as described in the previous section (*i.e.* at -1.1 V *vs.* Ag/AgCl for 1 h in 0.1 M Na_2SO_4 in water). The substrate with electrochemically-reduced GO (ErGO) flakes was then washed with water, dried in a N_2 flux and used for NBDT electrografting following the same parameters as for GO. Fig. III.20 displays BALM images in air before (Fig. III.20.a) and after grafting (Fig. III.20.b) as well as the global electrochemical signal and the local BALM reflectivity evolution on gold, single-layer and double-layer ErGO, during the first grafting cycle (Fig. III.20c). The full five cycles are reported in Fig. III.21. Obviously, the behavior of ErGO upon grafting strongly differs from the GO case.

In this second case, we observe that: *(i)* the grafting speed is slightly lower for gold than for single-layer and double-layer ErGO, the two latter being almost similar to each other; *(ii)* for the three types of areas the grafting starts at the same potential, close to 0 V *vs.* $Ag/AgNO_3$; *(iii)* as for the GO case, no edge effects are observed along the

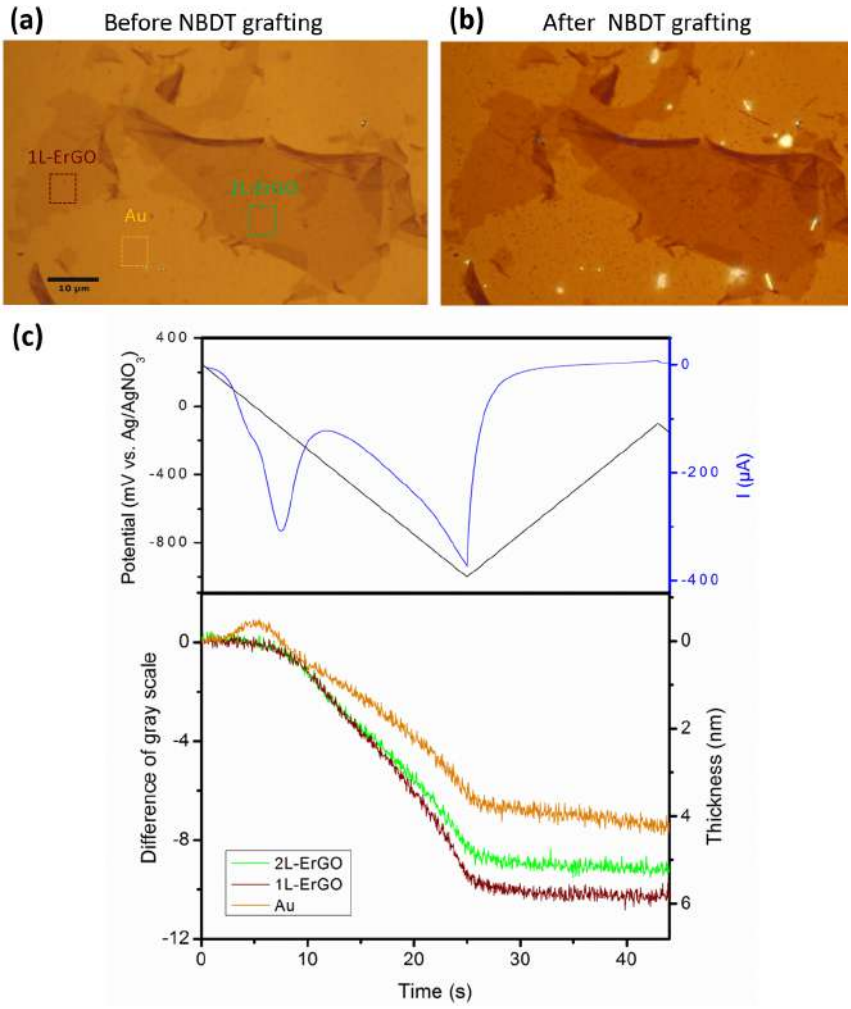

Figure III.20: Electrografting of NBDT on Electrochemically reduced Graphene Oxide. (a) BALM image in air before grafting. The colored dash boxes represent the areas used for reflectivity extraction on the bare gold surface (orange), on monolayer ErGO (brown), on two stacked ErGO layers (green), **(b)** BALM image in air after grafting, rinsing in acetonitrile and drying in a nitrogen flux, **(c)** upper panel: first cycle of the cyclic voltammetry, lower panel: change of reflectivity induced by the electrografting of NBDT and extracted in the area marked in (a).

ErGO flakes; *(iv)* at the end of the five cycles, gold areas have been grafted by $\sim$6 nm of NBDT, while GO layers have a final thickness increased by $\sim$7 nm. This contributes to increase the contrast between grafted-ErGO areas and grafted-gold areas as clearly seen on the after-grafting BALM image (Fig. III.20.b).

In terms of properties, rGO is slightly thinner, much more conductive (by several orders of magnitudes), more hydrophobic and optically less transparent than GO. These differences readily explain most of the experimental observations from Fig. III.17 and III.20. The change in transparency is evidenced by the fact that images of (not-grafted) ErGO are always more contrasted than images of GO, as discussed in section III.2. In

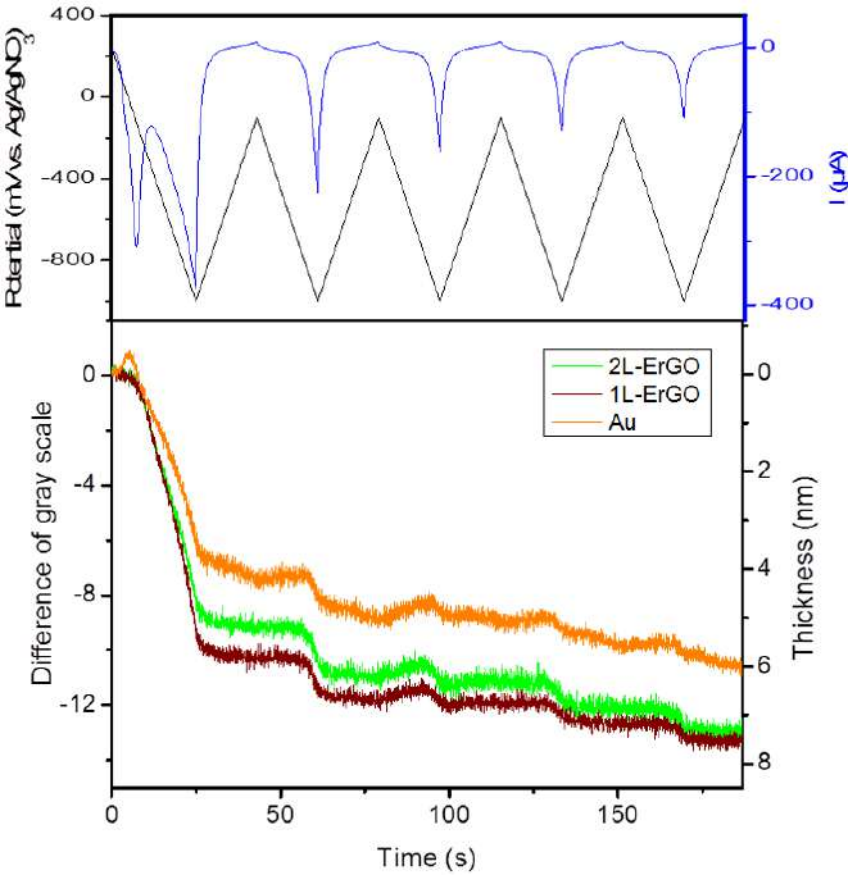

Figure III.21: Electrografting of NBDT on Electrochemically reduced Graphene Oxide. Upper panel: 5 cycles of the cyclic voltammetry, lower panel: change of reflectivity induced by the electrografting of NBDT.

terms of grafting, GO being electrically insulating, it screens the potential of the gold surface (working electrode), all the more that the number of layers increases. This simply accounts for the fact that the final contrast is reversed (grafted gold becomes the thicker part of the substrate in Fig. III.17) and for the leveling of the reflectivity for the three types of GO stacks. Conversely, ErGO is conductive which explains that the grafting of ErGO (single and double-layers) starts at very low potential close to 0 V *vs.* $Ag/AgNO_3$.

In terms of homogeneity, Fig. III.17 and III.20 do not provide evidence for a higher grafting rate at defects or edges. Several electrochemical studies on graphitic materials (graphite, graphene, graphene oxide) have concluded that the presence of defects or edges is favorable for charge transfer. [4, 303, 304] The difference in our case could come from the limited lateral resolution of an optical technique. This is however improbable considering the size of individual pixels in our images. It is more probable that the mild grafting conditions used in Fig. III.17 and III.20 (minimum potential -900 mV) are

favorable in terms of homogeneity (similarly to the case of gold electrodes). [294] Several studies also reported an increase in charge transfer when increasing the number of layers. [4, 303, 304] For example, the charge transfer kinetics has been observed to double with $FeCN_6^{3-}$ and $IrCl_6^{2-}$ on graphene when going from 1 to 2 layers. [305] These results could explain the fact that for ErGO, the grafting is faster for double-layer than single-layer and that both cases get grafted faster than gold.

Altogether, our results show that the chemical composition of the layer plays a crucial role in the kinetics of charge transfer and that BALM can reveal very subtle changes. It also paves the way for the investigation, at the local scale, of new materials electrografting, notably van der Walls heterostructures. Furthermore, BALM is not limited to gold as anti-reflective absorbing layer, but it can be extended to other metals (platinum, copper, silver, etc.) and the controlled deposition of many materials can be studied on BALM substrates.

III.4 Copper electrodeposition

BALM is not limited to the study of organic thin film electrografting since any material with a different refractive index than glass or the solvent modifies the reflectivity of the interface. Therefore the electrodeposition of metals can also be investigated. In practice, it is even easier as metals are highly absorbing materials, which means that even a small amount of electrodeposited material drastically changes the reflectivity. Metals particles and nanoparticles are well-known as surface modification methods to add new functionalities to surface (sensing, [306, 307] catalysis, [308] biomedical, [309, 310] etc.). The electrodeposition method is interesting on conductive substrates because it ensures a good electrical contact between the substrate and the particles. In certain cases, this method allows the control of the shape and size of particles by tuning the deposition process and electrolyte.

The mechanism of nucleation and growth of metal particles resulting from electrochemical deposition is mainly studied by an analysis of the current / time / voltage characteristics during deposition coupled to post-deposition imaging (AFM, SEM, TEM). [311–313] Comparisons between local observation and electrochemical signal are difficult because the current is averaged over a large number of particles with a certain dispersion of shape, size and spatial distribution. Another approach consists in reducing the size of the electrode to decrease the number of deposited particles. To

do so, Scanning ElectroChemical Microscopy (SECM) [314, 315] or Scanning Electro-Chemical Cell Microscopy (SECCM) [310] have been used. Recently, the use of optical microscopy techniques (darkfield, SPR and holography) helped the study of nanoparticles electrodeposition or dissolution by counting and sizing the particles. [316–321] The group of F. Kanoufi at Itodys (Paris-Diderot University) notably coupled optical observations with micro-electrode electrochemistry. [322–325] Here, we propose the use of the BALM microscopy technique to observe *in situ* electrodeposition processes of copper on gold.

Copper electrodeposition is well-known in the literature [326–330] and can thus serve as a model system. Nevertheless, the field lacks of fast and *in situ* characterization techniques to extract the number of nuclei, the surface coverage, etc. Furthermore, it is challenging to study the deposited particles as they are rapidly dissolved by the electrodeposition solution which modifies their size and shape after the process ended.

III.4.1 Copper on gold

The first step is to demonstrate the use of BALM coupled to electrochemical deposition. The following experiment studying the deposition of copper on gold was published in the Supplementary Material section of Ref. [3].

The BALM set-up is set in the electrochemistry configuration: the gold ARA layer (0.5 nm Cr + 3 nm Au) is used as working electrode, a gold mesh is used as counter electrode with an Ag/AgCl reference electrode. The electrodeposition of copper is performed in water with 10^{-2} M $CuSO_4$ electrolyte and the solution is adjusted at pH = 2 using diluted H_2SO_4. Then chronoamperometry experiments are performed and movies are taken at the same time. From the movies, series of images are selected and the surface coverage of copper on gold is extracted, as presented in Fig. III.22. Two different chronoamperometry experiments are performed for 10 minutes, one at -140 mV and the other at -160 mV *vs.* Ag/AgCl with the corresponding images extracted from Movie-3 and Movie-4 respectively. For each image, the surface coverage was extracted using the *Gimp* software and a mask with the same color threshold for all images.

From images one can see that the particles appear as bright spots growing with time. The number of nuclei is obviously higher for -160 mV than -140 mV, resulting in faster surface coverage even though the metal particles are bigger at -140 mV. It further

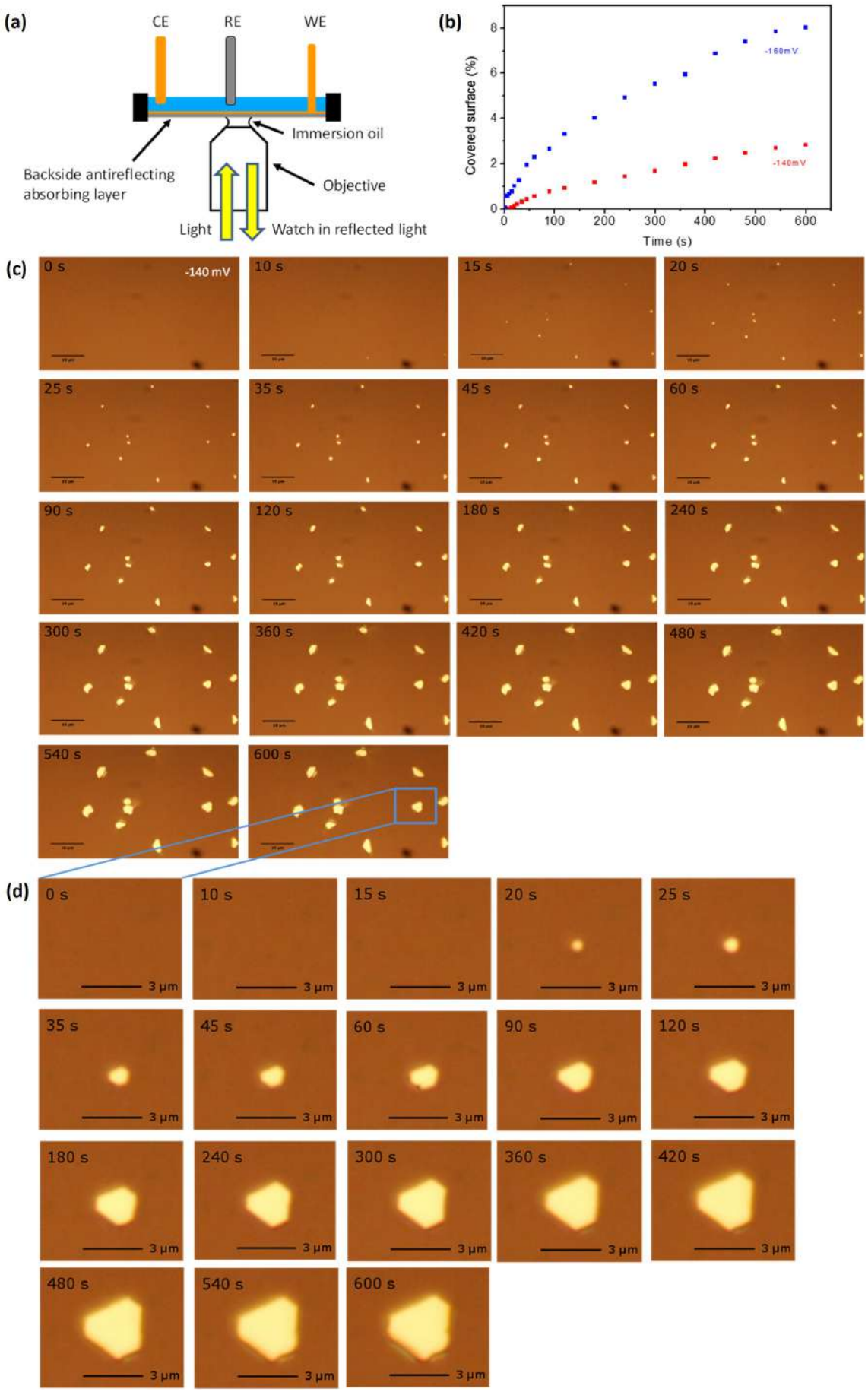
(a)
CE
RE
WE
Immersion oil
Backside antireflecting absorbing layer
Objective
Light
Watch in reflected light
(b)
Covered surface (%)
Time (s)
-160mV
-140mV
(c)
0 s
-140 mV
10 s
15 s
20 s
25 s
35 s
45 s
60 s
90 s
120 s
180 s
240 s
300 s
360 s
420 s
480 s
540 s
600 s
(d)
0 s
10 s
15 s
20 s
25 s
35 s
45 s
60 s
90 s
120 s
180 s
240 s
300 s
360 s
420 s
480 s
540 s
600 s
3 µm

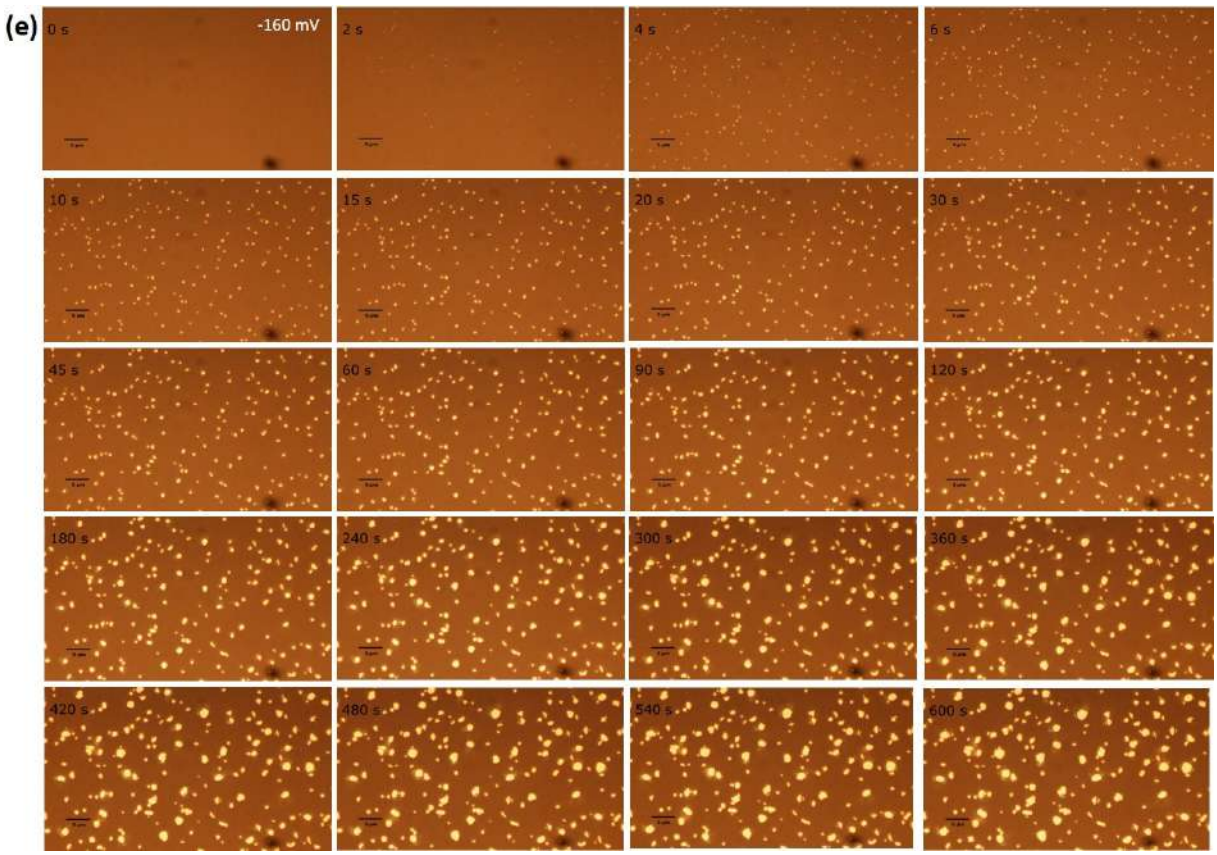

Figure III.22: BALM-coupled electrochemical setup for real-time imaging of the electrochemical deposition of copper. (a) Schematic representation of BALM coupled to electrochemistry; the ARA layer is connected and acts as working electrode (WE), a gold counter electrode (CE) and an Ag/AgCl reference electrode (RE) are immersed in the solution. **(b)** Temporal evolution of the deposition of copper under chronoamperometry at –140 mV and -160 mV *vs.* Ag/AgCl – scale bar 10 µm. **(c)** Example of BALM images of the electrodeposition of copper at –140 mV *vs.* Ag/AgCl. **(d)** Zoom of the rectangle area in blue during the same sequence. (e) Example of BALM images of the electrodeposition of copper at –160 mV *vs.* Ag/AgCl – scalebar 5 µm. [3]

indicates that the electrochemical potential controls the number of nucleation points as expected by the mechanism. [326] A numerical zoom on a particle grown at -140 mV is presented in Fig. III.22.d, it shows that this particle has well-defined crystallographic facets.

This preliminary experiment was performed early in the thesis, using a BALM slide without the 15 nm electrodes (preventing a voltage drop between the side and the center of the slide), therefore the applied potential is not fully reliable. Nevertheless, it shows that BALM is suited to investigate the electrodeposition of metal particles and that it can bring information on the number of nucleation points, the surface coverage and to a certain extend, on the crystalline nature of the particles. The lateral resolution

of BALM is limited by diffraction but it does not mean that particles smaller than this limit are not observable as discussed in section II.1.

Similar experiments using BALM were performed in the group of F. Kanoufi in 2018. [215,216] They notably established the relationship between BALM signal and particle size using an SEM calibration. They also showed that the limit of particle detection is around 10 nm in diameter. Microelectrodes were investigated in order to observe the entire working electrode surface and thus comparison between the BALM signal and the electrochemical response was precise. Furthermore, their BALM experiments comforted some nucleation mechanism and Ostwald ripening was observed *in situ* (small particles dissolve and redeposit onto larger particles).

III.4.2 Copper intercalation in graphene oxide

As for electrografting of diazonium salts, metal electrodeposition constitutes an ideal model system to study local surface modification effects on 2D materials. In the following, we study copper deposition on gold substrate on which graphene oxide flakes were deposited. Except few studies on graphene or HOPG, [311,331,332] the electrodeposition of metals on 2D materials was barely investigated. R. Dryfe and D. Lomax (University of Manchester) have reported the use of *in situ* AFM for the study of gold deposition on graphene [332] and the group of P. Unwin (University of Warwick) has investigated silver deposition on HOPG using SECCM. [331]

A GO modified gold surface was first electrodeposited with copper by chronoamperometry at 0 V *vs.* Ag/AgCl. A series of obtained images extracted from Movie-5 are presented in Fig. III.23 (it is strongly recommended to watch the movie). During the first 4 seconds of this experiment, no obvious change of the reflectivity is observed on the gold or the GO flakes. Then, very bright dots start to appear on gold and GO flakes. Interestingly, the changes are extremely selective in terms of GO thickness: after 5 seconds, the areas of the surface composed of 2 or more layers of GO are almost completely covered with white dots, while the GO monolayers and the gold substrate are still barely affected. Fig. III.23 constitutes a particularly clear example of the capability of BALM to observe local changes in heterogeneous samples and, specifically in the case of 2D materials, for processes that depend on the number of layers. In order to understand this preliminary result, we present below complementary experiments performed using cyclic voltammetry in place of chronoamperometry.

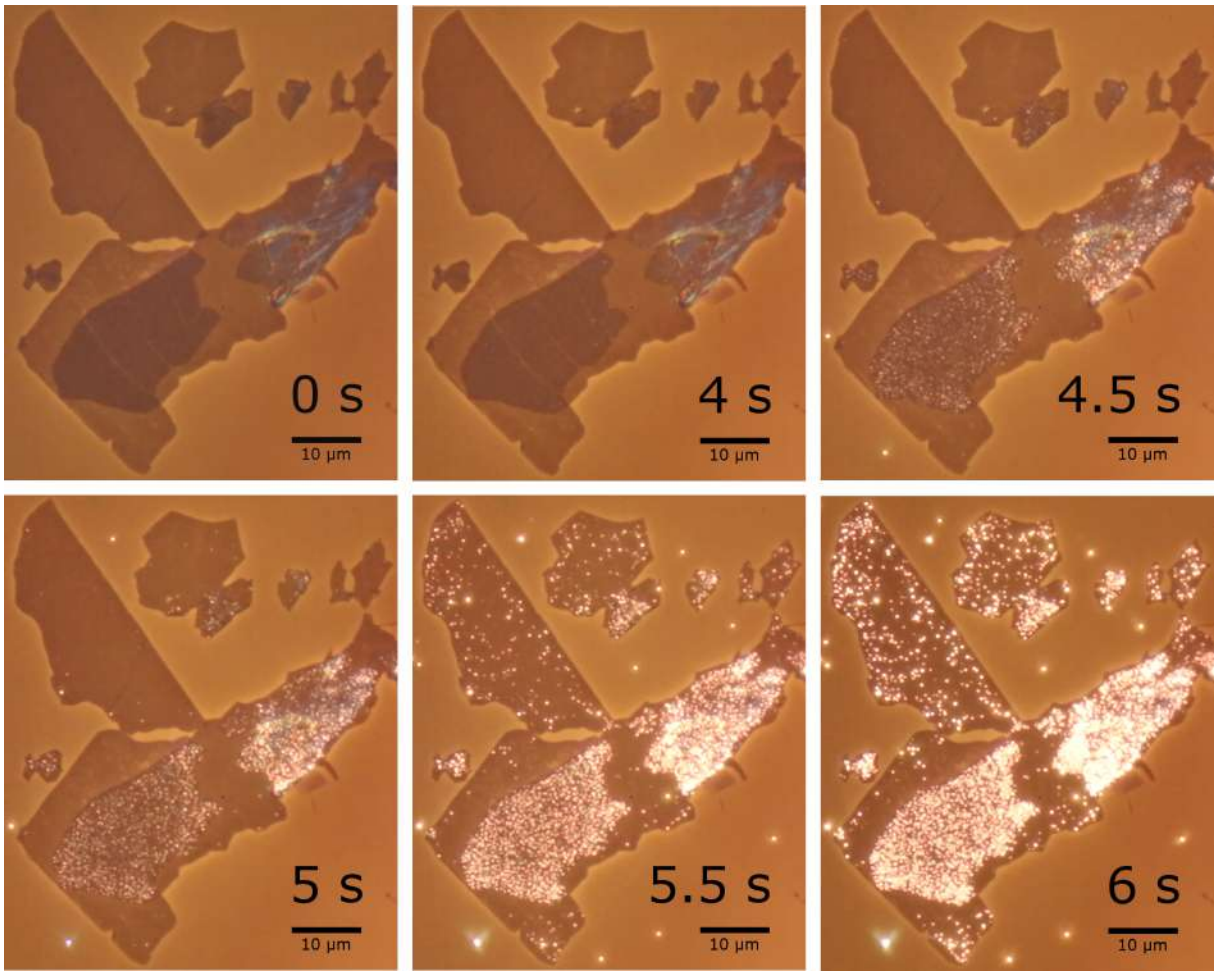

Figure III.23: Electrodeposition of copper on a BALM substrate covered with graphene oxide flakes by chronoamperometry, 0 V *vs.* Ag/AgCl.

We performed the electrodeposition of copper on BALM substrates partially covered with either graphene oxide or electrochemically reduced graphene oxide. The set-up corresponds to a gold ARA layer of 0.5 nm Cr + 3 nm Au as a working electrode, a platinum mesh as a counter electrode and an Ag/AgCl reference electrode. The deposition was performed in water with 10^{-2} M $CuSO_4$ electrolyte and the solution was adjusted at pH = 2 using diluted H_2SO_4. Graphene oxide is deposited on gold using the bubble technique and is either used directly or is first reduced by electrochemistry using the method developed in III.2. BALM images of the GO/gold and ErGO/gold samples taken in air before the deposition are presented in Fig. III.24. The contrast being better in air, these images allow identifying unambiguously the number of layers in selected aggregates of flakes that are then studied in liquid.

The electrodeposition is performed by Cyclic Voltammetry (500 mV to -200 mV *vs.* Ag/AgCl at 20 mV/s) and a movie is recorded at the same time. The electrochemical current response to this experiment is presented in Fig. III.24.b, it is typical of cop-

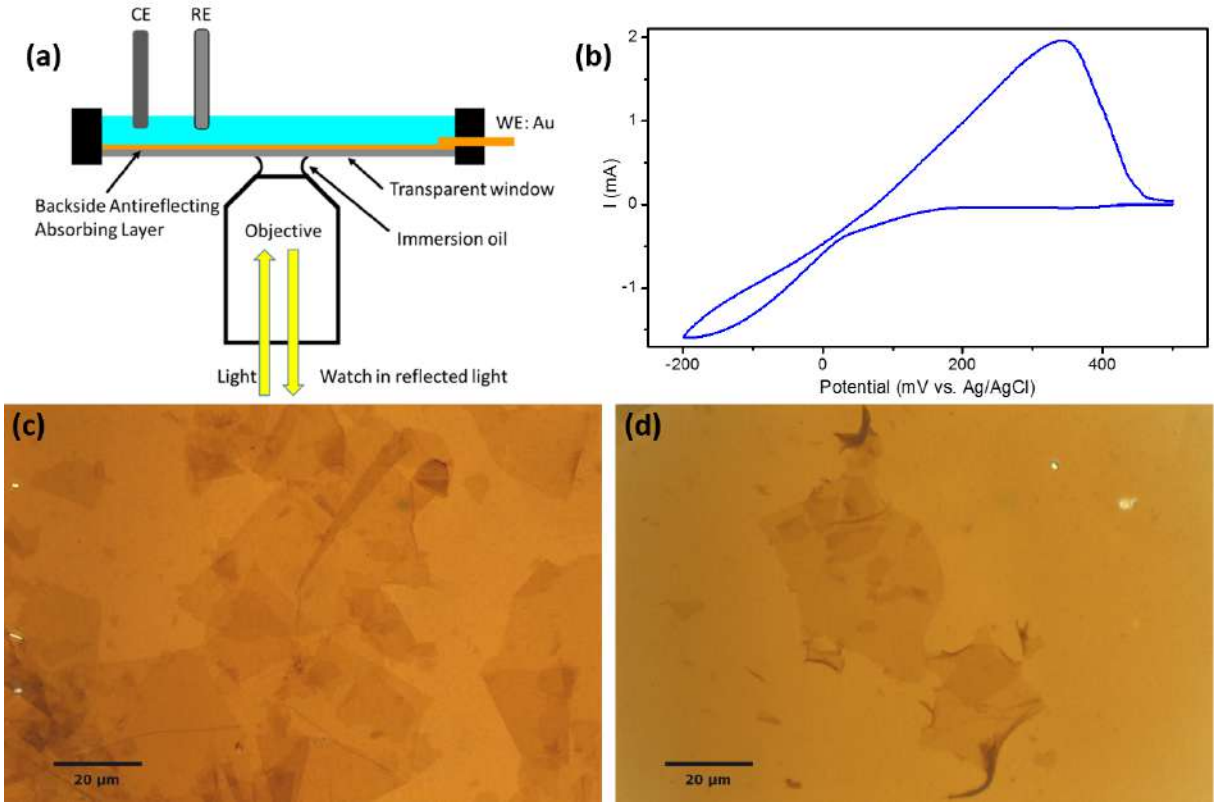

Figure III.24: Electrodeposition of copper on a BALM substrate covered with GO and ErGO flakes. (a) Schematic of the BALM set-up in configuration of electrochemistry, **(b)** typical voltammogram obtained during the electrodeposition of copper on a BALM substrate by cyclic voltammetry (20 mV/s, 500 to -200 mV *vs.* Ag/AgCl). BALM images in air and before electrodeposition, **(c)** of graphene oxide and **(d)** of electrochemically reduced graphene oxide.

per electrodeposition on the reduction part, and of electrodissolution in the oxidation part. [326, 333] Movies of the GO and ErGO surfaces captured during the CV are respectively labelled Movie-6 and Movie-7. From these movies, key images at interesting potentials are selected and presented in Fig. III.25 (deposition) and Fig. III.26 (dissolution).

Fig. III.25 presents the electrodeposition on GO (left colomn) and ErGO (right colomn). In both cases, a few bright spots starts to appear on the gold surface around 0 mV *vs.* Ag/AgCl and their number rapidly increases. At -23 mV, one can clearly see that the ErGO flakes do not show any such bright features whereas the thickest GO multilayers areas are already covered. The difference is particularly striking at -43 mV for which the shape of the different flakes gets highlighted: GO multilayers appear very bright and ErGO layers remain dark but are now fully surrounded by copper dots on gold. At even lower potential, -183 mV, all GO multilayers are fully bright while ErGO monolayers only

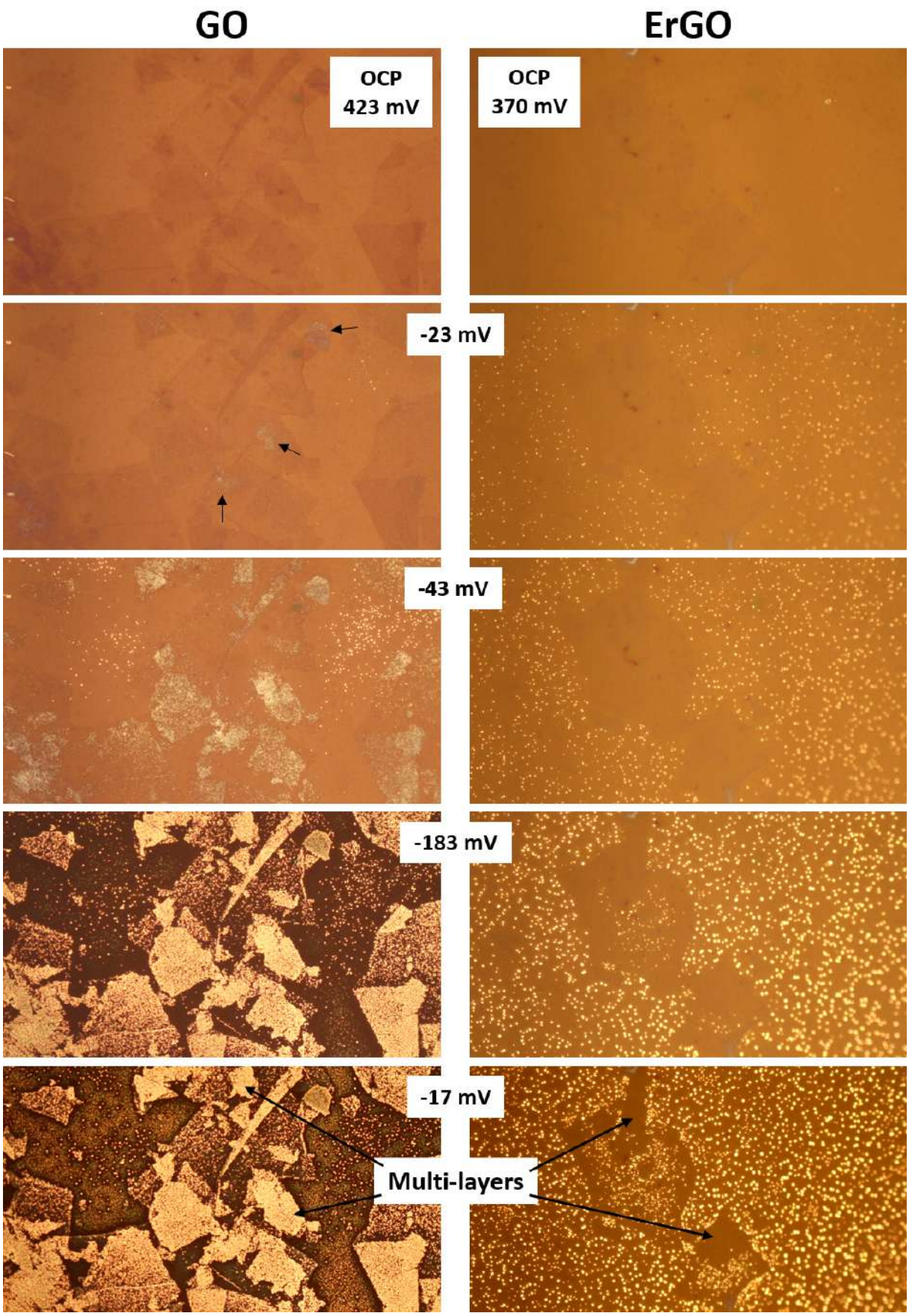

Figure III.25: BALM images during the electrodeposition of copper on BALM substrates covered with GO or ErGO flakes.

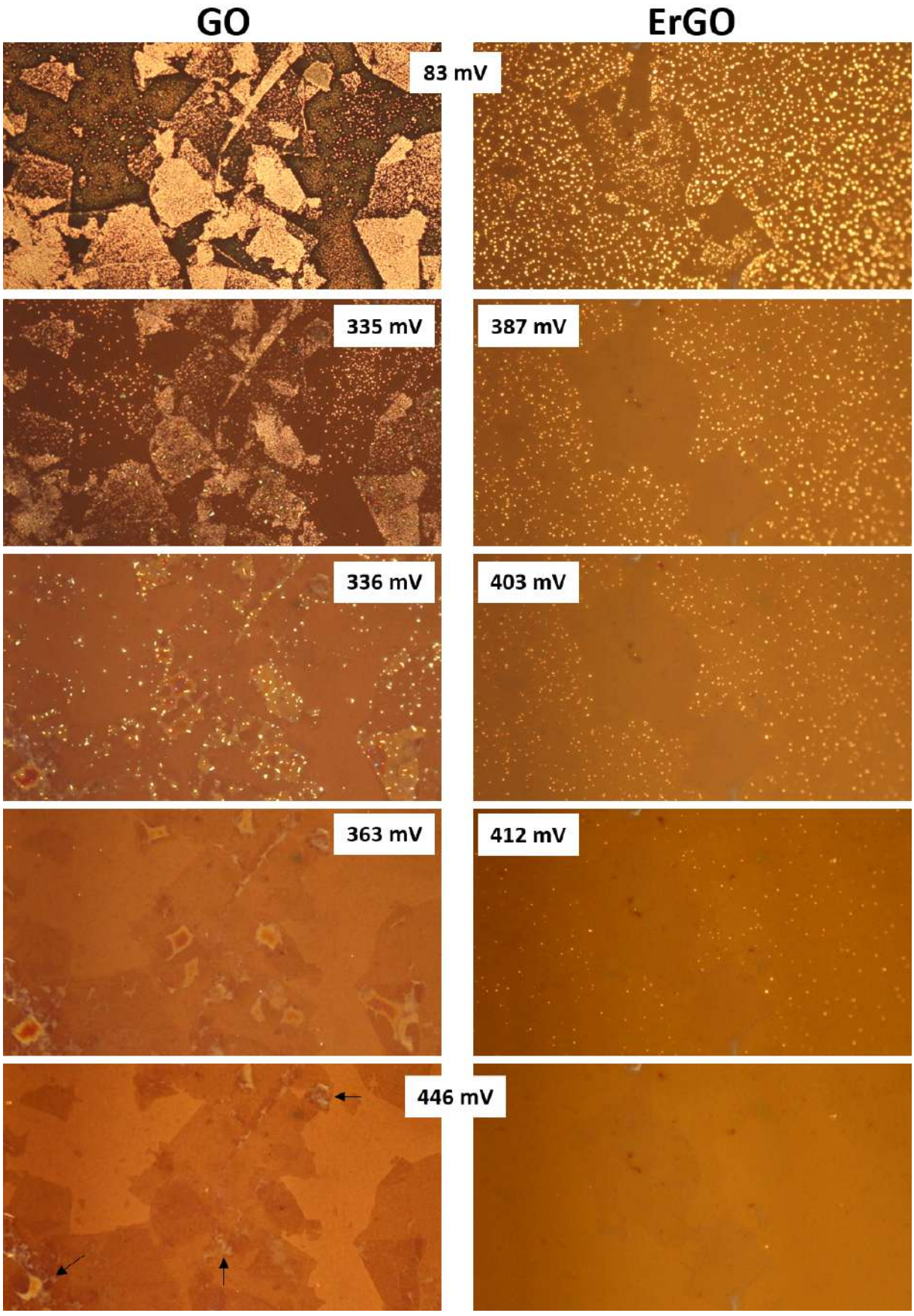

Figure III.26: BALM images during the electrodissolution of copper on BALM substrates covered with GO or ErGO flakes.

start to show the beginning of the deposition as small dots appear on their surfaces. The contrast of ErGO multilayers have not evolved yet. Interestingly, the edges of ErGO monolayers sides (*i.e.* close to gold) are less covered than the center of these flakes. This is consistent with the fact that the copper ions in the solution get depleted by the efficient deposition on bare gold, so that locally, close to the ErGO monolayer edges, the concentration is lower. When scanning backwards from -183 to -17 mV, small dots continue to appear on gold and the gold surface is almost completely covered with copper.

Fig. III.26 presents the electrodissolution of copper from the same samples at positive potentials. On the ErGO side, the experiment is exactly reversed: bright dots starts to be removed from the ErGO monolayers and then the gold surface gets back to its initial aspect. Note that the copper dissolution from gold takes place abruptly (in a very short potential range around 410 mV). On the GO side, the experiment is also reversible, but to a lower extend. Bright dots are entirely removed from the gold surface before 363 m V and from the GO mono- and bi-layers before 446 mV. However, GO multilayers remain brighter at this potential (see the tick GO areas marked with arrows).

Figure III.23, III.25 and III.26 show important differences in the copper deposition process as a function of the number of layers. This is particularly striking in the GO case where the GO monolayers are much less affected than double-layers and thick layers. Recently (June 2019), the group of R. Nair (University of Manchester) studied the electrochemical deposition of palladium and copper on graphene oxide sheets. [334] They demonstrated that palladium and copper intercalate between graphene oxide layers and that the palladium growth is self-limited to 5 nm in thickness whereas copper growth is not limited. They provided key structural characterizations to their study: optical images, AFM topography and HRTEM. The optical image after metal deposition is similar to our observations and the HRTEM study unambiguously proves that palladium is indeed intercalated between GO layers and not simply deposited on top.

Our experiments are in very good agreement with their study. It supports the idea that we observe *in situ* the intercalation of copper between GO layers. We show that the intercalation occurs first within the tick GO multilayers, then between the first and second layer and that finally, copper also gets deposited on GO single-layer, or between GO single-layers and gold (the latter hypothesis being favored by Nair and co-workers who suggested that palladium is electrodeposited below the GO monolayers). During the copper dissolution, the thick intercalated copper layers behave similarly to liquid

droplets (see notably the image at +363 mV) which may be due to highly concentrated copper diluted in water.

The ErGO experiments show the opposite behavior than the GO one as copper is not intercalated between ErGO multilayers. The electrodeposition on ErGO follows the trend of a blocking material which increases the over potential necessary to reduce copper at its surface when increasing the number of stacked layers. This result is counter intuitive as ErGO flakes have better electrical conductivity than GO but it is known that the Under Potential Deposition (UPD) of copper on carbon materials like rGO is unfavorable [335] whereas it is possible on gold. [336, 337] The difference between GO, ErGO and gold may be due to specific interactions between Cu^{2+} and oxygen groups. GO is indeed investigated by several groups for depollution/filtration application and specifically for the removal of Cu^{2+} from water. [338]

Something to notice is that in both cases (GO and ErGO), even after a full cycle of intercalation and de-intercalation, the materials remain intact (at the observation scale). Considering the vertical resolution of BALM confirmed in Chapter II with transparent molecules, it is very unlikely that copper residues remain on gold, single- and double-layers of GO and ErGO at 446 mV. Only thick GO stacks were not fully de-intercalated

The experiments presented in this section demonstrate that the redox state of graphene oxide controls the intercalation of copper and that this could be used to control the shape and size of metallic nanosheets. They are complementary to the one of Nair and co-workers who proved that copper is intercalated within GO flakes. BALM provides *in situ* information on the deposition dynamics and could be very useful in this developping context.

III.5 Conclusions on Chapter III

In this chapter, the combination of BALM and electrochemistry was discussed. We first showed that the ultrathin gold substrate is limited to potentials lower than 0.3 V *vs.* Ag/AgCl and that the slide cleaning prior electrochemistry has an impact on the stability of the substrate. The UV-ozone method has to be followed by a thermal treatment in order to produce stable and clean gold surfaces. Then, basic electrochemical methods were performed while monitoring the reflectivity of the interface. We showed that the BALM optical signal is modified when applying cyclic voltammetry, chronoamperometry and electrochemical impedance spectroscopy. This modification is due to the Pockels

effect which is related to the refractive index changes within the electrical double layer, therefore BALM is sensitive enough to probe the establishment of the double layer.

Then the ability of BALM to image precisely 2D materials was combined to electrochemical reactions. The dynamic of the electrochemical reduction of graphene oxide was followed *in situ* and the relationship between the number of stacked layers and the reduction time constants were determined. We also studied the electrografting of diazonium salts and showed that BALM provides equivalent information to the Electrochemical Quartz Crystal Microbalance (EQCM) but with a microscope configuration. It was used to demonstrate the higher grafting rate of TBPFe at edges of gold electrodes. We also used this configuration to probe the electrografting speed at graphene oxide and electrochemically reduced graphene oxide flakes. We showed the grafting efficiency dependence over the number of stacked layers as well as their electrical conductivity. Finally, BALM coupled to electrochemistry was extended to the electrodeposition of copper. Copper was first deposited on gold and showed the type of obtainable information (number of nuclei, surface coverage and crystalline nature of the particles). Then, GO and ErGO were deposited on gold and the electrodeposition of copper was directly observed. The nature of the deposition was demonstrated to be completely different as copper is intercalated between multilayers GO whereas ErGO does not allow intercalation to occur.

This chapter establishes the assets of BALM as a powerful tool to bridge electrochemistry and high-contrast 2D materials observation.

Conclusions & future directions

The objective of this thesis was to evaluate the potential of the Backside Absorbing Layer Microscopy (BALM) technique as a tool to study *in situ* and locally some of the optical, chemical and electrochemical properties of 2D materials, without using a scanning probe.

The main results were already summarized in sections II.5 and III.5. The developed experiments showed the versatility of BALM, its sub-nanometer sensitivity, its capability to study dynamical processes of surface reactions and especially for the local and time-resolved observation of heterogeneous surfaces, establishing the technique as a precious tool for nanoscience research laboratories.

We notably studied in details the parameters influencing the performances of the technique. We first investigated the impact of the thickness of the anti-reflecting absorbing layer and selected a 0.5 nm chromium / 3 nm gold combination as the trade-off for imaging molecular thin films and nanomaterials both in air and in water. This ARA coating on glass is particularly powerful to produce highly contrasted images of 2D materials (in particular graphene oxide and monolayers of transition metal dichalcogenides) and to observe reactions at the BALM substrate surface. The main limitation is that the gold anti-reflective layer is sensitive to oxidation which requires precautions when used for electrochemistry. The influence of the chromium adhesion layer on the electrochemical stability and on the optical properties of the ARA layer remains to be studied. ARA coatings produced by other methods could be useful in future work. In preliminary experiments not reported here (see the experimental part), we tested several options. For instance, we deposited an aminated silane SAM on glass prior gold deposition as it is known to promote adhesion. This method is useful for optical studies as it removes the highly light absorbing chromium layer and makes the system easier

to simulate. Unfortunately, the obtained coating is not stable within the electrochemical reduction window and in acidic media. Such substrates were not used in the reported experiments but could be used for BALM applications that do not require this particular chemical stability. Gold could also be replaced by any light absorbing materials like platinum, aluminum, etc. Interestingly, as initially proposed by D. Ausserré, graphene could also be used as ARA material in principle: it absorbs light in a broad spectral range, its rugosity is potentially ideal (atomic scale), the thickness can be tuned using multilayers. As a test, we deposited high-quality CVD grown graphene (provided by V. Bouchiat from Institut Néel, Grenoble) directly on glass and imaged the sample using the same inverted microscope as for BALM experiments (but without the gold ARA layer). The result is presented in the experimental section (Fig. Exp.1). Graphene mono- and multi-layers appear darker than glass both in air and in water confirming that by controlling the number of graphene layers, graphene-based ARA coatings could be produced. They would constitute promising carbon electrodes for electrochemical experiments coupled to BALM. However, one should notice that with the present status of graphene production and transfer methods, the homogeneity of such substrate would be an issue. Even with the large-scale, high-quality graphene domain used, it could be difficult to differentiate features coming from the graphene ARA layer from those of the added materials under study.

After the ARA thickness was studied, the refractive index of both the substrate and the top medium were shown to be adjustable, within certain limits. Indeed, the top medium refractive index has to be lower than the one of the substrate to achieve anti-reflective conditions with absorbing materials. When using glass, the top medium is limited to solvent having a refractive index below 1.5. And as it was shown, the closer the substrate and top medium refractive indexes are, the lower the gold thickness is to obtain efficient AR properties. This can be problematic as it is difficult to reproducibly produce smooth gold coatings with a thickness below 3 nm. At the exception of acetonitrile, acetone and ethyl ether, most of the common organic solvents have a refractive index higher than 1.4 (THF = 1.41, DMF = 1.43 and DMSO = 1.48). This limit can be overcome by changing the substrate with sapphire (n = 1.77). The top medium also restrains the material to observe as their refractive indexes have to be different to produce contrast.

The wavelength of the incoming light was used to understand and improve the contrast of MoS_2 monolayers and bilayers. The experiments were compared to numerical estimations and it was showed that BALM can contribute to discriminate the complex

refractive index values obtained by several groups using other methods. Measurements of (n,k) are usually done with more complex optical apparatus and compared to extended theoretical models. BALM provides additional information which can be confronted to the literature (for example, even with the simple approximations of the model, values of k_{MoS_2} below 2 cannot account for the observed BALM contrast in the blue spectral range). The wavelength study also showed that monochromatic sources can be used to discriminate different materials on the same sample as exemplified with MoS_2 and WS_2. In the future, another way to compare materials would be the use of the polarization. Polarizers could easily be added to study materials with anisotropic optical properties such as phosphorene. In terms of limitations, one should however keep in mind that filtering the light with band-pass filters or polarizers drastically decreases the reflected light signal which is already very low by principle. Low signal could prevent the recording of movies at regular acquisition speed and resolution. Further improvement of the set-up would thus require the use of laser sources for single wavelengths or of a high-power lamp with a monochromator for the continuous adjustment of λ.

Using the continuous deposition of an organic second layer on top of the gold substrate, we experimentally demonstrated several features of BALM: *(i)* It can follow the deposition of transparent organic molecules, with sub-nanometer vertical resolution even at the single pixel level; *(ii)* The parameters of a second layer can be adjusted to drastically improve the contrast of an observed material (such as graphene oxide); *(iii)* Any conventional transparent (or low k) material can be used coupled to the gold layer. In the future, such materials can provide new functionalities to the BALM substrate. For instance, PDMS could be used to couple BALM with microfluidic studies. Another perspective consists in exploiting aluminum oxide as an electrically insulating second layer to couple optical and electrical studies. Preliminary studies were initiated recently with connected MoS_2 flakes on glass/gold/alumina substrates.

The above mentioned wavelength and second layer studies were coupled to numerical estimations. The simple model used (Fresnel equations available in Comsol) is only a few steps away from being quantitative/predictive. It would further need to take into account additional parameters: different angles contributions to account for the numerical aperture of the objective, the surface roughness which can be significant for the thinnest gold layers, the exact complex refractive index of ultrathin gold and chromium layers, the exact spectral distribution of the light source (when not using monochro-

matic light) and the spectral sensitivity of the camera.

The configuration of the inverted microscope makes BALM suitable for its combination with electrochemistry. We first used this capacity to apply potentials on the ARA layer and study several electrochemical reactions. We showed that the substrate we selected is limited to potentials lower than 0.3 V *vs.* Ag/AgCl due to oxidation/degradation issues. Cyclic voltammetry and chronoamperometry were performed. They notable show that BALM is sensitive enough to probe the charge and discharge of the electrical double layer. Preliminary tests of optical electrochemical impedance spectroscopy were also initiated. The EIS experiments revealed some of the present limitations of the set-up: the sensitivity of the camera and its imaging rate which are too low to study phenomenon with sub-40 ms dynamics. Nevertheless, these limitations could be overcome with high-speed/high-sensitivity cameras which are progressively becoming standard.

The capabilities of the technique were used to observe electrochemical reduction reactions: the reduction of GO, the electrografting of diazonium salts and the electrodeposition of copper. Examples of such real-time studies are very scarce in literature, in particular in the field of 2D materials. The reflectivity signal was in particular demonstrated to be equivalent to the one of the electrochemical quartz crystal microbalance for organic layer deposition but in addition the microscope provides precious local information (such as the selectivity of certain processes as a function of layer number in stacks of GO or ErGO flakes). It has to be noted that the optical signal saturated for the study of thick TBPFe layers (above 50 nm) because of the limited dynamic of the camera. This was even more important for the metallic deposition as copper nucleation points directly appear as saturated bright spots due to the very high extinction coefficient of copper. A camera with a larger dynamic could be useful for the study of thick and/or light absorbing materials. On the other hand, other techniques such as ellipsometry already exist to study thick layers and the most difficult studies concern thin layers (below 50 nm) and 2D materials.

In a close future, I think that the Licsen team could advantageously put at profit the combination of BALM and electrochemistry to study electrocatalytic reactions like the Hydrogen Evolution Reaction (HER) and the Oxygen Reduction Reaction (ORR) at 2D materials surfaces or on CNTs, which are central to the group scientific thematics. In this domain, F. Kanoufi and co-workers showed that BALM can be used for the observation of hydrogen bubbles at the surface of gold. [339] This is interesting for the

HER study for which efficient platinum-free catalysts are challenging to develop. A particularly interesting 2D material to study for this reaction is MoS_2 monolayer. We performed some initial tests in this direction but we did not observe any bubble formation on MoS_2 or even on platinum deposited on gold. This may be because the current was too low at those areas to produce bubbles or the viscosity of our electrolyte was too low to retain bubbles at the gold surface (the observations reported in [339] were done in a viscous ionic liquid). A lot of work is needed to observe catalytic reactions with BALM and the field is in its infancy. One way to study reactions with such low refractive index modification at the surface could be to combine BALM with other probes like fluorescent ones which can be specific to the surrounding pH or oxygen level.

We coupled BALM with electrochemistry but it can obviously be further combined with many other characterization techniques that can fit on top of an inverted microscope. First and foremost, BALM can be used as an observation platform to speed up other characterizations by allowing the fast mapping of the sample and thus efficiently direct another technique toward an area of interest. Coupled techniques can be separated in two types: sequential or simultaneous experiments. Indeed, one should remind that a major fraction of the intense incoming light is transmitted through the substrate thus, if one wants to place a light sensitive technique such as Raman, photoluminescence, etc. on top, the imaging should be stopped or very well filtered during the measurements. Scanning probe techniques like AFM or SECM are not sensitive to light, therefore they can be performed simultaneously to the BALM observation. The coupling to SECM could be very powerful. It could for example provide the precise distance between the tip and the substrate (using a fluorescence labeling strategy [340]) as well as direct structural information of the mapped area which could be directly correlated to the local electrochemistal signal without SEM or AFM post-studies.

In a more global context, it would be appreciable to work more with biologists to implement new optical microscopy techniques. This type of coupling started in electrochemistry with fluorescence microscopy [341] and Surface Plasmon Resonance (SPR) [342] but it is still really specific to some particular systems. BALM could address more generic/typical systems.

BALM is highly versatile and the set-up does not require an expensive apparatus to be implemented. It starts to disseminate in the community. Recently, the group of A. Pénicaud at CRPP reported an image of individual single-wall carbon nanotubes (see the supporting information section of [217]). As already mentioned, the group of F. Kanoufi

at ITODYS implemented the technique and published three studies in the last years on its coupling to electrochemistry. [215, 216, 339] They notably studied the electrodeposition of silver nanoparticles and showed that the lateral resolution allow identifying particles as small as 10 nm in diameter. They also applied the microelectrode strategy to correlate the optical signal with the electrochemical current. In 2018, a PhD thesis supervised by F. Lagarde started at the ISA-Lyon (Institut des Sciences Analytiques) with the aim of using ARA substrates as sensitive and specific detection substrates for biological pathogens. In order to promote and facilitate the use of BALM, the experimental part hereafter gathers a series of key elements that could be useful to new users. It concerns the fabrication of the anti-reflective coatings by several methods, the set-up itself and a few home-made *Mathematica* scripts used to extract local data from movies and images.

To conclude, this work aimed at providing a thorough evaluation of the advantages and limitations of the BALM technique. Its remarkable advantages were evidenced by performing original experiments on molecular thin films and 2D materials and through the coupling of BALM to electrochemistry. The limitations were examined in details and whenever possible, improvements were proposed. I hope this work will contribute to establish BALM as a key technique for the nanoscience community.

Experimental section

Slide manufacturing

The production of thin metallic films on glass is well-known in the literature and gold coated cover slips with thicknesses as low as 10 nm can be bought from Aldrich. But, the deposition of gold on glass is not straightforward as the adhesion of noble metals on glass is poor. Thus, gold coatings with thicknesses lower than 10 nm are not commercials. The Watchlive start-up initially provided us with some BALM slides with 5 nm of gold. Due to the very large number of tests necessary for this work and the many different configurations used, it was decided to produce the coatings in the laboratory. More than 600 slides were necessary.

After the production of the gold coated glass slides, we characterized the deposited thickness by AFM. The rugosity and electrical conductivity of the coatings were also analyzed in some representative cases as they both relate to the continuity of the gold layer. Rugosity was around 0.3 nm RMS (extracted on 2*2 µm AFM images) for classical BALM slide, which is the resolution limit of our AFM. 2-probes electrical conductivity was quickly evaluated using a conventional multimeter. The obtained value for the typical BALM slides used for electrochemical experiments is around few ohms at the mm scale. This value was our reference for the different production methods. Note that less conductive substrates, which cannot be used for electrochemistry can still provide improved contrast in other types of experiments.

The most important parameter influencing the adhesion of metals on glass is the cleanliness of the glass surface prior deposition. Many different methods are used in the literature such as cleaning in a Piranha solution, in KOH, etc. We decided to clean the glass slides following a procedure developed in the laboratory by a former student (Thesis of T. Bourgeteau [343]):

- Sonication for 10 min at maximal power in Deionized (DI) water with soap (diluted

commercial Decon)

- Rinsing thoroughly with DI water
- Sonication for 10 min in DI water (twice)
- Rinsing with ethanol
- Sonication for 10 min in acetone
- Sonication for 10 min in isopropanol
- Drying with N_2
- 15 min UV-ozone cleaner
- Immediate use

The BALM anti-reflective coating (chromium + gold) was deposited directly after the cleaning process by thermal evaporation using a Joule heating system (Plassys). The deposition was always performed at a pressure below 5.10^{-6} mbar pressure and the deposition speed rate (monitored by a quartz crystal microbalance) was kept around 0.1 nm/s. After several tests, the minimal thickness of chromium to obtain a satisfactory adhesion with our equipment was found at 0.5 nm. For some experiments, the gold thickness was decreased to the minimum possible. It was found that 3 nm gold produces continuous films which are electrically conductive. Lower thicknesses presented higher electrical resistivity corresponding to poorly percolating gold particles.

In order to get rid of chromium notably for its highly light absorbing properties and possible impact on electrochemical experiments, we tried other methods. First, we investigated the use of silane-based SAMs which are known to self-assemble on glass and support the deposition of gold. We performed the vapor deposition of (3-aminopropyl)-trimethoxysilane. The cleaned glass slides and the silane solution were placed in a vacuum chamber, pumped to few mbars, closed for 30 s, pumped again and closed for 30 s. Finally, the slides were removed and directly placed in the thermal evaporator for gold only deposition. Using this method, the minimal gold thickness required to have a continuous film was 5 nm. Unfortunately, such coating was is not stable within the electrochemical reduction window described previously nor in acidic media. Therefore we preferred to keep the 0.5 nm Cr + 3 nm Au coating. But the above described method can nevertheless be used for other experiments if necessary.

Finally, we also investigated sputter deposition of gold using an equiment dedicated to the metallization of SEM samples. We succeeded in depositing continuous gold films with a 5 nm thickness but the repeatability was too low.

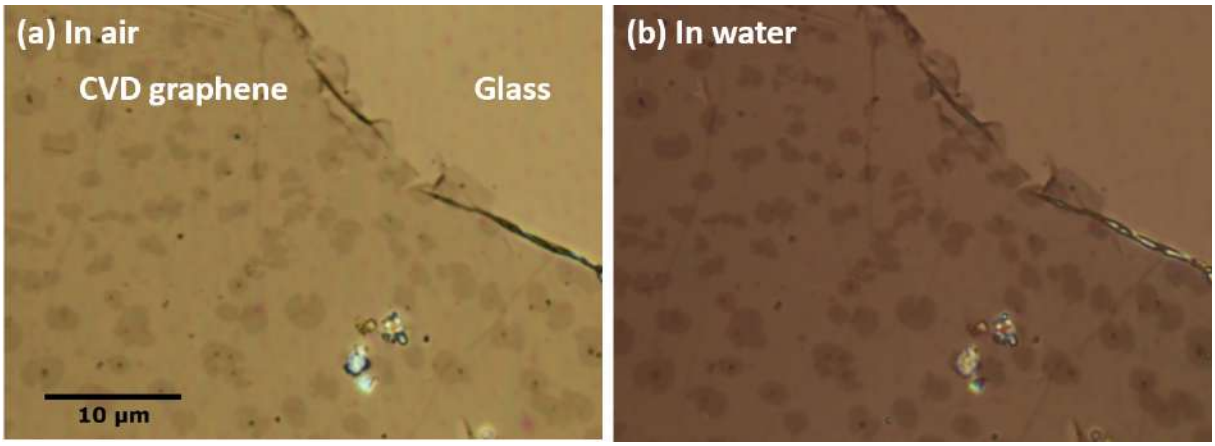

Figure Exp.1: Images of CVD graphene on glass using the same inverted microscope as BALM, **(a)** in air, **(b)** in water.

As mentioned in the conclusion, we studied 2D materials as ARA layer. To do so, we deposited high-quality CVD grown graphene directly on glass and we image the sample using the same BALM microscope (without the metallic coating). Images of graphene on glass in air and in water are presented in Fig. Exp.1. Mono- and multi-layers are darker than glass, thus it could be used as ARA layer in the inverted configuration. More uniform layers (without 2nd layer islands) would be needed to use such substrate for the observation of other 2D materials deposited on top.

Synthesis and transfer of 2D materials

Graphene oxide synthesis. GO was prepared as described by Morimoto *et al.* [344] Graphite (3 g) was added to H_2SO_4 (75 mL) and then $KMnO_4$ (9 g) was slowly added at 0°C under continuous stirring without exceeding 5°C. The mixture was kept at 35°C for 2 h before quenching with water (75 mL) under vigorous stirring and cooling so that temperature does not exceed 50°C. Finally, H_2O_2 (7.5 mL) was slowly added to the mixture cooled at 0°C. It was then purified by centrifugation until the pH became neutral and a small part of the final GO solution was freeze dried to measure the mass concentration.

Graphene oxide transfer by the bubble technique. This deposition method was developed and applied to GO by Joël Azevedo during his thesis. [345] A mixture of 0.8 mg/mL GO in water (using the final GO synthesis solution) with SDBS (Sodium dodecylbenzenesulfonate) at 1 CMC was prepared. Using a pipette, a semispherical bubble of this dispersion was deposited in a special chamber and let to drain for 30

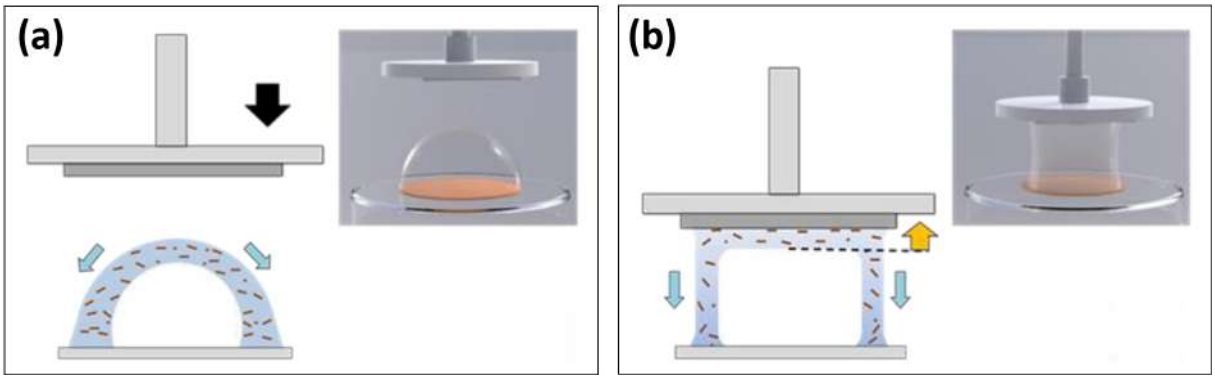

Figure Exp.2: GO transfer by the bubble technique. **(a)** A bubble of water and surfactant containing GO flakes is drained for 30 s, **(b)** the BALM substrate is placed up-side down on the bubble for GO deposition.

seconds. Then the substrate was slowly placed in contact with the top of the bubble and removed once the bubble blown up, as presented in Fig. Exp.2. The substrate was heated at 70°C for 10 min, the surfactant was eliminated of water, and finally the substrate was heated at 70°C for 10 min.

This deposition method was originally developed for oxidized silicon wafers therefore it has to be adapted to gold substrates which do not have the same surface properties. Though it remains more difficult to obtain un-folded / non-aggregated large flakes on BALM slides than on Si/SiO_2 and the method has to be continuously adapted.

MoS_2 and WS_2 CVD. The following synthesis is conventional in literature and has been progressively optimized at Licsen by several persons. A detailed description can notably be found in the thesis of H. Cassademont [346] The growth takes place in a quartz tube inserted in a single-chamber tubular oven, as presented in Fig. Exp.3. In the center of the tube, a crucible containing MoO_3 or WO_3 powder is covered with the target Si/SiO_2 sample (facing downward). The sample was previously covered by a thin film of PTAS (Perylene-3,4,9,10-tetracarboxylic acid tetrapotassium salt) which acts as a growth promoter. A second crucible containing sulfur powder is placed upstream at an adjustable distance d of the sample. The tube is thoroughly flushed with dry nitrogen, closed and brought to an adjusted nitrogen pressure. The nitrogen flow during the growth is measured by a flowmeter at the tube exit. The temperature in the center of the tube is ramped-up to T_{MAX} (650-800°C range) at 10°C/min. By adjusting the distance d, the sulfur temperature T_S is finely tuned (in the 150-250°C) range.

Obviously, there are a lot of adjustable parameters (PTAS thickness, N_2 pressure, N_2

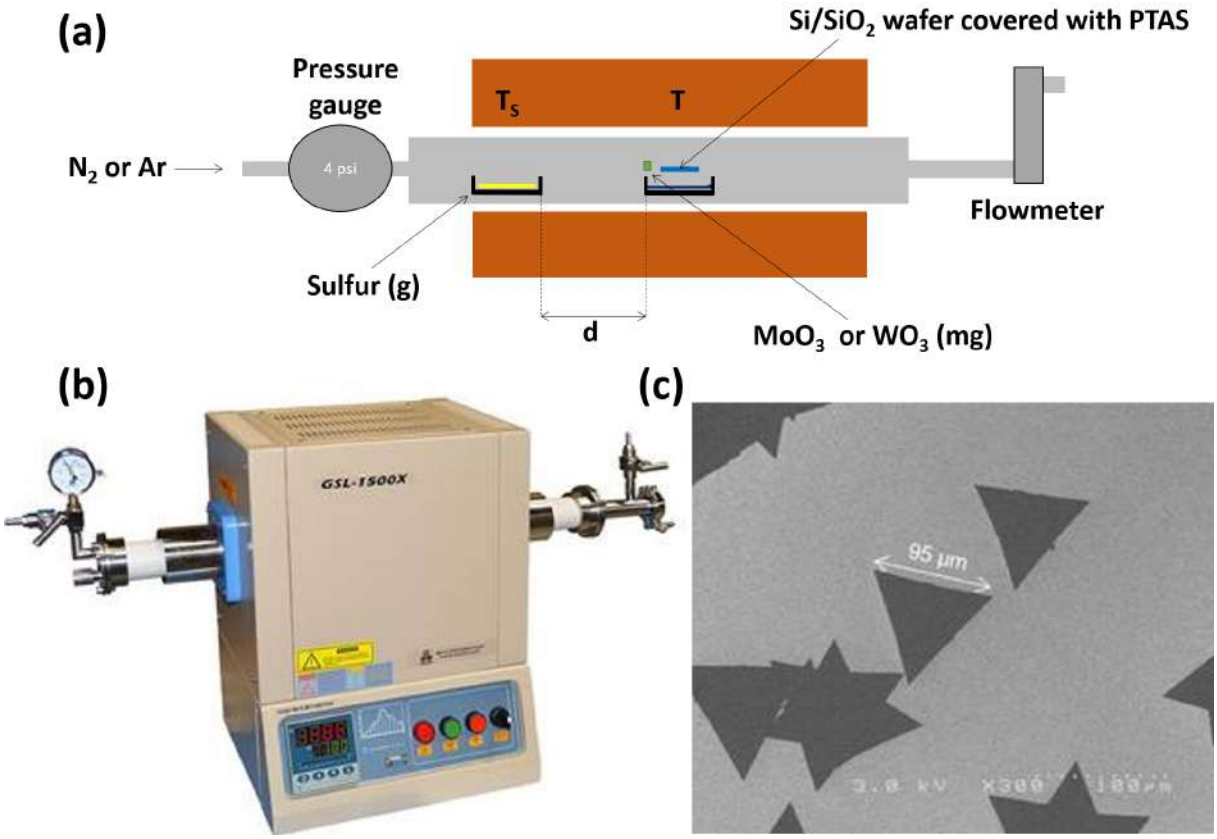

Figure Exp.3: CVD synthesis of MoS_2 and WS_2. (a) Schematic of the CVD synthesis, **(b)** picture of the CVD oven, **(c)** SEM image of large single-layer MoS_2 domains.

flow, T_{MAX}, T_S, mass of MoO_3 or WO_3, mass of S, growth time, sample-to-MoO_3 or WO_3 distance, etc.) that must be precisely adjusted to obtain single-layer MoS_2/WS_2 domains of large size (> 10 µm) and good crystallinity. The values of T_{MAX}, T_S and the N_2 pressure are particularly critical to insure the correct balance of the compounds in the gas phase. The sample surface treatments (and PTAS deposition conditions) are equally critical as they allow (or prevent) the seeding (nucleation) and lateral growth processes.

The study started at Licsen several years ago and its optimization is still ongoing. The grown materials are observed by optical microscopy, AFM and SEM as presented in Fig. Exp.3.c. Several samples were also studied by XPS, SECM [5], Raman, transport measurements, High-resolution TEM (CEA-Grenoble), photoluminescence (CEA-Grenoble) and KPFM (GeePs).

TMD transfer by PMMA coating. This transfer method is well described in the literature and a schematic is presented in Fig. Exp.4. TMDs were grown on Si/SiO_2 wafers therefore SiO_2 served as a sacrificial layer to free the TMD / PMMA membrane.

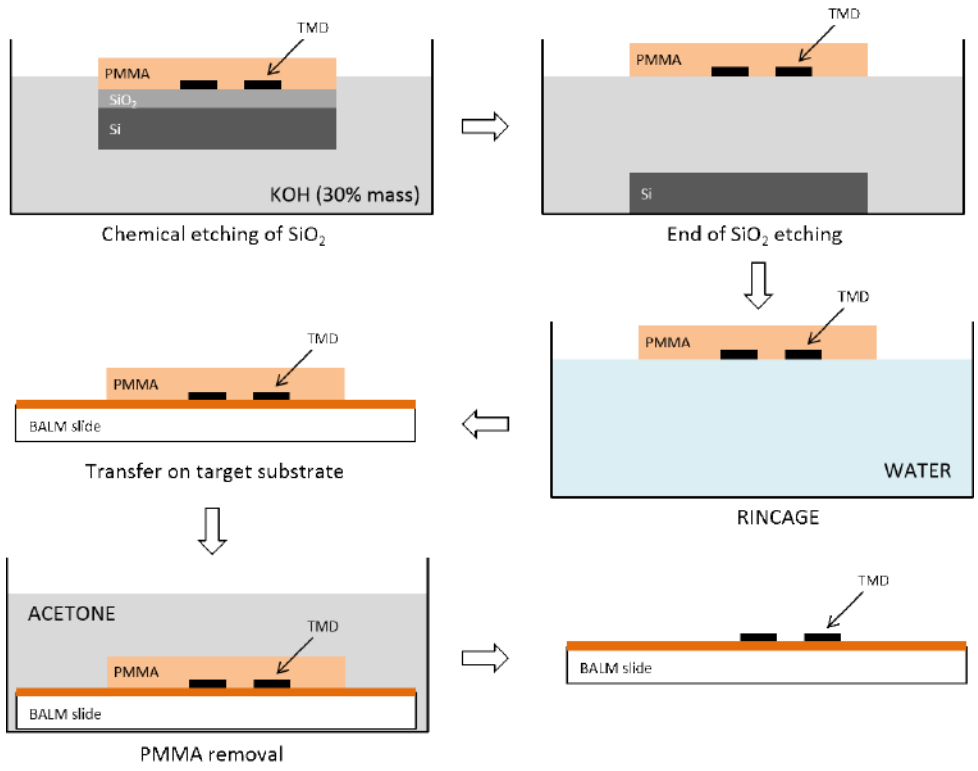

Figure Exp.4: Schematic of TMD transfer by PMMA coating.

In practice, PMMA is spin-coated on the wafer and is then placed in a KOH mixture (30% mass) to etch the SiO_2 layer. The PMMA membrane stays at the surface and is transferred in fresh water (at least twice) to remove KOH. Finally, the membrane is transferred to the target substrate, dried and placed in acetone to remove the PMMA which leaves the substrate with the TMDs domains at the surface.

BALM set-up and data analysis programs

BALM set-up. The inverted microscope is a Reitchert MeF3 A equipped with an halogen lamp (64655 HLX from Osram), a 63x oil immersion objective (HCX PL APO 63x/1.4 from Leica) and a Canon EOS 6D camera. When needed, the light was filtered by band-pass filters (10 nm FWHM) or optical density filters from Edmund optics. The light power sent to the interface is high as the reflected light is minimal, thus we tentatively measured the potential temperature evolution of the BALM slide surface using an home-made micro-fabricated resistive thermometer (produced by e-beam lithography on a glass slide). The electrical resistivity of the resistive wire was monitored while the light power was increased to its maximum. The thermometer was calibrated in a temperature controlled probe station. On the BALM microscope, no increase in tem-

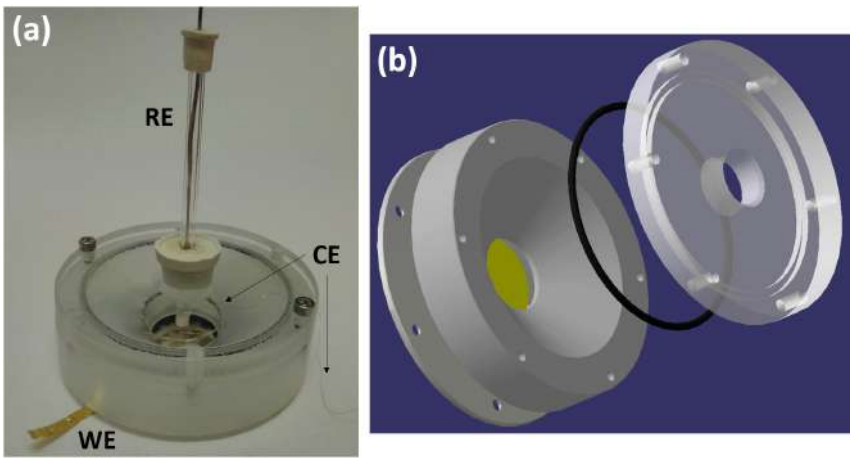

Figure Exp.5: BALM cell (b) in electrochemical configuration, **(c)** exploded view of the cell.

perature was measured, nonetheless as a precaution, we decided to add a band-pass filter (FESH0700 from Thorlabs), keeping only the 400-700 nm range to remove the near infrared part of the spectrum emitted by the halogen lamp.

The electrochemical cell was fabricated from Kel-F (3M), a polychlorotrifluoroethylene polymer which is highly resistant to chemicals and easy to process. The cell volume is at least 10 mL. We initially used a Viton o-ring seal to hold the BALM slide in the cell which is fine for water experiments but Viton swells when exposed to acetonitrile. We mostly used EPDM seals for ACN experiments as PTFE seals are not usable due to their low elasticity which occasionally induced leaks. The top side of the cell is closed with a glass window and sealed with a Viton o-ring. During electrochemical experiments, the BALM slide is connected to the potentiostat (SP-300 from Biologic) by a gold foil and the counter electrode is made from a platinum mesh, as presented in Fig. Exp.5. The hole in the center of the glass window serves to add the reference electrode to the cell as well as a gas pipe for experiments in controlled atmosphere.

Data analysis programs. The presented experiments required the development of several programs.

As an example, the most used one extracts the RGB values from movies and sequences of images in selected areas. It uses *Mathematica* to import the data, averages the RGB values (or work with a single color channel depending on the experiments) for the studied area and for each images, then the averaged values are exported as excel files with the corresponding time or image number for each value. The code for movies is as follows:

```
1- Direction = "C:.....";  %% file location
2- name = ;  %% file name without the extension
3- z1x = ; z1y = ; z2x = ; z2y = ; z3x = ; z3y = ;  %% top / left pixel coordinates of the three studied areas
4- width = ;  %% width of the square areas
5- RGB = ;  %% 1 to select the red channel, 2 for green, 3 for blue and if nothing, average the three channels
6- SetDirectory[Direction];
7- tfilm = Import[""<>ToString[numerof]<>".MOV", "Duration"];  %% import the duration of the movie
8- liste = {"Area 1 x" z1x, "Area 1 y" z1y, "Area 2 x" z2x, "Area 2 y" z2y, "Area 3 x" z3x, "Area 3 y" z3y, "Area width" l, "Duration" tfilm};  %% set the first value of the lists
9- listez1 = {"Area 1"}; listez2 = {"Area 2"}; listez3 = {"Area 3"}; listet = {"Time"};
10- nbimage = Dimensions[Import[""<>ToString[name]<>".MOV", "Frames"]];
11- nbi = nbimage[[1]];  %% import the number of images in the movie
12- For[i = 1, i < (nbi + 1), i++,  %% feedback loop to process all images one by one
13-     Print[N[i/nbi*100]];  %% print the advancement at each processed images in percent
14-     imageI = Import[""<>ToString[name]<>".MOV", {"Data", i, i}];  %% import the image data to process
15-     zone1 = Take[imageI, {z1y, z1y + width}, {z1x, z1x + l}, {color}];
16-     zone2 = Take[imageI, {z2y, z2y + width}, {z2x, z2x + l}, {color}];
17-     zone3 = Take[imageI, {z3y, z3y + width}, {z3x, z3x + l}, {color}];  %% extract the selected RGB channel data from the three areas
18-     moy1 = N[Mean[Mean[Mean[zone1]]]];
19-     moy2 = N[Mean[Mean[Mean[zone2]]]];
20-     moy3 = N[Mean[Mean[Mean[zone3]]]];  %% average the data over the areas
21-     listez1 = Flatten[{listez1, moy1}];
22-     listez2 = Flatten[{listez2, moy2}];
23-     listez3 = Flatten[{listez3, moy3}];  %% implement the averaged value in a list
24-     time = N[(i - 1)*tfilm/nbi];  %% add the corresponding time of the extracted image
25-     listet = Flatten[{listet, time}];  %% implement the time in a list
26- ];
27- Export[""  <> ToString[name] <> ".xlsx", Join[{liste}, Transpose[{listet, listez1, listez2, listez3}]]];  %% export the lists in an excel file
```

The code for movies is easily modified for sequences of images by replacing the importation of data.

A Python program was created to extract averaged RGB values in selected ares directly from the computer screen with the camera feedback. We regularly used it as a first information of the success (or not) of an experiment. Indeed, the overnight *Mathematica* treatment of movies cannot be used alone to detect experimental anomalies (such as a connection issue to the potentiostat for example). The program takes screenshots of the camera feedback screen at 25 Hz, the averaged RGB values are extracted on a chosen area and displayed in real-time. The following code extracts the RGB values of three areas at the same time, the code (Python 2.7) is as follows:

```
1- from Tkinter import *
```

```
2- import ImageGrab
3- l = 25 %% width of the averaged area
4- x1 = 550
5- y1 = 400 %% top / left pixel coordinates of the averaged areas
6- def couleur():
7-      px = ImageGrab.grab().load()
8-      R = []
9-      G = []
10-     B = []
11-     for y in range(y1, y1+l):
12-         for x in range(x1, x1+l):
13-         color = px[x,y]
14-         R.extend([color[0]])
15-         G.extend([color[1]])
16-         B.extend([color[2]])
17-     mR = sum(R)/float(len(R))
18-     mG = sum(G)/float(len(G))
19-     mB = sum(B)/float(len(B))
20-     mGrey = (mR + mG + mB)/3
21-     moyR.set("%.2f" % (mR))
22-     moyG.set("%.2f" % (mG))
23-     moyB.set("%.2f" % (mB))
24-     moyGrey.set("%.2f" % (mGrey))
25-     Mafenetre.after(40,couleur)
26- Mafenetre = Tk()
27- Mafenetre.title('Color changes')
28- moyR = StringVar()
29- moyG = StringVar()
30- moyB = StringVar()
31- moyGrey = StringVar()
32- LabelR = Label(Mafenetre, textvariable = moyR, fg = 'red', bg = 'white')
33- LabelR.pack(side = LEFT, padx = 5, pady = 5)
34- LabelG = Label(Mafenetre, textvariable = moyG, fg = 'green', bg = 'white')
35- LabelG.pack(side = LEFT, padx = 5, pady = 5)
36- LabelB = Label(Mafenetre, textvariable = moyB, fg = 'blue', bg = 'white')
37- LabelB.pack(side = LEFT, padx = 5, pady = 5)
38- LabelGrey = Label(Mafenetre, textvariable = moyGrey, fg = 'grey', bg = 'white')
39- LabelGrey.pack(side = LEFT, padx = 5, pady = 5)
40- Bouton1 = Button(Mafenetre, text = 'Stop', command = Mafenetre.destroy)
41- Bouton1.pack(side = BOTTOM)
42- couleur()
43- Mafenetre.mainloop()
```

The program needs to be first edit with idle, then x/y modification if needed and finally F5 to start the program loop.

The synchronization of movies with electrochemical experiments was done using a *Labview* (2014, 14.0.1) program. Before the potentiostat starts, a 5 V output trigger

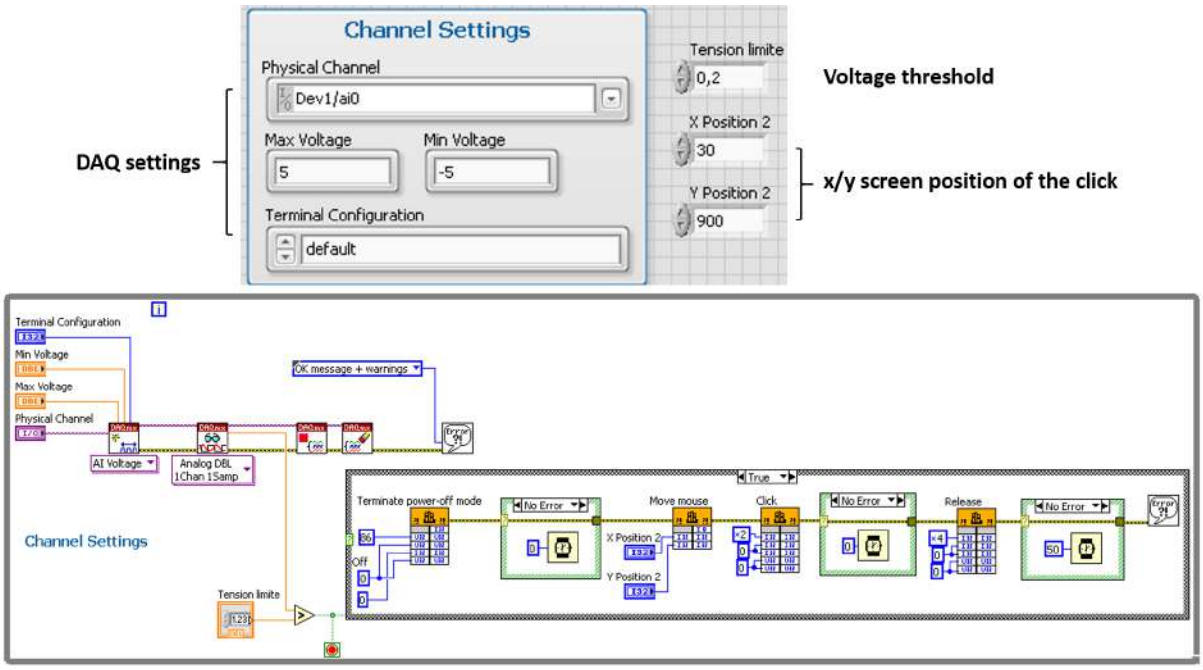

Figure Exp.6: Labview program for the synchronization of electrochemical experiments with the BALM movies.

signal is added and this trigger signal is read by the program using a DAQ from National Instruments, which starts the acquisition. The code is presented in Fig. Exp.6.

Finally, another *Mathematica* program was created to produce a movie from the electrochemical signal, as presented in Movie-6 and Movie-7. The applied potential and obtained current from the cyclic voltammetry experiments were saved in a text file. It was then imported by the program, a chain of images with E/I data was created and compiled as a movie. The code is as follows:

```
1- Direction = "C:.....";
2- name = ;
3- Potentialmax = ; Potentialmin = ; Currentmax = ; Currentmin = ; %% set the voltammogram limits
4- scanspeed = ; %% scan speed of the CV
5- nbpoint = ; %% number of points per seconds
6- fps = scanspeed/nbpoint;
7- SetDirectory[Direction];
8- listed = Import[""<>ToString[name]<>".txt", {"Data"}];
9- nbimage = Dimensions[listed];
10- nbi = nbimage[[1]];
11- liste = {};
12- For[i = 1, i < (nbi + 1), i = i + nbpoint,
13-      listea = {Take[listed, i]};
14-      liste = Catenate[{liste, listea}]; 15- ];
16- table = ListPlot[#, PlotRange → {{Potentialmin, Potentialmax}, {Currentmin, Currentmax}}, PlotStyle
→ {PointSize[.002], RGBColor[0, 0, 1]}] & /@ liste;
17- Export[""<>ToString[name]<>".avi", table, "FrameRate" → fps];
```

References

[1] K. Jaouen, R. Cornut, D. Ausserré, S. Campidelli, and V. Derycke, *Ideal optical contrast for 2D material observation using bi-layer antireflection absorbing substrates*, **Nanoscale**, 11 (13), 6129–6135, **2019**.
URL http://dx.doi.org/10.1039/C8NR09983A

[2] K. Jaouen, F. Lebon, B. Jousselme, S. Campidelli, R. Cornut, and V. Derycke, *Optical monitoring of diazonium electrografting on gold and graphene oxide using Backside Absorbing Layer Microscopy*, **Submitted**.

[3] S. Campidelli, R. Abou Khachfe, K. Jaouen, J. Monteiller, C. Amra, M. Zerrad, R. Cornut, V. Derycke, and D. Ausserré, *Backside absorbing layer microscopy: Watching graphene chemistry*, **Science Advances**, 3 (5), e1601724, **2017**.
URL http://dx.doi.org/10.1126/sciadv.1601724

[4] K. Jaouen, O. Henrotte, S. Campidelli, B. Jousselme, V. Derycke, and R. Cornut, *Localized electrochemistry for the investigation and the modification of 2D materials*, **Applied Materialstoday**, 8, 116–124, **2017**.
URL http://dx.doi.org/10.1016/j.apmt.2017.05.001

[5] O. Henrotte, T. Bottein, H. Casademont, K. Jaouen, T. Bourgeteau, S. Campidelli, V. Derycke, B. Jousselme, and R. Cornut, *Electronic Transport of MoS_2 Monolayered Flakes Investigated by Scanning Electrochemical Microscopy*, **Chemphyschem**, 18 (19), 2777–2781, **2017**.
URL http://dx.doi.org/10.1002/cphc.201700343

[6] A. K. Geim and K. S. Novoselov, *The rise of graphene*, **Nature Materials**, 6 (3), 183–191, **2007**.
URL http://dx.doi.org/10.1038/nmat1849

[7] Y. Zhu, S. Murali, W. Cai, X. Li, J. W. Suk, J. R. Potts, and R. S. Ruoff, *Graphene and Graphene Oxide: Synthesis, Properties, and Applications*, **Advanced Materials**, 22 (35), 3906–3924, **2010**.
URL http://dx.doi.org/10.1002/adma.201001068

[8] K. S. Novoselov, A. Mishchenko, A. Carvalho, and A. H. C. Neto, *2D materials and van der Waals heterostructures*, **Science**, 353 (6298), aac9439, **2016**.
URL http://dx.doi.org/10.1126/science.aac9439

[9] S. Z. Butler, S. M. Hollen, L. Cao, Y. Cui, J. A. Gupta, H. R. Gutiérrez, T. F. Heinz, S. S. Hong, J. Huang, A. F. Ismach, E. Johnston-Halperin, M. Kuno, V. V. Plashnitsa, R. D. Robinson, R. S. Ruoff, S. Salahuddin, J. Shan, L. Shi, M. G. Spencer, M. Terrones, W. Windl, and J. E. Goldberger, *Progress, Challenges, and Opportunities in Two-Dimensional Materials Beyond Graphene*, **ACS Nano**, 7 (4), 2898–2926, **2013**.
URL http://dx.doi.org/10.1021/nn400280c

[10] X. Huang, Z. Zeng, and H. Zhang, *Metal dichalcogenide nanosheets: preparation, properties and applications*, **Chemical Society Reviews**, 42 (5), 1934–1946, **2013**.
URL http://dx.doi.org/10.1039/C2CS35387C

[11] G. R. Bhimanapati, Z. Lin, V. Meunier, Y. Jung, J. Cha, S. Das, D. Xiao, Y. Son, M. S. Strano, V. R. Cooper, L. Liang, S. G. Louie, E. Ringe, W. Zhou, S. S. Kim, R. R. Naik, B. G. Sumpter, H. Terrones, F. Xia, Y. Wang, J. Zhu, D. Akinwande, N. Alem, J. A. Schuller, R. E. Schaak, M. Terrones, and J. A. Robinson, *Recent Advances in Two-Dimensional Materials beyond Graphene*, **ACS Nano**, 9 (12), 11509–11539, **2015**.
URL http://dx.doi.org/10.1021/acsnano.5b05556

[12] K. S. Novoselov, A. K. Geim, S. V. Morozov, D. Jiang, Y. Zhang, S. V. Dubonos, I. V. Grigorieva, and A. A. Firsov, *Electric Field Effect in Atomically Thin Carbon Films*, **Science**, 306 (5696), 666–669, **2004**.
URL http://dx.doi.org/10.1126/science.1102896

[13] H. Zhang, J. Huang, Y. Wang, R. Liu, X. Huai, J. Jiang, and C. Anfuso, *Atomic force microscopy for two-dimensional materials: A tutorial review*, **Optics Communications**, 406, 3–17, **2018**.
URL http://dx.doi.org/10.1016/j.optcom.2017.05.015

[14] I. Jung, M. Pelton, R. Piner, D. A. Dikin, S. Stankovich, S. Watcharotone, M. Hausner, and R. S. Ruoff, *Simple Approach for High-Contrast Optical Imaging and Characterization of Graphene-Based Sheets*, **Nano Letters**, 7 (12), 3569–3575, **2007**.
URL http://dx.doi.org/10.1021/nl0714177

[15] P. Braeuninger-Weimer, S. Funke, R. Wang, P. Thiesen, D. Tasche, W. Vioel, and S. Hofmann, *Fast, Noncontact, Wafer-Scale, Atomic Layer Resolved Imaging of Two-Dimensional Materials by Ellipsometric Contrast Micrography*, **Acs Nano**, 12 (8), 8555–8563, **2018**.
URL http://dx.doi.org/10.1021/acsnano.8b04167

[16] A. T. L. Tan, J. Kim, J.-K. Huang, L.-J. Li, and J. Huang, *Seeing Two-Dimensional Sheets on Arbitrary Substrates by Fluorescence Quenching Microscopy*, **Small**, 9 (19), 3253–3258, **2013**.
URL http://dx.doi.org/10.1002/smll.201300049

[17] P. Blake, E. W. Hill, A. H. Castro Neto, K. S. Novoselov, D. Jiang, R. Yang, T. J. Booth, and A. K. Geim, *Making graphene visible*, **Applied Physics Letters**, 91 (6), 063124, **2007**.
URL http://dx.doi.org/10.1063/1.2768624

[18] D. S. L. Abergel, A. Russell, and V. I. Fal'ko, *Visibility of graphene flakes on a dielectric substrate*, **Applied Physics Letters**, 91 (6), 063125, **2007**.
URL http://dx.doi.org/10.1063/1.2768625

[19] K. F. Mak, C. Lee, J. Hone, J. Shan, and T. F. Heinz, *Atomically Thin MoS_2: A New Direct-Gap Semiconductor*, **Physical Review Letters**, 105 (13), 136805, **2010**.
URL http://dx.doi.org/10.1103/PhysRevLett.105.136805

[20] L. Li, Y. Yu, G. J. Ye, Q. Ge, X. Ou, H. Wu, D. Feng, X. H. Chen, and Y. Zhang, *Black phosphorus field-effect transistors*, **Nature Nanotechnology**, 9 (5), 372–377, **2014**.
URL http://dx.doi.org/10.1038/nnano.2014.35

[21] D. J. Late, B. Liu, H. S. S. R. Matte, C. N. R. Rao, and V. P. Dravid, *Rapid Characterization of Ultrathin Layers of Chalcogenides on SiO_2/Si Substrates*, **Advanced Functional Materials**, 22 (9), 1894–1905, **2012**.
URL http://dx.doi.org/10.1002/adfm.201102913

[22] I. Jung, M. Vaupel, M. Pelton, R. Piner, D. A. Dikin, S. Stankovich, J. An, and R. S. Ruoff, *Characterization of thermally reduced graphene oxide by imaging ellipsometry*, **Journal of Physical Chemistry C**, 112 (23), 8499–8506, **2008**.
URL http://dx.doi.org/10.1021/jp802173m

[23] O. Albrektsen, R. L. Eriksen, S. M. Novikov, D. Schall, M. Karl, S. I. Bozhevolnyi, and A. C. Simonsen, *High resolution imaging of few-layer graphene*, **Journal of Applied Physics**, 111 (6), 064305, **2012**.
URL http://dx.doi.org/10.1063/1.3694660

[24] J. Kim, F. Kim, and J. Huang, *Seeing graphene-based sheets*, **Materials Today**, 13 (3), 28–38, **2010**.
URL http://dx.doi.org/10.1016/S1369-7021(10)70031-6

[25] E. Treossi, M. Melucci, A. Liscio, M. Gazzano, P. Samorì, and V. Palermo, *High-Contrast Visualization of Graphene Oxide on Dye-Sensitized Glass, Quartz, and Silicon by Fluorescence Quenching*, **Journal of the American Chemical Society**, 131 (43), 15576–15577, **2009**.
URL http://dx.doi.org/10.1021/ja9055382

[26] J. R. Kyle, A. Guvenc, W. Wang, M. Ghazinejad, J. Lin, S. Guo, C. S. Ozkan, and M. Ozkan, *Centimeter-Scale High-Resolution Metrology of Entire CVD-Grown Graphene Sheets*, **Small**, 7 (18), 2599–2606, **2011**.
URL http://dx.doi.org/10.1002/smll.201100263

[27] J. R. Kyle, C. S. Ozkan, and M. Ozkan, *Industrial graphene metrology*, **Nanoscale**, 4 (13), 3807–3819, **2012**.
URL http://dx.doi.org/10.1039/c2nr30093a

[28] R. J. Stöhr, R. Kolesov, K. Xia, R. Reuter, J. Meijer, G. Logvenov, and J. Wrachtrup, *Super-resolution Fluorescence Quenching Microscopy of Graphene*, **ACS Nano**, 6 (10), 9175–9181, **2012**.
URL http://dx.doi.org/10.1021/nn303510p

[29] R. Li, P. Georgiades, H. Cox, S. Phanphak, I. S. Roberts, T. A. Waigh, and J. R. Lu, *Quenched Stochastic Optical Reconstruction Microscopy (qSTORM) with Graphene Oxide*, **Scientific Reports**, 8, 16928, **2018**.
URL http://dx.doi.org/10.1038/s41598-018-35297-4

[30] D. Bing, Y. Wang, J. Bai, R. Du, G. Wu, and L. Liu, *Optical contrast for identifying the thickness of two-dimensional materials*, **Optics Communications**, 406, 128–138, **2018**.
URL http://dx.doi.org/10.1016/j.optcom.2017.06.012

[31] X. Lin, Z. Si, W. Fu, J. Yang, S. Guo, Y. Cao, J. Zhang, X. Wang, P. Liu, K. Jiang, and W. Zhao, *Intelligent identification of two-dimensional nanostructures by machine-learning optical microscopy*, **Nano Research**, 11 (12), 6316–6324, **2018**.
URL http://dx.doi.org/10.1007/s12274-018-2155-0

[32] Y.-L. Liu, C.-C. Yu, K.-T. Lin, E.-Y. Wang, T.-C. Yang, H.-L. Chen, C.-W. Chen, C.-K. Chang, L.-C. Chen, and K.-H. Chen, *Nondestructive Characterization of the Structural Quality and Thickness of Large-Area Graphene on Various Substrates*, **Analytical Chemistry**, 86 (15), 7192–7199, **2014**.
URL http://dx.doi.org/10.1021/ac501557c

[33] H. Arjmandi-Tash, L. Jiang, and G. F. Schneider, *Rupture index: A quantitative measure of sub-micrometer cracks in graphene*, **Carbon**, 118, 556–560, **2017**.
URL http://dx.doi.org/10.1016/j.carbon.2017.03.054

[34] X. H. Kong, H. X. Ji, R. D. Piner, H. F. Li, C. W. Magnuson, C. Tan, A. Ismach, H. Chou, and R. S. Ruoff, *Non-destructive and rapid evaluation of chemical vapor deposition graphene by dark field optical microscopy*, **Applied Physics Letters**, 103 (4), 043119, **2013**.
URL http://dx.doi.org/10.1063/1.4816752

[35] X. Wu, G. Zhong, and J. Robertson, *Nondestructive optical visualisation of graphene domains and boundaries*, **Nanoscale**, 8 (36), 16427–16434, **2016**.
URL http://dx.doi.org/10.1039/C6NR04642H

[36] D. Ding, H. Hibino, and H. Ago, *Grain Boundaries and Gas Barrier Property of Graphene Revealed by Dark-Field Optical Microscopy*, **The Journal of Physical Chemistry C**, 122 (1), 902–910, **2018**.
URL http://dx.doi.org/10.1021/acs.jpcc.7b10210

[37] W. Li, S. Moon, M. Wojcik, and K. Xu, *Direct Optical Visualization of Graphene and Its Nanoscale Defects on Transparent Substrates*, **Nano Letters**, 16 (8), 5027–5031, **2016**.
URL http://dx.doi.org/10.1021/acs.nanolett.6b01804

[38] D. Akinwande, C. J. Brennan, J. S. Bunch, P. Egberts, J. R. Felts, H. Gao, R. Huang, J.-S. Kim, T. Li, Y. Li, K. M. Liechti, N. Lu, H. S. Park, E. J. Reed, P. Wang, B. I. Yakobson, T. Zhang, Y.-W. Zhang, Y. Zhou, and Y. Zhu, *A review on mechanics and mechanical properties of 2D materials—Graphene and beyond*, **Extreme Mechanics Letters**, 13, 42–77, **2017**.
URL http://dx.doi.org/10.1016/j.eml.2017.01.008

[39] K. Liu and J. Wu, *Mechanical properties of two-dimensional materials and heterostructures*, **Journal of Materials Research**, 31 (7), 832–844, **2016**.
URL http://dx.doi.org/10.1557/jmr.2015.324

[40] J. H. Kim, J. H. Jeong, N. Kim, R. Joshi, and G.-H. Lee, *Mechanical properties of two-dimensional materials and their applications*, **Journal of Physics D: Applied Physics**, 52 (8), 083001, **2018**.
URL http://dx.doi.org/10.1088/1361-6463/aaf465

[41] X. Li, M. Sun, C. Shan, Q. Chen, and X. Wei, *Mechanical Properties of 2D Materials Studied by In Situ Microscopy Techniques*, **Advanced Materials Interfaces**, 5 (5), 1701246, **2018**.
URL http://dx.doi.org/10.1002/admi.201701246

[42] K. Elibol, B. C. Bayer, S. Hummel, J. Kotakoski, G. Argentero, and J. C. Meyer, *Visualising the strain distribution in suspended two-dimensional materials under local deformation*, **Scientific Reports**, 6, 28485, **2016**.
URL http://dx.doi.org/10.1038/srep28485

[43] A. I. Altan and J. Chen, *In situ chemical probing of hole defects and cracks in graphene at room temperature*, **Nanoscale**, 10 (23), 11052–11063, **2018**.
URL http://dx.doi.org/10.1039/C8NR03109F

[44] D.-M. Tang, D. G. Kvashnin, S. Najmaei, Y. Bando, K. Kimoto, P. Koskinen, P. M. Ajayan, B. I. Yakobson, P. B. Sorokin, J. Lou, and D. Golberg, *Nanomechanical cleavage of molybdenum disulphide atomic layers*, **Nature Communications**, 5, 3631, **2014**.
URL http://dx.doi.org/10.1038/ncomms4631

[45] D. L. Duong, G. H. Han, S. M. Lee, F. Gunes, E. S. Kim, S. T. Kim, H. Kim, Q. H. Ta, K. P. So, S. J. Yoon, S. J. Chae, Y. W. Jo, M. H. Park, S. H. Chae, S. C. Lim, J. Y. Choi, and Y. H. Lee, *Probing graphene grain boundaries with optical microscopy*, **Nature**, 490 (7419), 235–239, **2012**.
URL http://dx.doi.org/10.1038/nature11562

[46] J. Wang, X. Xu, R. Qiao, J. Liang, C. Liu, B. Zheng, L. Liu, P. Gao, Q. Jiao, D. Yu, Y. Zhao, and K. Liu, *Visualizing grain boundaries in monolayer $MoSe_2$ using mild H_2O vapor etching*, **Nano Research**, 11 (8), 4082–4089, **2018**.
URL http://dx.doi.org/10.1007/s12274-018-1991-2

[47] X. Fan, S. Wagner, P. Schädlich, F. Speck, S. Kataria, T. Haraldsson, T. Seyller, M. C. Lemme, and F. Niklaus, *Direct observation of grain boundaries in graphene through vapor hydrofluoric acid (VHF) exposure*, **Science Advances**, 4 (5), eaar5170, **2018**.
URL http://dx.doi.org/10.1126/sciadv.aar5170

[48] T. H. Ly, D. L. Duong, Q. H. Ta, F. Yao, Q. A. Vu, H. Y. Jeong, S. H. Chae, and Y. H. Lee, *Nondestructive Characterization of Graphene Defects*, **Advanced Functional Materials**, 23 (41), 5183–5189, **2013**.
URL http://dx.doi.org/10.1002/adfm.201300493

[49] T. H. Ly, M.-H. Chiu, M.-Y. Li, J. Zhao, D. J. Perello, M. O. Cichocka, H. M. Oh, S. H. Chae, H. Y. Jeong, F. Yao, L.-J. Li, and Y. H. Lee, *Observing Grain Boundaries in CVD-Grown Monolayer Transition Metal Dichalcogenides*, **ACS Nano**, 8 (11), 11401–11408, **2014**.
URL http://dx.doi.org/10.1021/nn504470q

[50] Y. Rong, K. He, M. Pacios, A. W. Robertson, H. Bhaskaran, and J. H. Warner, *Controlled Preferential Oxidation of Grain Boundaries in Monolayer Tungsten Disulfide for Direct Optical Imaging*, **ACS Nano**, 9 (4), 3695–3703, **2015**.
URL http://dx.doi.org/10.1021/acsnano.5b00852

[51] D.-W. Shin, D. Sung, J. S. Hong, M. Kim, S. S. Yoon, Y.-J. Song, G. Kim, S. Hong, and J.-B. Yoo, *Observation of graphene grain boundaries through selective adsorption of rhodamine B using fluorescence microscopy*, **Carbon**, 108, 72–78, **2016**.
URL http://dx.doi.org/10.1016/j.carbon.2016.07.001

[52] S. U. Yu, B. Park, Y. Cho, S. Hyun, J. K. Kim, and K. S. Kim, *Simultaneous Visualization of Graphene Grain Boundaries and Wrinkles with Structural Information by Gold Deposition*, **ACS Nano**, 8 (8), 8662–8668, **2014**.
URL http://dx.doi.org/10.1021/nn503550d

[53] H. Goncalves, M. Belsley, C. Moura, T. Stauber, and P. Schellenberg, *Enhancing visibility of graphene on arbitrary substrates by microdroplet condensation*, **Applied Physics Letters**, 97 (23), 231905, **2010**.
URL http://dx.doi.org/10.1063/1.3527081

[54] D. W. Kim, Y. H. Kim, H. S. Jeong, and H.-T. Jung, *Direct visualization of large-area graphene domains and boundaries by optical birefringency*, **Nature Nanotechnology**, 7 (1), 29–34, **2012**.
URL http://dx.doi.org/10.1038/nnano.2011.198

[55] J.-H. Son, S.-J. Baeck, M.-H. Park, J.-B. Lee, C.-W. Yang, J.-K. Song, W.-C. Zin, and J.-H. Ahn, *Detection of graphene domains and defects using liquid crystals*, **Nature Communications**, 5, 3484, **2014**.
URL http://dx.doi.org/10.1038/ncomms4484

[56] M. A. Shehzad, S. Hussain, J. Lee, J. Jung, N. Lee, G. Kim, and Y. Seo, *Study of Grains and Boundaries of Molybdenum Diselenide and Tungsten Diselenide Using Liquid Crystal*, **Nano Letters**, 17 (3), 1474–1481, **2017**.
URL http://dx.doi.org/10.1021/acs.nanolett.6b04491

[57] D. W. Kim, J. M. Ok, W.-B. Jung, J.-S. Kim, S. J. Kim, H. O. Choi, Y. H. Kim, and H.-T. Jung, *Direct Observation of Molybdenum Disulfide, MoS_2, Domains by Using a Liquid Crystalline Texture Method*, **Nano Letters**, 15 (1), 229–234, **2015**.
URL http://dx.doi.org/10.1021/nl5034528

[58] G. Yang and J. Kim, *Probing patterned defects on graphene using differential interference contrast observation*, **Applied Physics Letters**, 106 (8), 081901, **2015**.
URL http://dx.doi.org/10.1063/1.4908289

[59] H. Ago, S. Fukamachi, H. Endo, P. Solís-Fernández, R. Mohamad Yunus, Y. Uchida, V. Panchal, O. Kazakova, and M. Tsuji, *Visualization of Grain Structure and Boundaries of Polycrystalline Graphene and Two-Dimensional Materials by Epitaxial Growth of Transition Metal Dichalcogenides*, **ACS Nano**, 10 (3), 3233–3240, **2016**.
URL http://dx.doi.org/10.1021/acsnano.5b05879

[60] X. Liu, B. Qiu, Q. Chen, Z. Ni, Y. Jiang, M. Long, and L. Gui, *Characterization of graphene layers using super resolution polarization parameter indirect microscopic imaging*, **Optics Express**, 22 (17), 20446–20456, **2014**.
URL http://dx.doi.org/10.1364/OE.22.020446

[61] K. S. Novoselov, D. Jiang, F. Schedin, T. J. Booth, V. V. Khotkevich, S. V. Morozov, and A. K. Geim, *Two-dimensional atomic crystals*, **Proceedings of the National Academy of Sciences**, 102 (30), 10451–10453, **2005**.
URL http://dx.doi.org/10.1073/pnas.0502848102

[62] M. H. Gass, U. Bangert, A. L. Bleloch, P. Wang, R. R. Nair, and A. K. Geim, *Free-standing graphene at atomic resolution*, **Nature Nanotechnology**, 3 (11), 676–681, **2008**.
URL http://dx.doi.org/10.1038/nnano.2008.280

[63] S. H. Dave, C. Gong, A. W. Robertson, J. H. Warner, and J. C. Grossman, *Chemistry and Structure of Graphene Oxide via Direct Imaging*, **ACS Nano**, 10 (8), 7515–7522, **2016**.
URL http://dx.doi.org/10.1021/acsnano.6b02391

[64] A. Hashimoto, K. Suenaga, A. Gloter, K. Urita, and S. Iijima, *Direct evidence for atomic defects in graphene layers*, **Nature**, 430 (7002), 870, **2004**.
URL http://dx.doi.org/10.1038/nature02817

[65] J. Kotakoski, A. V. Krasheninnikov, U. Kaiser, and J. C. Meyer, *From Point Defects in Graphene to Two-Dimensional Amorphous Carbon*, **Physical Review Letters**, 106 (10), 105505, **2011**.
URL http://dx.doi.org/10.1103/PhysRevLett.106.105505

[66] H. Wang, K. Li, Y. Cheng, Q. Wang, Y. Yao, U. Schwingenschlögl, X. Zhang, and W. Yang, *Interaction between single gold atom and the graphene edge: A study via aberration-corrected transmission electron microscopy*, **Nanoscale**, 4 (9), 2920–2925, **2012**.
URL http://dx.doi.org/10.1039/C2NR00059H

[67] X. Zhang, Z. Jin, L. Wang, J. A. Hachtel, E. Villarreal, Z. Wang, T. Ha, Y. Nakanishi, C. S. Tiwary, J. Lai, L. Dong, J. Yang, R. Vajtai, E. Ringe, J. C. Idrobo, B. I. Yakobson, J. Lou, V. Gambin, R. Koltun, and P. M. Ajayan, *Low Contact Barrier in 2H/1T' $MoTe_2$ In-Plane Heterostructure Synthesized by Chemical Vapor Deposition*, **ACS Applied Materials & Interfaces**, 11 (13), 12777–12785, **2019**.
URL http://dx.doi.org/10.1021/acsami.9b00306

[68] L. Brown, R. Hovden, P. Huang, M. Wojcik, D. A. Muller, and J. Park, *Twinning and Twisting of Tri- and Bilayer Graphene*, **Nano Letters**, 12 (3), 1609–1615, **2012**.
URL http://dx.doi.org/10.1021/nl204547v

[69] Y.-C. Lin, D. O. Dumcenco, H.-P. Komsa, Y. Niimi, A. V. Krasheninnikov, Y.-S. Huang, and K. Suenaga, *Properties of Individual Dopant Atoms in Single-Layer MoS_2: Atomic Structure, Migration, and Enhanced Reactivity*, **Advanced Materials**, 26 (18), 2857–2861, **2014**.
URL http://dx.doi.org/10.1002/adma.201304985

[70] R. G. Mendes, J. Pang, A. Bachmatiuk, H. Q. Ta, L. Zhao, T. Gemming, L. Fu, Z. Liu, and M. H. Rümmeli, *Electron-Driven In Situ Transmission Electron Microscopy of 2D Transition Metal Dichalcogenides and Their 2D Heterostructures*, **ACS Nano**, 13 (2), 978–995, **2019**.
URL http://dx.doi.org/10.1021/acsnano.8b08079

[71] C. Luo, C. Wang, X. Wu, J. Zhang, and J. Chu, *In Situ Transmission Electron Microscopy Characterization and Manipulation of Two-Dimensional Layered Materials beyond Graphene*, **Small**, 13 (35), 1604259, **2017**.
URL http://dx.doi.org/10.1002/smll.201604259

[72] D. Graf, F. Molitor, K. Ensslin, C. Stampfer, A. Jungen, C. Hierold, and L. Wirtz, *Spatially resolved raman spectroscopy of single- and few-layer graphene*, **Nano Letters**, 7 (2), 238–242, **2007**.
URL http://dx.doi.org/10.1021/nl061702a

[73] R. W. Havener, S.-Y. Ju, L. Brown, Z. Wang, M. Wojcik, C. S. Ruiz-Vargas, and J. Park, *High-Throughput Graphene Imaging on Arbitrary Substrates with Widefield Raman Spectroscopy*, **ACS Nano**, 6 (1), 373–380, **2012**.
URL http://dx.doi.org/10.1021/nn2037169

[74] F. Schedin, E. Lidorikis, A. Lombardo, V. G. Kravets, A. K. Geim, A. N. Grigorenko, K. S. Novoselov, and A. C. Ferrari, *Surface-Enhanced Raman Spectroscopy of Graphene*, **ACS Nano**, 4 (10), 5617–5626, **2010**.
URL http://dx.doi.org/10.1021/nn1010842

[75] X. Ling, L. Xie, Y. Fang, H. Xu, H. Zhang, J. Kong, M. S. Dresselhaus, J. Zhang, and Z. Liu, *Can Graphene be used as a Substrate for Raman Enhancement?*, **Nano Letters**, 10 (2), 553–561, **2010**.
URL http://dx.doi.org/10.1021/nl903414x

[76] N. Zhang, L. Tong, and J. Zhang, *Graphene-Based Enhanced Raman Scattering toward Analytical Applications*, **Chemistry of Materials**, 28 (18), 6426–6435, **2016**.
URL http://dx.doi.org/10.1021/acs.chemmater.6b02925

[77] B. Soundiraraju and B. K. George, *Two-Dimensional Titanium Nitride (Ti_2N) MXene: Synthesis, Characterization, and Potential Application as Surface-Enhanced Raman Scattering Substrate*, **ACS Nano**, 11 (9), 8892–8900, **2017**.
URL http://dx.doi.org/10.1021/acsnano.7b03129

[78] Y. Saito, P. Verma, K. Masui, Y. Inouye, and S. Kawata, *Nano-scale analysis of graphene layers by tip-enhanced near-field Raman spectroscopy*, **Journal of Raman Spectroscopy**, 40 (10), 1434–1440, **2009**.
URL http://dx.doi.org/10.1002/jrs.2366

[79] S. Mignuzzi, N. Kumar, B. Brennan, I. S. Gilmore, D. Richards, A. J. Pollard, and D. Roy, *Probing individual point defects in graphene via near-field Raman scattering*, **Nanoscale**, 7 (46), 19413–19418, **2015**.
URL http://dx.doi.org/10.1039/C5NR04664E

[80] J. Stadler, T. Schmid, and R. Zenobi, *Nanoscale Chemical Imaging of Single-Layer Graphene*, **ACS Nano**, 5 (10), 8442–8448, **2011**.
URL http://dx.doi.org/10.1021/nn2035523

[81] M. Richard-Lacroix, Y. Zhang, Z. Dong, and V. Deckert, *Mastering high resolution tip-enhanced Raman spectroscopy: towards a shift of perception*, **Chemical Society Reviews**, 46 (13), 3922–3944, **2017**.
URL http://dx.doi.org/10.1039/C7CS00203C

[82] M. D. Sonntag, J. M. Klingsporn, L. K. Garibay, J. M. Roberts, J. A. Dieringer, T. Seideman, K. A. Scheidt, L. Jensen, G. C. Schatz, and R. P. Van Duyne, *Single-Molecule Tip-Enhanced Raman Spectroscopy*, **The Journal of Physical Chemistry C**, 116 (1), 478–483, **2012**.
URL http://dx.doi.org/10.1021/jp209982h

[83] R. R. Nair, P. Blake, A. N. Grigorenko, K. S. Novoselov, T. J. Booth, T. Stauber, N. M. R. Peres, and A. K. Geim, *Fine structure constant defines visual transparency of graphene*, **Science**, 320 (5881), 1308–1308, **2008**.
URL http://dx.doi.org/10.1126/science.1156965

[84] K. P. Dhakal, D. L. Duong, J. Lee, H. Nam, M. Kim, M. Kan, Y. H. Lee, and J. Kim, *Confocal absorption spectral imaging of MoS_2: optical transitions depending on the atomic thickness of intrinsic and chemically doped MoS_2*, **Nanoscale**, 6 (21), 13028–13035, **2014**.
URL http://dx.doi.org/10.1039/C4NR03703K

[85] A. Castellanos-Gomez, J. Quereda, H. P. v. d. Meulen, N. Agraït, and G. Rubio-Bollinger, *Spatially resolved optical absorption spectroscopy of single- and few-layer MoS_2 by hyperspectral imaging*, **Nanotechnology**, 27 (11), 115705, **2016**.
URL http://dx.doi.org/10.1088/0957-4484/27/11/115705

[86] R. Frisenda, Y. Niu, P. Gant, A. J. Molina-Mendoza, R. Schmidt, R. Bratschitsch, J. Liu, L. Fu, D. Dumcenco, A. Kis, D. P. D. Lara, and A. Castellanos-Gomez, *Micro-reflectance and transmittance spectroscopy: a versatile and powerful tool to characterize 2D materials*, **Journal of Physics D: Applied Physics**, 50 (7), 074002, **2017**.
URL http://dx.doi.org/10.1088/1361-6463/aa5256

[87] Z. H. Ni, H. M. Wang, J. Kasim, H. M. Fan, T. Yu, Y. H. Wu, Y. P. Feng, and Z. X. Shen, *Graphene Thickness Determination Using Reflection and Contrast Spectroscopy*, **Nano Letters**, 7 (9), 2758–2763, **2007**.
URL http://dx.doi.org/10.1021/nl071254m

[88] V. G. Kravets, A. N. Grigorenko, R. R. Nair, P. Blake, S. Anissimova, K. S. Novoselov, and A. K. Geim, *Spectroscopic ellipsometry of graphene and an exciton-shifted van Hove peak in absorption*, **Physical Review B**, 81 (15), 155413, **2010**.
URL http://dx.doi.org/10.1103/PhysRevB.81.155413

[89] H. Yang, H. Hu, Y. Wang, and T. Yu, *Rapid and non-destructive identification of graphene oxide thickness using white light contrast spectroscopy*, **Carbon**, 52, 528–534, **2013**.
URL http://dx.doi.org/10.1016/j.carbon.2012.10.005

[90] M. Bruna and S. Borini, *Optical constants of graphene layers in the visible range*, **Applied Physics Letters**, 94 (3), 031901, **2009**.
URL http://dx.doi.org/10.1063/1.3073717

[91] Y.-C. Chang, C.-H. Liu, C.-H. Liu, Z. Zhong, and T. B. Norris, *Extracting the complex optical conductivity of mono- and bilayer graphene by ellipsometry*, **Applied Physics Letters**, 104 (26), 261909, **2014**.
URL http://dx.doi.org/10.1063/1.4887364

[92] S. Funke, B. Miller, E. Parzinger, P. Thiesen, A. W. Holleitner, and U. Wurstbauer, *Imaging spectroscopic ellipsometry of MoS_2*, **Journal of Physics: Condensed Matter**, 28 (38), 385301, **2016**.
URL http://dx.doi.org/10.1088/0953-8984/28/38/385301

[93] A. Matković, A. Beltaos, M. Milićević, U. Ralević, B. Vasić, D. Jovanović, and R. Gajić, *Spectroscopic imaging ellipsometry and Fano resonance modeling of graphene*, **Journal of Applied Physics**, 112 (12), 123523, **2012**.
URL http://dx.doi.org/10.1063/1.4771875

[94] Y. V. Morozov and M. Kuno, *Optical constants and dynamic conductivities of single layer MoS_2, $MoSe_2$, and WSe_2*, **Applied Physics Letters**, 107 (8), 083103, **2015**.
URL http://dx.doi.org/10.1063/1.4929700

[95] M. Vaupel, A. Dutschke, U. Wurstbauer, F. Hitzel, and A. Pasupathy, *Topography, complex refractive index, and conductivity of graphene layers measured by correlation of optical interference contrast, atomic force, and back scattered electron microscopy*, **Journal of Applied Physics**, 114 (18), 183107, **2013**.
URL http://dx.doi.org/10.1063/1.4831937

[96] U. Wurstbauer, C. Röling, U. Wurstbauer, W. Wegscheider, M. Vaupel, P. H. Thiesen, and D. Weiss, *Imaging ellipsometry of graphene*, **Applied Physics Letters**, 97 (23), 231901, **2010**.
URL http://dx.doi.org/10.1063/1.3524226

[97] H.-L. Liu, C.-C. Shen, S.-H. Su, C.-L. Hsu, M.-Y. Li, and L.-J. Li, *Optical properties of monolayer transition metal dichalcogenides probed by spectroscopic ellipsometry*, **Applied Physics Letters**, 105 (20), 201905, **2014**.
URL http://dx.doi.org/10.1063/1.4901836

[98] S. Khadir, P. Bon, D. Vignaud, E. Galopin, N. McEvoy, D. McCloskey, S. Monneret, and G. Baffou, *Optical Imaging and Characterization of Graphene and Other 2D Materials Using Quantitative Phase Microscopy*, **ACS Photonics**, 4 (12), 3130–3139, **2017**.
URL http://dx.doi.org/10.1021/acsphotonics.7b00845

[99] X. Wang, Y. P. Chen, and D. D. Nolte, *Strong anomalous optical dispersion of graphene: complex refractive index measured by Picometrology*, **Optics Express**, 16 (26), 22105–22112, **2008**.
URL http://dx.doi.org/10.1364/OE.16.022105

[100] W. Jie, Z. Yang, G. Bai, and J. Hao, *Luminescence in 2D Materials and van der Waals Heterostructures*, **Advanced Optical Materials**, 6 (10), 1701296, **2018**.
URL http://dx.doi.org/10.1002/adom.201701296

[101] A. M. van der Zande, P. Y. Huang, D. A. Chenet, T. C. Berkelbach, Y. You, G.-H. Lee, T. F. Heinz, D. R. Reichman, D. A. Muller, and J. C. Hone, *Grains and grain boundaries in highly crystalline monolayer molybdenum disulphide*, **Nature Materials**, 12 (6), 554–561, **2013**.
URL http://dx.doi.org/10.1038/nmat3633

[102] V. Carozo, Y. Wang, K. Fujisawa, B. R. Carvalho, A. McCreary, S. Feng, Z. Lin, C. Zhou, N. Perea-López, A. L. Elías, B. Kabius, V. H. Crespi, and M. Terrones, *Optical identification of sulfur vacancies: Bound excitons at the edges of monolayer tungsten disulfide*, **Science Advances**, 3 (4), e1602813, **2017**.
URL http://dx.doi.org/10.1126/sciadv.1602813

[103] L. Tao, K. Chen, Z. Chen, W. Chen, X. Gui, H. Chen, X. Li, and J.-B. Xu, *Centimeter-Scale CVD Growth of Highly Crystalline Single-Layer MoS_2 Film with Spatial Homogeneity and the Visualization of Grain Boundaries*, **ACS Applied Materials & Interfaces**, 9 (13), 12073–12081, **2017**.
URL http://dx.doi.org/10.1021/acsami.7b00420

[104] H. R. Gutiérrez, N. Perea-López, A. L. Elías, A. Berkdemir, B. Wang, R. Lv, F. López-Urías, V. H. Crespi, H. Terrones, and M. Terrones, *Extraordinary Room-Temperature Photoluminescence in Triangular WS_2 Monolayers*, **Nano Letters**, 13 (8), 3447–3454, **2013**.
URL http://dx.doi.org/10.1021/nl3026357

[105] Y. Sheng, X. Wang, K. Fujisawa, S. Ying, A. L. Elias, Z. Lin, W. Xu, Y. Zhou, A. M. Korsunsky, H. Bhaskaran, M. Terrones, and J. H. Warner, *Photoluminescence Segmentation within Individual Hexagonal Monolayer Tungsten Disulfide Domains Grown by Chemical Vapor Deposition*, **ACS Applied Materials & Interfaces**, 9 (17), 15005–15014, **2017**.
URL http://dx.doi.org/10.1021/acsami.6b16287

[106] S. Park, M. S. Kim, H. Kim, J. Lee, G. H. Han, J. Jung, and J. Kim, *Spectroscopic Visualization of Grain Boundaries of Monolayer Molybdenum Disulfide by Stacking Bilayers*, **ACS Nano**, 9 (11), 11042–11048, **2015**.
URL http://dx.doi.org/10.1021/acsnano.5b04977

[107] L. Karvonen, A. Säynätjoki, M. J. Huttunen, A. Autere, B. Amirsolaimani, S. Li, R. A. Norwood, N. Peyghambarian, H. Lipsanen, G. Eda, K. Kieu, and Z. Sun, *Rapid visualization of grain boundaries in monolayer MoS_2 by multiphoton microscopy*, **Nature Communications**, 8, 15714, **2017**.
URL http://dx.doi.org/10.1038/ncomms15714

[108] D. F. Ogletree, P. J. Schuck, A. F. Weber-Bargioni, N. J. Borys, S. Aloni, W. Bao, S. Barja, J. Lee, M. Melli, K. Munechika, S. Whitelam, and S. Wickenburg, *Revealing Optical Properties of Reduced-Dimensionality Materials at Relevant Length Scales*, **Advanced Materials**, 27 (38), 5693–5719, **2015**.
URL http://dx.doi.org/10.1002/adma.201500930

[109] W. Bao, N. J. Borys, C. Ko, J. Suh, W. Fan, A. Thron, Y. Zhang, A. Buyanin, J. Zhang, S. Cabrini, P. D. Ashby, A. Weber-Bargioni, S. Tongay, S. Aloni, D. F. Ogletree, J. Wu, M. B. Salmeron, and P. J. Schuck, *Visualizing nanoscale excitonic relaxation properties of disordered edges and grain boundaries in monolayer molybdenum disulfide*, **Nature Communications**, 6, 7993, **2015**.
URL http://dx.doi.org/10.1038/ncomms8993

[110] C. Kastl, R. J. Koch, C. T. Chen, J. Eichhorn, S. Ulstrup, A. Bostwick, C. Jozwiak, T. R. Kuykendall, N. J. Borys, F. M. Toma, S. Aloni, A. Weber-Bargioni, E. Rotenberg, and A. M. Schwartzberg, *Effects of Defects on Band Structure and Excitons in WS_2 Revealed by Nanoscale Photoemission Spectroscopy*, **ACS Nano**, 13 (2), 1284–1291, **2019**.
URL http://dx.doi.org/10.1021/acsnano.8b06574

[111] Y. Lee, S. Park, H. Kim, G. H. Han, Y. H. Lee, and J. Kim, *Characterization of the structural defects in CVD-grown monolayered MoS_2 using near-field photoluminescence imaging*, **Nanoscale**, 7 (28), 11909–11914, **2015**.
URL http://dx.doi.org/10.1039/C5NR02897C

[112] Y. Okuno, O. Lancry, A. Tempez, C. Cairone, M. Bosi, F. Fabbri, and M. Chaigneau, *Probing the nanoscale light emission properties of a CVD-grown MoS_2 monolayer by tip-enhanced photoluminescence*, **Nanoscale**, 10 (29), 14055–14059, **2018**.
URL http://dx.doi.org/10.1039/C8NR02421A

[113] W. Su, N. Kumar, S. Mignuzzi, J. Crain, and D. Roy, *Nanoscale mapping of excitonic processes in single-layer MoS_2 using tip-enhanced photoluminescence microscopy*, **Nanoscale**, 8 (20), 10564–10569, **2016**.
URL http://dx.doi.org/10.1039/C5NR07378B

[114] N. Mao, J. Tang, L. Xie, J. Wu, B. Han, J. Lin, S. Deng, W. Ji, H. Xu, K. Liu, L. Tong, and J. Zhang, *Optical Anisotropy of Black Phosphorus in the Visible Regime*, **Journal of the American Chemical Society**, 138 (1), 300–305, **2016**.
URL http://dx.doi.org/10.1021/jacs.5b10685

[115] A. T. Hoang, S. M. Shinde, A. K. Katiyar, K. P. Dhakal, X. Chen, H. Kim, S. W. Lee, Z. Lee, and J.-H. Ahn, *Orientation-dependent optical characterization of atomically thin transition metal ditellurides*, **Nanoscale**, 10 (46), 21978–21984, **2018**.
URL http://dx.doi.org/10.1039/C8NR07592A

[116] H. Zeng, G.-B. Liu, J. Dai, Y. Yan, B. Zhu, R. He, L. Xie, S. Xu, X. Chen, W. Yao, and X. Cui, *Optical signature of symmetry variations and spin-valley coupling in atomically thin tungsten dichalcogenides*, **Scientific Reports**, 3, 1608, **2013**.
URL http://dx.doi.org/10.1038/srep01608

[117] X. Yin, Z. Ye, D. A. Chenet, Y. Ye, K. O'Brien, J. C. Hone, and X. Zhang, *Edge Nonlinear Optics on a MoS_2 Atomic Monolayer*, **Science**, 344 (6183), 488–490, **2014**.
URL http://dx.doi.org/10.1126/science.1250564

[118] J. Cheng, T. Jiang, Q. Ji, Y. Zhang, Z. Li, Y. Shan, Y. Zhang, X. Gong, W. Liu, and S. Wu, *Kinetic Nature of Grain Boundary Formation in As-Grown MoS_2 Monolayers*, **Advanced Materials**, 27 (27), 4069–4074, **2015**.
URL http://dx.doi.org/10.1002/adma.201501354

[119] S.-K. Mo, *Angle-resolved photoemission spectroscopy for the study of two-dimensional materials*, **Nano Convergence**, 4 (1), 6, **2017**.
URL http://dx.doi.org/10.1186/s40580-017-0100-7

[120] M. Cattelan and N. A. Fox, *A Perspective on the Application of Spatially Resolved ARPES for 2D Materials*, **Nanomaterials**, 8 (5), 284, **2018**.
URL http://dx.doi.org/10.3390/nano8050284

[121] C. Zhang, A. Johnson, C.-L. Hsu, L.-J. Li, and C.-K. Shih, *Direct Imaging of Band Profile in Single Layer MoS_2 on Graphite: Quasiparticle Energy Gap, Metallic Edge States, and Edge Band Bending*, **Nano Letters**, 14 (5), 2443–2447, **2014**.
URL http://dx.doi.org/10.1021/nl501133c

[122] S. M. Hus and A.-P. Li, *Spatially-resolved studies on the role of defects and boundaries in electronic behavior of 2D materials*, **Progress in Surface Science**, 92 (3), 176–201, **2017**.
URL http://dx.doi.org/10.1016/j.progsurf.2017.07.001

[123] S. Hussain, K. Xu, S. Ye, L. Lei, X. Liu, R. Xu, L. Xie, and Z. Cheng, *Local electrical characterization of two-dimensional materials with functional atomic force microscopy*, **Frontiers of Physics**, 14 (3), 33401, **2019**.
URL http://dx.doi.org/10.1007/s11467-018-0879-7

[124] D. Wu, X. Li, L. Luan, X. Wu, W. Li, M. N. Yogeesh, R. Ghosh, Z. Chu, D. Akinwande, Q. Niu, and K. Lai, *Uncovering edge states and electrical inhomogeneity in MoS_2 field-effect transistors*, **Proceedings of the National Academy of Sciences**, 113 (31), 8583–8588, **2016**.
URL http://dx.doi.org/10.1073/pnas.1605982113

[125] Y. Almadori, N. Bendiab, and B. Grévin, *Multimodal Kelvin Probe Force Microscopy Investigations of a Photovoltaic WSe_2/MoS_2 Type-II Interface*, **ACS Applied Materials & Interfaces**, 10 (1), 1363–1373, **2018**.
URL http://dx.doi.org/10.1021/acsami.7b14616

[126] Y. Vaknin, R. Dagan, and Y. Rosenwaks, *Pinch-Off Formation in Monolayer and Multilayers MoS_2 Field-Effect Transistors*, **Nanomaterials**, 9 (6), 882, **2019**.
URL http://dx.doi.org/10.3390/nano9060882

[127] H. Zhong, Z. Liu, J. Wang, A. Pan, G. Xu, and K. Xu, *Measuring the local mobility of graphene on semiconductors*, **Physical Review Materials**, 2 (4), 043801, **2018**.
URL http://dx.doi.org/10.1103/PhysRevMaterials.2.043801

[128] R. Kumar, D. Varandani, and B. R. Mehta, *Nanoscale interface formation and charge transfer in graphene/silicon Schottky junctions; KPFM and CAFM studies*, **Carbon**, 98, 41–49, **2016**.
URL http://dx.doi.org/10.1016/j.carbon.2015.10.075

[129] J.-P. Tetienne, N. Dontschuk, D. A. Broadway, A. Stacey, D. A. Simpson, and L. C. L. Hollenberg, *Quantum imaging of current flow in graphene*, **Science Advances**, 3 (4), e1602429, **2017**.
URL http://dx.doi.org/10.1126/sciadv.1602429

[130] P. Bøggild, D. M. A. Mackenzie, P. R. Whelan, D. H. Petersen, J. D. Buron, A. Zurutuza, J. Gallop, L. Hao, and P. U. Jepsen, *Mapping the electrical properties of large-area graphene*, **2D Materials**, 4 (4), 042003, **2017**.
URL http://dx.doi.org/10.1088/2053-1583/aa8683

[131] J. Azevedo, C. Bourdillon, V. Derycke, S. Campidelli, C. Lefrou, and R. Cornut, *Contactless Surface Conductivity Mapping of Graphene Oxide Thin Films Deposited on Glass with Scanning Electrochemical Microscopy*, **Analytical Chemistry**, 85 (3), 1812–1818, **2013**.
URL http://dx.doi.org/10.1021/ac303173d

[132] T. Bourgeteau, S. Le Vot, M. Bertucchi, V. Derycke, B. Jousselme, S. Campidelli, and R. Cornut, *New Insights into the Electronic Transport of Reduced Graphene Oxide Using Scanning Electrochemical Microscopy*, **The Journal of Physical Chemistry Letters**, 5 (23), 4162–4166, **2014**.
URL http://dx.doi.org/10.1021/jz502224f

[133] A. Bellunato, H. Arjmandi Tash, Y. Cesa, and G. F. Schneider, *Chemistry at the Edge of Graphene*, **ChemPhysChem**, 17 (6), 785–801, **2016**.
URL http://dx.doi.org/10.1002/cphc.201500926

[134] X. S. Chu, A. Yousaf, D. O. Li, A. A. Tang, A. Debnath, D. Ma, A. A. Green, E. J. G. Santos, and Q. H. Wang, *Direct Covalent Chemical Functionalization of Unmodified Two-Dimensional Molybdenum Disulfide*, **Chemistry of Materials**, 30 (6), 2112–2128, **2018**.
URL http://dx.doi.org/10.1021/acs.chemmater.8b00173

[135] D. O. Li, X. S. Chu, and Q. H. Wang, *Reaction Kinetics for the Covalent Functionalization of Two-Dimensional MoS_2 by Aryl Diazonium Salts*, **Langmuir**, 35 (17), 5693–5701, **2019**.
URL http://dx.doi.org/10.1021/acs.langmuir.8b04288

[136] Q. H. Wang, C.-J. Shih, G. L. C. Paulus, and M. S. Strano, *Evolution of Physical and Electronic Structures of Bilayer Graphene upon Chemical Functionalization*, **Journal of the American Chemical Society**, 135 (50), 18866–18875, **2013**.
URL http://dx.doi.org/10.1021/ja4083914

[137] A. Jacobsen, F. M. Koehler, W. J. Stark, and K. Ensslin, *Towards electron transport measurements in chemically modified graphene: effect of a solvent*, **New Journal of Physics**, 12 (12), 125007, **2010**.
URL http://dx.doi.org/10.1088/1367-2630/12/12/125007

[138] R. Sharma, J. H. Baik, C. J. Perera, and M. S. Strano, *Anomalously Large Reactivity of Single Graphene Layers and Edges toward Electron Transfer Chemistries*, **Nano Letters**, 10 (2), 398–405, **2010**.
URL http://dx.doi.org/10.1021/nl902741x

[139] X. Wang, J. Zhang, X. Zhang, and Y. Zhu, *Characterization, uniformity and photo-catalytic properties of graphene/TiO_2 nanocomposites via Raman mapping*, **Optics Express**, 25 (18), 21496–21508, **2017**.
URL http://dx.doi.org/10.1364/OE.25.021496

[140] S. Wang, R. Wang, X. Liu, X. Wang, D. Zhang, Y. Guo, and X. Qiu, *Optical Spectroscopy Investigation of the Structural and Electrical Evolution of Controllably Oxidized Graphene by a Solution Method*, **The Journal of Physical Chemistry C**, 116 (19), 10702–10707, **2012**.
URL http://dx.doi.org/10.1021/jp212184n

[141] J. M. Englert, P. Vecera, K. C. Knirsch, R. A. Schäfer, F. Hauke, and A. Hirsch, *Scanning-Raman-Microscopy for the Statistical Analysis of Covalently Functionalized Graphene*, **ACS Nano**, 7 (6), 5472–5482, **2013**.
URL http://dx.doi.org/10.1021/nn401481h

[142] F. M. Koehler, A. Jacobsen, K. Ensslin, C. Stampfer, and W. J. Stark, *Selective Chemical Modification of Graphene Surfaces: Distinction Between Single- and Bilayer Graphene*, **Small**, 6 (10), 1125–1130, **2010**.
URL http://dx.doi.org/10.1002/smll.200902370

[143] S. Niyogi, E. Bekyarova, M. E. Itkis, H. Zhang, K. Shepperd, J. Hicks, M. Sprinkle, C. Berger, C. N. Lau, W. A. deHeer, E. H. Conrad, and R. C. Haddon, *Spectroscopy of Covalently Functionalized Graphene*, **Nano Letters**, 10 (10), 4061–4066, **2010**.
URL http://dx.doi.org/10.1021/nl1021128

[144] H. Lim, J. S. Lee, H.-J. Shin, H. S. Shin, and H. C. Choi, *Spatially Resolved Spontaneous Reactivity of Diazonium Salt on Edge and Basal Plane of Graphene without Surfactant and Its Doping Effect*, **Langmuir**, 26 (14), 12278–12284, **2010**.
URL http://dx.doi.org/10.1021/la101254k

[145] M. P. McDonald, A. Eltom, F. Vietmeyer, J. Thapa, Y. V. Morozov, D. A. Sokolov, J. H. Hodak, K. Vinodgopal, P. V. Kamat, and M. Kuno, *Direct Observation of Spatially Heterogeneous Single-Layer Graphene Oxide Reduction Kinetics*, **Nano Letters**, 13 (12), 5777–5784, **2013**.
URL http://dx.doi.org/10.1021/nl402057j

[146] D. A. Sokolov, Y. V. Morozov, M. P. McDonald, F. Vietmeyer, J. H. Hodak, and M. Kuno, *Direct Observation of Single Layer Graphene Oxide Reduction through Spatially Resolved, Single Sheet Absorption/Emission Microscopy*, **Nano Letters**, 14 (6), 3172–3179, **2014**.
URL http://dx.doi.org/10.1021/nl500485n

[147] B. J. Tyler, B. Brennan, H. Stec, T. Patel, L. Hao, I. S. Gilmore, and A. J. Pollard, *Removal of Organic Contamination from Graphene with a Controllable Mass-Selected Argon Gas Cluster Ion Beam*, **The Journal of Physical Chemistry C**, 119 (31), 17836–17841, **2015**.
URL http://dx.doi.org/10.1021/acs.jpcc.5b03144

[148] P. Kovaříček, V. Vrkoslav, J. Plšek, Z. Bastl, M. Fridrichová, K. Drogowska, and M. Kalbáč, *Extended characterization methods for covalent functionalization of graphene on copper*, **Carbon**, 118, 200–207, **2017**.
URL http://dx.doi.org/10.1016/j.carbon.2017.03.020

[149] J. S. Wallace, A. Quinn, J. A. Gardella, J. Hu, E. S.-W. Kong, and H.-I. Joh, *Time-of-flight secondary ion mass spectrometry as a tool for evaluating the plasma-induced hydrogenation of graphene*, **Journal of Vacuum Science & Technology B**, 34 (3), 03H113, **2016**.
URL http://dx.doi.org/10.1116/1.4942086

[150] E. A. Muller, B. Pollard, and M. B. Raschke, *Infrared Chemical Nano-Imaging: Accessing Structure, Coupling, and Dynamics on Molecular Length Scales*, **The Journal of Physical Chemistry Letters**, 6 (7), 1275–1284, **2015**.
URL http://dx.doi.org/10.1021/acs.jpclett.5b00108

[151] P. Patoka, G. Ulrich, A. E. Nguyen, L. Bartels, P. A. Dowben, V. Turkowski, T. S. Rahman, P. Hermann, B. Kästner, A. Hoehl, G. Ulm, and E. Rühl, *Nanoscale plasmonic phenomena in CVD-grown MoS_2 monolayer revealed by ultra-broadband synchrotron radiation based nano-FTIR spectroscopy and near-field microscopy*, **Optics Express**, 24 (2), 1154–1164, **2016**.
URL http://dx.doi.org/10.1364/OE.24.001154

[152] B. Warner, T. G. Gill, V. Caciuc, N. Atodiresei, A. Fleurence, Y. Yoshida, Y. Hasegawa, S. Blügel, Y. Yamada-Takamura, and C. F. Hirjibehedin, *Guided Molecular Assembly on a Locally Reactive 2D Material*, **Advanced Materials**, 29 (43), 1703929, **2017**.
URL http://dx.doi.org/10.1002/adma.201703929

[153] M. Z. Hossain, M. A. Walsh, and M. C. Hersam, *Scanning Tunneling Microscopy, Spectroscopy, and Nanolithography of Epitaxial Graphene Chemically Modified with Aryl Moieties*, **Journal of the American Chemical Society**, 132 (43), 15399–15403, **2010**.
URL http://dx.doi.org/10.1021/ja107085n

[154] X. Wang, X. Shen, Z. Wang, R. Yu, and L. Chen, *Atomic-Scale Clarification of Structural Transition of MoS_2 upon Sodium Intercalation*, **ACS Nano**, 8 (11), 11394–11400, **2014**.
URL http://dx.doi.org/10.1021/nn505501v

[155] P. Gao, L. Wang, Y. Zhang, Y. Huang, and K. Liu, *Atomic-Scale Probing of the Dynamics of Sodium Transport and Intercalation-Induced Phase Transformations in MoS_2*, **ACS Nano**, 9 (11), 11296–11301, **2015**.
URL http://dx.doi.org/10.1021/acsnano.5b04950

[156] M. Kan, J. Y. Wang, X. W. Li, S. H. Zhang, Y. W. Li, Y. Kawazoe, Q. Sun, and P. Jena, *Structures and Phase Transition of a MoS_2 Monolayer*, **The Journal of Physical Chemistry C**, 118 (3), 1515–1522, **2014**.
URL http://dx.doi.org/10.1021/jp4076355

[157] S. Chen, L. Wang, R. Shao, J. Zou, R. Cai, J. Lin, C. Zhu, J. Zhang, F. Xu, J. Cao, J. Feng, J. Qi, and P. Gao, *Atomic structure and migration dynamics of MoS_2/Li_xMoS_2 interface*, **Nano Energy**, 48, 560–568, **2018**.
URL http://dx.doi.org/10.1016/j.nanoen.2018.03.076

[158] Q. Huang, L. Wang, Z. Xu, W. Wang, and X. Bai, *In-situ TEM investigation of MoS_2 upon alkali metal intercalation*, **Science China Chemistry**, 61 (2), 222–227, **2018**.
URL http://dx.doi.org/10.1007/s11426-017-9128-0

[159] P. Gao, Y.-Y. Zhang, L. Wang, S. Chen, Y. Huang, X. Ma, K. Liu, and D. Yu, *In situ atomic-scale observation of reversible sodium ions migration in layered metal dichalcogenide SnS_2 nanostructures*, **Nano Energy**, 32, 302–309, **2017**.
URL http://dx.doi.org/10.1016/j.nanoen.2016.12.051

[160] F. R. Bagsican, A. Winchester, S. Ghosh, X. Zhang, L. Ma, M. Wang, H. Murakami, S. Talapatra, R. Vajtai, P. M. Ajayan, J. Kono, M. Tonouchi, and I. Kawayama, *Adsorption energy of oxygen molecules on graphene and two-dimensional tungsten disulfide*, **Scientific Reports**, 7 (1), 1774, **2017**.
URL http://dx.doi.org/10.1038/s41598-017-01883-1

[161] Y. Sun, Q. Wu, and G. Shi, *Graphene based new energy materials*, **Energy & Environmental Science**, 4 (4), 1113–1132, **2011**.
URL http://dx.doi.org/10.1039/C0EE00683A

[162] L. Dai, *Functionalization of Graphene for Efficient Energy Conversion and Storage*, **Accounts of Chemical Research**, 46 (1), 31–42, **2013**.
URL http://dx.doi.org/10.1021/ar300122m

[163] J. Hou, Y. Shao, M. W. Ellis, R. B. Moore, and B. Yi, *Graphene-based electrochemical energy conversion and storage: fuel cells, supercapacitors and lithium ion batteries*, **Physical Chemistry Chemical Physics**, 13 (34), 15384–15402, **2011**.
URL http://dx.doi.org/10.1039/C1CP21915D

[164] N. G. Sahoo, Y. Pan, L. Li, and S. H. Chan, *Graphene-Based Materials for Energy Conversion*, **Advanced Materials**, 24 (30), 4203–4210, **2012**.
URL http://dx.doi.org/10.1002/adma.201104971

[165] M. Arai, S. Masubuchi, K. Nose, Y. Mitsuda, and T. Machida, *Fabrication of 10-nm-scale nanoconstrictions in graphene using atomic force microscopy-based local anodic oxidation lithography*, **Japanese Journal of Applied Physics**, 54, 04DJ06, **2015**.
URL http://dx.doi.org/10.7567/JJAP.54.04DJ06

[166] M. Ahmad, Y. Seo, and Y. J. Choi, *Nanographene device fabrication using atomic force microscope*, **IET Micro Nano Letters**, 8 (8), 422–425, **2013**.
URL http://dx.doi.org/10.1049/mnl.2013.0199

[167] L. Weng, L. Zhang, Y. P. Chen, and L. P. Rokhinson, *Atomic force microscope local oxidation nanolithography of graphene*, **Applied Physics Letters**, 93 (9), 093107, **2008**.
URL http://dx.doi.org/10.1063/1.2976429

[168] J. M. Mativetsky, E. Treossi, E. Orgiu, M. Melucci, G. P. Veronese, P. Samorì, and V. Palermo, *Local Current Mapping and Patterning of Reduced Graphene Oxide*, **Journal of the American Chemical Society**, 132 (40), 14130–14136, **2010**.
URL http://dx.doi.org/10.1021/ja104567f

[169] J. Azevedo, L. Fillaud, C. Bourdillon, J.-M. Noel, F. Kanoufi, B. Jousselme, V. Derycke, S. Campidelli, and R. Cornut, *Localized Reduction of Graphene Oxide by Electrogenerated Naphthalene Radical Anions and Subsequent Diazonium Electrografting*, **Journal of the American Chemical Society**, 136 (13), 4833–4836, **2014**.
URL http://dx.doi.org/10.1021/ja500189u

[170] K. Torbensen, M. Kongsfelt, K. Shimizu, E. B. Pedersen, T. Skrydstrup, S. U. Pedersen, and K. Daasbjerg, *Patterned Carboxylation of Graphene Using Scanning Electrochemical Microscopy*, **Langmuir**, 31 (15), 4443–4452, **2015**.
URL http://dx.doi.org/10.1021/la504500m

[171] X. Chia and M. Pumera, *Characteristics and performance of two-dimensional materials for electrocatalysis*, **Nature Catalysis**, 1 (12), 909, **2018**.
URL http://dx.doi.org/10.1038/s41929-018-0181-7

[172] C. L. Bentley, J. Edmondson, G. N. Meloni, D. Perry, V. Shkirskiy, and P. R. Unwin, *Nanoscale Electrochemical Mapping*, **Analytical Chemistry**, 91 (1), 84–108, **2019**.
URL http://dx.doi.org/10.1021/acs.analchem.8b05235

[173] M. Velický, P. S. Toth, C. R. Woods, K. S. Novoselov, and R. A. W. Dryfe, *Electrochemistry of the Basal Plane versus Edge Plane of Graphite Revisited*, **The Journal of Physical Chemistry C**, 123 (18), 11677–11685, **2019**.
URL http://dx.doi.org/10.1021/acs.jpcc.9b01010

[174] G. Zhang, S.-y. Tan, A. N. Patel, and P. R. Unwin, *Electrochemistry of $Fe^{3+/2+}$ at highly oriented pyrolytic graphite (HOPG) electrodes: kinetics, identification of major electroactive sites and time effects on the response*, **Physical Chemistry Chemical Physics**, 18 (47), 32387–32395, **2016**.
URL http://dx.doi.org/10.1039/C6CP06472H

[175] N. L. Ritzert, V. A. Szalai, and T. P. Moffat, *Mapping Electron Transfer at MoS_2 Using Scanning Electrochemical Microscopy*, **Langmuir**, 34 (46), 13864–13870, **2018**.
URL http://dx.doi.org/10.1021/acs.langmuir.8b02731

[176] T. Sun, H. Zhang, X. Wang, J. Liu, C. Xiao, S. U. Nanayakkara, J. L. Blackburn, M. V. Mirkin, and E. M. Miller, *Nanoscale mapping of hydrogen evolution on metallic and semiconducting MoS_2 nanosheets*, **Nanoscale Horizons**, 4 (3), 619–624, **2019**.
URL http://dx.doi.org/10.1039/C8NH00346G

[177] C. L. Bentley, M. Kang, F. M. Maddar, F. Li, M. Walker, J. Zhang, and P. R. Unwin, *Electrochemical maps and movies of the hydrogen evolution reaction on natural crystals of molybdenite (MoS_2): basal vs. edge plane activity*, **Chemical Science**, 8 (9), 6583–6593, **2017**.
URL http://dx.doi.org/10.1039/C7SC02545A

[178] A. Kumatani, C. Miura, H. Kuramochi, T. Ohto, M. Wakisaka, Y. Nagata, H. Ida, Y. Takahashi, K. Hu, S. Jeong, J.-i. Fujita, T. Matsue, and Y. Ito, *Chemical Dopants on Edge of Holey Graphene Accelerate Electrochemical Hydrogen Evolution Reaction*, **Advanced Science**, 6 (10), 1900119, **2019**.
URL http://dx.doi.org/10.1002/advs.201900119

[179] D.-Q. Liu, B. Tao, H.-C. Ruan, C. L. Bentley, and P. R. Unwin, *Metal support effects in electrocatalysis at hexagonal boron nitride*, **Chemical Communications**, 55 (5), 628–631, **2019**.
URL http://dx.doi.org/10.1039/C8CC08517J

[180] J. Hui, S. Pakhira, R. Bhargava, Z. J. Barton, X. Zhou, A. J. Chinderle, J. L. Mendoza-Cortes, and J. Rodríguez-López, *Modulating Electrocatalysis on Graphene Heterostructures: Physically Impermeable Yet Electronically Transparent Electrodes*, **ACS Nano**, 12 (3), 2980–2990, **2018**.
URL http://dx.doi.org/10.1021/acsnano.8b00702

[181] S. Kolagatla, P. Subramanian, and A. Schechter, *Nanoscale mapping of catalytic hotspots on Fe, N-modified HOPG by scanning electrochemical microscopy-atomic force microscopy*, **Nanoscale**, 10 (15), 6962–6970, **2018**.
URL http://dx.doi.org/10.1039/C8NR00849C

[182] J. Zhang, J. Wu, X. Zou, K. Hackenberg, W. Zhou, W. Chen, J. Yuan, K. Keyshar, G. Gupta, A. Mohite, P. M. Ajayan, and J. Lou, *Discovering superior basal plane active two-dimensional catalysts for hydrogen evolution*, **Materials Today**, 25, 28–34, **2019**.
URL http://dx.doi.org/10.1016/j.mattod.2019.02.014

[183] J. Zhang, J. Wu, H. Guo, W. Chen, J. Yuan, U. Martinez, G. Gupta, A. Mohite, P. M. Ajayan, and J. Lou, *Unveiling Active Sites for the Hydrogen Evolution Reaction on Monolayer MoS_2*, **Advanced Materials**, 29 (42), 1701955, **2017**.
URL http://dx.doi.org/10.1002/adma.201701955

[184] J. Zhang, A. Yang, X. Wu, J. v. d. Groep, P. Tang, S. Li, B. Liu, F. Shi, J. Wan, Q. Li, Y. Sun, Z. Lu, X. Zheng, G. Zhou, C.-L. Wu, S.-C. Zhang, M. L. Brongersma, J. Li, and Y. Cui, *Reversible and selective ion intercalation through the top surface of few-layer MoS_2*, **Nature Communications**, 9 (1), 5289, **2018**.
URL http://dx.doi.org/10.1038/s41467-018-07710-z

[185] N. B. Schorr, A. G. Jiang, and J. Rodríguez-López, *Probing Graphene Interfacial Reactivity via Simultaneous and Colocalized Raman–Scanning Electrochemical Microscopy Imaging and Interrogation*, **Analytical Chemistry**, 90 (13), 7848–7854, **2018**.
URL http://dx.doi.org/10.1021/acs.analchem.8b00730

[186] A. Kumar, A. Sebastian, S. Das, and E. Ringe, *In Situ Optical Tracking of Electroablation in Two-Dimensional Transition-Metal Dichalcogenides*, **Acs Applied Materials & Interfaces**, 10 (47), 40773–40780, **2018**.
URL http://dx.doi.org/10.1021/acsami.8b14585

[187] W. Li, M. Wojcik, and K. Xu, *Optical Microscopy Unveils Rapid, Reversible Electrochemical Oxidation and Reduction of Graphene*, **Nano Letters**, 19 (2), 983–989, **2019**.
URL http://dx.doi.org/10.1021/acs.nanolett.8b04216

[188] T. Chen, Y. Zhang, and W. Xu, *Observing the Heterogeneous Electro-redox of Individual Single-Layer Graphene Sheets*, **ACS Nano**, 10 (9), 8434–8442, **2016**.
URL http://dx.doi.org/10.1021/acsnano.6b03327

[189] H. Li, Z. Ying, B. Lyu, A. Deng, L. Wang, T. Taniguchi, K. Watanabe, and Z. Shi, *Electrode-Free Anodic Oxidation Nanolithography of Low-Dimensional Materials*, **Nano Letters**, 18 (12), 8011–8015, **2018**.
URL http://dx.doi.org/10.1021/acs.nanolett.8b04166

[190] A. I. Dago, S. Sangiao, R. Fernández-Pacheco, J. M. De Teresa, and R. Garcia, *Chemical and structural analysis of sub-20 nm graphene patterns generated by scanning probe lithography*, **Carbon**, 129, 281–285, **2018**.
URL http://dx.doi.org/10.1016/j.carbon.2017.12.033

[191] C. Rubio-Verdú, G. Sáenz-Arce, J. Martinez-Asencio, D. C. Milan, M. Moaied, J. J. Palacios, M. J. Caturla, and C. Untiedt, *Graphene flakes obtained by local electro-exfoliation of graphite with a STM tip*, **Physical Chemistry Chemical Physics**, 19 (11), 8061–8068, **2017**.
URL http://dx.doi.org/10.1039/C6CP07236D

[192] E. Pinilla-Cienfuegos, S. Mañas-Valero, E. Navarro-Moratalla, S. Tatay, A. Forment-Aliaga, and E. Coronado, *Local Oxidation Nanolithography on Metallic Transition Metal Dichalcogenides Surfaces*, **Applied Sciences**, 6 (9), 250, **2016**.
URL http://dx.doi.org/10.3390/app6090250

[193] C. J. Shearer, A. D. Slattery, A. J. Stapleton, J. G. Shapter, and C. T. Gibson, *Accurate thickness measurement of graphene*, **Nanotechnology**, 27 (12), 125704, **2016**.
URL http://dx.doi.org/10.1088/0957-4484/27/12/125704

[194] G. Kang, M. Yang, M. S. Mattei, G. C. Schatz, and R. P. Van Duyne, *In Situ Nanoscale Redox Mapping Using Tip-Enhanced Raman Spectroscopy*, **Nano Letters**, 19 (3), 2106–2113, **2019**.
URL http://dx.doi.org/10.1021/acs.nanolett.9b00313

[195] Y. Yuan, M. Li, Z. Bai, G. Jiang, B. Liu, T. Wu, Z. Chen, K. Amine, and J. Lu, *The Absence and Importance of Operando Techniques for Metal-Free Catalysts*, **Advanced Materials**, 31 (13), 1805609, **2019**.
URL http://dx.doi.org/10.1002/adma.201805609

[196] Y. Wu and N. Liu, *Visualizing Battery Reactions and Processes by Using In Situ and In Operando Microscopies*, **Chem**, 4 (3), 438–465, **2018**.
URL http://dx.doi.org/10.1016/j.chempr.2017.12.022

[197] S. M. Tan and M. Pumera, *Two-Dimensional Materials on the Rocks: Positive and Negative Role of Dopants and Impurities in Electrochemistry*, **ACS Nano**, 13 (3), 2681–2728, **2019**.
URL http://dx.doi.org/10.1021/acsnano.8b07795

[198] E. Abbe, *Beiträge zur Theorie des Mikroskops und der mikroskopischen Wahrnehmung*, **Archiv für mikroskopische Anatomie**, 9 (1), 413–418, **1873**.
URL http://dx.doi.org/10.1007/BF02956173

[199] A. A. Michelson, *Studies in Optics*, University of Chicago Press, **1927**.
URL https://archive.org/details/in.ernet.dli.2015.86849/page/n5

[200] A. Fresnel, *Mémoire sur la loi des modifications que la réflextion imprime à la lumière*, **1823**.
URL https://www.academie-sciences.fr/pdf/dossiers/Fresnel/Fresnel_pdf/Mem1823_p393.pdf

[201] M. Born and E. Wolf, *Principles of Optics: Electromagnetic Theory of Propagation, Interference and Diffraction of Light*, Elsevier, **2013**.

[202] S. Chattopadhyay, Y. F. Huang, Y. J. Jen, A. Ganguly, K. H. Chen, and L. C. Chen, *Anti-reflecting and photonic nanostructures*, **Materials Science and Engineering: R: Reports**, 69 (1), 1–35, **2010**.
URL http://dx.doi.org/10.1016/j.mser.2010.04.001

[203] H. K. Raut, V. A. Ganesh, A. S. Nair, and S. Ramakrishna, *Anti-reflective coatings: A critical, in-depth review*, **Energy & Environmental Science**, 4 (10), 3779–3804, **2011**.
URL http://dx.doi.org/10.1039/C1EE01297E

[204] M. K. Hedayati and M. Elbahri, *Antireflective Coatings: Conventional Stacking Layers and Ultrathin Plasmonic Metasurfaces, A Mini-Review*, **Materials**, 9 (6), 497, **2016**.
URL http://dx.doi.org/10.3390/ma9060497

[205] M. A. Kats, R. Blanchard, P. Genevet, and F. Capasso, *Nanometre optical coatings based on strong interference effects in highly absorbing media*, **Nature Materials**, 12 (1), 20–24, **2013**.
URL http://dx.doi.org/10.1038/NMAT3443

[206] C. F. Guo, T. Sun, F. Cao, Q. Liu, and Z. Ren, *Metallic nanostructures for light trapping in energy-harvesting devices*, **Light-Science & Applications**, 3, e161, **2014**.
URL http://dx.doi.org/10.1038/lsa.2014.42

[207] T. Oyama, H. Ohsaki, Y. Tachibana, Y. Hayashi, Y. Ono, and N. Horie, *A new layer system of anti-reflective coating for cathode ray tubes*, **Thin Solid Films**, 351 (1-2), 235–240, **1999**.
URL http://dx.doi.org/10.1016/S0040-6090(99)00214-X

[208] F. F. Schlich and R. Spolenak, *Strong interference in ultrathin semiconducting layers on a wide variety of substrate materials*, **Applied Physics Letters**, 103 (21), 213112, **2013**.
URL http://dx.doi.org/10.1063/1.4833537

[209] M. A. Kats, D. Sharma, J. Lin, P. Genevet, R. Blanchard, Z. Yang, M. M. Qazilbash, D. N. Basov, S. Ramanathan, and F. Capasso, *Ultra-thin perfect absorber employing a tunable phase change material*, **Applied Physics Letters**, 101 (22), 221101, **2012**.
URL http://dx.doi.org/10.1063/1.4767646

[210] H. Dotan, O. Kfir, E. Sharlin, O. Blank, M. Gross, I. Dumchin, G. Ankonina, and A. Rothschild, *Resonant light trapping in ultrathin films for water splitting*, **Nature Materials**, 12 (2), 158–164, **2013**.
URL http://dx.doi.org/10.1038/NMAT3477

[211] J. Park, J.-H. Kang, A. P. Vasudev, D. T. Schoen, H. Kim, E. Hasman, and M. L. Brongersma, *Omnidirectional Near-Unity Absorption in an Ultrathin Planar Semiconductor Layer on a Metal Substrate*, **Acs Photonics**, 1 (9), 812–821, **2014**.
URL http://dx.doi.org/10.1021/ph500093d

[212] R. M. A. Azzam and N. M. Bashara, *Ellipsometry and polarized light*, North-Holland Pub. Co., **1977**.

[213] S. G. Moiseev and S. V. Vinogradov, *Design of antireflection composite coating based on metal nanoparticles*, **Physics of Wave Phenomena**, 19 (1), 47–51, **2011**.
URL http://dx.doi.org/10.3103/S1541308X11010109

[214] D. Ausserre, R. Abou Khachfe, L. Roussille, G. Brotons, L. Vonna, F. Lemarchand, M. Zerrad, and C. Amra, *Anti-Reflecting Absorbing Layers for Electrochemical and Biophotonic Applications*, **Journal of Nanomedicine & Nanotechnology**, 5 (4), 214, **2014**.
URL http://dx.doi.org/10.4172/2157-7439.1000214

[215] J.-F. Lemineur, J.-M. Noël, D. Ausserré, C. Combellas, and F. Kanoufi, *Combining electrodeposition and optical microscopy for probing size-dependent single nanoparticle electrochemistry*, **Angewandte Chemie International Edition**, 57 (37), 11998–12002, **2018**.
URL http://dx.doi.org/10.1002/anie.201807003

[216] J.-F. Lemineur, J.-M. Noël, C. Combellas, D. Ausserré, and F. Kanoufi, *The promise of antireflective gold electrodes for optically monitoring the electro-deposition of single silver nanoparticles*, **Faraday Discussions**, 210, 381–395, **2018**.
URL http://dx.doi.org/10.1039/C8FD00037A

[217] G. Bepete, N. Izard, F. Torres-Canas, A. Derré, A. Sbardelotto, E. Anglaret, A. Pénicaud, and C. Drummond, *Hydroxide Ions Stabilize Open Carbon Nanotubes in Degassed Water*, **ACS Nano**, 12 (8), 8606–8615, **2018**.
URL http://dx.doi.org/10.1021/acsnano.8b04341

[218] D. Ausserré, L. Roussille, M. Zerrad, F. Lemarchand, and C. Amra, *Procédés optiques pour l'observation d'échantillons et pour la détection ou le dosage d'espèces chimiques ou biologiques*, **2014**.
URL https://bases-brevets.inpi.fr/fr/document/FR2993987.html

[219] D. Ausserré, C. Amra, M. Zerrad, and R. Abou Khachfe, *Supports amplificateurs de contraste pour l'observation d'un échantillon, leur procédés de fabrication et leurs utilisations*, **2015**.
URL https://bases-brevets.inpi.fr/fr/document/FR3012131.html

[220] D. Ausserré, C. Amra, M. Zerrad, and R. Abou Khachfe, *Procédé de fabrication de supports amplificateurs de contraste*, **2015**.
URL https://bases-brevets.inpi.fr/fr/document/FR3012132.html

[221] D. Ausserré, R. Abou Khachfe, and G. Brotons, *Dispositif et appareil électrochimique et procédés mettant en œuvre un tel appareil*, **2015**.
URL https://bases-brevets.inpi.fr/fr/document/FR3017743.html

[222] S. Campidelli, R. Cornut, V. Derycke, D. Ausserré, and M. Ausserré, *Supports amplificateurs de contraste utilisant un matériau bidimensionnel*, **2017**.
URL https://bases-brevets.inpi.fr/fr/document/FR3045826.html

[223] S. Campidelli, R. Cornut, V. Derycke, D. Ausserré, and M. Ausserré, *Procédé et appareil de positionnement d'un micro- ou nano-objet sous contrôle visuel*, **2017**.
URL https://bases-brevets.inpi.fr/fr/document/FR3050275.html

[224] J. Azevedo, S. Campidelli, D. He, R. Cornut, M. Bertucchi, S. Sorgues, J.-J. Benattar, C. Colbeau-Justin, and V. Derycke, *Versatile Wafer-Scale Technique for the Formation of Ultrasmooth and Thickness-Controlled Graphene Oxide Films Based on Very Large Flakes*, **Acs Applied Materials & Interfaces**, 7 (38), 21270–21277, **2015**.
URL http://dx.doi.org/10.1021/acsami.5b05540

[225] S. Pei and H.-M. Cheng, *The reduction of graphene oxide*, **Carbon**, 50 (9), 3210–3228, **2012**.
URL http://dx.doi.org/10.1016/j.carbon.2011.11.010

[226] X. Gao, J. Jang, and S. Nagase, *Hydrazine and Thermal Reduction of Graphene Oxide: Reaction Mechanisms, Product Structures, and Reaction Design*, **Journal of Physical Chemistry C**, 114 (2), 832–842, **2010**.
URL http://dx.doi.org/10.1021/jp909284g

[227] S. Rasul, A. Alazmi, K. Jaouen, M. N. Hedhili, and P. M. F. J. Costa, *Rational design of reduced graphene oxide for superior performance of supercapacitor electrodes*, **Carbon**, 111, 774–781, **2017**.
URL http://dx.doi.org/10.1016/j.carbon.2016.10.066

[228] Benjamin, P. and Weaver, C., *Adhesion of metal films to glass*, **Proceedings of the Royal Society of London. Series A. Mathematical and Physical Sciences**, 254 (1277), 177–183, **1960**.
URL http://dx.doi.org/10.1098/rspa.1960.0013

[229] R. C. Williams and R. C. Backus, *The Electron-Micrographic Structure of Shadow-Cast Films and Surfaces*, **Journal of Applied Physics**, 20 (1), 98–106, **1949**.
URL http://dx.doi.org/10.1063/1.1698244

[230] E. R. Dobrovinskaya, L. A. Lytvynov, and V. Pishchik, *Properties of Sapphire*, in *Sapphire: Material, Manufacturing, Applications*, Micro- and Opto-Electronic Materials, Structures, and Systems, Springer US, Boston, MA, **2009**.
URL http://dx.doi.org/10.1007/978-0-387-85695-7_2

[231] L. Gao, F. Lemarchand, and M. Lequime, *Comparison of different dispersion models for single layer optical thin film index determination*, **Thin Solid Films**, 520 (1), 501–509, **2011**.
URL http://dx.doi.org/10.1016/j.tsf.2011.07.028

[232] H. Zhang, Y. Ma, Y. Wan, X. Rong, Z. Xie, W. Wang, and L. Dai, *Measuring the Refractive Index of Highly Crystalline Monolayer MoS_2 with High Confidence*, **Scientific Reports**, 5, 8440, **2015**.
URL http://dx.doi.org/10.1038/srep08440

[233] W. Lee, E. Malmberg, and J. Calvert, *Photodecomposition of diazonium salt solutions*, **Journal of the American Chemical Society**, 83 (8), 1928–1934, **1961**.
URL http://dx.doi.org/10.1021/ja01469a036

[234] L. D. Burke, D. T. Buckley, and J. A. Morrissey, *Novel view of the electrochemistry of gold*, **Analyst**, 119 (5), 841–845, **1994**.
URL http://dx.doi.org/10.1039/AN9941900841

[235] L. D. Burke and P. F. Nugent, *The electrochemistry of gold: I the redox behaviour of the metal in aqueous media*, **Gold Bulletin**, 30 (2), 43–53, **1997**.
URL http://dx.doi.org/10.1007/BF03214756

[236] L. D. Burke and P. F. Nugent, *The electrochemistry of gold: II the electrocatalytic behaviour of the metal in aqueous media*, **Gold Bulletin**, 31 (2), 39–50, **1998**.
URL http://dx.doi.org/10.1007/BF03214760

[237] T. Smith, *The hydrophilic nature of a clean gold surface*, **Journal of Colloid and Interface Science**, 75 (1), 51–55, **1980**.
URL http://dx.doi.org/10.1016/0021-9797(80)90348-3

[238] J. C. Love, L. A. Estroff, J. K. Kriebel, R. G. Nuzzo, and G. M. Whitesides, *Self-Assembled Monolayers of Thiolates on Metals as a Form of Nanotechnology*, **Chemical Reviews**, 105 (4), 1103–1170, **2005**.
URL http://dx.doi.org/10.1021/cr0300789

[239] X.-M. Lin, Y. Cui, Y.-H. Xu, B. Ren, and Z.-Q. Tian, *Surface-enhanced Raman spectroscopy: substrate-related issues*, **Analytical and Bioanalytical Chemistry**, 394 (7), 1729–1745, **2009**.
URL http://dx.doi.org/10.1007/s00216-009-2761-5

[240] L. M. Fischer, M. Tenje, A. R. Heiskanen, N. Masuda, J. Castillo, A. Bentien, J. Émneus, M. H. Jakobsen, and A. Boisen, *Gold cleaning methods for electrochemical detection applications*, **Microelectronic Engineering**, 86 (4), 1282–1285, **2009**.
URL http://dx.doi.org/10.1016/j.mee.2008.11.045

[241] D. E. King, *Oxidation of gold by ultraviolet light and ozone at 25 ° C*, **Journal of Vacuum Science & Technology A**, 13 (3), 1247–1253, **1995**.
URL http://dx.doi.org/10.1116/1.579869

[242] H. Tsai, E. Hu, K. Perng, M. Chen, J.-C. Wu, and Y.-S. Chang, *Instability of gold oxide Au_2O_3*, **Surface Science**, 537 (1), L447–L450, **2003**.
URL http://dx.doi.org/10.1016/S0039-6028(03)00640-X

[243] D. Berman and J. Krim, *Impact of oxygen and argon plasma exposure on the roughness of gold film surfaces*, **Thin Solid Films**, 520 (19), 6201–6206, **2012**.
URL http://dx.doi.org/10.1016/j.tsf.2012.06.033

[244] E. Tokunaga, Y. Nosaka, M. Hirabayashi, and T. Kobayashi, *Pockels effect of water in the electric double layer at the interface between water and transparent electrode*, **Surface Science**, 601 (3), 735–741, **2007**.
URL http://dx.doi.org/10.1016/j.susc.2006.11.001

[245] Y. Nosaka, M. Hirabayashi, T. Kobayashi, and E. Tokunaga, *Gigantic optical Pockels effect in water within the electric double layer at the electrode-solution interface*, **Physical Review B**, 77 (24), 241401, **2008**.
URL http://dx.doi.org/10.1103/PhysRevB.77.241401

[246] H. Kanemaru, Y. Nosaka, A. Hirako, K. Ohkawa, T. Kobayashi, and E. Tokunaga, *Electrooptic effect of water in electric double layer at interface of GaN electrode*, **Optical Review**, 17 (3), 352–356, **2010**.
URL http://dx.doi.org/10.1007/s10043-010-0064-x

[247] H. Kanemaru, S. Yukita, H. Namiki, Y. Nosaka, T. Kobayashi, and E. Tokunaga, *Giant Pockels effect of polar organic solvents and water in the electric double layer on a transparent electrode*, **RSC Advances**, 7 (72), 45682–45690, **2017**.
URL http://dx.doi.org/10.1039/C7RA05875F

[248] Y. Suzuki, K. Osawa, S. Yukita, T. Kobayashi, and E. Tokunaga, *Anomalously large electro-optic Pockels effect at the air-water interface with an electric field applied parallel to the interface*, **Applied Physics Letters**, 108 (19), 191103, **2016**.
URL http://dx.doi.org/10.1063/1.4949273

[249] S. Yukita, Y. Suzuki, N. Shiokawa, T. Kobayashi, and E. Tokunaga, *Mechanisms of the anomalous Pockels effect in bulk water*, **Optical Review**, 25 (2), 205–214, **2018**.
URL http://dx.doi.org/10.1007/s10043-018-0407-6

[250] S. Yukita, N. Shiokawa, H. Kanemaru, H. Namiki, T. Kobayashi, and E. Tokunaga, *Deflection switching of a laser beam by the Pockels effect of water*, **Applied Physics Letters**, 100 (17), 171108, **2012**.
URL http://dx.doi.org/10.1063/1.4705154

[251] I. Z. Kozma, P. Krok, and E. Riedle, *Direct measurement of the group-velocity mismatch and derivation of the refractive-index dispersion for a variety of solvents in the ultraviolet*, **JOSA B**, 22 (7), 1479–1485, **2005**.
URL http://dx.doi.org/10.1364/JOSAB.22.001479

[252] C. E. Shannon, *Communication in the Presence of Noise*, **Proceedings of the IRE**, 37 (1), 10–21, **1949**.
URL http://dx.doi.org/10.1109/JRPROC.1949.232969

[253] A. d. Poulpiquet, B. Goudeau, P. Garrigue, N. Sojic, S. Arbault, T. Doneux, and L. Bouffier, *A snapshot of the electrochemical reaction layer by using 3 dimensionally resolved fluorescence mapping*, **Chemical Science**, 9 (32), 6622–6628, **2018**.
URL http://dx.doi.org/10.1039/C8SC02011F

[254] F. Miomandre, E. Lépicier, S. Munteanu, O. Galangau, J. F. Audibert, R. Méallet-Renault, P. Audebert, and R. B. Pansu, *Electrochemical Monitoring of the Fluorescence Emission of Tetrazine and Bodipy Dyes Using Total Internal Reflection Fluorescence Microscopy Coupled to Electrochemistry*, **ACS Applied Materials & Interfaces**, 3 (3), 690–696, **2011**.
URL http://dx.doi.org/10.1021/am100980u

[255] S. Mao, H. Pu, and J. Chen, *Graphene oxide and its reduction: modeling and experimental progress*, **RSC Advances**, 2 (7), 2643–2662, **2012**.
URL http://dx.doi.org/10.1039/C2RA00663D

[256] T. Kuila, A. K. Mishra, P. Khanra, N. H. Kim, and J. H. Lee, *Recent advances in the efficient reduction of graphene oxide and its application as energy storage electrode materials*, **Nanoscale**, 5 (1), 52–71, **2012**.
URL http://dx.doi.org/10.1039/C2NR32703A

[257] C. K. Chua and M. Pumera, *Chemical reduction of graphene oxide: a synthetic chemistry viewpoint*, **Chemical Society Reviews**, 43 (1), 291–312, **2014**.
URL http://dx.doi.org/10.1039/c3cs60303b

[258] R. K. Singh, R. Kumar, and D. P. Singh, *Graphene oxide: strategies for synthesis, reduction and frontier applications*, **RSC Advances**, 6 (69), 64993–65011, **2016**.
URL http://dx.doi.org/10.1039/C6RA07626B

[259] A. Viinikanoja, Z. Wang, J. Kauppila, and C. Kvarnström, *Electrochemical reduction of graphene oxide and its in situ spectroelectrochemical characterization*, **Physical Chemistry Chemical Physics**, 14 (40), 14003–14009, **2012**.
URL http://dx.doi.org/10.1039/C2CP42253K

[260] J. Zhao, S. Pei, W. Ren, L. Gao, and H.-M. Cheng, *Efficient Preparation of Large-Area Graphene Oxide Sheets for Transparent Conductive Films*, **ACS Nano**, 4 (9), 5245–5252, **2010**.
URL http://dx.doi.org/10.1021/nn1015506

[261] Y. Shao, J. Wang, M. Engelhard, C. Wang, and Y. Lin, *Facile and controllable electrochemical reduction of graphene oxide and its applications*, **Journal of Materials Chemistry**, 20 (4), 743–748, **2010**.
URL http://dx.doi.org/10.1039/B917975E

[262] D. Yang, A. Velamakanni, G. Bozoklu, S. Park, M. Stoller, R. D. Piner, S. Stankovich, I. Jung, D. A. Field, C. A. Ventrice, and R. S. Ruoff, *Chemical analysis of graphene oxide films after heat and chemical treatments by X-ray photoelectron and Micro-Raman spectroscopy*, **Carbon**, 47 (1), 145–152, **2009**.
URL http://dx.doi.org/10.1016/j.carbon.2008.09.045

[263] D. Belanger and J. Pinson, *Electrografting: a powerful method for surface modification*, **Chemical Society Reviews**, 40 (7), 3995–4048, **2011**.
URL http://dx.doi.org/10.1039/c0cs00149j

[264] R. L. McCreery, *Molecular Electronic Junctions*, **Chemistry of Materials**, 16 (23), 4477–4496, **2004**.
URL http://dx.doi.org/10.1021/cm049517q

[265] V. Stockhausen, J. Ghilane, P. Martin, G. Trippé-Allard, H. Randriamahazaka, and J.-C. Lacroix, *Grafting Oligothiophenes on Surfaces by Diazonium Electroreduction: A Step toward Ultrathin Junction with Well-Defined Metal/Oligomer Interface*, **Journal of the American Chemical Society**, 131 (41), 14920–14927, **2009**.
URL http://dx.doi.org/10.1021/ja9047009

[266] H. Casademont, L. Fillaud, X. Lefèvre, B. Jousselme, and V. Derycke, *Electrografted Fluorinated Organic Ultrathin Film as Efficient Gate Dielectric in MoS_2 Transistors*, **The Journal of Physical Chemistry C**, 120 (17), 9506–9510, **2016**.
URL http://dx.doi.org/10.1021/acs.jpcc.6b01630

[267] A. Chaussé, M. M. Chehimi, N. Karsi, J. Pinson, F. Podvorica, and C. Vautrin-Ul, *The Electrochemical Reduction of Diazonium Salts on Iron Electrodes. The Formation of Covalently Bonded Organic Layers and Their Effect on Corrosion*, **Chemistry of Materials**, 14 (1), 392–400, **2002**.
URL http://dx.doi.org/10.1021/cm011212d

[268] C. Cao, Y. Zhang, C. Jiang, M. Qi, and G. Liu, *Advances on Aryldiazonium Salt Chemistry Based Interfacial Fabrication for Sensing Applications*, **ACS Applied Materials & Interfaces**, 9 (6), 5031–5049, **2017**.
URL http://dx.doi.org/10.1021/acsami.6b16108

[269] B. D. Assresahegn, T. Brousse, and D. Bélanger, *Advances on the use of diazonium chemistry for functionalization of materials used in energy storage systems*, **Carbon**, 92, 362–381, **2015**.
URL http://dx.doi.org/10.1016/j.carbon.2015.05.030

[270] F. Alloin, L. Crepel, L. Cointeaux, J.-C. Leprêtre, F. Fusalba, and S. Martinet, *The Interest of Diazonium Chemistry for Aqueous Lithium-Ion Battery*, **Journal of The Electrochemical Society**, 160 (5), A3171–A3178, **2013**.
URL http://dx.doi.org/10.1149/2.026305jes

[271] J. Pinson and F. Podvorica, *Attachment of organic layers to conductive or semiconductive surfaces by reduction of diazonium salts*, **Chemical Society Reviews**, 34 (5), 429–439, **2005**.
URL http://dx.doi.org/10.1039/B406228K

[272] T. Menanteau, M. Dias, E. Levillain, A. J. Downard, and T. Breton, *Electrografting via Diazonium Chemistry: The Key Role of the Aryl Substituent in the Layer Growth Mechanism*, **The Journal of Physical Chemistry C**, 120 (8), 4423–4429, **2016**.
URL http://dx.doi.org/10.1021/acs.jpcc.5b12565

[273] M. C. R. González, P. Carro, L. Vázquez, and A. H. Creus, *Mapping nanometric electronic property changes induced by an aryl diazonium sub-monolayer on HOPG*, **Physical Chemistry Chemical Physics**, 18 (42), 29218–29225, **2016**.
URL http://dx.doi.org/10.1039/C6CP05910D

[274] T. Menanteau, E. Levillain, A. J. Downard, and T. Breton, *Evidence of monolayer formation via diazonium grafting with a radical scavenger: electrochemical, AFM and XPS monitoring*, **Physical Chemistry Chemical Physics**, 17 (19), 13137–13142, **2015**.
URL http://dx.doi.org/10.1039/C5CP01401H

[275] D. R. Jayasundara, R. J. Cullen, L. Soldi, and P. E. Colavita, *In Situ Studies of the Adsorption Kinetics of 4-Nitrobenzenediazonium Salt on Gold*, **Langmuir**, 27 (21), 13029–13036, **2011**.
URL http://dx.doi.org/10.1021/la202862p

[276] T. J. Neubert, F. Rösicke, G. Sun, S. Janietz, M. A. Gluba, K. Hinrichs, N. H. Nickel, and J. Rappich, *Functionalization of gold and graphene electrodes by p-maleimido-phenyl towards thiol-sensing systems investigated by EQCM and IR ellipsometric spectroscopy*, **Applied Surface Science**, 421, 755–760, **2017**.
URL http://dx.doi.org/10.1016/j.apsusc.2017.04.235

[277] S. Chernyy, A. Bousquet, K. Torbensen, J. Iruthayaraj, M. Ceccato, S. U. Pedersen, and K. Daasbjerg, *Elucidation of the Mechanism of Redox Grafting of Diazotated Anthraquinone*, **Langmuir**, 28 (25), 9573–9582, **2012**.
URL http://dx.doi.org/10.1021/la301391s

[278] A. Laforgue, T. Addou, and D. Bélanger, *Characterization of the Deposition of Organic Molecules at the Surface of Gold by the Electrochemical Reduction of Aryldiazonium Cations*, **Langmuir**, 21 (15), 6855–6865, **2005**.
URL http://dx.doi.org/10.1021/la047369c

[279] X. Shan, U. Patel, S. Wang, R. Iglesias, and N. Tao, *Imaging Local Electrochemical Current via Surface Plasmon Resonance*, **Science**, 327 (5971), 1363–1366, **2010**.
URL http://dx.doi.org/10.1126/science.1186476

[280] O. Andersson, C. Ulrich, F. Björefors, and B. Liedberg, *Imaging SPR for detection of local electrochemical processes on patterned surfaces*, **Sensors and Actuators B: Chemical**, 134 (2), 545–550, **2008**.
URL http://dx.doi.org/10.1016/j.snb.2008.05.042

[281] C. A. Mandon, L. J. Blum, and C. A. Marquette, *Aryl Diazonium for Biomolecules Immobilization onto SPRi Chips*, **ChemPhysChem**, 10 (18), 3273–3277, **2009**.
URL http://dx.doi.org/10.1002/cphc.200900599

[282] B. P. Corgier, S. Bellon, M. Anger-Leroy, L. J. Blum, and C. A. Marquette, *Protein-Diazonium Adduct Direct Electrografting onto SPRi-Biochip*, **Langmuir**, 25 (16), 9619–9623, **2009**.
URL http://dx.doi.org/10.1021/la900762s

[283] X. Shan, I. Díez-Pérez, L. Wang, P. Wiktor, Y. Gu, L. Zhang, W. Wang, J. Lu, S. Wang, Q. Gong, J. Li, and N. Tao, *Imaging the electrocatalytic activity of single nanoparticles*, **Nature Nanotechnology**, 7 (10), 668–672, **2012**.
URL http://dx.doi.org/10.1038/nnano.2012.134

[284] A. Cumurcu, X. Feng, L. D. Ramos, M. A. Hempenius, P. Schön, and G. J. Vancso, *Sub-nanometer expansions of redox responsive polymer films monitored by imaging ellipsometry*, **Nanoscale**, 6 (20), 12089–12095, **2014**.
URL http://dx.doi.org/10.1039/C4NR02852J

[285] Y. Yu and G. Jin, *Influence of electrostatic interaction on fibrinogen adsorption on gold studied by imaging ellipsometry combined with electrochemical methods*, **Journal of Colloid and Interface Science**, 283 (2), 477–481, **2005**.
URL http://dx.doi.org/10.1016/j.jcis.2004.09.021

[286] S. Munteanu, N. Garraud, J. P. Roger, F. Amiot, J. Shi, Y. Chen, C. Combellas, and F. Kanoufi, *In Situ, Real Time Monitoring of Surface Transformation: Ellipsometric Microscopy Imaging of Electrografting at Microstructured Gold Surfaces*, **Analytical Chemistry**, 85 (4), 1965–1971, **2013**.
URL http://dx.doi.org/10.1021/ac3034085

[287] S. Munteanu, J. Paul Roger, Y. Fedala, F. Amiot, C. Combellas, G. Tessier, and F. Kanoufi, *Mapping fluxes of radicals from the combination of electrochemical activation and optical microscopy*, **Faraday Discussions**, 164 (0), 241–258, **2013**.
URL http://dx.doi.org/10.1039/C3FD00024A

[288] M. Ceccato, L. T. Nielsen, J. Iruthayaraj, M. Hinge, S. U. Pedersen, and K. Daasbjerg, *Nitrophenyl Groups in Diazonium-Generated Multilayered Films: Which are Electrochemically Responsive?*, **Langmuir**, 26 (13), 10812–10821, **2010**.
URL http://dx.doi.org/10.1021/la1006428

[289] T. Menanteau, E. Levillain, and T. Breton, *Electrografting via Diazonium Chemistry: From Multilayer to Monolayer Using Radical Scavenger*, **Chemistry of Materials**, 25 (14), 2905–2909, **2013**.
URL http://dx.doi.org/10.1021/cm401512c

[290] A. Ghorbal, F. Grisotto, M. Laudé, J. Charlier, and S. Palacin, *The in situ characterization and structuring of electrografted polyphenylene films on silicon surfaces. An AFM and XPS study*, **Journal of Colloid and Interface Science**, 328 (2), 308–313, **2008**.
URL http://dx.doi.org/10.1016/j.jcis.2008.09.033

[291] A. Benedetto, M. Balog, P. Viel, F. Le Derf, M. Sallé, and S. Palacin, *Electro-reduction of diazonium salts on gold: Why do we observe multi-peaks?*, **Electrochimica Acta**, 53 (24), 7117–7122, **2008**.
URL http://dx.doi.org/10.1016/j.electacta.2008.05.001

[292] S. Bouden, J. Pinson, and C. Vautrin-Ul, *Electrografting of diazonium salts: A kinetics study*, **Electrochemistry Communications**, 81, 120–123, **2017**.
URL http://dx.doi.org/10.1016/j.elecom.2017.06.007

[293] Y.-P. Lin, C. H. Bennett, T. Cabaret, D. Vodenicarevic, D. Chabi, D. Querlioz, B. Jousselme, V. Derycke, and J.-O. Klein, *Physical Realization of a Supervised Learning System Built with Organic Memristive Synapses*, **Scientific Reports**, 6, 31932, **2016**.
URL http://dx.doi.org/10.1038/srep31932

[294] F. Lebon, R. Cornut, V. Derycke, and B. Jousselme, *Fine growth control of electrografted homogeneous thin films on patterned gold electrodes*, **Electrochimica Acta**, 318, 754–761, **2019**.
URL http://dx.doi.org/10.1016/j.electacta.2019.06.115

[295] M. Quintana, E. Vazquez, and M. Prato, *Organic Functionalization of Graphene in Dispersions*, **Accounts of Chemical Research**, 46 (1), 138–148, **2013**.
URL http://dx.doi.org/10.1021/ar300138e

[296] X. Chen and A. R. McDonald, *Functionalization of Two-Dimensional Transition-Metal Dichalcogenides*, **Advanced Materials**, 28 (27), 5738–5746, **2016**.
URL http://dx.doi.org/10.1002/adma.201505345

[297] D. R. Dreyer, S. Park, C. W. Bielawski, and R. S. Ruoff, *The chemistry of graphene oxide*, **Chemical Society Reviews**, 39 (1), 228–240, **2009**.
URL http://dx.doi.org/10.1039/B917103G

[298] P. Huang, L. Jing, H. Zhu, and X. Gao, *Diazonium Functionalized Graphene: Microstructure, Electric, and Magnetic Properties*, **Accounts of Chemical Research**, 46 (1), 43–52, **2013**.
URL http://dx.doi.org/10.1021/ar300070a

[299] G. L. C. Paulus, Q. H. Wang, and M. S. Strano, *Covalent Electron Transfer Chemistry of Graphene with Diazonium Salts*, **Accounts of Chemical Research**, 46 (1), 160–170, **2013**.
URL http://dx.doi.org/10.1021/ar300119z

[300] J. Greenwood, T. H. Phan, Y. Fujita, Z. Li, O. Ivasenko, W. Vanderlinden, H. Van Gorp, W. Frederickx, G. Lu, K. Tahara, Y. Tobe, H. Uji-i, S. F. L. Mertens, and S. De Feyter, *Covalent Modification of Graphene and Graphite Using Diazonium Chemistry: Tunable Grafting and Nanomanipulation*, **ACS Nano**, 9 (5), 5520–5535, **2015**.
URL http://dx.doi.org/10.1021/acsnano.5b01580

[301] K. C. Knirsch, N. C. Berner, H. C. Nerl, C. S. Cucinotta, Z. Gholamvand, N. McEvoy, Z. Wang, I. Abramovic, P. Vecera, M. Halik, S. Sanvito, G. S. Duesberg, V. Nicolosi, F. Hauke, A. Hirsch, J. N. Coleman, and C. Backes, *Basal-Plane Functionalization of Chemically Exfoliated Molybdenum Disulfide by Diazonium Salts*, **ACS Nano**, 9 (6), 6018–6030, **2015**.
URL http://dx.doi.org/10.1021/acsnano.5b00965

[302] W. Gao, M. Majumder, L. B. Alemany, T. N. Narayanan, M. A. Ibarra, B. K. Pradhan, and P. M. Ajayan, *Engineered Graphite Oxide Materials for Application in Water Purification*, **ACS Applied Materials & Interfaces**, 3 (6), 1821–1826, **2011**.
URL http://dx.doi.org/10.1021/am200300u

[303] A. G. Güell, N. Ebejer, M. E. Snowden, J. V. Macpherson, and P. R. Unwin, *Structural Correlations in Heterogeneous Electron Transfer at Monolayer and Multilayer Graphene Electrodes*, **Journal of the American Chemical Society**, 134 (17), 7258–7261, **2012**.
URL http://dx.doi.org/10.1021/ja3014902

[304] M. Velický, D. F. Bradley, A. J. Cooper, E. W. Hill, I. A. Kinloch, A. Mishchenko, K. S. Novoselov, H. V. Patten, P. S. Toth, A. T. Valota, S. D. Worrall, and R. A. W. Dryfe, *Electron Transfer Kinetics on Mono- and Multilayer Graphene*, **ACS Nano**, 8 (10), 10089–10100, **2014**.
URL http://dx.doi.org/10.1021/nn504298r

[305] A. T. Valota, P. S. Toth, Y.-J. Kim, B. H. Hong, I. A. Kinloch, K. S. Novoselov, E. W. Hill, and R. A. W. Dryfe, *Electrochemical investigation of chemical vapour deposition monolayer and bilayer graphene on the microscale*, **Electrochimica Acta**, 110, 9–15, **2013**.
URL http://dx.doi.org/10.1016/j.electacta.2013.03.187

[306] D. Hernández-Santos, M. B. González-García, and A. C. García, *Metal-Nanoparticles Based Electroanalysis*, **Electroanalysis**, 14 (18), 1225–1235, **2002**.
URL http://dx.doi.org/10.1002/1521-4109(200210)14:18<1225::AID-ELAN1225>3.0.CO;2-Z

[307] J. N. Anker, W. P. Hall, O. Lyandres, N. C. Shah, J. Zhao, and R. P. Van Duyne, *Biosensing with plasmonic nanosensors*, **Nature Materials**, 7 (6), 442–453, **2008**.
URL http://dx.doi.org/10.1038/nmat2162

[308] M. T. M. Koper, *Structure sensitivity and nanoscale effects in electrocatalysis*, **Nanoscale**, 3 (5), 2054–2073, **2011**.
URL http://dx.doi.org/10.1039/C0NR00857E

[309] Q. A. Pankhurst, J. Connolly, S. K. Jones, and J. Dobson, *Applications of magnetic nanoparticles in biomedicine*, **Journal of Physics D: Applied Physics**, 36 (13), R167–R181, **2003**.
URL http://dx.doi.org/10.1088/0022-3727/36/13/201

[310] B. D. Chithrani, A. A. Ghazani, and W. C. W. Chan, *Determining the Size and Shape Dependence of Gold Nanoparticle Uptake into Mammalian Cells*, **Nano Letters**, 6 (4), 662–668, **2006**.
URL http://dx.doi.org/10.1021/nl052396o

[311] C. Bosch-Navarro, J. P. Rourke, and N. R. Wilson, *Controlled electrochemical and electroless deposition of noble metal nanoparticles on graphene*, **RSC Advances**, 6 (77), 73790–73796, **2016**.
URL http://dx.doi.org/10.1039/C6RA14836K

[312] J. Ustarroz, U. Gupta, A. Hubin, S. Bals, and H. Terryn, *Electrodeposition of Ag nanoparticles onto carbon coated TEM grids: A direct approach to study early stages of nucleation*, **Electrochemistry Communications**, 12 (12), 1706–1709, **2010**.
URL http://dx.doi.org/10.1016/j.elecom.2010.10.002

[313] H. E. M. Hussein, R. J. Maurer, H. Amari, J. J. P. Peters, L. Meng, R. Beanland, M. E. Newton, and J. V. Macpherson, *Tracking Metal Electrodeposition Dynamics from Nucleation and Growth of a Single Atom to a Crystalline Nanoparticle*, **ACS Nano**, 12 (7), 7388–7396, **2018**.
URL http://dx.doi.org/10.1021/acsnano.8b04089

[314] R. Tel-Vered and A. J. Bard, *Generation and Detection of Single Metal Nanoparticles Using Scanning Electrochemical Microscopy Techniques*, **The Journal of Physical Chemistry B**, 110 (50), 25279–25287, **2006**.
URL http://dx.doi.org/10.1021/jp064434d

[315] J. Velmurugan, J.-M. Noël, W. Nogala, and M. V. Mirkin, *Nucleation and growth of metal on nanoelectrodes*, **Chemical Science**, 3 (11), 3307–3314, **2012**.
URL http://dx.doi.org/10.1039/C2SC21005C

[316] C. M. Hill and S. Pan, *A Dark-Field Scattering Spectroelectrochemical Technique for Tracking the Electrodeposition of Single Silver Nanoparticles*, **Journal of the American Chemical Society**, 135 (46), 17250–17253, **2013**.
URL http://dx.doi.org/10.1021/ja4075387

[317] C. Batchelor-McAuley, A. Martinez-Marrades, K. Tschulik, A. N. Patel, C. Combellas, F. Kanoufi, G. Tessier, and R. G. Compton, *Simultaneous electrochemical and 3D optical imaging of silver nanoparticle oxidation*, **Chemical Physics Letters**, 597, 20–25, **2014**.
URL http://dx.doi.org/10.1016/j.cplett.2014.02.007

[318] A. N. Patel, A. Martinez-Marrades, V. Brasiliense, D. Koshelev, M. Besbes, R. Kuszelewicz, C. Combellas, G. Tessier, and F. Kanoufi, *Deciphering the Elementary Steps of Transport-Reaction Processes at Individual Ag Nanoparticles by 3D Superlocalization Microscopy*, **Nano Letters**, 15 (10), 6454–6463, **2015**.
URL http://dx.doi.org/10.1021/acs.nanolett.5b02921

[319] C. M. Hill, R. Bennett, C. Zhou, S. Street, J. Zheng, and S. Pan, *Single Ag Nanoparticle Spectroelectrochemistry via Dark-Field Scattering and Fluorescence Microscopies*, **The Journal of Physical Chemistry C**, 119 (12), 6760–6768, **2015**.
URL http://dx.doi.org/10.1021/jp511637a

[320] Y. Fang, W. Wang, X. Wo, Y. Luo, S. Yin, Y. Wang, X. Shan, and N. Tao, *Plasmonic Imaging of Electrochemical Oxidation of Single Nanoparticles*, **Journal of the American Chemical Society**, 136 (36), 12584–12587, **2014**.
URL http://dx.doi.org/10.1021/ja507097y

[321] K. Wonner, M. V. Evers, and K. Tschulik, *The electrochemical dissolution of single silver nanoparticles enlightened by hyperspectral dark-field microscopy*, **Electrochimica Acta**, 301, 458–464, **2019**.
URL http://dx.doi.org/10.1016/j.electacta.2019.01.129

[322] V. Brasiliense, A. N. Patel, A. Martinez-Marrades, J. Shi, Y. Chen, C. Combellas, G. Tessier, and F. Kanoufi, *Correlated Electrochemical and Optical Detection Reveals the Chemical Reactivity of Individual Silver Nanoparticles*, **Journal of the American Chemical Society**, 138 (10), 3478–3483, **2016**.
URL http://dx.doi.org/10.1021/jacs.5b13217

[323] V. Brasiliense, J. Clausmeyer, P. Berto, G. Tessier, C. Combellas, W. Schuhmann, and F. Kanoufi, *Monitoring Cobalt-Oxide Single Particle Electrochemistry with Subdiffraction Accuracy*, **Analytical Chemistry**, 90 (12), 7341–7348, **2018**.
URL http://dx.doi.org/10.1021/acs.analchem.8b00649

[324] V. Brasiliense, J. Clausmeyer, A. L. Dauphin, J.-M. Noël, P. Berto, G. Tessier, W. Schuhmann, and F. Kanoufi, *Opto-electrochemical In Situ Monitoring of the Cathodic Formation of Single Cobalt Nanoparticles*, **Angewandte Chemie International Edition**, 56 (35), 10598–10601, **2017**.
URL http://dx.doi.org/10.1002/anie.201704394

[325] V. Brasiliense, P. Berto, C. Combellas, G. Tessier, and F. Kanoufi, *Electrochemistry of Single Nanodomains Revealed by Three-Dimensional Holographic Microscopy*, **Accounts of Chemical Research**, 49 (9), 2049–2057, **2016**.
URL http://dx.doi.org/10.1021/acs.accounts.6b00335

[326] D. Grujicic and B. Pesic, *Electrodeposition of copper: the nucleation mechanisms*, **Electrochimica Acta**, 47 (18), 2901–2912, **2002**.
URL http://dx.doi.org/10.1016/S0013-4686(02)00161-5

[327] P.-C. Hsu, Y. Chu, J.-M. Yi, C.-L. Wang, S.-R. Wu, Y. Hwu, and G. Margaritondo, *Dynamical growth behavior of copper clusters during electrodeposition*, **Applied Physics Letters**, 97 (3), 033101, **2010**.
URL http://dx.doi.org/10.1063/1.3464550

[328] E. Gileadi and V. Tsionsky, *Studies of Electroplating Using an EQCM. I. Copper and Silver on Gold*, **Journal of The Electrochemical Society**, 147 (2), 567–574, **2000**.
URL http://dx.doi.org/10.1149/1.1393234

[329] M. Nagar, A. Radisic, K. Strubbe, and P. M. Vereecken, *The Effect of the Substrate Characteristics on the Electrochemical Nucleation and Growth of Copper*, **Journal of The Electrochemical Society**, 163 (12), D3053–D3061, **2016**.
URL http://dx.doi.org/10.1149/2.0081612jes

[330] F. Qiao and A. C. West, *The impact of cations on nucleus density during copper electrodeposition*, **Electrochimica Acta**, 150, 8–14, **2014**.
URL http://dx.doi.org/10.1016/j.electacta.2014.10.135

[331] S. C. S. Lai, R. A. Lazenby, P. M. Kirkman, and P. R. Unwin, *Nucleation, aggregative growth and detachment of metal nanoparticles during electrodeposition at electrode surfaces*, **Chemical Science**, 6 (2), 1126–1138, **2015**.
URL http://dx.doi.org/10.1039/C4SC02792B

[332] D. J. Lomax and R. A. W. Dryfe, *Electrodeposition of Au on basal plane graphite and graphene*, **Journal of Electroanalytical Chemistry**, 819, 374–383, **2018**.
URL http://dx.doi.org/10.1016/j.jelechem.2017.11.023

[333] P. Lammel, B. Torun, C. Kleber, and G. Grundmeier, *In-situ AFM study of the electrodeposition of copper on plasma modified carbon fibre-reinforced polymer surfaces*, **Surface and Coatings Technology**, 221, 22–28, **2013**.
URL http://dx.doi.org/10.1016/j.surfcoat.2013.01.022

[334] Y. Su, E. Prestat, C. Hu, V. K. Puthiyapura, M. Neek-Amal, H. Xiao, K. Huang, V. G. Kravets, S. J. Haigh, C. Hardacre, F. M. Peeters, and R. R. Nair, *Self-Limiting Growth of Two-Dimensional Palladium between Graphene Oxide Layers*, **Nano Letters**, 19 (7), 4678–4683, **2019**.
URL http://dx.doi.org/10.1021/acs.nanolett.9b01733

[335] S. Wu, Z. Yin, Q. He, G. Lu, Q. Yan, and H. Zhang, *Nucleation Mechanism of Electrochemical Deposition of Cu on Reduced Graphene Oxide Electrodes*, **The Journal of Physical Chemistry C**, 115 (32), 15973–15979, **2011**.
URL http://dx.doi.org/10.1021/jp201667p

[336] M. J. Williamson, R. M. Tromp, P. M. Vereecken, R. Hull, and F. M. Ross, *Dynamic microscopy of nanoscale cluster growth at the solid–liquid interface*, **Nature Materials**, 2 (8), 532, **2003**.
URL http://dx.doi.org/10.1038/nmat944

[337] S. Manne, P. K. Hansma, J. Massie, V. B. Elings, and A. A. Gewirth, *Atomic-Resolution Electrochemistry with the Atomic Force Microscope: Copper Deposition on Gold*, **Science**, 251 (4990), 183–186, **1991**.
URL http://dx.doi.org/10.1126/science.251.4990.183

[338] S.-T. Yang, Y. Chang, H. Wang, G. Liu, S. Chen, Y. Wang, Y. Liu, and A. Cao, *Folding/aggregation of graphene oxide and its application in Cu^{2+} removal*, **Journal of Colloid and Interface Science**, 351 (1), 122–127, **2010**.
URL http://dx.doi.org/10.1016/j.jcis.2010.07.042

[339] T. J. Stockmann, J.-F. Lemineur, H. Liu, C. Cometto, M. Robert, C. Combellas, and F. Kanoufi, *Single $LiBH_4$ nanocrystal stochastic impacts at a micro water/ionic liquid interface*, **Electrochimica Acta**, 299, 222–230, **2019**.
URL http://dx.doi.org/10.1016/j.electacta.2018.12.105

[340] V. Sundaresan, K. Marchuk, Y. Yu, E. J. Titus, A. J. Wilson, C. M. Armstrong, B. Zhang, and K. A. Willets, *Visualizing and Calculating Tip–Substrate Distance in Nanoscale Scanning Electrochemical Microscopy Using 3-Dimensional Super-Resolution Optical Imaging*, **Analytical Chemistry**, 89 (1), 922–928, **2017**.
URL http://dx.doi.org/10.1021/acs.analchem.6b04073

[341] L. Bouffier and T. Doneux, *Coupling electrochemistry with in situ fluorescence (confocal) microscopy*, **Current Opinion in Electrochemistry**, 6 (1), 31–37, **2017**.
URL http://dx.doi.org/10.1016/j.coelec.2017.06.015

[342] T. Yuan and W. Wang, *Studying the electrochemistry of single nanoparticles with surface plasmon resonance microscopy*, **Current Opinion in Electrochemistry**, **2017**.
URL http://dx.doi.org/10.1016/j.coelec.2017.06.009

[343] T. Bourgeteau, *Development of hybrid photocathodes for solar hydrogen production*, Ph.D. thesis, Ecole Polytechnique, **2015**.
URL https://tel.archives-ouvertes.fr/tel-01870902

[344] N. Morimoto, T. Kubo, and Y. Nishina, *Tailoring the Oxygen Content of Graphite and Reduced Graphene Oxide for Specific Applications*, **Scientific Reports**, 6, 21715, **2016**.
URL http://dx.doi.org/10.1038/srep21715

[345] J. Azevedo, *Assemblage contrôlé de graphène et de nanotubes de carbone par transfert de films de tensioactifs pour le photovoltaïque*, Ph.D. thesis, Université Paris-Sud, **2013**.
URL https://tel.archives-ouvertes.fr/tel-00846430/

[346] H. Casademont, *Semi-conducteurs 2D pour l'électronique flexible : évaluation du potentiel du MoS_2 monocouche en tant que matériau de canal*, Ph.D. thesis, Université Paris-Saclay, **2016**.
URL https://tel.archives-ouvertes.fr/tel-01428418

Résumé en français

La microscopie optique sur substrats antireflets est un outil de caractérisation simple et puissant qui a notamment permis l'isolation du graphène en 2004 malgré son épaisseur mono-atomique.

Depuis, le domaine d'étude des matériaux bidimensionnels (2D) s'est rapidement développé, tant au niveau fondamental qu'appliqué. Les matériaux 2D ont de très nombreuses propriétés intéressantes (optiques, électriques, chimiques, mécaniques, etc.) et sont envisagé pour de nombreuses applications. De par leur épaisseur nanométrique, leur caractérisation est difficile. Il est donc nécessaire de combiner plusieurs techniques pour obtenir des informations complémentaires. De plus, les matériaux 2D sont hétérogènes (nombre de couches, bords, défauts, etc.) et leur synthèse, leur transfert sur différents substrats et leur vieillissement éventuel produisent des matériaux avec des propriétés extrêmement différentes. Pour certaines applications, cette hétérogénéité confère aux matériaux d'excellentes propriétés. Par exemple, les défauts et les bords du graphène ou du MoS_2 sont responsables de leurs propriétés catalytiques. Il est donc essentiel de caractériser localement les matériaux 2D afin de comprendre les relations entre structures et propriétés, et permettre par la suite le design de dispositifs plus efficaces par la fabrication de matériaux mieux contrôlés.

La plupart des techniques actuelles de caractérisations locales des matériaux 2D sont basées sur les microscopies électronique ou les microscopies à sondes locales. Néanmoins la découverte du graphène n'a été possible qu'avec l'aide d'un microscope optique et grâce à l'utilisation d'un substrat antireflet (300 nm SiO_2/Si) qui rend le graphène visible au microscope et permet de localiser les feuillets à étudier par d'autres techniques.

Dans un premier chapitre, cette thèse présente les méthodes de caractérisations locales de matériaux 2D avec une attention particulière pour les méthodes optiques, les caractérisations *in situ* et les méthodes ne nécessitant pas de sondes locales.

Les techniques utilisées pour caractériser les matériaux 2D plus spécifiquement étudiés dans cette thèse sont également considérés plus en détails. Ces matériaux sont l'oxyde de graphène (GO) et l'oxyde de graphène réduit (rGO), ainsi que les monocouches de dichalcogénures de métaux de transition (Transition Metal Dichalcogenide, TMDs) tels que le disulfure de molybdène (MoS_2) et le disulfure de tungstène (WS_2).

Cette thèse se consacre à une technique récente de microscopie optique à fort contraste, nommée "Backside Absorbing Layer Microscopy" (BALM). Cette technique a été proposée par le Prof. D. Aussérré de l'université du Maine, et est basée sur l'utilisation originale de couches antireflets très minces (2-5 nm) et fortement absorbantes (métalliques), tel que présenté sur la figure R.1.a.

Dans le second chapitre, le principe des revêtements antireflets utilisés pour l'observation du graphène en 2004 et d'autres matériaux par la suite est tout d'abord décrit. Il est basé sur le choix d'un revêtement transparent ayant une épaisseur et des propriétés optiques définies par les équations de Fresnel, de sorte que la lumière réfléchie par le substrat soit quasi nulle. Ce type de revêtement produit des images très contrastées des matériaux déposés à leur surface car le ration entre la lumière réfléchie par le substrat et par le matériau d'étude est très grand. BALM se distingue par l'utilisation d'un revêtement très absorbant (souvent métallique comme l'or), ce qui modifie les paramètres issus des équations de Fresnel pour obtenir des conditions antireflet. Il faut en effet que l'épaisseur du métal soit nanométrique et que la lumière passe d'abord par le milieu ayant le plus grand indice de réfraction, qui est dans ce cas un substrat en verre. Le substrat est ainsi composé d'une fine couche d'or (2-5 nm) déposée sur un substrat en verre et l'observation se fait en configuration inversée, comme présenté sur la figure R.1.b. Ainsi lors de l'ajout d'un matériau à la surface de l'or, il apparaît avec un fort contraste (figure R.1.c).

Les expériences présentées ensuite ont notamment pour but d'évaluer les mérites de la technique BALM pour l'étude des matériaux 2D et de leur réactivité chimique et électrochimique.

Ainsi, nous avons tout d'abord étudié les différents leviers permettant d'améliorer les conditions d'observation des matériaux 2D pour deux cas modèles : l'oxyde de graphène et les monocouches de MoS_2. Les trois paramètres permettant d'ajuster les conditions d'antireflet sont l'épaisseur du revêtement, l'indice de réfraction des milieux incidents et émergents ainsi que la longueur d'onde. L'analyse du rôle de l'épaisseur

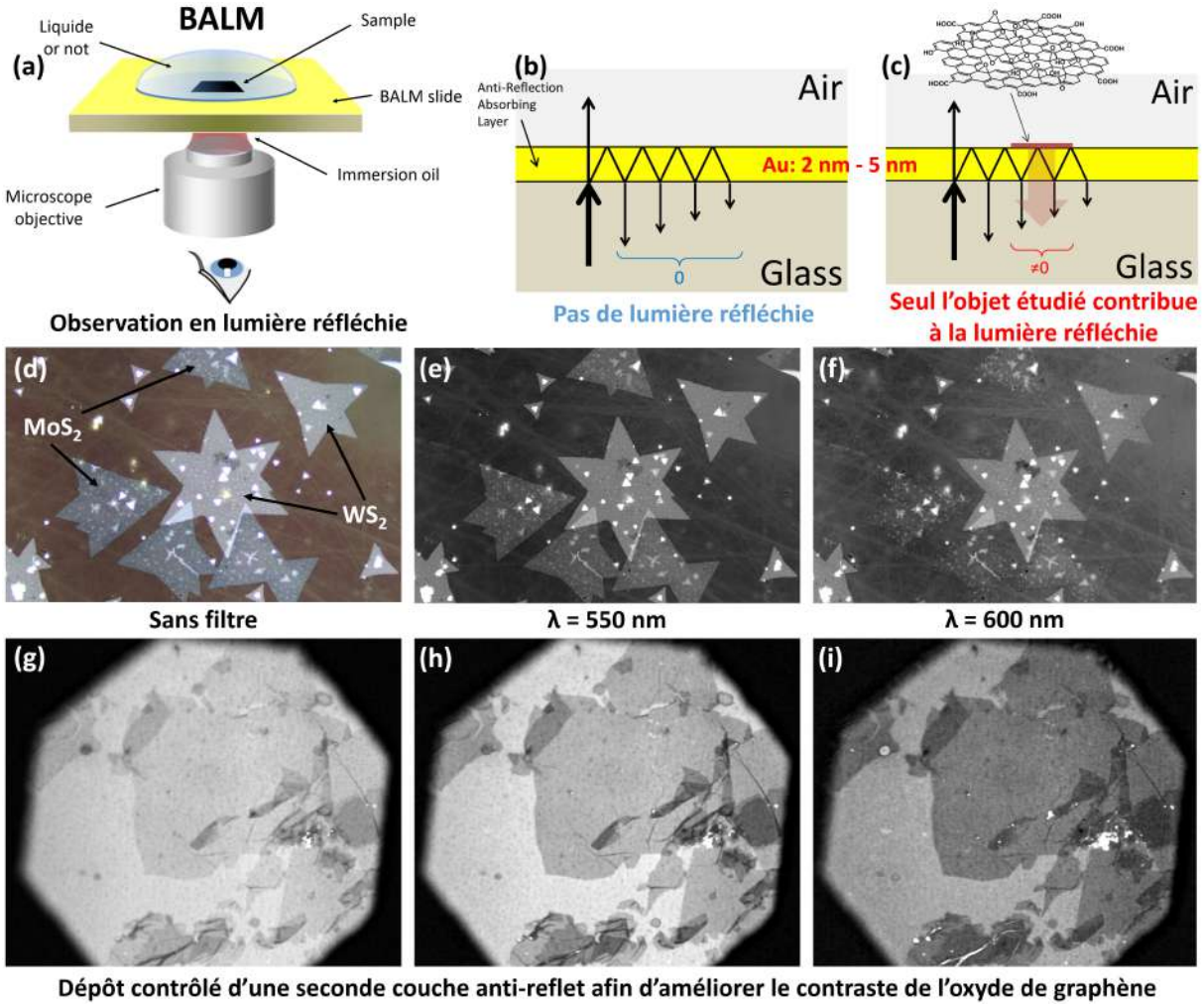

FIGURE R.1: (a-c) Représentation schématique du principe de la microscopie optique BALM. (b) La fine couche d'or associée à la configuration inversée (lumière venant du verre) produit des interférences destructives. Il n'y a donc presque pas de lumière réfléchie. (c) Si un matériau est déposé à la surface, il est observé avec un très bon contraste. **(d-f)** Images BALM d'une surface présentant des monocouches de MoS_2 et de WS_2. Pour λ = 600 nm le contraste de la monocouche de MoS_2 est presque nul par rapport au substrat ce qui permet de différencier les matériaux. **(g-i)** Images BALM extraites d'un film pris pendant le dépôt contrôlé d'une seconde couche antireflet organique sur de l'oxyde de graphène, le contraste est triplé entre (g) et (i).

d'or nous a permis d'en déduire un revêtement BALM produisant un bon contraste pour l'observation du GO, à la fois dans l'air et l'eau. Ce revêtement est constitué de 0,5 nm de chrome comme couche d'accroche, plus 3 nm d'or et consititue le substrat de référence pour la suite de la thèse (sauf pour certaines expériences très spécifiques). Ensuite, nous avons montré que le contraste du GO peut être doublé en utilisant le bon indice de réfraction pour le milieu émergent.

Nous avons également étudié l'influence de la longueur d'onde sur le contraste. Pour cela, nous nous sommes intéressés aux monocouches de MoS_2 qui possèdent des propriétés optiques beaucoup plus dépendantes de la longueur d'onde que le graphène ou le GO. Tout d'abord, les images BALM et AFM ont été comparées afin de mettre en évidence la capacité de BALM à observer les monocouches de MoS_2 ainsi que les défauts issus de la méthode de croissance (nucléation de deuxièmes couches) et du transfert (plis, recouvrements de domaines). Par la suite, nous avons déterminé le contraste de la monocouche en fonction de la longueur d'onde. Ces résultats ont été comparés à des résultats de simulation numérique utilisant un modèle simple. Nous avons ainsi montré que BALM peut aider à préciser les mesures d'indice de réfraction obtenues par d'autres techniques. Nous avons également utilisés la dépendance en longueur d'onde des monocouches de MoS_2 et de WS_2 afin d'obtenir les conditions dans lesquelles les monocouches de MoS_2 présentent un contraste nul vis-à-vis de substrat alors que le WS_2 est toujours bien contrasté. Il est ainsi possible de différencier les matériaux, comme présenté à la figure R.1.d-f.

Dans la dernière partie de ce deuxième chapitre, nous avons étudié la dynamique de dépôt de couches moléculaires par photodéposition contrôlée. Pour cela, nous avons utilisé la photo-dimérisation du NBDT dont le produit est insoluble dans l'eau et donc se dépose sur la surface exposée à la lumière. Ces expériences ont notamment permis de montrer l'extrême sensibilité (très inférieure au nanomètre même à l'échelle du pixel individuel) de BALM pour ce type de mesures. Elles permettent également de montrer l'apport significatif de l'ajout d'une seconde couche organique et transparente au-dessus du film d'or afin d'améliorer encore les performances du revêtement antireflet. Nous avons étendu l'apport d'une seconde couche antireflet à des matériaux plus communs (comme le PMMA) et ainsi augmenté le contraste de l'oxyde de graphène.

L'un des atouts principaux de BALM est sa combinaison à d'autres techniques car le microscope inversé laisse un espace disponible à l'opposé de la mesure. Il est en particulier facile d'ajouter un liquide sur le substrat d'observation, tel que présenté sur la figure R.2.a. De plus, le revêtement antireflet est conducteur ce qui en fait un candidat parfait comme électrode de travail dans une configuration d'électrochimie. L'observation de l'interface entre l'or et l'électrolyte est réalisée à travers le revêtement antireflet qui sert aussi d'électrode de travail. Nous nous sommes donc particulièrement intéressés au couplage de mesures optiques et électrochimiques pour lesquelles le revêtement BALM sert d'électrode de travail.

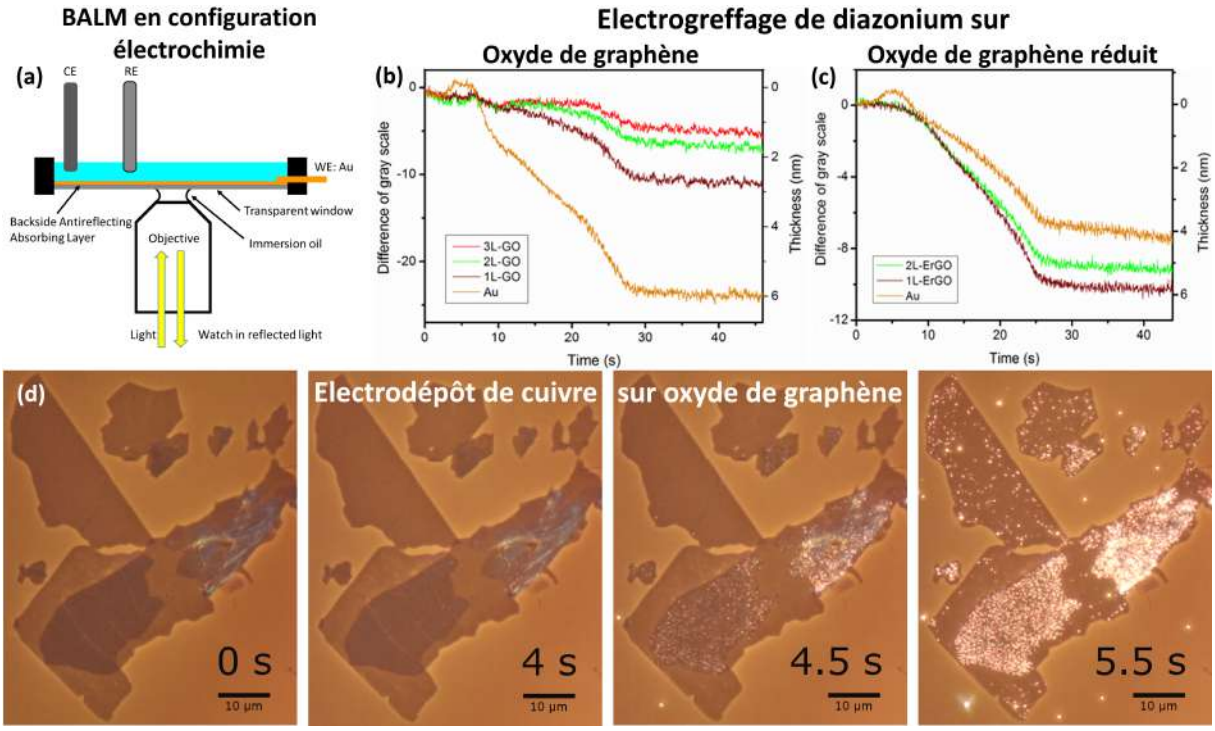

FIGURE R.2: (a) Schéma du dispositif BALM en configuration électrochimie, **(b-c)** Suivie optique de l'électrogreffage de sels de diazonium par voltamétrie cyclique, (b) sur une surface d'or et de GO, (c) sur une surface d'or et de rGO, il est montré que l'état de réduction du GO influence grandement l'épaisseur de la couche déposée. **(d)** images BALM extraites d'un film pris pendant l'électro-dépôt de cuivre sur GO. On observe ainsi l'intercalation préférentielle du cuivre entre les multicouches de GO.

Dans un dernier chapitre, nous avons d'abord étudié la plage de stabilité électrochimique de l'or car son épaisseur nanométrique le rend très sensible. Nous avons ainsi observé la dégradation de la surface pour des potentiels supérieurs à 0,3 V *vs.* Ag/AgCl. Par contre le substrat étant très stable pour les potentiels inférieurs à 0,3 V, nous avons décidé de nous intéresser principalement à des réactions de réduction dans cette thèse. Par la suite, l'impact du protocole de nettoyage des substrats BALM sur la voltamétrie a été étudié. La technique originellement utilisée était l'exposition à l'UV-ozone mais nous avons montré que celle-ci oxydait l'or à la surface, ce qui détériore drastiquement la surface d'observation lors de l'application de potentiels. Nous avons donc ajouté une étape de recuit après le traitement à l'ozone, ce qui permet une réduction de l'or sans altérer la surface. Nous avons ainsi déterminé un protocole de préparation des substrats antireflets combinant l'UV-Ozone et un recuit thermique produisant des substrats avec le moins de contaminations possible et une bonne stabilité en électrochimie.

Ensuite, l'impact du potentiel à l'électrode sur la réflectivité de l'interface or / électrolyte suivie en direct par la mesure optique BALM a été étudié. Pour cela nous avons effectué des études en voltamétrie cyclique et ainsi observé en direct l'effet Pockels qui correspond à un changement d'indice de réfraction lors de l'application d'un champ électrique. Nous avons ainsi observé la différence d'indice de réfraction entre la double couche électrochimique et la solution loin de l'électrode. De plus, nous avons étudié la dynamique de l'effet Pockels par chronoampérométrie, et donc suivi optiquement et en direct le chargement de la double couche électrochimique. Enfin, une évaluation préliminaire du couplage des mesures optiques et de la spectroscopie d'impédance électrochimique a pu montrer la gamme de fréquences atteignable par le montage expérimental actuel. Finalement, nous nous sommes intéressés à différents transferts de charges (médiateurs redox et réactions faradiques) et à leur influence sur le signal BALM.

L'étape suivante de ce travail consiste à combiner l'électrochimie à l'observation de matériaux 2D afin d'étudier localement leurs propriétés. Ceci est fait au travers de trois études.

Tout d'abord, nous avons étudié optiquement et *in situ* la dynamique de réduction électrochimique de l'oxyde de graphène (GO). Cela nous a permis la comparaison des vitesses de réduction des monocouches et des bicouches de GO, et montre la relation entre le nombre de couches et les constantes de temps associées à la réduction.

Ensuite, nous avons étudié l'électro-greffage de couches minces organiques par réduction de sels de diazonium avec dans un premier temps la comparaison entre BALM et la technique de microbalance à quartz qui est classiquement utilisée pour étudier la dynamique de dépôt sur surface. Nous avons mis en évidence l'équivalence entre le signal BALM qui est local et le changement de fréquence de la microbalance qui est moyenné sur toute la surface d'étude. Par la suite, cet atout de BALM a permis d'observer l'électro-greffage d'électrodes d'or et ainsi de montrer un effet de sur-greffage des bords d'électrodes dans certaines conditions de greffage d'un sel de diazonium (un complexe de type trisbipyridine de fer, TBPFe). Finalement, nous avons étudié l'électro-greffage de nitrobenzene diazonium (NBDT) sur une surface comportant des feuillets d'oxyde de graphène ou d'oxyde de graphène réduit électrochimiquement. Les résultats optiques de cette étude sont présentés sur la figure R.2.b-c, et montrent l'influence de la réduction du GO sur l'épaisseur et la cinétique de greffage.

Enfin, la possibilité de coupler BALM à l'électrochimie a été étendue à l'étude de l'électro-dépôt de métaux tel que le cuivre. Nous avons tout d'abord démontré l'intérêt de la technique pour observer en direct l'électro-dépôt de particules de cuivre sur un substrat d'or et ainsi obtenu des informations concernant le nombre de particules déposées, le pourcentage de surface couverte ainsi que la nature cristalline ou amorphe des particules. Par la suite, l'électro-dépôt de cuivre sur des surfaces présentant, soit du GO soit du rGO, a permis d'observer un comportement totalement opposé entre ces deux matériaux : le rGO bloque le dépôt de particules à sa surface alors que le GO permet l'intercalation très efficace du cuivre entre les multicouches, comme présenté sur la figure R.2.d.

En combinant versatilité et fort-contraste, la technique BALM est ainsi établie comme un outil très prometteur pour l'étude des matériaux 2D et en particulier pour la caractérisation locale et *in situ* de leur réactivité chimique et électrochimique. De plus, l'espace disponible au-dessus d'un microscope inversé en fait une plateforme d'observation pouvant être combinée à l'avenir avec beaucoup d'autres techniques de caractérisation telles que les microscopie à sondes locales (AFM, SECM, etc.) ou encore à la microscopie de fluorescence. Finalement, nous avons aussi démontré l'utilité de l'ajout d'une seconde couche antireflet pour apporter de nouvelles fonctionnalités suivant le type de matériau déposé comme du PDMS pour la micro-fluidique ou encore un isolant comme l'alumine pour coupler à l'avenir mesures optique et transistors à base de matériaux 2D.

Titre : Backside Absorbing Layer Microscopy : un nouvel outil pour l'étude des matériaux 2D

Mots clés : Backside Absorbing Layer Microscopy BALM, matériaux 2D, couches antireflets, caractérisations locales et *in situ*, propriétés optiques et électrochimiques

Résumé : La microscopie optique sur substrats antireflets est un outil de caractérisation simple et puissant qui a notamment permis l'isolation du graphène en 2004. Depuis, le domaine d'étude des matériaux bidimensionnels (2D) s'est rapidement développé, tant au niveau fondamental qu'appliqué. Ces matériaux ultraminces présentent des inhomogénéités (bords, joints de grains, multicouches, etc.) qui impactent fortement leurs propriétés physiques et chimiques. Ainsi leur caractérisation à l'échelle locale est primordiale.
Cette thèse s'intéresse à une technique récente de microscopie optique à fort contraste, nommée BALM, basée sur l'utilisation originale de couches antireflets très minces (2-5 nm) et fortement absorbantes (métalliques). Elle a notamment pour but d'évaluer les mérites de cette technique pour l'étude des matériaux 2D et de leur réactivité chimique. Ainsi, les différents leviers permettant d'améliorer les conditions d'observation des matériaux 2D ont tout d'abord été étudiés et optimisés pour deux matériaux modèles : l'oxyde de graphène et les monocouches de MoS_2. L'étude de la dynamique de dépôt de couches moléculaires a notamment permis de montrer à la fois l'extrême sensibilité de BALM pour ce type de mesures et l'apport significatif des multicouches antireflets pour l'augmentation du contraste lors de l'observation des matériaux 2D. L'un des atouts principaux de BALM venant de sa combinaison à d'autres techniques, nous nous sommes particulièrement intéressés au couplage de mesures optiques et électrochimiques pour lesquelles le revêtement antireflet sert d'électrode de travail. Nous avons ainsi pu étudier optiquement la dynamique de réduction électrochimique de l'oxyde de graphène (GO), l'électro-greffage de couches minces organiques par réduction de sels de diazonium sur le GO et sa forme réduite (rGO), ainsi que l'intercalation d'ions métalliques entre feuillets de GO.
En combinant versatilité et fort-contraste, BALM est ainsi établi comme un outil prometteur pour l'étude des matériaux 2D et en particulier pour la caractérisation locale et *in situ* de leur réactivité chimique et électrochimique.

Title: Backside Absorbing Layer Microscopy: a new tool for the investigation of 2D materials

Keywords: Backside Absorbing Layer Microscopy BALM, 2D materials, anti-reflective coatings, local and *in situ* characterizations, optical and electrochemical properties

Abstract: Optical microscopy based on anti-reflective coatings is a simple yet powerful characterization tool which notably allowed the first observation of graphene in 2004. Since then, the field of two-dimensional (2D) materials has developed rapidly both at the fundamental and applied levels. These ultrathin materials present inhomogeneities (edges, grain boundaries, multilayers, etc.) which strongly impact their physical and chemical properties. Thus their local characterization is essential.
This thesis focuses on a recent enhanced-contrast optical microscopy technique, named BALM, based on ultrathin (2-5 nm) and strongly light-absorbing (metallic) anti-reflective layers. The goal is notably to evaluate the benefits of this technique for the study of 2D materials and their chemical reactivity. The various levers to improve 2D materials observation were investigated and optimized for two model materials: graphene oxide and MoS_2 monolayers. The investigation of molecular layer deposition dynamic notably showed the extreme sensitivity of BALM for such measurements and the significant contribution of multilayers anti-reflective coatings to enhance contrast during the observation of 2D materials. One of the main assets of BALM comes from its combination to other techniques. We particularly considered the coupling between optical measurements and electrochemistry for which the anti-reflective layer serves as working electrode. We investigated optically the dynamic of electrochemical reduction of Graphene Oxide (GO), the electrografting of organic layers by diazonium salts reduction on GO and its reduced form (rGO), as well as the intercalation of metallic ions within GO sheets.
By combining versatility and high-contrast, BALM is established as a promising tool for the study of 2D materials, especially for the local and *in situ* characterization of their chemical and electrochemical reactivity.

Université Paris-Saclay

Espace Technologique / Immeuble Discovery

Route de l'Orme aux Merisiers RD 128 / 91190 Saint-Aubin, France